Spring 5-15-2023

Wide-field optical imaging of neurological disorders and sleep in mice

Lindsey M. Brier

WASHINGTON UNIVERSITY IN ST. LOUIS

Division of Biology and Biomedical Sciences
Neurosciences

Dissertation Examination Committee:
Joseph Culver, Chair
Mark Anastasio
Erik Herzog
Timothy Holy
Robyn Klein
Jin-Moo Lee

Wide-Field Optical Imaging of Neurological Disorders and Sleep in Mice

by

Lindsey Michelle Brier

A dissertation presented to
Washington University in St. Louis
in partial fulfillment of the
requirements for the degree
of Doctor of Philosophy

May 2023
St. Louis, Missouri

Contents

0.1 List of Figures

0.2 List of Tables

0.3 List of Acronyms

Aβ ..... Amyloid beta

AD ..... Alzheimer's Disease

AMBC ..... Allen mouse brain connectivity

ANOVA ..... Analysis of variance

APC ..... Axonal projection connectivity

ASE ..... Acute septic encephalopathy

BOLD ..... Blood-oxygen-level-dependent

CA ..... Cornu ammonis

CNS ..... Central nervous system

DCI ..... Delayed cerebral ischemia

D/Dex ..... Dexmedetomidine

DG ..... Dentate gyrus

DMSO ..... Dimethyl sulfoxide

DOT ..... Diffuse optical tomography

dpi ..... Days post infection

DVARS ..... Spatial root mean square of the data after temporal differentiation

EC ..... Entorhinal cortex

ECA ..... External carotid artery

EEG ..... Electroencephalogram

EMCCD ..... Electron multiplying charge-coupled device

EMG ..... Electromyography

eNOS ..... Endothelial nitric oxide synthase

FC ..... Functional connectivity

FFA ..... Fusiform face area

FFT ..... Fast Fourier transform

fMRI ..... Functional magnetic resonance imaging

fNIRS ..... Functional near infrared spectroscopy

FOV ..... Field-of-view

FWE ..... Family-wise error

FWHM ..... Full width half maximum

GECI ..... Genetically engineered calcium indicator

GVTD ..... Global variance of the temporal derivatives

HbO_2 ..... Oxygenated hemoglobin

HbR ..... De-oxygenated hemoglobin

HBSS ..... Hank's balanced salt solution

HF ..... Huynh-Feldt

i.c. ..... Intracranial

ICA ..... Internal carotid artery

ICU ..... Intensive care unit

i.p. ..... Intraperitoneal

IFNγR ..... Interferon gamma receptor

K/X ..... Ketamine/Xylazine

LED ..... Light-emitting diode

LPS ..... Lipopolysaccharide

MA ..... Mouse adapted

MCA ..... Middle cerebral artery

MEG ..... Magnetoencephalography

MFC ..... Multivariate functional connectivity

MMP ..... Matrix metalloproteinase

MVPA ..... Multivariate pattern analysis

MVPD ..... Multivariate pattern dependence

NIA ..... National Institute of Aging

NMDA ..... N-methyl-D-aspartate

N/NREM ..... Non-rapid eye movement

n.s. ..... Not significant

OIS ..... Optical intrinsic signal

OLS ..... Ordinary least squares

PA ..... Prediction accuracy

PBS ..... Phosphate buffered saline

PC ..... Principal component

PCA ..... Principal component analysis

p.f.u. ..... Plaque forming units

PostC ..... Postconditioning

pSTS ..... Posterior superior temporal sulcus

PT ..... Photothrombotic

QC ..... Quality control

R ..... Reproducibility

REM ..... Rapid eye movement

RFT ..... Random field theory

RMS ..... Root mean squared

ROI ..... Region of interest

RSV ..... Resveratrol

S1H ..... Somatosensory 1 hindpaw

SAH ..... Subarachnoid hemorrhage

sCMOS ..... Scientific complementary metal-oxide-semiconductor

SEM ..... Standard error of the mean

SGZ ..... Subgranular zone

SIRT1 ..... Sirtuin1

SNR ..... Signal-to-noise ratio

Ss ..... Somatosensory

SVD ..... Singular value decomposition

SVR ..... Support vector regression

tMCAO ..... Transient middle cerebral artery occlusion

USD ..... United States dollars

W ..... Wake

WOI ..... Wide-field optical imaging

WT ..... Wild-type

ZIKV ..... Zika virus

0.4 Acknowledgments

The following work is the product of multiple collaborations, interactions, and discussions with so many people that I have truly enjoyed working with and it would be a thesis in and of itself if I were to list all that I am grateful for here. So I will attempt to briefly, but thoroughly, address those that stood out as extremely influential and supportive:

First and foremost, I would like to thank my mentor, Joe. I was rotating in the NIL when I was advised to consider Joe's lab, AKA the "cool, drummer, optics guy". Kalyan excluded, I have never met another graduate student who started a punk rock band with their mentor, which I think speaks for itself when explaining our personal and professional relationship to others. Joe's musical guidance was often the same as when writing manuscripts: "less stressed grad student... more punk rock". I have enjoyed working in Joe's lab immensely. It's an incredibly welcoming environment, and we are encouraged to become independent thinkers very early on. This allowed me to stretch out and work on multiple incredibly interesting collaborations and create a hefty network of connections. Networking was always stressed by Joe, and not just within the US. Although he sent me to multiple conferences domestically (San Francisco, San Diego, DC, Miami, Chicago) he also supported me presenting my work in Canada and Japan. Not only has he provided multiple forms of support (e.g., intellectual, financial) but he has also put up with a barrage of slack messages from said stressed grad student. Together, we have co-authored at least 10 papers, with more on the way, so I'd say we rocked out. It was insanely fun working with you, *thank you*.

My thesis committee has been incredibly helpful and supportive during this journey. Erik Herzog was on my qual committee and has a knack for asking the most insightful (and hardest) biological questions, which has truly helped shape my paper on encephalopathy. Tim Holy asks the most challenging and thought provoking technical questions, and I truly enjoyed talking optics with him as well as TA-ing for his new statistical thinking in the

neurosciences class. I have had a very fruitful collaboration with Jin-Moo Lee, who has provided me with immense support on multiple manuscripts (sleep, LPS, SVR), as well as on my grant applications. Robyn Klein has provided invaluable counsel and assistance with the Zika project as well as guidance through the many administrative roles she has taken on in addition to running her lab. Finally, it has been a pleasure working with Mark Anastasio on the many projects applying machine learning algorithms to our optical data.

In addition to guiding me through the development of my thesis, I had the opportunity to work with a number of mentors on my thesis committee on interesting optical imaging application projects. Within the Lee, Klein, and Anastasio labs, I would like to specifically thank Eric Landsness, Shannon Agner, and Xiaohui Zhang for fruitful day-to-day discussions, collaborations, and manuscript writing. I would also like to thank Julian Clarke in Greg Zipfel's lab, and Sarah Smith in Azad Bonni's lab for working with me on extremely cool translational neuroimaging projects.

During my lab tenure, there were multiple students/faculty I interacted with. In particular, "the Adams" (Bauer and Eggebrecht) were significant players around the lab who made not only excellent band mates, but were always available and could fill in as mentors when Joe was unavailable. Patrick Wright and Jon Bumstead were great mentors that showed me the ropes before they left for their respective post doc/job. The Culver lab environment was incredibly fun, and I have so many fond memories hanging out/working with Arefeh Sherafati, Alexa Svoboda, Sean Rafferty, Mariel Schroeder (mom), Zack Markow, Paul Lin, Annie Bice, Seana Gaines, and Dana Wilhelm. But an extra special shout out goes to Ayy Ray Ray, Hay Hay, and Kay Kay (i.e., Rachel Rahn, Hunter Banks, Kalyan Tripathy). Make it be known my labmates were the reasons I got up and went into lab every morning (err... afternoon).

I have been incredibly fortunate to make some of the best friends ever here in St. Louis. I specifically would like to thank Sindhu (Lindhu forever), Ram, Allison, Chinwe (buddy),

Tam, Leeran, Rachel, and Lindsey for the emotional support and for always being up for games, food, venting (when needed), and laughs (always). My time in the MSTP (so far) would not have been nearly as great without my awesome band mates and co- Chuner, Ethan, Chris, Dillan, and Sarah. Yes, Kalyan, you get thanked separately (and again)- thanks for being the bunny to my sockhead.

Outside of St. Louis, I have so many friends and family that have supported me throughout this journey. Starting back at Allen High School, I made some of my best friends ever in Cera and Brian, who always supported the parallel development of my scientific and musical interests. At the University of Houston, I hit the jackpot with Aiat as my roommate, and through her, met Gulden, Laura (weird cheese friend), Dana, and the DeBakey crew: Fatima, Dasha, Rida, and Dema (acquaintance). Thank you guys, for believing in me, encouraging me, and being awesome women in science. My lab experience at U of H inspired my current pursuits and would not have been possible had it not been for the guidance and teachings of John Craft Jr. and accompanying shenanigans by Jeff and Amir. Also at U of H, Dr. Vida was the first professor I had that pushed me to start thinking about a basic science career and was incredibly encouraging and supportive in my applications for scholarships as well as MD/PhD programs. Extended family make annual baseball pilgrimages to see the St. Louis Cardinals (and my brother and I... and Ted Drewes) and I am so thankful to have such a wonderful, supportive, and fun family. My parents have been there for it all... whether teaching me multiplication with Hershey's chocolate or pulling their hair out over late night physics tutoring sessions (sorry about that). They have been unwavering in their support, have always believed in me, and been my biggest (and loudest) cheerleaders. A very special thanks to my brother, and WUStL MSTP alum, Matthew Brier. Although we will always be siblings and throw jabs at each other, thank you for always preparing me for what's to come.

The work herein was supported by numerous grants made to a variety of individuals

by the NIH and other funding organizations. My work in Joe's lab is specifically funded by R01NS099429, and R01NS090874. Additionally, NIA grant F30AG061932 funds my research work and ongoing development as a physician scientist.

Lindsey M. Brier

Washington University in St. Louis

May 2023

To Mom and Dad.

ABSTRACT OF THE DISSERTATION

Wide-Field Optical Imaging of Neurological Disorders and Sleep in Mice

by

Lindsey Michelle Brier

Doctor of Philosophy in Biology & Biomedical Sciences

Neurosciences

Washington University in St. Louis, 2023

Professor Joseph P. Culver, Chairperson

Neuroimaging has revolutionized the way in which we understand the hierarchical organization of the amazingly complex, interconnected human brain. Neuroimaging techniques, like functional magnetic resonance imaging (fMRI), have provided high quality structural and functional data, providing multiple in-depth analyses and biomarkers of disease processes. In animal models, mechanistic studies can uncover root pathologies that aren't explorable in humans. In mice, brain functional connectivity (FC) can be measured via Optical Intrinsic Signal (OIS) imaging – a modality that measures vascular reactivity as a surrogate for neural activity via quantification of fluctuations in oxygenated-hemoglobin (similar to the blood oxygen level dependent (BOLD) signal used in fMRI).

Another advantage of optical neuroimaging in mice is the expression of genetically encoded calcium indicators (GECIs), which provide cell-specific and network-level functional imaging of brain activity at speeds up to at least 4Hz. Imaging in higher frequency bands (compared to <0.2Hz in fMRI or other hemoglobin-based imaging modalities) allows for resolution of neural specific phenomena on the order of milliseconds, such as the global ∼1Hz slow oscillation that is characteristic of anesthesia and non-rapid eye movement (NREM) sleep. We imaged mice expressing the GECI GCaMP6 in excitatory neurons while awake, in NREM (verified by EEG), or under ketamine/xylazine (K/X) or Dexmedetomidine (Dex) anesthesia and reconcile discrepancies between activity dynamics observed with hemoglobin

vs. calcium (GCaMP6) imaging. Alterations in correlation structure were most obvious in delta band calcium NREM and anesthesia data, resulting in maps with large regions of polarized positive and negative correlations covering the field-of-view (FOV). We use principal component analysis (PCA) to provide evidence that the slow oscillation superimposes on FC rather than replaces FC patterns typical of the alert state.

While consciousness state can oscillate on the order of seconds, many studies of disease processes are most informative across a longer period of time. Surgical preparations coupled with optical imaging allow for longitudinal experiments on varying timescales. For example, sequalae of subarachnoid hemorrhage (SAH) include vasospasm, microvessel thrombi, and other delayed cerebral ischemic (DCI) events around 3 days post SAH. These DCI events have been shown to coincide with up-regulation of the neuroprotective peptide Sirtuin1 (SIRT1), using an endovascular perforation mouse model. Here, we display global FC disruption caused by SAH and DCI events in parallel with behavioral deterioration. Normal brain connectivity and behavior was maintained during SAH and DCI via two different treatments targeting SIRT1 activation. SIRT1-specific (resveratrol) and non-specific (hypoxic conditioning) treatments both protected against the FC deficits induced by SAH and DCI, with the latter providing the largest protective effect. This indicates that conditioning-based strategies targeting SIRT1-directed mechanisms provide multifaceted neurovascular protection in experimental SAH – data that further supports the overarching hypothesis that conditioning-based therapy is a powerful approach with great potential for improving patient outcome after aneurysmal SAH.

Studies involving focal injury (e.g., stroke, SAH) usually exhibit functional deficits surrounding the injured tissue, however, it is less clear how diffuse processes, such as novel models of acute septic encephalopathy (i.e., Delirium), and encephalitis caused by Zika virus infection, alter brain dynamics. Septic encephalopathy leads to major and costly burdens for a large percentage of admitted hospital patients. Elderly patients are at an increased risk,

especially those with dementia. Current treatments are aimed at sedation to combat mental status changes and are not aimed at the underlying cause of encephalopathy. Indeed, the underlying pathology linking together peripheral infection and altered neural function has not been established, largely because good, acutely accessible readouts of encephalopathy in animal models do not exist. In-depth behavioral testing in animals lasts multiple days, outlasting the time frame of acute encephalopathy. Here, we propose optical fluorescent imaging of neural FC as a readout of encephalopathy in a mouse model of acute sepsis. Imaging and basic behavioral assessment was performed at baseline, Hr8, Hr24, and Hr72 following injection of either lipopolysaccharide (LPS) or phosphate buffered saline (PBS). Neural FC strength decreased at Hr8 and returned to baseline by Hr72 in somatosensory and parietal cortical regions. Additionally, neural fluctuations transiently declined at Hr8 and returned to baseline by Hr72. Both FC strength and neural fluctuation tone correlated with behavioral neuroscore indicating this imaging methodology is a sensitive and acute readout of encephalopathy.

Zika virus (ZIKV) emerged as a prominent global health concern due to the severe neurologic injury in infants born to adults who had ZIKV infection during pregnancy. However, neurologic manifestations in healthy adults were subsequently reported during Zika pandemics in South America and Southeast Asia. In this population, infection can result in severe cases of encephalitis and have lasting impacts on cognition, and learning and memory, even after recovery from acute infection. Recent studies have uncovered extensive ZIKV-related neural apoptosis within the trisynaptic circuit involving the entorhinal cortex, the cornu ammonis, and the dentate gyrus of the hippocampus in adult mice. However, there are many contributing regions and circuits involved in cognition and learning and memory outside of this trisynaptic circuit. Communication within the cortex and between the cortex and hippocampus is necessary for a variety of neurological processes, such as performing cognitive tasks or for memory consolidation during sleep. Here, we investigate cortical net-

works and connectivity utilizing wide-field optical fluorescence imaging. We demonstrate that functional deficits congregate in regions of cortex that are highly communicative with hippocampus, such as somatosensory and retrosplenial cortices. Further, we prove that these functional imaging deficits are correlated with other metrics of disease severity, such as encephalitis score and increased delta power, providing a potentially useful clinical biomarker of disease. Finally, these imaging deficits resolve after recovery from acute infection.

While optical methods have obvious advantages when used to study animal models, the technique is relatively novel (compared to fMRI) therefore, there are many avenues for data processing algorithms to improve. Similar to fMRI, historically, optical methods use a remarkably simple bivariate Pearson-based approach to mapping FC, leading to quick and easy-to-interpret models of brain networks but also susceptibility to global sources of variance (e.g., motion, Mayer waves). Previously, we demonstrated the binarizing effect of the slow oscillation on FC during NREM and K/X anesthesia. While PCA effectively removed the slow oscillation, it is reasonable to assume that a biological process cannot be completely explained in algebraically orthogonal components. Therefore, we pioneer a multivariate approach to imputing individual neural networks from spontaneous neuroimaging data in mice in an effort to map connectivity with less susceptibility to confounding variance. Calcium dynamics in all brain pixels are holistically weighted via support vector regression to predict activity in a region of interest (ROI). This approach yielded remarkably high prediction accuracy, suggesting the optimized pixel weights represent multivariate functional connectivity (MFC) strength with the ROI. Additionally, MFC maps were largely impervious to the slow oscillation. Moreover, MFC maps more closely aligned with anatomical connectivity as modeled through axonal projection images, than FC maps. Lastly, MFC analysis provided a more powerful connectivity deficit detection following stroke compared to standard FC. These results show that MFC has several performance and conceptual advantages over standard FC and should be considered more broadly within the FC analysis community.

Further, with study of diffuse processes (e.g., LPS and ZIKV infection), statistical developments are crucial to solve the multiple comparisons problem when examining all cortical regions within the FOV. Therefore, part of this thesis focuses on the development of a streamlined, open source, user friendly data processing toolbox that contains multiple statistical approaches to make the aforementioned studies possible. Together, the following presents the multiple ways wide-field optical imaging can be used to learn more about the brain's functional architecture in health and disease.

0.6 Preface

The work presented herein is the product of multiple collaborations starting from my rotation in the Culver lab in 2016 to present. The specific chapters of this thesis will examine the work resultant in first authorship (or co-first) manuscripts, representing my primary efforts. One of the following chapters is now published, thus, figures and text are/is used with permission.

- **Chapter 1:** No copyrighted material.
- **Chapter 2:** No copyrighted material.
- **Chapter 3:** Contains material copyrighted by the Society of Photo-optical Instrumentation Engineers (*Neurophotonics*) which is used with permission [34].
- **Chapter 4:** No copyrighted material.
- **Chapter 5:** No copyrighted material.
- **Chapter 6:** No copyrighted material.
- **Chapter 7:** No copyrighted material.
- **Chapter 8:** No copyrighted material.

Lindsey Michelle Brier

Washington University in St. Louis

May 2023

quit it with the

DUCK!!!!!!!!!!!!!!!!!!!!!!!!!!!!!!!!

J. P. Culver

Chapter 1

The Biology of the Neurological Disorders and Sleep Explored with Optical Imaging

The work herein covers the functional neuroimaging of multiple neurological disorders as well as the healthy brain at rest. As optical imaging in mice is relatively novel (compared to functional magnetic resonance imaging; fMRI), part of this work also focuses on the development of data processing and handling of common statistical conundrums. The following chapter proposes organizational schemes for the work to follow as well as introduces each biological topic.

1.1 Functional Neuroimaging in Humans

Functional neuroimaging allows systems level investigation of brain processes in both humans and animal models [81, 259]. Human neuroimaging, mostly through functional magnetic resonance imaging (fMRI), is an attractive method to use clinically for diagnostic purposes and

in the laboratory to probe various research questions due to the non-invasive nature of data acquisition. Further, decades of work have gone into the development of streamlined, user friendly, and open source software for fMRI data processing [76] to provide motion scrubbed [198], high signal-to-noise ratio (SNR) recordings. The signal in fMRI data is based on fluctuations in blood oxygenation yielding a metabolically delayed surrogate measure of neural activity. Still, many aspects of human brain activity and disease have been studied using fMRI, providing multiple breakthroughs that are readily applicable to clinical diagnostics and treatment. However, there are multiple areas of human disease that preclude application of this non-invasive technique. Additionally, there is great utility in being able to control the genetic and environmental manipulations of an animal model. Therefore, there has been an increase in the use of various animal models of disease for fMRI study.

1.2 Functional Neuroimaging in Mice

Mouse brain dynamics and networks have significant similarity to the function and organization of human brain dynamics and networks. However, fMRI in mice has many logistical and technical challenges due to the relatively small size of the mouse brain. This necessitates an extremely powerful magnet, and other specially engineered components, increasing the cost and exclusivity of small animal fMRI significantly. Optical imaging can provide cellular resolution with widely-available off-the-shelf components [41]. Recently, wide-field optical imaging (WOI) has been used to perform "mesoscopic" recording of brain dynamics across the entire dorsal cortical surface of the mouse, meaning the potential cellular resolution is blurred to comparable fMRI resolution to create around 100μm pixels in order to image quickly to increase the temporal resolution of the imaging system [34, 265, 151]. A similar hemoglobin-based dynamic is captured with WOI due to the differential wavelength absorption patterns of oxygenated and de-oxygenated hemoglobin [149]. Additionally, with

the advent of optically excitable genetically encoded calcium indicators (GECIs), many WOI systems are equipped to perform concurrent hemoglobin and calcium-based recording [234], the latter expanding the temporal dynamic range of functional neuroimaging studies up to 8Hz. This has allowed for mouse functional neuroimaging studies to focus in on blood-based and cell-specific (e.g., neural) brain network dynamics and be readily accessible to a wide variety of laboratories. Therefore, a depth of literature has been created, however this work has lagged behind the developments in human fMRI. The work in this thesis aims to both 1) draw from and develop data processing algorithms within the fMRI software development literature and apply them to WOI data and 2) use these techniques to pioneer novel functional neuroimaging studies of various biological phenomenon inaccessible to fMRI.

1.3 Functional Neuroimaging of Sleep

One of the unique challenges in imaging animal models (compared to humans) is the propensity of researchers to utilize anesthesia or animals fall asleep during an experimental paradigm. Specifically, mice enter and exit the various stages of sleep (e.g., non-rapid eye movement NREM, rapid eye movement REM) on the order of seconds, which significantly alters brain dynamics compared to the awake, alert state [265, 169]. Most noticeably, during NREM and some forms of anesthesia, a $\sim$1Hz quasi-periodic global "slow oscillation" propagates from anterior to posterior brain regions throughout the duration of these sleep stages [235, 158]. Additional changes can include the presence of sleep spindles (bursts of 10-12Hz frequency activity) [188] and alterations in infraslow (traditionally, $<$0.2Hz) brain connectivity [136]. Indeed, sleep is a necessary and important phenomenon for maintaining whole-body homeostasis, resting, repairing, and cleaning up after various brain processes during the day [264]. Importantly, altered or dysfunctional sleep often results in toxin accumulation and subsequent increases in risk for various pathologies (e.g., cancer, Alzheimer's Disease, stroke) [123].

Despite this, little is known about the specific mechanisms through which sleep manages and maintains normal brain function. Historically, sleep is studied using electroencephalogram (EEG), which excels at temporal sampling, but is spatially limited due to sparse sampling and the difficulties associated with solving the inverse localization problem [98]. Specifically, it is not well understood how brain dynamics alter network connections throughout all spectral bands that get altered in sleep/anesthesia. From another point of view, it is not understood to what extent sleep/anesthesia alters brain dynamics and thus confounds processes specific to healthy functioning or disease phenotypes in neuroimaging experiments utilizing animal models.

1.4 Functional Neuroimaging of Focal Stroke

The mouse models of disease studied throughout this work focus on two large umbrella types: 1) focal and 2) diffuse. Stroke is a focal debilitating disease in which the blood supply to the brain is compromised, thus resulting in oxygen-deprived necrotic tissue. A photothrombotic model of stroke is used throughout to produce a focal deficit of neural activity in an experimenter specified manner in order to illustrate the usefulness and advantages of various analytical algorithms to localize and visualize the core of the stroke pathology [133]. A sub-type of stroke, subarachnoid hemorrhage (SAH), results in neurological deficits due to the rupturing of a blood vessel and subsequent starvation of the surrounding parenchyma of oxygen. Occurrence of SAH is in about 30,000 Americans per year, with a 30% mortality rate and 50% having long term deficits outlasting the time frame of SAH [131, 37, 102]. A novel endovascular perforation model of SAH involves a nylon suture perforating the internal carotid artery bifurcation and most closely models the pathology behind human SAH. Clinically, delayed cerebral ischemia (DCI) events initiated by SAH are the biggest treatable risk factor for poor outcome and is adequately modeled through the endovascular perforation

mouse model [32]. Large artery vasospasm was long thought to be the major contributor to DCI in the acute time frame following SAH [152], however, recent work has indicated major roles played by autoregulatory breakdown [196], microvessel thrombi [247], and blood brain barrier breakdown [255]. Here, we investigate the effects of this endovascular perforation model of SAH and subsequent DCI on brain functional connectivity (FC).

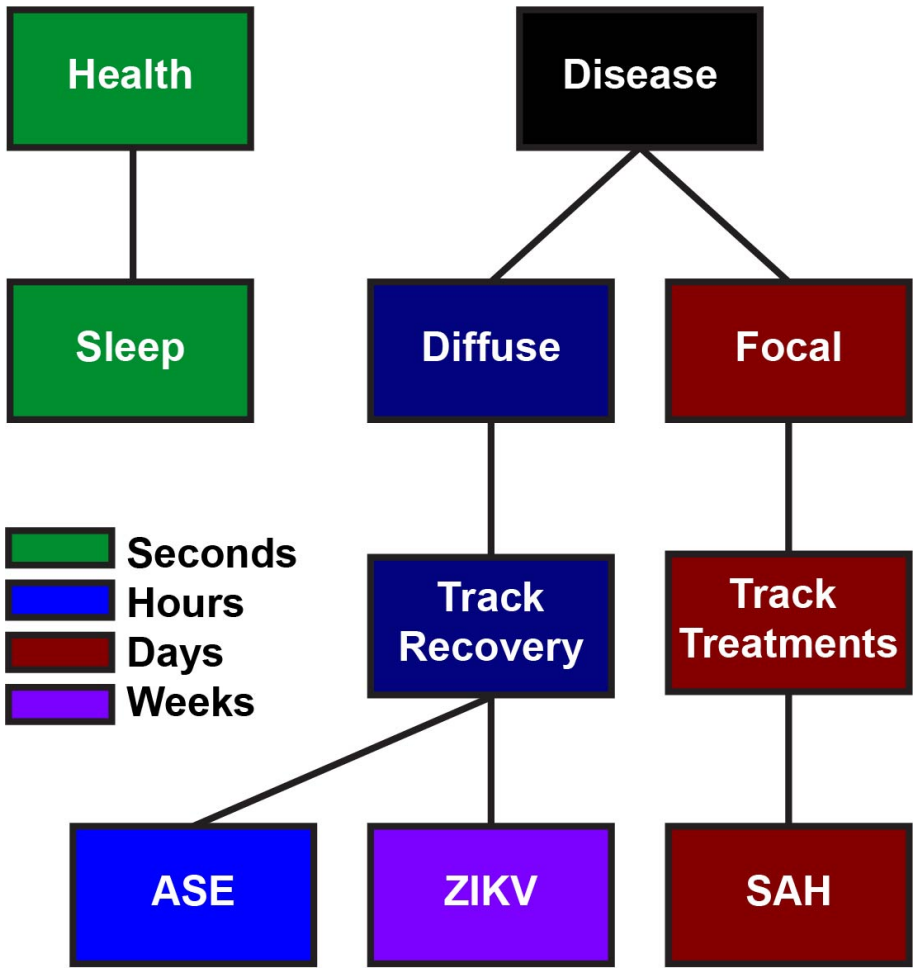

Figure 1.1: Categorizing neuroimaging projects in health and disease

1.5 Functional Neuroimaging of Diffuse Encephalopathy and Encephalitis

Encephalopathy or encephalitis is a diffuse brain disease that may or may not have origins within the central nervous system (CNS). A significant clinical conundrum lies in the cases of delirium or encephalopathy that are initiated by peripheral infection (e.g., acute septic encephalopathy ASE). Acute mental status changes occur in up to 80% of intensive care unit (ICU) or 20% of general hospital stays, imposing a significant resource and cost burden on hospitals and patients themselves [216, 125]. Further, many accidents occur due to mental status changes and confusion and treatments are aimed at sedation and treatment of the peripheral infection rather than any underlying neurological phenomenon. Because of this, neurological deficits can outlast the time frame of active infection. Little is known about the underlying cause of ASE largely because good, acutely-available readouts of encephalopathy in relevant animal models do not exist. Indeed, behavioral testing, which is the "gold standard" in judging mental status deficits, takes multiple days and outlasts the time-frame of ASE. Here, we propose FC of mice injected with a peripheral immune stimulus as a sensitive and timely biomarker of ASE. Similarly, Zika virus (ZIKV) rose to prominent global health concern due to congenital defects associated with ZIKV infection [206], but also due to neurological deficits induced in an infected adult [43, 44]. ZIKV exhibits a semi-specific tropism for hippocampal regions and results in learning and memory defects [89]. There is not a clear picture of the complete pathogenesis and phenotype of ZIKV infection. Specifically, it is not well understood what other brain regions are altered during active infection and how those regions may influence the resultant phenotypic presentation.

1.6 Functional Neuroimaging on Varying Timescales

Interestingly, the fruit salad of projects presented here result in multiple stories all spanning incremental time frames. As mentioned previously, mice go in and out of sleep stages on the order of seconds. Our investigation of sleep includes WOI and concurrent EEG monitoring for sleep stage. The EEG is used to categorize the WOI data as awake, NREM, REM, or movement artifact in 10 second epochs [34]. Next, our mouse model of encephalopathy involves peripheral injection of an immune stimulus and imaging is performed over the next 72 hours to model the time course of ASE. This includes monitoring at baseline, peak disease, and recovery. The SAH model used here results in DCI events at 3 days post endovascular perforation, in line with the time frame described in the current DCI literature. Finally, ZIKV infection results in peak encephalitis at 1 week post infection and we image the ZIKV infected mice at peak infection (1 week post) and after recovery (6 weeks post).

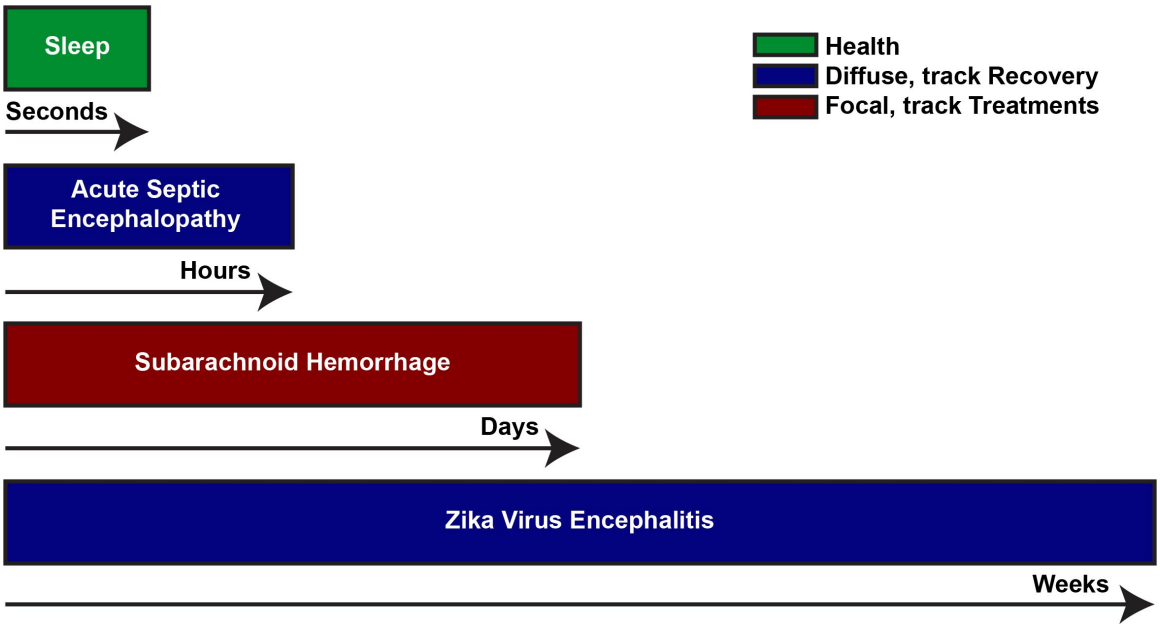

Figure 1.2: Categorizing neuroimaging projects in time

1.7 Functional Neuroimaging during Recovery and Treatment

The last way to categorize these projects is by looking at them as efforts to understand how brain networks function in health, disease, recovery, and under treatment. The investigation of the effects of sleep and anesthesia on brain network connectivity is performed in otherwise wild-type mice. Both the studies of ASE and ZIKV cover peak encephalopathy/encephalitis and follow each model to recovery (recovery as defined in ASE through this novel biomarker and subsequent behavior score, and recovery as defined in the existent ZIKV literature). Lastly, SAH is studied in the context of peak disease and multiple imposed treatment paradigms. Of particular interest were conditioning based treatments that would harness the brain's intrinsic resistance to disease. Specifically, we investigate the effects of hypoxic postconditioning on mitigating the effects of DCI after SAH. Additionally, we isolate the specific upregulation of Sirtuin1 activity and probe the efficacy of Sirtuin1 agonists as a method to treat DCI.

1.8 Method Development for WOI

This thesis starts and ends with a chapter on various method development projects to supplement the biological narratives. As optical neuroimaging is relatively novel compared to fMRI, there are multiple avenues for borrowing and developing algorithms from fMRI to fit the WOI data. We pull some ideas from this literature and pioneer a few novel algorithms for statistical handling of the multiple comparisons problem. We also propose a multivariate approach to modeling functional connectivity and compare to the standard Pearson-based approach.

Chapter 2

General Methods: An Open Source Statistical and Data Processing Toolbox for Wide-Field Optical Imaging in Mice

This chapter will introduce the various technical and/or data processing algorithms that have been either streamlined or developed. All code mentioned below is available in a user-friendly open-source GitHub repository (link in Methods). Unless otherwise specified, the data in the remaining chapters have undergone the data processing and statistical testing described here.

2.1 Introduction

Functional neuroimaging has enhanced our study of systems neuroscience and understanding of neural networks [81, 80]. Mainly, this has been accomplished with blood oxygen level

dependent (BOLD) fluctuations in functional magnetic resonance (fMRI) data in human subjects [113]. In order to better understand human conditions, there has been an increase in functional neuroimaging in animal models, also performed using fMRI [239, 180, 50]. However, the relatively small size of the mouse brain offers multiple technical and logistical challenges with fMRI. Therefore, there has been a transition to using wide-field optical imaging (WOI) techniques in the mouse, yielding similar blood-based surrogates of neural activity at a similar spatial scale [259]. The advent of genetically encoded calcium indicators (GECIs) enables cell-specific labelling and increased temporal resolution compared to traditionally measured hemodynamics [265, 34, 151]. Combined hemoglobin and fluorophore imaging is readily available with optical imaging systems and harnesses the advantages of GECIs as well as maintains a translatable blood-based recording directly comparable to human fMRI. WOI analysis faces many of the same procedural steps and therefore difficulties as those experienced with fMRI analysis, such as data processing, visualization, and statistical testing. However, the relative novelty of WOI compared to fMRI means that there is a need for many of the solutions within the fMRI community to be translated to the WOI data analysis communities.

One of the biggest statistical challenges within the functional neuroimaging community is the problem of correcting for multiple statistical tests. Many solutions have been proposed within the fMRI community [147, 104], however, none have been translated into an easy-to-use WOI toolbox. Historically, functional connectivity (FC) is examined using both a seed-based and a matrix-based approach [246]. For seed-based maps, common practice includes performing a pixel or voxel-wise statistical test (e.g., student's t) resulting in thousands of tests being performed within the field-of-view (FOV). The most stringent correction (i.e., Bonferroni), assumes each statistical test is independent [1]. This is certainly not the case when examining neighboring pixels within a brain region for multiple reasons. For most mesoscopic WOI instruments, the full-width half-maximum (FWHM) spans multiple

pixels thus rendering each pixel not independent from an instrumentation point of view. Additionally, from a biological point of view, it is reasonable to assume an amount of dependence between neighboring pixels within the same brain region. A more plausible approach borrowed from fMRI to handle the multiple comparisons problem weights a larger area of continuous neighboring significant pixels as more likely to be a statistically significant finding, compared to isolated pixels surviving an individual statistical test [85, 106]. However, this approach has not been translated from voxel to pixel space and applied to two-dimensional WOI data.

Although FC matrices inherently go through a certain amount of data reduction, a well-sampled FOV can still lead to hundreds of multiple comparisons. A simple data reduction technique to display the average FC value within an entire cortical area (as determined by the Paxinos atlas [259]) can be just as informative, giving a sense of inter and intra-cortical connectivity. Then, a Bonferroni correction would be more appropriate as comparisons become between inter-cortical and regions are less (though still could be) likely to be dependent (compared to intra-cortical region dependence). Here, we provide a mouse optical data processing toolbox to streamline and make pre-processing steps transparent and user friendly. Within it, we apply the fMRI cluster size-based approach to determining statistical significance to wide-field optical FC mapping in the context of photothrombotic stroke. Additionally, we provide our methods in data reduction and matrix enrichment testing to be used throughout the WOI community.

2.2 Methods

2.2.1 Animals

For bilateral FC analysis, four 3-4 month old mice (2 male, 2 female) were imaged at baseline (Day 0) and on Day 3 post photothrombotic stroke to left somatosensory forepaw cortex.

For FC matrix analysis, a total of 16 female (ranging from 3-7 months old) mice were used. All mice (N=20) were Thy1-GCaMP6f (Jackson Laboratories Strain: C57BL/6J-Tg(Thy1-GCaMP6f)GP5.5Dkim; stock: 024276). These mice express the protein GCaMP6f in excitatory neurons, primarily in cortical layers ii, iii, v, and vi [265]. All studies were approved by the Washington University School of Medicine Animals Studies Committee and follow the guidelines of the National Institutes of Health's Guide for the Care and Use of Laboratory Animals.

2.2.2 Surgical Preparations

Prior to imaging, typical surgical preparations were implemented [34, 218]. Briefly, an optically transparent plexiglass window was implanted with translucent dental cement (C&B-Metabond, Parkell Inc., Edgewood, New York) following a midline incision and clearing of skin and periosteal membranes. The window covered the majority of the dorsal cortical surface and provided an anchor for head fixation and allowed for chronic, repeatable imaging. The N=16 mice used for FC matrix computation had stainless steel EEG self-tapping screws (BASI Inc., West Lafayette, IN, USA) fixed at approximately -1mm posterior to bregma, and +/- 5mm lateral to bregma (near barrel/auditory cortex), although EEG recording was omitted for the present report. The dataset used in the following analyses consists of two ten-minute imaging runs from each mouse in the N=16 group. One ten-minute run from one mouse was discarded due to increased variance in the raw light levels.

2.2.3 Photothrombosis

In N=4 (2 male, 2 female, all are mice that did not receive EEG screws), mice were secured in a stereotaxic frame under isoflurane anesthesia. 200 μl of Rose Bengal (Sigma Aldrich) dissolved in saline (10 g/liter) was injected intraperitoneally. After 4 minutes, a 532-nm

diode-pumped solid-state laser (Shanghai Laser & Optics Century) was focused to 2.2mm left and 0.5mm anterior to bregma with a 0.5mm spot size and at 23mW for 10 minutes [133]. Mice were imaged at baseline (i.e., prior to photothrombosis (Day 0), and 72 hours post (Day 3). The dataset used in the following analyses consists of two five-minute imaging runs from each mouse.

2.2.4 Fluorescence and Optical Intrinsic Signal (OIS) Imaging

Mice were head-fixed in a stereotaxic frame and body secured in a black felt pouch for imaging. Sequentially firing LEDs (Mightex Systems, Pleasanton California) passed through a series of dichroic lenses (Semrock, Rochester New York) into a liquid light guide (Mightex Systems, Pleasanton California) that terminated in a 75mm f/1.8 lens (Navitar, Rochester New York) to focus the light onto the dorsal cortical surface. LEDs consisted of 470nm (GCaMP6f excitation), 530nm, 590nm, and 625nm light. An sCMOS camera (Zyla 5.5, Andor Technologies, Belfast, Northern Ireland, United Kingdom) coupled to an 85mm f/1.4 camera lens (Rokinon, New York New York) was used to capture fluorescence/reflectance produced at 16.8 Hz per wavelength of LED. A 515nm longpass filter (Semrock, Rochester New York) was used to discard GCaMP6f excitation light. Cross polarization (Adorama, New York New York) between the illumination lens and collection lens discarded artifacts due to specular reflection. The field-of-view (FOV) recorded covered the majority of the convexity of the cerebral cortex (1.1cm^2), extending from the olfactory bulb to the superior colliculus. All imaging data were binned in 156x156 pixel^2 images at approximately 100 μm^2 per pixel.

2.2.5 Imaging Data Processing

Image processing followed methods previously described [265, 149] and summarized here. Images were spatially downsampled to 78x78 pixel^2 and a frame of ambient baseline light levels was subtracted from the time series data. Data were temporally downsampled by a factor of 2 and then spatially and temporally detrended. The logarithmic mean of frames corresponding to reflection data produced by the 530nm, 590nm, and 625nm light were used to solve the modified Beer Lambert law to yield fluctuations in oxygenated and deoxygenated hemoglobin. Frames corresponding to fluorescence data were mean normalized and corrected by approximating hemoglobin absorption of the excitation and emission light, following which the logarithmic mean was taken. All data were spatially smoothed with a 5x5 Gaussian filter. The global signal was regressed from the time series data, data were Affine transformed to common Paxinos atlas space and data were filtered with a 0.4-4.0Hz Butterworth bandpass filter.

2.2.6 Functional Connectivity

Functional connectivity (FC) analysis refers to the calculation of a Pearson correlation coefficient between two time traces:

$$\rho_{x,y} = \frac{cov(x,y)}{\sigma_x \sigma_y} \tag{2.1}$$

where ρ is the Pearson correlation coefficient between time trace x and y, $cov(x,y)$ is the covariance between time trace x and y, and σ are the standard deviations within time traces x and y. For bilateral FC maps, the Pearson correlation coefficient is computed between pixels on the left-hand side of the brain and the respective mirror imaged pixel on the right-hand side. For FC matrices, the Pearson correlation between the average time trace within two seed regions is computed.

2.2.7 Cluster Size-Based Statistical Thresholding

A challenge with analyzing the statistical significance in functional imaging is managing the multiple comparisons problem. Here, we used a cluster size-based method that leverages the spatial connection between pixels, and credits large clusters as having more statistical significance than small clusters with the same peak t-value. More specifically, we used a cluster-size based thresholding method to analyze FC maps, and to ensure the family-wise error (FWE) rate did not exceed 5%. A random field theory (RFT) approach was adapted from the fMRI and DOT literature [106, 85]. Using RFT, we are able to approximate the expected number of clusters (m) in an image at a given z-score threshold (Z_t):

$$E[m] = R * 4\ln(2) * 2\pi^{-\frac{3}{2}} * Z_t e^{-\frac{1}{2}*Z_t^2} \tag{2.2}$$

Which holds true for increasing values of Z_t. Here, we use $Z_t = 3.09$ which corresponds to a false positive rate of 0.001 at the pixel level. R represents the number of resolution elements provided by the optical system:

$$R = \frac{x^2}{FWHM^2} \tag{2.3}$$

Where x is the number of pixels in the image in one dimension and $FWHM$ is the full width half maximum of the point spread function estimated from the spatial autocorrelation of a fully processed image in one dimension. Here, we use $pixels = 78$ pixels and calculate a $FWHM$ of about 14 pixels. We are able to then approximate the expected number of pixels (N) above Z_t by:

$$E[N] = E[m] * E[n] \tag{2.4}$$

Where n is the pixel count within a cluster and:

$$E[n] = \frac{2\pi FWHM^2}{Z_t^2 \Gamma(2) 4\ln(2)} \tag{2.5}$$

where Γ is the gamma function. The probability that n will exceed any threshold, x, can be modeled by the exponential function:

$$P(n \geq x) = e^{-\beta x} \tag{2.6}$$

Where β can be expressed as:

$$\beta = \frac{\Gamma(2) E[m]}{E[N]} \tag{2.7}$$

Substituting equation 2.5 into equation 2.4 and then the newly formed equation into equation 2.7 rearranges the above to:

$$\beta = \frac{\Gamma(2)^2 Z_t^2 4\ln(2)}{2\pi FWHM^2} \tag{2.8}$$

Providing an equation (with all previously solved for values) that varies with the inverse of the squared $FWHM$. We only want clusters to survive thresholding with a family wise error rate of 0.05 (α), therefore, we want to find the pixel count threshold, k_α, that would result in at least one cluster surviving threshold when there is no true significant difference, 5% of the time. Essentially, we are asking for a k_α where the following is true:

$$P(n \geq k_\alpha) = \alpha \tag{2.9}$$

Assuming no clusters are a true positive. Which, mathematically speaking, is the same as solving for 1 minus the probability that no clusters have a pixel count above threshold k_α:

$$P(n \geq k_\alpha) = \sum_{i=1}^{\infty} P(m = i)[1 - P(n < k_\alpha)^i] = 1 - e^{-E[m] * P(n \geq k_\alpha)} \tag{2.10}$$

Which yields:

$$k_\alpha = \frac{1}{\beta} \ln \left(\frac{-E[m]}{\ln(1 - \alpha)} \right) \tag{2.11}$$

After substituting equation 2.6 into equation 2.10 and solving for k_α.

Pixel-wise t-tests were performed on connectivity maps to compare Day 0 and Day 3 results. These t-test maps were then thresholded, leaving pixels with a t-value corresponding to $p < 0.05$. Any clusters of surviving pixels with a pixel count greater than k_α survived significance testing according to this cluster size-based technique throughout the manuscript.

2.2.8 Matrix Enrichment

The challenge of managing the multiple comparisons problem is still present with FC matrix analysis. Additionally, the non-intuitive presentation of such analysis precludes interpretation by non-imaging groups. Therefore, we have established a simple solution to both problems. The average intra-cortical region Pearson correlation coefficient is stored in the same surface area as presented in the individual seed method. This data reduction method increases the maximum Bonferroni p-value threshold by an order of magnitude as well as increases the readability of the plots.

2.2.9 Data and Code Availability

In order to promote validation and comparative analyses by external groups, data and specific code will be made available on request. The toolbox presented here, (for WOI pre-processing and analysis) is available online (Mouse WOI GitHub) and was used for all present analysis. Example data is available on Figshare (Sample Data).

2.3 Results

2.3.1 Toolbox Overview

We seek to distribute a comprehensive, easy-to-use, open-source toolbox for mouse WOI data processing and analysis. Within this toolbox, we have translated multiple techniques from the human fMRI literature to the WOI mouse world. The toolbox is largely split up into three pipelines (Figure 2.1). User input is needed to organize mouse and instrument specific details to be read in, along with a single frame (Figure 2.1A). That single frame is used for the creation of mask and seed files. Binary masks are created using the roipoly.m function in MATLAB and the user traces the outline of the brain regions present in the FOV. Seed regions (for FC analysis and affine transform) are created by the user identifying the anterior suture and lambda. Based on user input in Figure 2.1A, pre-processing of the data is performed following the steps outlined in Figure 2.1B. Instrumentation details from Figure 2.1A will allow the program to split up the imaging frames to solve for either hemoglobin, fluorophore, or both concentration changes over time. All these steps are organized into independent sub-routines, allowing the user to add or subtract steps within the master script as needed. There are optional quality control (QC) outputs before and after the data is optionally temporally filtered that can be used for data scrubbing procedures. After pre-processing of the data, the analysis pipelines are largely similar (Figure 2.1C). First, the analysis is performed on each individual run for each individual mouse, followed by an averaging across mice. A statistical comparison is then performed on the data (user specified) and the cluster size-based thresholding is used to determine regions of statistical significance. Only with the seed-based FC analysis are matrices produced and matrix enrichment occurs.

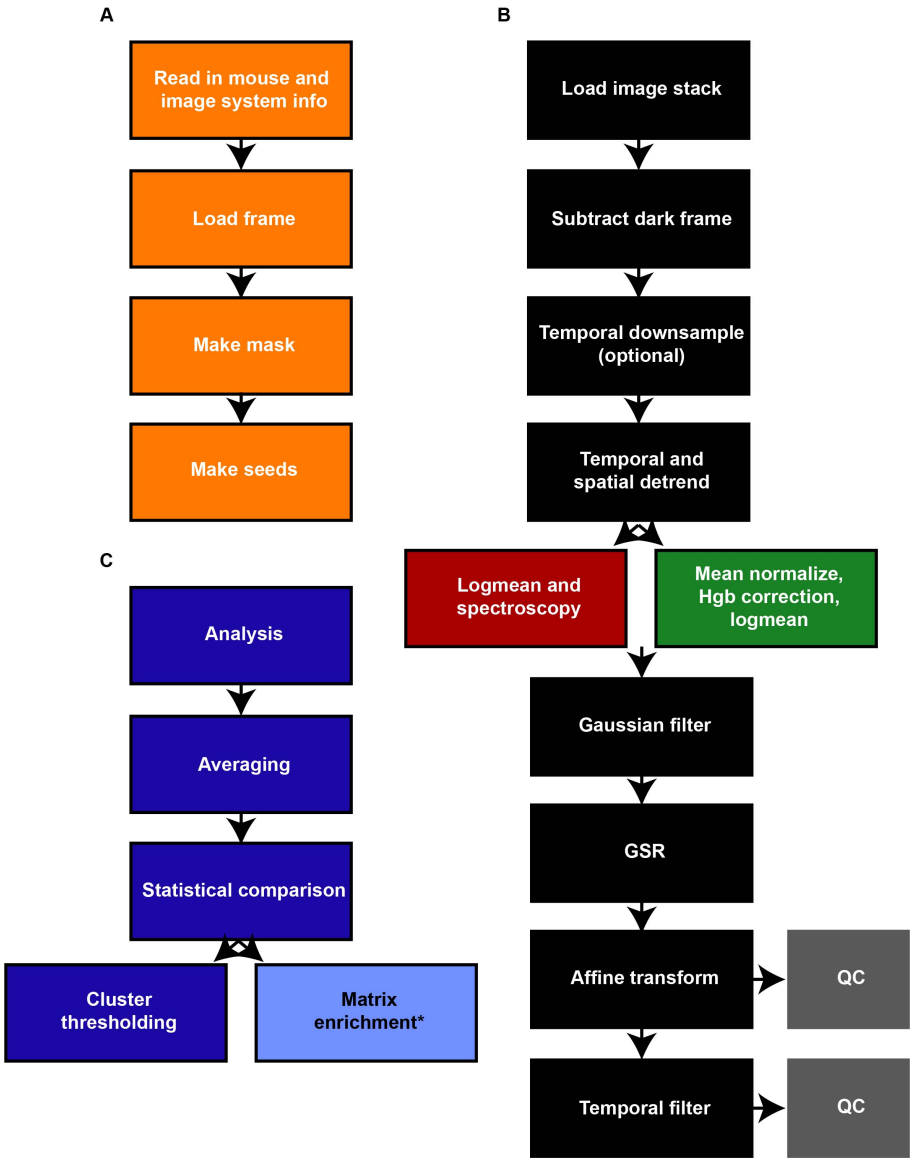

Figure 2.1: A) User input needed for these steps. Excel sheet with mouse information as well as image system information is read into the pipeline. A single frame is loaded and a user defined binary mask (using the roipoly.m function) and seed locations are created. B) These steps will run without user input. Step-wise illustration of the data pre-processing pipeline color-coded for hemoglobin (red), fluorophore (green), or both (black, grey) specific steps. C) After the pre-processing steps in A),B), the toolbox supports various types of data analysis and all follow the illustrated analysis pipeline. The initial analysis is performed per run, per mouse, followed by averaging across mice. A pixel-wise statistical comparison is performed (e.g., t-test) and the cluster-based thresholding technique is implemented for significance. *Only for seed-wise FC are matrices created and fed through the enrichment pipeline.

2.3.2 Cluster Size-Based Thresholding Applied to Stroke Data

A cluster size-based statistical thresholding method [85, 106] was adapted from the fMRI and DOT literature and used to select clusters of size k_α (expressed in number of pixels) with $p<0.05$ by the pixel-wise paired t-test method that satisfies the pixel-wise false positive rate (set by Zt) and overall family-wise error rate (Figure 2.2A,B). Using this cluster size cutoff, we were able to compare bilateral FC maps at baseline (N=4, Day 0) and 72 hours post (N=4, Day 3) photothrombotic stroke (Figure 2.2C). Photothrombosis was induced in left somatosensory cortex which resulted in loss of homotopic FC at Day 3. A pixel-wise t-test was performed and thresholded to only display regions with $p<0.05$ (note, this map is not corrected for multiple comparisons). Using the cluster-size based threshold (FWE=0.05) we were able to localize a somatosensory anchored deficit. Using the Bonferroni correction for multiple comparisons, no regions survived this stringent cutoff, resulting in no significant differences between Day 0 and Day 3 with this method.

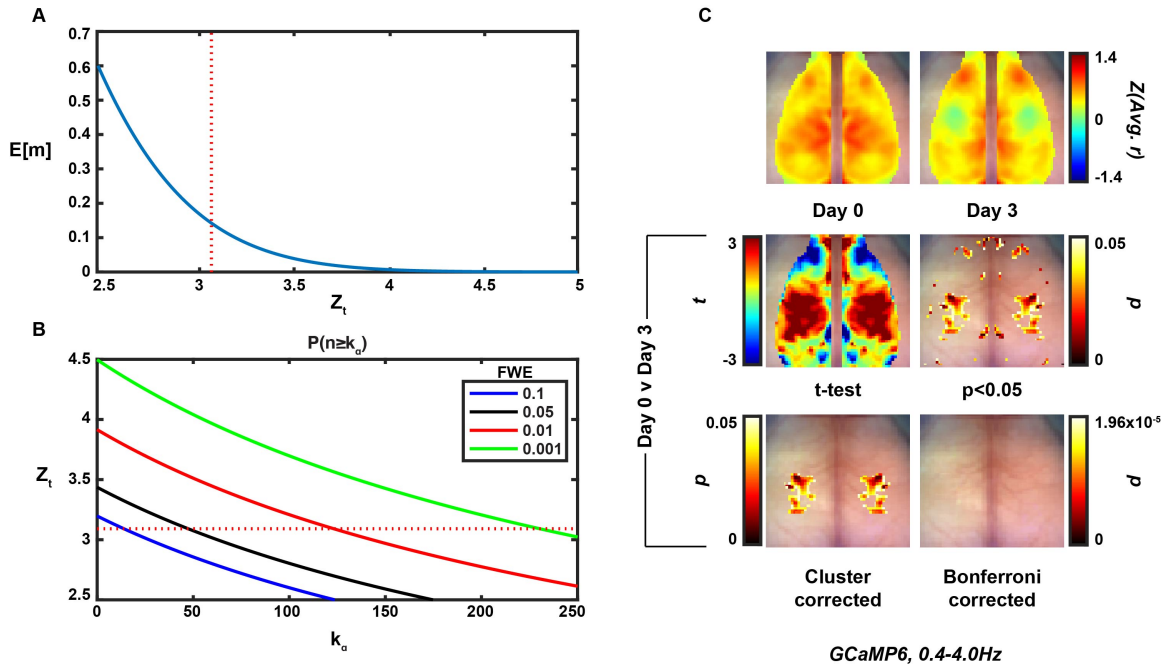

Figure 2.2: A) The relationship between the pixel-wise false positive rate (determined by Zt, dashed red line is Zt=3.09 which corresponds to p=0.001) and the expected number of clusters to survive thresholding due to chance (E[m]). B) The relationship between the pixel-wise false positive rate (determined by Zt, dashed red line is Zt=3.09 which corresponds to p=0.001), the family-wise error rate (here, 0.05) and cluster size needed for significance. C) (top row) Average (N=4) bilateral FC maps pre (left) and three days post (right) photothrombotic stroke to left somatosensory forepaw cortex. (middle row) Pixel-wise paired t-test (left) and thresholded image for pixels with p¡0.05 (right). (bottom row) Thresholded image with FWE=0.05 using the cluster size-based method (left) and image with Bonferroni correction for multiple comparisons (right).

2.3.3 Matrix Enrichment Presents Easily Digestible Resting State FC

Mice that had not undergone any experimental manipulations were imaged and FC matrices utilizing all standard seeds in the FOV were computed (N=16, Figure 2.3A). A one-sided t-test was performed on each matrix index to isolate significant positive or negative correlations (Figure 2.3B). A Bonferroni correction for multiple comparisons resulted in a number of significant positive and negative correlations present at rest in non-experimental mice (Figure 2.3C). To decrease the number of comparisons and improve readability of plots, a data reduction technique was implemented to "enrich" the FC matrices (N=16, Figure 2.3D). Similarly, a comparison-wise one-sided t-test was performed (Figure 2.3E) and the matrix was thersholded using a Bonferroni correction for multiple comparisons (Figure 2.3F).

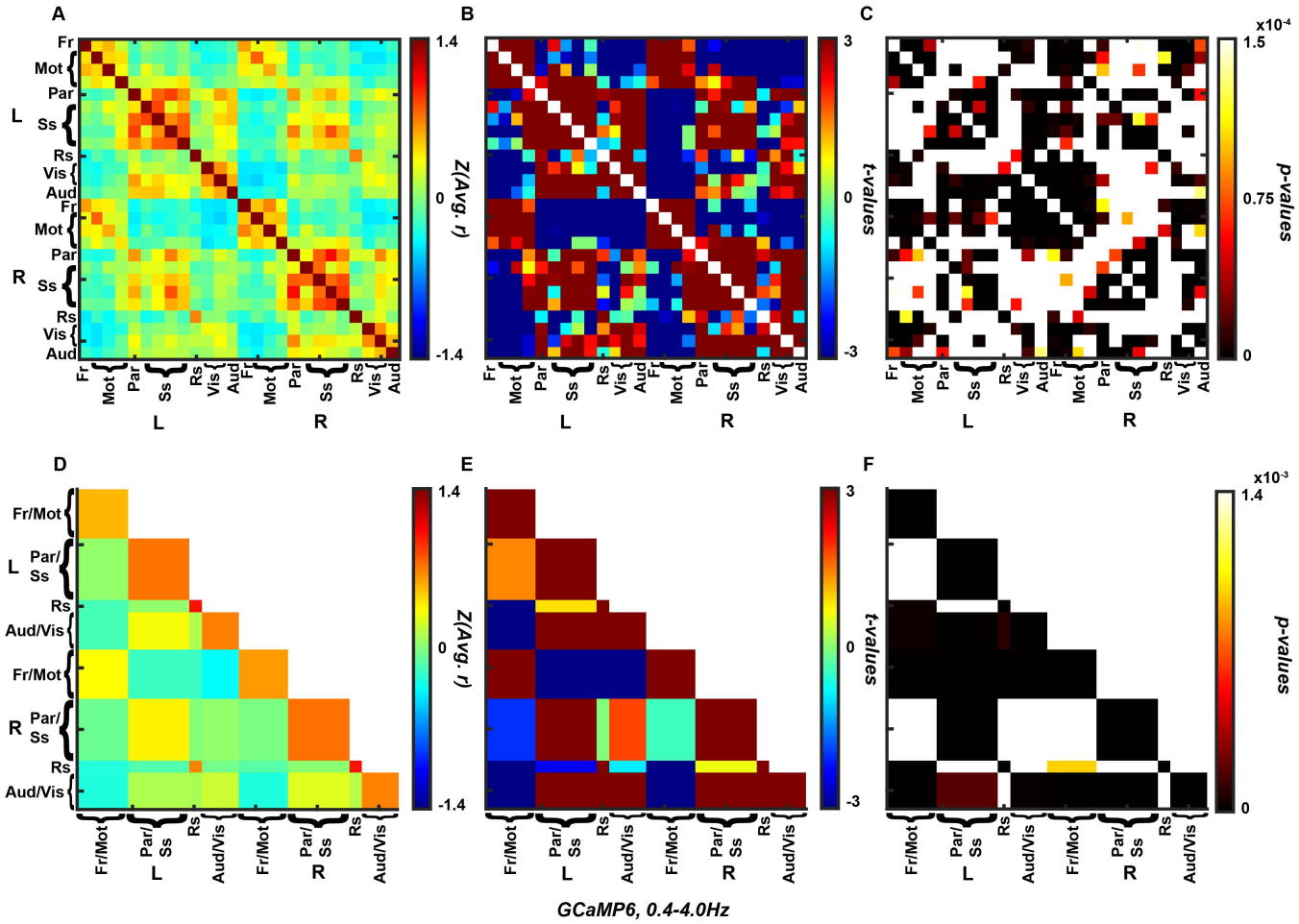

Figure 2.3: A) Average (N=16) traditional FC matrix. B) Comparison-wise one-sided t-test. C) Matrix thresholded for p-values beneath the Bonferroni threshold for significance (p=1.5x10-4). D) Average (N=16) enriched FC matrix. E) Comparison-wise one-sided t-test. F) Matrix thresholded for p-values beneath the Bonferroni threshold for significance (p=1.4x10-3).

2.4 Discussion

Wide-field optical imaging (WOI), especially of mice expressing genetically encoded calcium indicators (GECIs), provides cell-specific, improved temporal resolution recordings of calcium transients across the entire mouse cortex [265, 34, 151]. Functional neuroimaging analysis pipelines have been thoroughly developed in the functional magnetic resonance imaging (fMRI) literature [76, 14], however, despite having many similarities, these analytical techniques have not been translated into a comprehensive, user friendly mouse WOI toolbox. Here, we provide a toolbox that pre-processes data according to previous reports [265, 149]. We also implement some statistical approaches from the fMRI literature to handle the massive multiple comparisons problem present in all functional neuroimaging data.

The spatial resolution afforded by techniques such as fMRI or WOI allow neuroscience inquiries with network-level spatial specificity [81, 34]. However, treating each voxel or pixel as an independent measure will result in an almost always insurmountable correction for multiple comparisons (e.g., using the Bonferroni correction). Therefore, there has been significant work done in the fMRI literature to develop more appropriate algorithms to address this [85]. The cluster extent-based thresholding statistical approach operates on the hypothesis that neighboring pixels are likely not independent samples (i.e., a Bonferroni correction for multiple comparisons would be too stringent) and therefore large-grouped differences via independent pixel-wise statistical tests are more likely to represent a significant change somewhere within that cluster. Here, this method is set up to have a family wise error (FWE) rate of 5%, meaning in the collection of thresholded pixel-wise t-tests, there is a 5% chance of having at least one false positive result. An advantage of this technique is it allows for spatial specificity of an activation or change in connectivity by considering all the pixels of voxels in the FOV. However, this method only works as well as the initial analysis does in specifically isolating an activation or change, since the rightful conclusion of

a cluster surviving thresholding is that a change or activation occurred within that cluster. Here, we translate this method used in 3-dimensional fMRI to 2-dimensional WOI data and demonstrate the ability to localize a somatosensory-based deficit three days after a photothrombotic event to left somatosensory cortex (Figure 2.2C).

Another approach to solving the multiple comparisons problem is through data reduction. However, there is a tradeoff between losing spatial specificity and minimizing numbers of comparisons. One commonly used summary of FC using multiple seeds is by presenting FC matrices. This way, instead of having multiple seed-based FC maps consisting of as many pixels or voxels in the FOV, each brain region is reduced to one or more seed regions. However, a well sampled FOV can still reasonably result in hundreds of comparisons, making a Bonferroni correction for multiple comparisons a stringent threshold to pass. Here, we propose reducing the data within a common seed x seed FC matrix to have one singular value per cortical region. Neighboring cortical regions with small surface areas (e.g., Frontal, Parietal, Auditory) were grouped into the neighboring larger functionally similar cortical region to enhance data reduction. Also note that with at least Auditory and Frontal cortex, these cortical regions can often be outside of the FOV [34]. Not only does this still capture inter and intra-cortical dynamics, but the multiple comparisons problem becomes more feasibly solved by a Bonferroni correction for multiple comparisons (both because the threshold increases by an order of magnitude but also because it is more-but not completely-reasonable to treat values from differing brain regions as independent recordings). Shown here, we are able to isolate the strongly positive and negative correlations across the dorsal cortical surface of the mouse by performing a one-sided t-test at each matrix index (Figure 2.3).

2.5 Conclusions

This toolbox fills a much-needed gap between the fMRI and WOI data processing communities. Shown throughout are examples of statistical measures that were developed for fMRI being applied to FC calculated with the WOI data. However, the toolbox is also set up to compute seed-wise FC, spectral content, multivariate FC, node degree [103], and a neurovascular coupling approximation [265] (all analyses that fit into the outline in Figure 2.1C), which can all be plotted topographically and corrected via cluster-based thresholding. The wide distribution and use of this toolbox will greatly aid groups that are hoping to start imaging mouse models of health and disease to better understand how brain dynamics might change in humans.

Chapter 3

Separability of Calcium Slow Waves and Functional Connectivity during Wake, Sleep, and Anesthesia

Intrinsic neural activity organizes into distinct, functional networks, even at rest. However, many functional neuroimaging studies of mice are performed under anesthesia or without monitoring for small epochs of sleep. Here, we combine optical functional neuroimaging with electroencephalography monitoring for wake/sleep and image mice under multiple anesthetics. We uncover the spectral dependent functional effects of anesthesia and sleep using hemoglobin and calcium based imaging contrasts. This work has been previously published [34].

3.1 Introduction

Correlation analysis of spontaneous brain activity has been increasingly used in systems neuroscience [27, 203, 221, 15]. This methodology provides a powerful approach for map-

ping various cognitive processes as well as understanding specific clinical populations [13]. Specifically, functional connectivity (FC) analysis maps coordinate brain activity at rest in a remarkably reproducible manner [9]. Canonically, FC analysis is performed on data filtered in the infraslow band, that is, 0.009-0.08Hz [118]. In addition, brain activity used in this type of analysis is typically derived from hemodynamic fluctuations calculated by using imaging modalities such as functional magnetic resonance imaging (fMRI) [26] or diffuse optical tomography (DOT) [73] in humans. Alternatively, wide-field optical imaging modalities such as optical intrinsic signal imaging (OIS), allow for the same FC analysis to be performed in mice [259]. More recently, FC patterns extracted from wide-field optical imaging have been identified within neural calcium dynamics in mice that express calcium sensitive fluorescent reporters that are genetically encoded (i.e., GECI's) [150, 242, 265]. These fluorophores have extended the temporal frequency range in which FC can be studied and provide detailed maps of FC across the whole cortex [234]. Another advantage of fluorophore imaging is that fluorescence is dependent on cell-specific calcium flux, providing a more direct readout of neural activity that is independent of neurovascular coupling. However, recording fluorescence fluctuations in higher frequency bands, such as the delta band (historically 0.4-4.0Hz), introduces new potential confounds. In particular, the delta band "slow oscillation" that is a hallmark of NREM sleep appears to be a distinct physiological phenomenon from resting state functional connectivity and it will be important to understand the potential confounding effects of these slow oscillations on FC analysis.

The "slow oscillation" (alternatively, UP and DOWN states) refers to a particular electrophysiological phenomenon in the delta band first described in anesthetized cats by Steriade and colleagues [224]. The defining feature is quasi-periodic (nominally, 0.5 - 1.5 Hz) high amplitude fluctuations of neural excitability synchronously affecting the entire cerebral cortex. The slow oscillation is a defining feature of natural slow wave sleep and plays a crucial role in memory consolidation [176]. The slow oscillation is also present under some forms

of anesthesia [47]. As the mouse functional brain imaging literature expands into higher frequencies (e.g. the delta band), it will be imperative to understand the effect different brain states (wake vs anesthesia vs natural sleep) have upon correlation structures, since the traditional correlation analysis used in FC mapping may be confounded by the presence of large amplitude delta-band activity.

Resting state fMRI studies in humans have demonstrated reliable FC changes during sleep and anesthesia compared to wake in the infraslow frequency band which does not encompass slow oscillation dynamics [136, 195, 209, 230, 167]. Utilizing the higher temporal resolution of GECIs, we have previously shown much larger changes in delta band correlation structures due to ketamine/xylazine anesthesia compared to wake [265]. Other groups have suggested that the slow oscillation has a significant impact on delta band correlation structures, particularly driven by the globally synchronous high amplitude slow oscillation propagations [46, 75, 170]. Specifically, delta band FC during ketamine/xylazine anesthesia produces a nearly binary pattern with large regions of correlations and anti-correlations. In contrast, delta band FC during wake shows more focal homotopic connectivity patterns [265]. No comparison currently exists for delta band FC during any of the stages of natural sleep in the GECI literature. Therefore, the comparative effects of the slow oscillation on correlation structures, induced either spontaneously during natural sleep or mechanistically by anesthesia, have not been evaluated. It is not clear how correlation structures compare across brain states, frequency bands, or calcium/hemoglobin dynamics analyzed in the mouse. Finally, it is not clear to what extent the slow oscillation is a distinct phenomenon, i.e., whether it replaces or superimposes on top of underlying wake-like spontaneous activity.

Herein, we exploit genetically engineered mice with the calcium indicator GCaMP6 driven by the Thy1 promoter in excitatory neurons [265] to directly compare wide-field correlation structures of hemoglobin and calcium signals in both the infraslow and delta bands during wakefulness, two types of anesthesia, and non-rapid eye movement (NREM) sleep. Ad-

ditionally, we evaluate the separability of the slow oscillation from spontaneous wake-like FC patterns. In order to rigorously address these questions, we have concurrently acquired GECI/OIS imaging of calcium and hemoglobin dynamics together with electroencephalography/electromyography (EEG/EMG) to enable accurate assessment of arousal state. We use a linear decomposition analysis, specifically, Principal Component Analysis (PCA), to separate the slow oscillation from ongoing intrinsic activity in order to determine whether the slow oscillation replaces wake-like intrinsic delta activity during sleep/anesthesia or rather superimposes on it.

3.2 Methods

3.2.1 Animals

A total of six, three-month-old transgenic GCaMP6 Thy1/C57BL6 male mice (JAX Strain: C57BL/6J-Tg(Thy1-GCaMP6f)GP5.5Dkim; stock: 024276) were used in the present study.

3.2.2 Surgery

Prior to data collection, the mice underwent surgical implantation of two stainless steel lateral EEG bone screws located at -1mm posterior to bregma, and +/- 5mm lateral to bregma, a cerebellum bone screw to act as reference, and an EMG wire placed in the neck (Figure 3.1A). Using previously described methods [218], a Plexiglass head cap was then fixed with a translucent adhesive cement (C&B-Metabond, Parkell Inc., Edgewood, NY, USA) to allow for chronic, repeated imaging. Animals were allowed one week to recover and housed in group cages on 12h/12h light/dark cycles with lights on at 6:00 A.M. All studies were approved by the Washington University School of Medicine Animal Studies Committee and followed the guidelines of the National Institutes of Health's Guide for the Care and Use

of Laboratory Animals.

3.2.3 Anesthesia

Animals were serially imaged under 2 different anesthetic agents: ketamine/xylazine (86.9 mg/kg ketamine and 13.4 mg/kg xylazine), and dexmedetomidine ("dex", 0.5ug/g). These anesthetics are, respectively, an NMDA receptor antagonist (ketamine) [220] and an alpha-2 adrenergic agonist (xylazine, dex) [91]. These specific anesthetics were selected to obtain findings across commonly used anesthetics in mice (ketamine/xylazine) [39] and humans (dex) [56, 175]. Although slow oscillations have been reported after ketamine alone [47, 4] xylazine is commonly adjunctively used in rodent experiments to maximally synergize analgesia, immobility, muscle relaxation, and sedation [226, 257]. The anesthetic experiments consisted of 30 minutes of recording spontaneous wake followed by intraperitoneal injection of the anesthetic agent and recording for a subsequent 60 minutes (Figure 3.1B). In the case of dex, after 60 minutes of recording, the reversal agent, atipamezole, at a dosing of 0.5ug/g at 50ug/ml, was given. Between all recording sessions there was a minimum of two to four days to allow for sufficient washout of anesthetic agents and the order of the agents administered was randomized.

3.2.4 Sleep Deprivation

After a washout period of two to four days post anesthetic use, the second part of the experiment consisted of 6 hours of sleep deprivation starting at lights-on using novel objects, followed by an hour of continuous recording. Sleep deprivation was necessary to increase the amount of NREM data that could be collected during an hour imaging session with a head-fixed animal and was performed by placing the mice in a novel, enriched environment as previously reported [236]. If the animal was noted to be behaviorally sleeping (immobile,

eyes closed), new objects and bedding material were placed in their cage. Alternatively, objects were moved to different locations within the cage, or puffs of air were directed at the immobile animals while direct handling was kept to a minimum. Animals were not disturbed while actively awake (feeding, moving, grooming).

3.2.5 Awake Imaging

After one to four days post-sleep deprivation, the mice were imaged for 60 minutes of spontaneous wake data for baseline comparison.

3.2.6 Imaging

As previously described [265], animals were placed in a black, felt pouch with their heads secured in place under the LEDs (Figure 3.1A). An overhead camera was used for imaging. Mice were acclimatized to the apparatus the week prior to data collection. Sequential illumination was provided by four LEDs: 454nm (GCaMP excitation), 523nm, 595nm, and 640nm (Mightex Systems, Pleasanton, CA, USA). Images were acquired with a cooled, frame-transfer EMCCD camera (iXon 897, Andor Technologies, Belfast, Northern Ireland, United Kingdom) in combination with an 85mm f/1.4 camera lens (Rokinon, New York, NY, USA) at a frame rate of 16.8 Hz per LED channel. Allowing for a modest buffer beyond the Nyquist frequency of 8.4Hz, this set-up allowed for calcium data analysis at frequencies up to 6Hz. The field-of-view covered most of the convexity of the cerebral cortex with anterior-posterior coverage from the olfactory bulb to the superior colliculus. The resulting pixel resolution was approximately $78\mu m^2$. For each mouse, the recording duration was between 60 to 90 minutes per brain state. All imaging data were acquired in 5-minute imaging "runs".

3.2.7 EEG Data Analysis

On the day of recording, the EEG screws and EMG wire were connected to an amplifier and data was collected at 10,000 Hz (Power Lab EEG Amplifier, AD Instruments, Dunedin, New Zealand). This data was then down-sampled to 256 Hz offline. The authors (L.M.B. and E.C.L.) scored the EEG and EMG data in 10 second epochs according to standard criteria [184] as either wake, sleep, anesthesia, or movement artifact. The EEG data was low-pass filtered at 40 Hz to remove artifacts primarily associated with motor activity, then a 10-second Hann window was applied to each epoch. Finally, the fast Fourier transform (FFT) was computed and squared to obtain the EEG power.

3.2.8 Image Processing

GCaMP6/hemoglobin images underwent image processing as described elsewhere [265, 150] and summarized here. A binary brain mask was created and applied by tracing along the field-of-view framed by the scalp retraction procedure using the roipoly.m procedure in MATLAB. After first subtracting the ambient light levels, temporal detrending was performed by fitting the data with a fourth order polynomial that was subsequently regressed out of the time series for each pixel. Spatial detrending was performed by pixel-wise averaging time traces to generate a regressor for the time series data. The fluorescence and 523nm reflectance data were mean normalized and the ratio of the fluorescence emission data divided by the 523 nm reflectance data was used to correct the fluorescence data for absorption dynamics due to oxygenated-hemoglobin (HbO_2) and deoxygenated-hemoglobin (HbR) dynamics. The modified Beer-Lambert law was solved using the 523nm, 595nm, and 640nm wavelength reflected intensities to yield oxygenated- and deoxygenated-hemoglobin fluctuations. Images were smoothed with a 5x5 Gaussian filter. The time traces for all pixels within the brain mask were averaged to compute a global signal, which then was removed

by regression from every pixel's individual time trace in order to eliminate globally shared variance. Power spectral analysis of the GCaMP6 and HbO_2 signals was computed with a Hann window and FFT. For zero-lag correlation computations a Butterworth band-pass filter of 0.009 to 0.08 Hz or 0.7 to 3.0 Hz was applied to the data and seed-based zero-lag Pearson correlation coefficients were calculated per pixel using pre-specified seed locations. The 0.009-0.08 Hz band was chosen to replicate infraslow analysis typically done in fMRI [80]. The 0.7-3.0 Hz band encompasses the three instantiations of the slow oscillation produced by NREM sleep and the two anesthetics used in this study (Figure 3.2A). In the following, we refer to this frequency range as "delta," which differs somewhat from the conventional definition of "delta" used in human EEG (0.4-4.0 Hz) [62]. Seeds corresponded to the left cingulate, motor, somatosensory, retrosplenial, auditory, visual, and parietal cortices and were selected to represent the major cortical regions (defined by function) within the field-of-view of the imaging system. The specific cortical location within each region was based off of previously published canonical seed locations in the Paxinos atlas space and were slightly modified (frontal and olfactory seeds were excluded because of the slightly more condensed field-of-view presented here) [259, 265]. A Fisher z-transform was applied to the correlation coefficients before averaging and performing statistics (see below). The z-transformed averaged data was then reverse transformed to correlation coefficients.

We used lag analysis to capture the propagation properties of delta activity considered as an average. Specifically, the data were re-processed without global brain signal regression. Lagged cross-correlations were computed for single pixel traces versus the global brain signal. The correlation max was found as in Wright et al., 2017 [265] and the corresponding shift by cubic spline interpolation (in msec) defined as voxelwise lag. In addition, cross-correlation analysis between the delta EEG and GCaMP6 PCA data was performed. The max pixelwise correlation was plotted as an image, as well as the lag shift necessary to produce the max correlation.

3.2.9 Artifact Rejection

During the EEG/EMG scoring, any fluctuations in EMG signal were scored as "artifact" and the corresponding EEG/GCaMP/Hemoglobin data were discarded. A binary spatial mask, as described above, was applied to all analyses to account for imaging artifact generated by non-brain regions.

3.2.10 Statistics

A total of six, three-month-old transgenic GCaMP6 Thy1/C57BL6 male mice (JAX Strain: C57BL/6J-Tg(Thy1-GCaMP6f)GP5.5Dkim; stock: 024276) were used in the present study. The intent was to study five mice in each brain state. However, owing to one mortality (likely due to multiple anesthetic administrations), one of the original five-mouse cohort died and was replaced by a sixth mouse. Figure 3.4 lists which mouse was studied in each of the experimental states. With the mix of paired and independent data-points collected here, there is no established method to exchange condition labels within the dataset to justify using a permutated linear mixed model approach and no other mixed model approach has been proposed or validated for this purpose. Therefore, to quantify our contention regarding brain state dependent correlation patterns and that post-principal component removal (see below) ketamine/xylazine, dex, and NREM functional patterns resemble wake FC, a random effects statistic [86] at each pixel (mean/std) was calculated. Briefly, random effects analysis attempts to predict an outcome based on a linear combination of multiple variables that explain the heterogeneity within a sample. Here, we use this type of analysis to locate pixels that cross a pre-determined threshold considering all the mice used for each brain state. Pixels at which the correlation strength exceeded the predetermined threshold were considered statistically significant. Binary maps indicating functional connections significantly greater than 0 (using a threshold for pixels with a random effects statistic greater than 2.58) were

created. The regions specific to each modulated brain state (anesthesia/sleep) and wake were quantified separately by summing uniquely significant pixels in each case in order to evaluate whether FC patterns were consistent across brain state.

3.2.11 Principal Component Analysis

Singular value decomposition (SVD) analysis was computed on all of the 0.7-3.0 Hz filtered GCaMP6 data using MATLAB to remove the first three principal components and analyze them independently. Representations of PCs were computed by normalizing the δF/F signal to a 0 to 1 scale and then averaging across mice. The amount of variance each PC represented was computed.

3.3 Results

3.3.1 Optical System with Simultaneous EEG to Accurately Classify Brain State

As described elsewhere [265, 267], we evaluated correlation patterns during wake and anesthesia using wide-field, whole dorsal cortex (olfactory bulb to superior colliculus) optical imaging. To examine the influence of brain state on correlation structures, EEG/EMG recordings were simultaneously collected for scoring specific time epochs as wake, NREM sleep, anesthesia, or movement artifact (Figure 3.1A). The experimental protocol involved recording calcium and hemoglobin dynamics across the cortex during wake (W), natural NREM sleep (N), and two different anesthetized states: ketamine/xylazine (K/X) and dexmedetomidine ("dex", D) (Figure 3.1B). Ketamine/xylazine and dex are known to induce slow oscillations similar to those observed during NREM sleep [3, 7]. Dex has the added advantage of being reversible with atipamezole [210, 175].

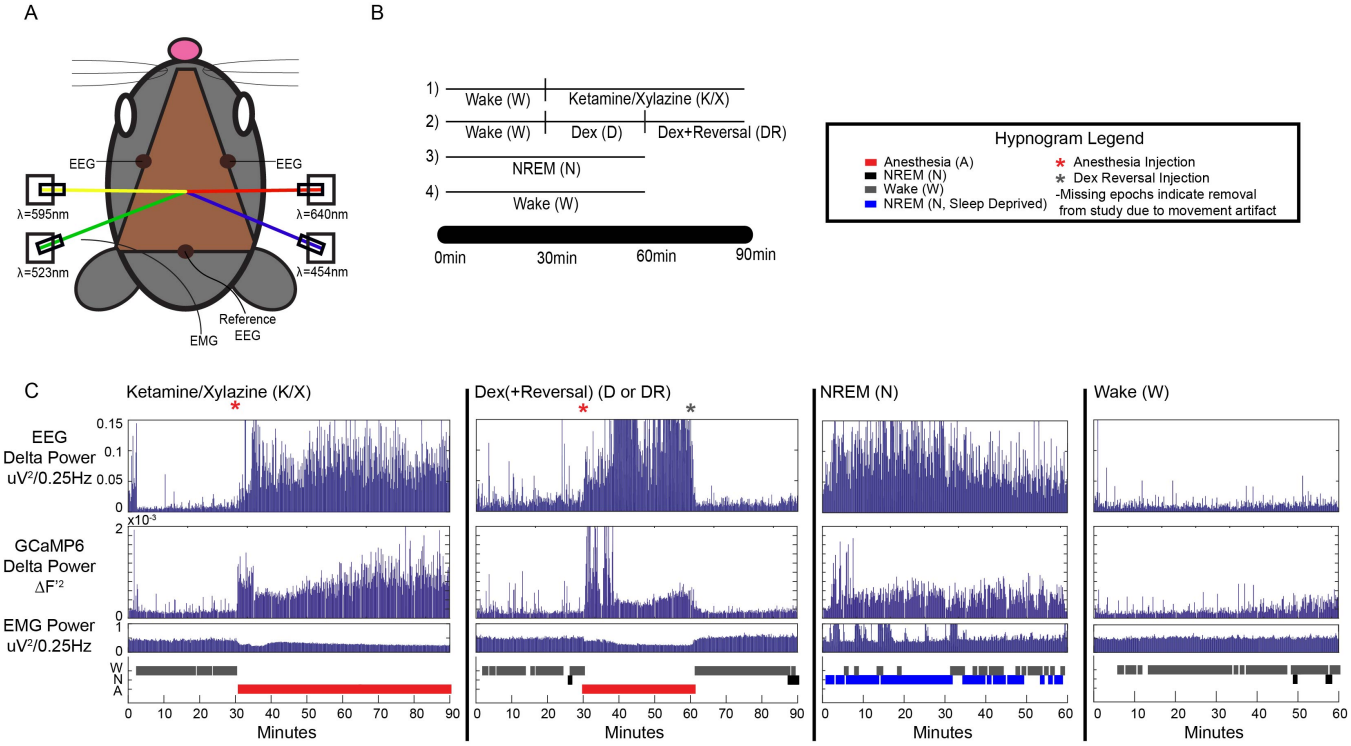

Figure 3.1: A) Mouse head schematic of chronically implanted Plexiglass window used for consistent, repeated imaging experiments (brown). Two EEG screws were implanted bilaterally in the skull, with a reference EEG electrode near the cerebellum and EMG wire threaded through the neck as shown. Optical Intrinsic Signal Imaging (OIS) was performed using sequential LED illumination supplied by three LEDs (523nm, 595nm, and 640nm). GCaMP6 fluorescence imaging was performed using a 454nm LED for excitation. B) Outline of experimental design. For experiments 1) and 2), 30 minutes of spontaneous wake data was acquired, injection of the anesthetic followed, with the reversal agent given in run 2) at 60 minutes to reverse the effects of dex. In runs 3) and 4), 60 minutes of spontaneous NREM (if sleep deprived) or wake (if not sleep deprived) data was acquired to be scored. C) Example delta (0.7-3.0Hz) power time course for EEG and GCaMP6 data with corresponding EMG and hypnogram for one mouse during ketamine/xylazine (K/X), dex (D), dex+reversal (DR), NREM (N), and wake (W).

To classify brain state, EEG and EMG was scored in 10 second epochs by standard criteria [184] as either wake, NREM sleep, anesthesia, or artifact and visualized using hypnograms (Figure 3.1C, see Figure 3.3 for quantification of time spent in each brain state). Delta power analysis of the EEG and GCaMP6 signals revealed increases in delta power aligned with transition of brain state score, indicating NREM sleep/anesthesia, and relative decreases in delta power aligned with wake (Figure 3.1C). As previously demonstrated [265], during sleep and anesthesia, there was an increase in the whole-brain GCaMP6 fluorescence power, mostly within the 0.7-3 Hz frequency band relative to wake or after dex reversal (Figure 3.2A). This narrower frequency band, relative to the more traditionally defined 0.4-4Hz delta band, was used for analysis in the present study going forward in order to focus on frequency content sensitive to the states in this study. The delta increase was specific to the GCaMP6 data under anesthesia and natural sleep. No detectable brain state specific changes were present in the hemoglobin data - presumably due to limited hemoglobin dynamics at frequencies above $\sim$0.2 Hz [8, 107].

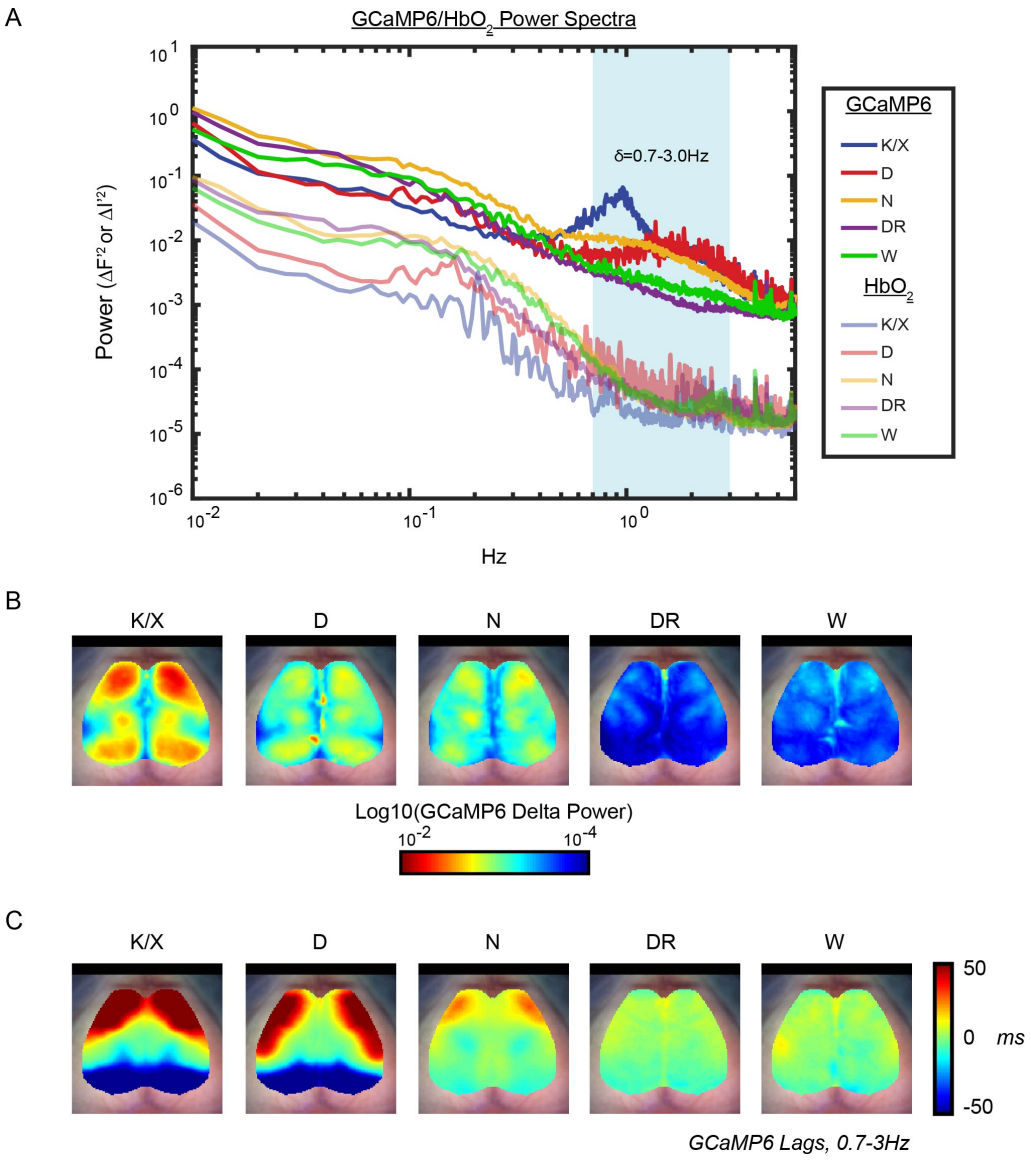

Figure 3.2: A) The average (n=5) GCaMP6 (solid lines) and HbO_2 (translucent lines) power for each brain state plotted with the delta band (0.7-3.0Hz) highlighted. B) Log10 average (n=5) GCaMP6 delta (0.7-3.0Hz) power topographs for each brain state. C) Average (n=5) GCaMP6 delta lag topographies for each brain state.

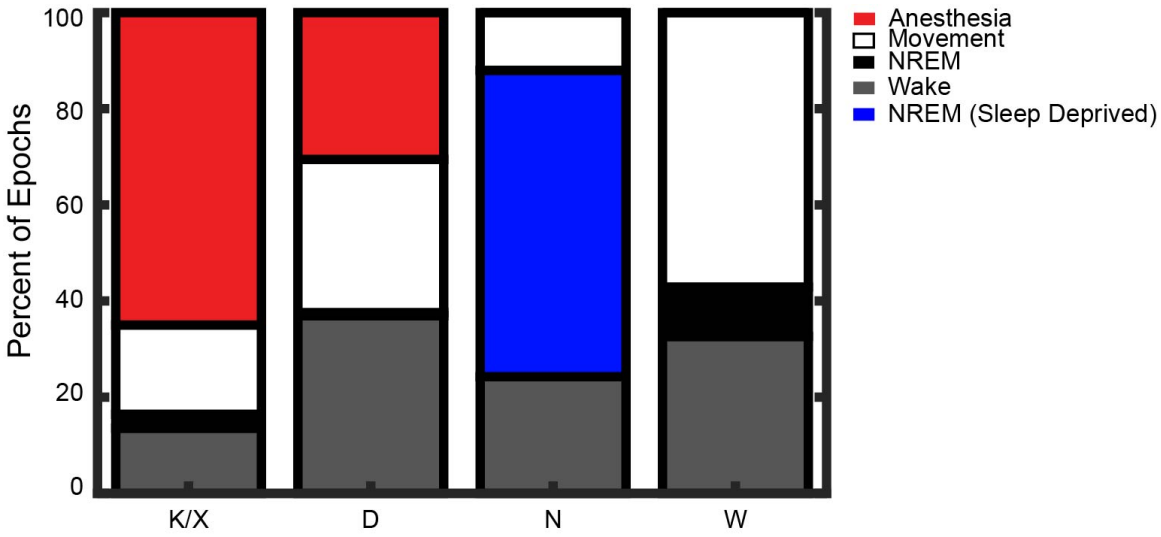

Figure 3.3: A) Bar graph showing percent of total data spent in each brain state (n=5). Data is categorized as either anesthesia, movement artifact, natural sleep, wake, or natural sleep (post sleep deprivation).

Given the increase in the spatially averaged delta power, we investigated topographic differences in the power of the fluorescence signal in the 0.7-3 Hz range of the GCaMP6 data (Figure 3.2B). There was a significant increase in the delta power under anesthesia and during NREM sleep, and this increase was significantly modulated across distinct cortical regions, especially in motor, somatosensory, and visual areas relative to wake and dex reversal (power topography maps for each individual mouse are shown in Figure 3.4). Further, as shown first using scalp EEG recordings [159] and later calcium dynamics [179], the dominant spatial property of the slow oscillation is the anterior to posterior propagation of the slow wave. This feature was captured in our GCaMP6 sleep/anesthesia data and displayed in real time (Figure 3.6, Figure 3.5A). Using single pixel cross-correlation analysis with the global brain signal, "lag" analysis captured a front-to-back topography across the anesthesia and natural sleep states which was absent in wake (Figure 3.2C). Collectively, these results support the accurate classification of the different brain states and set the stage for further brain state-specific correlation analysis with the calcium (GCaMP6) and hemoglobin data.

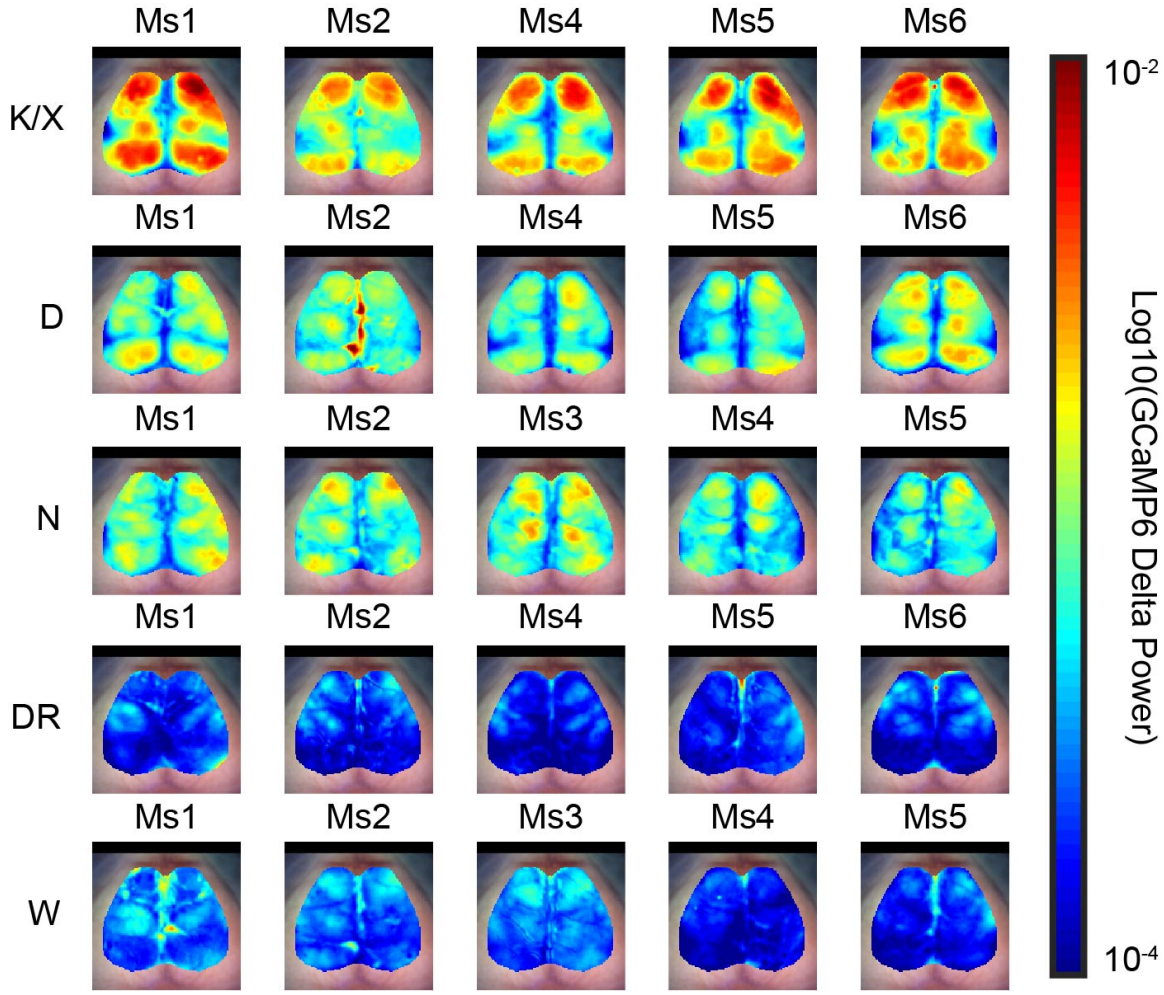

Figure 3.4: A) Log10 average delta (0.7-3.0Hz) power for each brain state for each individual mouse included in the present study.

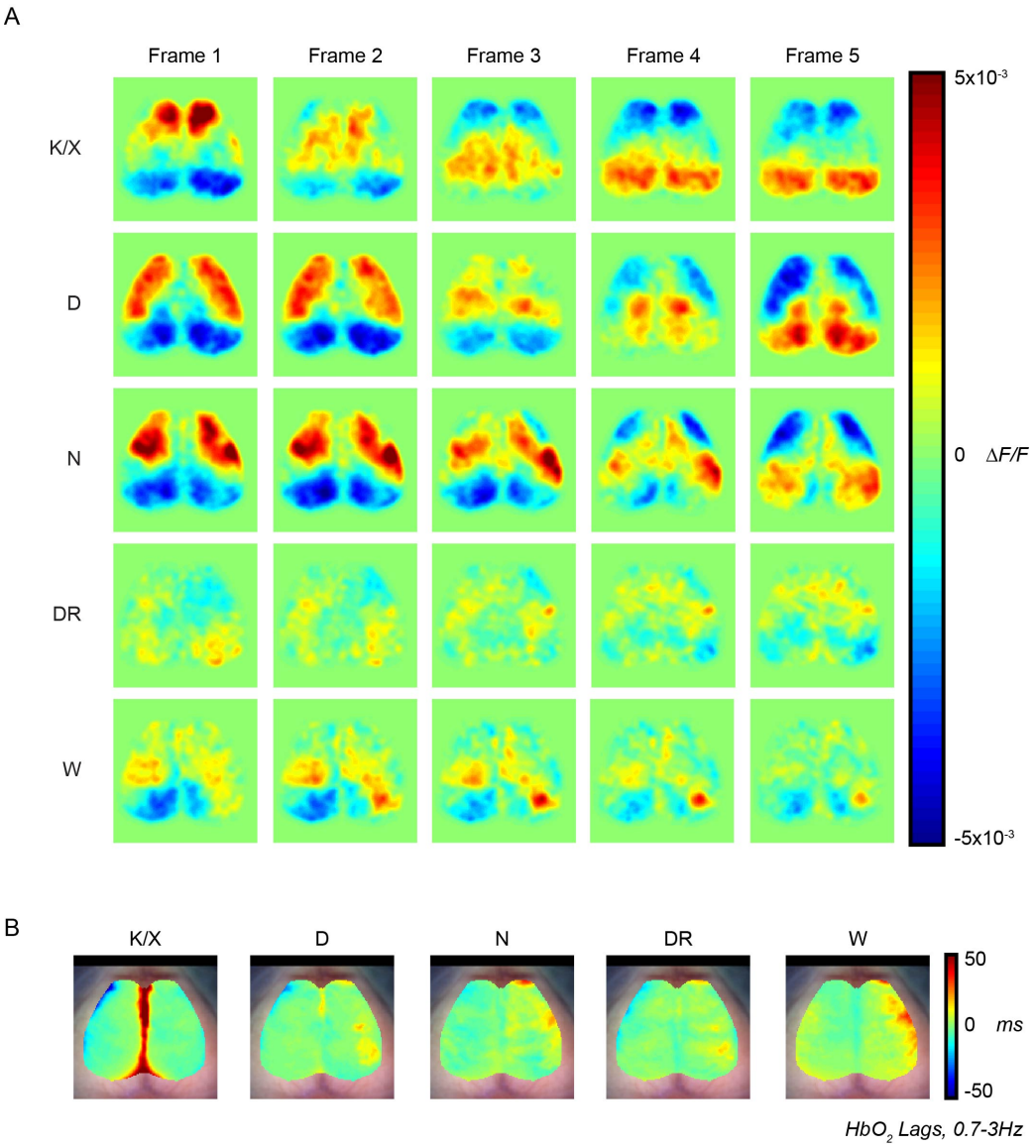

Figure 3.5: A) Five example sequential delta GCaMP6 frames taken from each brain state to illustrate the propagating slow oscillation in the anesthesia and NREM data, compared to wake. Frames were smoothed with a 2 x 2 Gaussian filter. B) Average (n=5) lag topography maps computed using the HbO_2 data in the delta band.

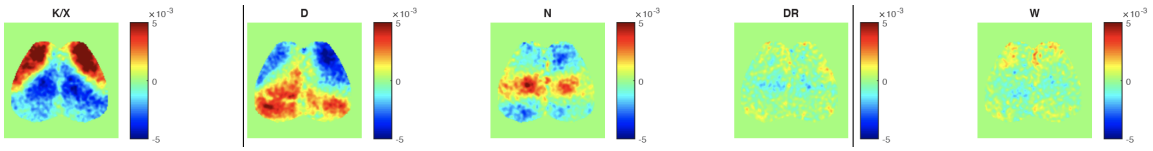

Figure 3.6: Still of a 20 second movie in real time of example GCaMP6 data (δF/F) from one mouse in each brain state: ketamine/xylazine (K/X), dex (D), NREM (N), dex+reversal (DR), and wake (W). Movies were smoothed with a 2 x 2 Gaussian filter. See [34] for movie.

3.3.2 Hemoglobin and GCaMP6 Infraslow Correlation Structures Modestly Change across Brain State, while GCaMP6 Delta Correlation Structures Appear More State Dependent

Given that our wide-field calcium spectral data shows differences between wake and sleep/anesthesia in the delta band, and that has largely been attributed to the presence of the slow oscillation, we then tested the hypothesis that hemoglobin and GCaMP6 correlation structures within the infraslow (0.009-0.08Hz) frequency range would not vary with brain state due to the slow oscillation being filtered out of the data. Seed-based, zero-lag correlational analysis with both the calcium and hemoglobin signal in the infraslow range showed the previously demonstrated [259] contralateral homotopic correlations and anti-correlations between functionally distinct regions (Figures 3.7A and 3.7B, top) i.e., "functional connectivity". To quantify spatial similarity across brain state and calcium/hemoglobin dynamics, we calculated significant topographic patterns using a random effects analysis across the five mice in each brain state. This analysis created binary maps representing areas of functional connectivity (FC) with correlation strength significantly greater than 0 (Figures 3.7A and 3.7B, middle). The binary map for each brain state (besides wake) was then compared to the wake binary map and the overlap between the two brain states is shown in green. Also mapped are brain regions with significant correlation structures unique to either wake (white) or the anesthesia/sleep/dex reversal brain states (blue). The area unique to each modulated brain state (blue) or wake (white) (Figures 3A and 3B, bottom) made up, on average, less than 15% of the entire field-of-view in both the hemoglobin and GCaMP6 data.

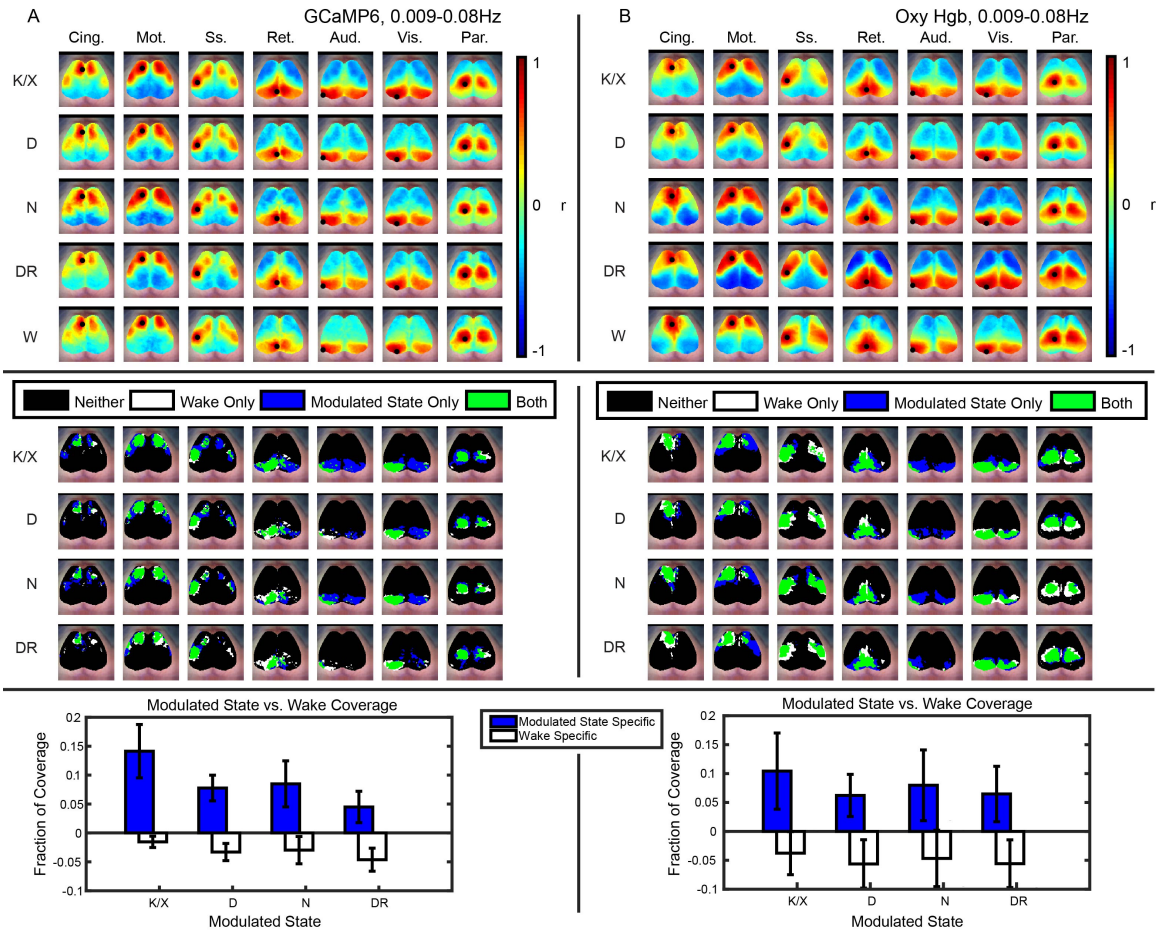

Figure 3.7: Top: Seed based zero-lag correlation maps (n=5) across brain state calculated on A) GCaMP6 or B) oxygenated hemoglobin (HbO_2) data within the infraslow band. Middle: Random effects overlap maps created by comparing each brain state to wake using A) GCaMP6 or B) oxygenated hemoglobin data. Bottom: Fraction of significant pixels within the field-of-view unique to either the modulated brain state (blue) or wake state (white). Error bars are standard deviations across seeds.

Next, we performed the same seed-based correlation analysis in the delta range (0.7-3.0 Hz) on the GCaMP6 data, anticipating an exaggerated difference in FC across brain states due to the presence of the slow oscillation. Hemoglobin dynamics were not analyzed in this band as they did not demonstrate a peak in this spectral region. A highly symmetric topography marked by anti-phase relations across anterior vs. posterior areas was observed only in anesthesia and sleep (Figure 3.8A). In contrast, this pattern was absent in the wake state (Figure 3.8A, lowest row), which instead produced FC structures with contralateral homotopic correlations and anti-correlations between functionally distinct regions. These differences were confirmed with random effects analysis by creating binary maps and performing the same overlap calculations as described previously (Figure 3.9A, top, and Figure 3.9B). The fraction of coverage unique to each modulated brain state was greater in the delta range relative to the infraslow range and was different between each modulated brain state.

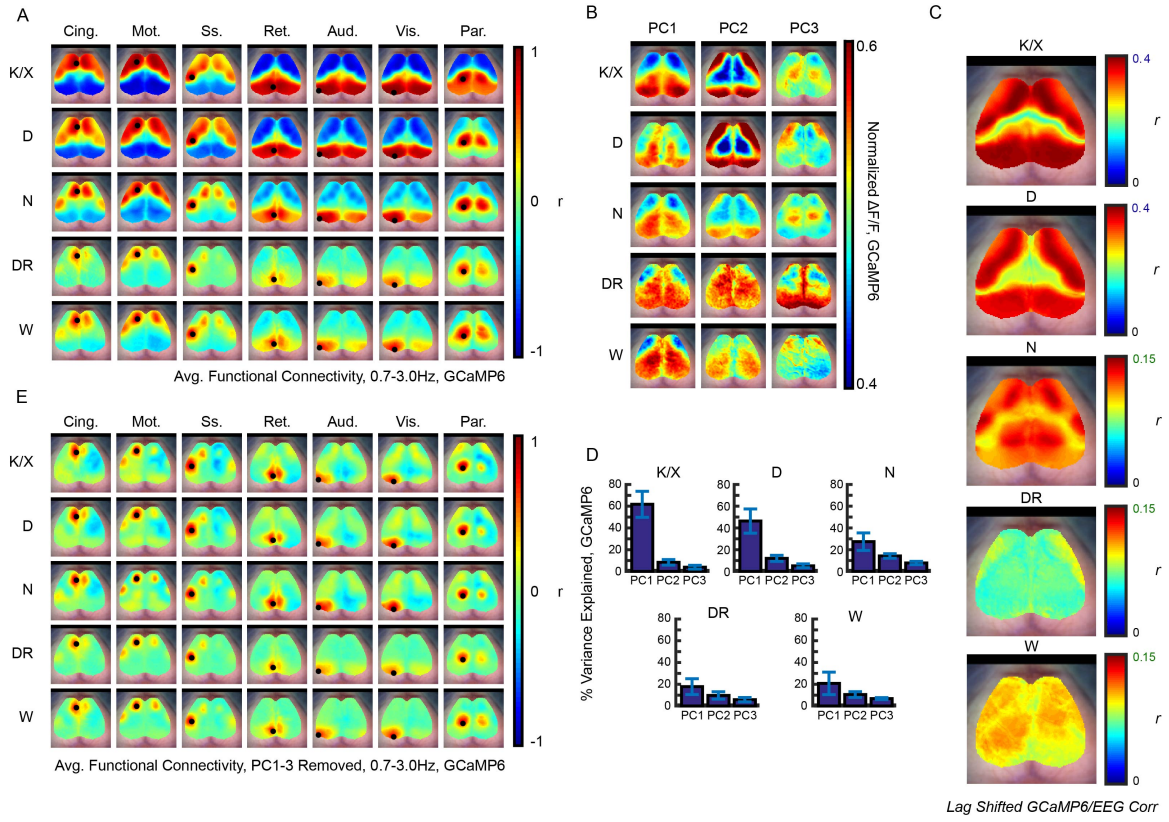

Figure 3.8: A) Zero-lag correlation maps for ketamine/xylazine (K/X), dex (D), NREM (N), dex + reversal (DR), and wake (W) states averaged across all mice (n=5). B) Representations of the first 3 PCs for each brain state averaged across all mice (n=5). C) The average (n=5) max cross-correlation between the lag-shifted summed first three PCs and delta EEG trace. D) The average (n=5) percent variability in the data accounted for by the first three PCs in each brain state. Error bars are standard deviations of the mean. E) Functional connectivity analysis (n=5) performed on the data in each brain state after the first three PCs had been removed.

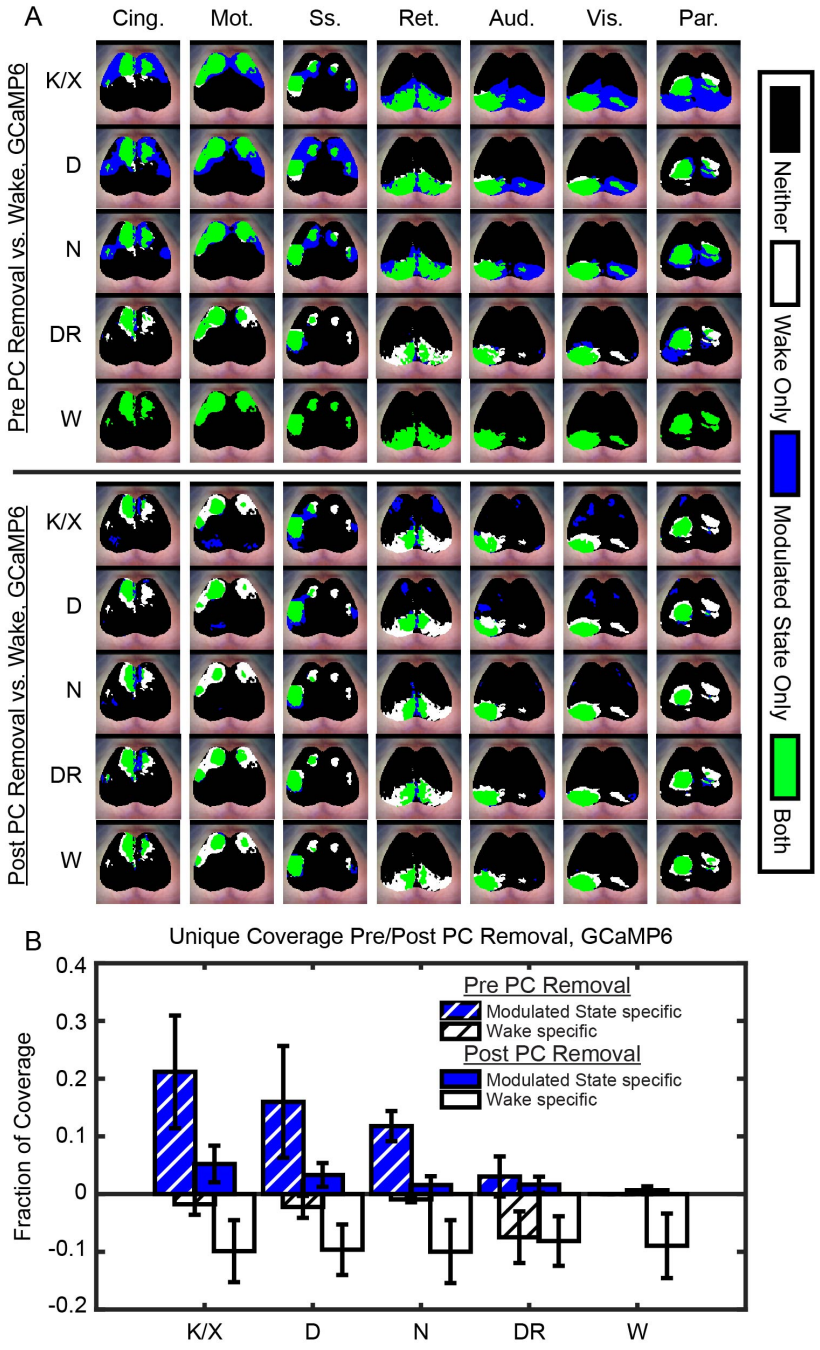

Figure 3.9: A) Binary maps representing statistically significant functional correlations (random effects analysis, n=5) pre and post PC removal overlaid between wake and ketamine/xylazine (K/X), dex (D), NREM (N), or dex+reversal (DR). B) Quantification of the percent brain coverage by unique functional correlations due to ketamine/xylazine, dex/dex+reversal, or NREM (blue), or wake (white) pre and post PC removal. Error bars are standard deviations across seeds.

3.3.3 The Slow Oscillation is Superimposed on Wake FC Patterns

Given the differences in correlation structure within the delta range of the GCaMP6 data, we next investigated whether principal component analysis (PCA) could be used to separate or remove the delta spatio-temporal feature (the slow oscillation) present during sleep and anesthesia from other spontaneous brain activity. We hypothesized that removal of the slow oscillation would reveal FC maps similar to the delta GCaMP6 wake maps, specifically, homotopic correlations and anti-correlations between functionally distinct regions. PCA on the delta GCaMP6 data revealed striking differences in the first three principal components (PCs) contrasting wake vs. NREM and anesthesia (Figure 3.8B). Specifically, the summation of PC1, PC2, and PC3 captured the major front-to-back feature of the slow oscillation during NREM and anesthesia (Figure 3.11). Compared to previously reported correlation coefficients between GCaMP6 and EEG [114], the cross correlation between these summed PCs and the filtered delta EEG trace resulted in high correlation coefficients in the sleep/anesthesia data when corrected for lag between the two signals (Figure 3.8C and Figure 3.10). This suggests that these first 3 PCs have captured characteristic features of NREM sleep and anesthesia. The first 3 PCs accounted for approximately 45%, 60%, and 70% of the variance in the sleep, dex and ketamine/xylazine states, respectively, but only 35% and 34%, respectively, in the wake and dex reversal states (Figure 3.8D). These observations combined suggested that removal of the first 3 PCs should greatly reduce the variance attributable to the slow oscillation in the NREM/anesthesia data. The results of this maneuver are shown in Figure 3.8E, which illustrates a striking similarity of correlation structure across all brain states. Further, after removal of the first 3 PC's, all brain states are qualitatively similar to unmodified delta in the wake state (Figure 3.8A, lowest row; see also Figure 3.12 for similar spontaneous data across all brain states). To quantify this observation, we evaluated the topographic similarity of FC maps computed in the PC 1-3 removed data compared to unmodified delta wake (Figure 3.9A, middle). FC features unique to ketamine/xylazine,

dex, and NREM (blue) were greatly attenuated post PC removal, with only minor loss of homotopic FC typical of wake (Figure 3.9B, white). Prior to PC 1-3 removal, modulated state specific FC topography differed by as much as 50% across states. Post PC 1-3 removal, modulated state specific FC topography decreased over four-fold, became more uniform and similar to unmodified wake. These results suggest that the slow oscillation is superimposed onto canonical wake delta FC.

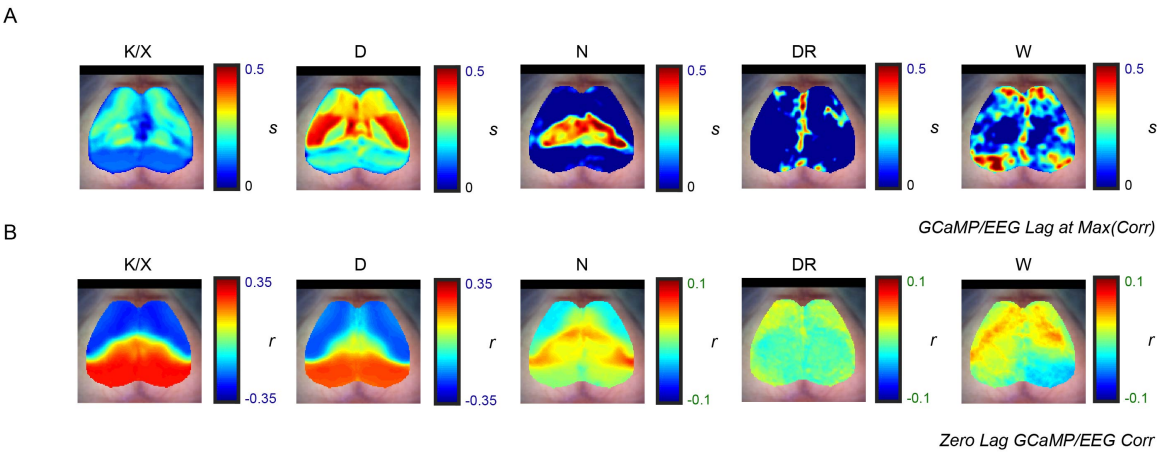

Figure 3.10: A) Average shift (n=5) necessary to maximally cross-correlate the summed first 3 delta GCaMP6 PCs with the delta EEG trace. Lags were smoothed with a 2 x 2 Gaussian filter. B) Average (n=5) zero-lag cross correlations between the summed first 3 delta GCaMP6 PCs and delta EEG.

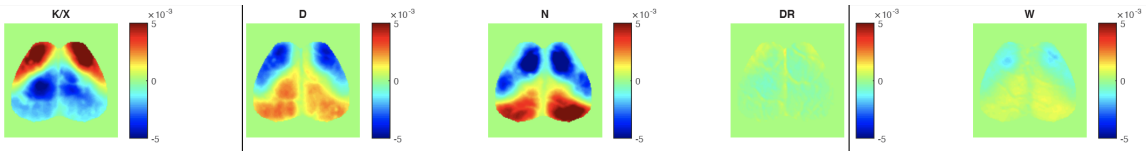

Figure 3.11: Still of a 20 second movie in real time of GCaMP6 data (δF/F) from one mouse using only the summed first 3 PCs in each brain state: ketamine/xylazine (K/X), dex (D), NREM (N), dex+reversal (DR), and wake (W). Movies were smoothed with a 2 x 2 Gaussian filter. See [34] for movie.

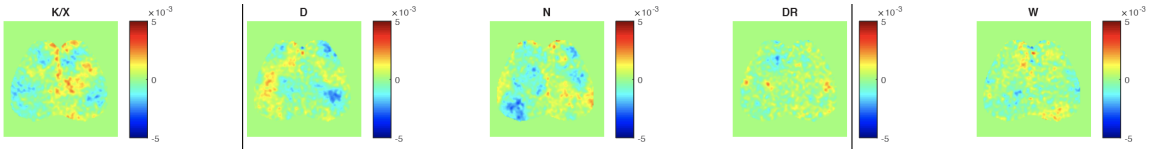

Figure 3.12: Still of a 20 second movie in real time of GCaMP6 data (δF/F) from one mouse after PCs 1-3 were removed from each brain state: ketamine/xylazine (K/X), dex (D), NREM (N), dex+reversal (DR), and wake (W). Movies were smoothed with a 2 x 2 Gaussian filter. See [34] for movie.

3.4 Discussion

We studied wake, NREM sleep, and anesthesia in transgenic mice expressing a genetically encoded calcium indicator using seed-based zero-lag correlation analysis (Figures 3.7, 3.8) and found brain state-, calcium/hemoglobin-, and frequency-dependent changes in FC structure. Specifically, within the infraslow frequency range, spontaneous hemoglobin activity patterns were roughly maintained across all brain states while neural activity patterns were slightly more varied. Neural activity within the delta range during sleep and anesthesia was dominated by the slow oscillation propagating in an anterior-to-posterior direction (Figure 3.6, Figure 3.5A). Thus, we observed greater differences in correlation structure across brain states here. Finally, correlation structures that are qualitatively similar to wake delta FC patterns were recovered after linear decomposition removed the slow oscillation from delta neural activity data.

Previous FC studies of sleep and anesthesia have been conducted mostly in humans using fMRI, which effectively is restricted to temporal frequencies in the infraslow range (0.009-0.08 Hz) [8, 107]. Above 0.2 Hz, hemodynamic signal power becomes essentially flat, which corresponds to a noise floor [111]. Specifically, power in the oxygenated hemoglobin (HbO_2) signal follows a 1/f spectral characteristic at infraslow frequencies, with minor changes in power across brain states. However, above infraslow frequencies, power across all brain states begins to be impacted by the aforementioned noise floor. This view is further supported by the present lag analysis performed on the delta-band hemoglobin data, which generated a topography dominated by vascular features (Figure 3.5B). Nevertheless, our HbO_2 infraslow correlation data showed modest brain state-dependent changes consistent with prior reports [136, 209, 230, 117]. Changes in correlation structure were slightly greater in the GCaMP6 infraslow data across brain state (e.g. the larger amplitude of ketamine/xylazine specific FC, Figure 3.7A, bottom). These results could reflect the faster dynamics provided by GCaMP6

fluorescence compared to HbO_2 imaging.

In addition to infraslow dynamics, calcium imaging provides useful information at delta range frequencies [234], including the ability to study the sleep- and anesthesia-associated ∼1Hz slow oscillation. It is this phenomenon that seems to drive the different correlation maps across brain state in the delta band. The strong nearly binary correlation/anti-correlation pattern seen in the sleep/anesthesia data visually captures a travelling wave, a defining feature of the slow oscillation [159]. Notably, the difference between anesthesia and wake (Figure 3.9B) is greater than the difference between NREM and wake, potentially suggesting that NREM architecture is "intermediate" to the anesthesia and wake architecture.

The present work is more comprehensive than previous similar studies in that we included sleep without anesthesia, more specifically NREM, and included two commonly used anesthetics– dexmedetomidine and ketamine/xylazine- in addition to baseline wake data. These comprehensive experimental conditions provide a foundation to evaluate the interaction between the slow oscillation and FC. Spontaneous neural activity often exhibits a "1/f" (scale-free) spectral characteristic [111, 83]. However, as shown by others [46, 168, 265], and again here, there may actually exist two regimes in the power spectral densities of spontaneous EEG as well as calcium signals under anesthesia or during NREM (see Figure 3.2). The notion of superimposed spontaneous neural activity has been used before to describe "1/f-like" vs. oscillatory processes [83]. It is plausible then that the removal of the sharp discontinuity of the 1/f spectral characteristic in ketamine/xylazine, and the broader 1/f discontinuity in the dex and NREM data is representative of a superimposed oscillatory event. Applying principal component analysis (PCA) to the NREM/anesthesia data, we observed that the slow oscillation was largely confined to the first three PCs. This was further reinforced by the high correlation between the delta EEG trace and the pixel wise isolated PCs, as well as the striking similarity between the delta GCaMP6 lag analysis topography (Figure 3.2C) and the lag structures generated from the delta EEG and GCaMP6 PCA cross-correlation

analysis (Figure 3.10). The increased GCaMP6 PCA/EEG correlation in the anesthesia and sleep brain states (Figure 3.8C) relative to wake could be explained by global events driving the synchrony between the two manifestations of the slow oscillation. It should be further noted that discrepancies between the GCaMP6 and EEG data are to be expected, as EEG reports widely synchronous field potentials, whereas calcium imaging is more directly related to neural firing. Building on the observation that the first three PCs encompassed the slow oscillation, we demonstrated that wake-like delta spontaneous activity (as quantified through seed-correlation maps) could be recovered, and sharp spectral increases could be removed (Figure 3.13A) from slow oscillation-dominated data by removal of the first three PCs. Further, following delta band-pass filtering, GCaMP6 time series following PC 1-3 removal are very similar to that recorded during wake (Figures 3.13B,C, shaded panels). These results indicate that "wake-like" cortical activity persists during brain states dominated by the slow oscillation (e.g., NREM sleep and anesthesia) regardless of mechanism of slow oscillation induction. Thus, during these brain states, the slow oscillation superimposes on, rather than replaces, persistent wake-like ongoing activity, the correlation structure of which is largely determined by anatomical connectivity [183, 115, 122].

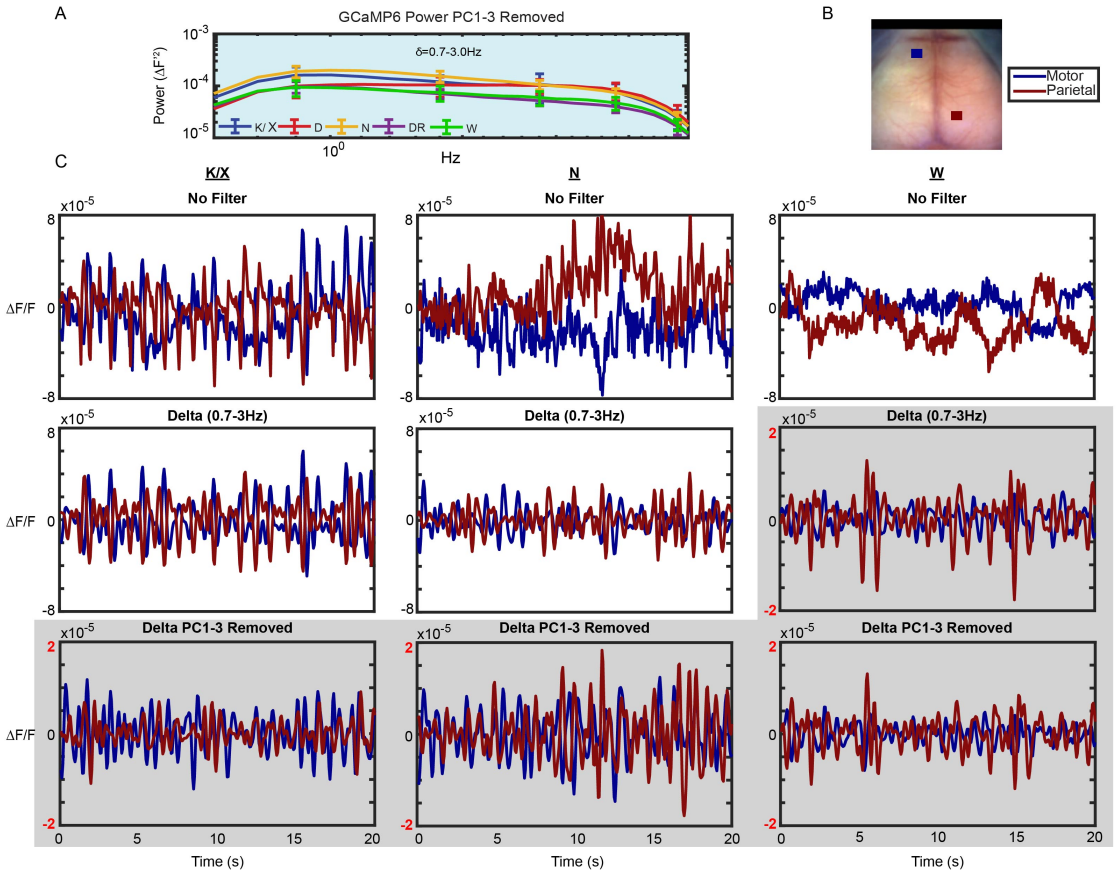

Figure 3.13: A) Average (n=5) GCaMP6 power spectra of the 0.7-3.0 Hz filtered, PC 1-3 removed data. B) Graphic delineating motor and parietal areas used to create time traces in C). C) Spatially averaged time traces from the pixels in B) shown across 20 seconds for broadband (top), delta (middle), and PC 1-3 removed (bottom) GCaMP6 data. Shading is included to illustrate the comparison of the PC removed data to unmodified delta wake data.

Ketamine/xylazine and dexmedetomidine both induce stereotypical, invariant instantiations of the slow oscillation [175, 5]. Ketamine is an NMDA receptor antagonist, while xylazine and dex both activate alpha-2 adrenergic receptors. Discrepant findings across the different forms of anesthesia could be in part due to the the 40x increase in sedative efficacy of dex compared to xylazine [257], but much more likely the antagonism of NMDA receptors and the downstream fine tuning of excitation and inhibition leading to prolonged DOWN states [47]. This could explain the similar spatiotemporal properties of the slow oscillations induced by ketamine/xylazine and dex (Figure 3.2) and the higher frequency at which dex-induced slow oscillations propagate (Figure 3.2A). By comparison, the calcium activity during NREM sleep was much more varied (Figure 3.6) than during anesthesia states. This variability may be attributable to variability in slow oscillation wave origin, amplitude, or direction of propagation [215]. Alternatively, the complexity of the calcium dynamics during NREM relative to anesthesia may result from a mixing of lower amplitude slow oscillations with relatively higher amplitude spontaneous wake-like activity. Even during wake, the first two PCs included features suggestive of the slow oscillation (Figure 3.8B, Figure 3.11), albeit in greatly attenuated magnitude and contributing to less variance. This result potentially reflects micro-sleep [105, 112] or brief periods of reduced alertness within the 10-second EEG epochs used to score the optical data [252].

3.5 Caveats, Future Directions, and Conclusions

Sleep deprivation over six hours prior to calcium (GCaMP6) imaging was used to increase the quantity of NREM sleep. This is a potential caveat as sleep deprivation has been reported to change the shape, incidence, and amplitude of slow oscillations [251]. It remains to be determined whether wide-field image acquisition of freely behaving natural sleep is possible for extended durations and if differences between non-sleep-deprived and sleep-deprived sleep

exist. However, this issue presumably does not impact the present anesthesia results.

On the other hand, it has been reported that slow wave activity reflects sleep pressure, i.e., that the prevalence of slow waves at the start of NREM is proportional to prior wake time [29]. Although the present study was not designed to examine this effect, it is possible that reduced power in the dex reversal data [175], as compared to normal wake (Figures 2A,B, Figure 3.4), reflects reduced sleep pressure following 30 minutes of anesthesia-induced slow oscillations. Future experiments controlling for time spent asleep versus wake in sleep-deprived and non-sleep-deprived brain states could rigorously address this question.

Finally, while algorithms more sophisticated than PCA may provide improved removal of the slow oscillation, PCA works sufficiently to establish this concept. As expected with PCA, the first 3 PCs may include some variance not specifically tied to the slow oscillation. Further, the match between Figure 3.8E and wake topography (lowest row of Figure 3.8A) is not perfect. However, the match is sufficient to demonstrate our principal claim, that after removing the slow oscillation, the remaining signals reflect patterns (Figure 3.8E) expected of FC in the wake state (Figure 3.8A, bottom row) and, importantly, that these features do not suggest artifact. Recovery of focal FC patterns post linear decomposition supports the idea that the slow oscillation superimposes on wake-like intrinsic activity.

Prior studies have made inferences about changes in connectivity across experimental brain states or under the global synchronization of anesthesia [224, 28, 258]. In the future, it will thus be important to closely monitor the brain state of the animal when conducting FC analysis. The present study presents promising avenues of future study to focus on the transition between sleep and wake or the specific cortical activity underlying sleep. More broadly, this work opens up new avenues of research that may elucidate underlying mechanisms of sleep and sleep disturbances consequent to disease. For example, our findings may have implications for understanding how sleep and Alzheimer's disease interact [146, 124], or how anesthesia influences post-operative delirium [141].

Chapter 4

Transient Disruption of Functional Connectivity and Depression of Neural Fluctuations in a Mouse Model of Acute Septic Encephalopathy

Alterations in functional connectivity often serve as clinically relevant biomarkers as well as readouts of underlying pathology in animal models. Here, we propose a novel mouse model of acute septic encephalopathy using basic behavioral assessment and functional neuroimaging. Cases of altered mental status (e.g., Delirium) can resolve on the order of hours. We track mice from baseline, to peak disease, through recovery and report the functional alterations that occur in parallel with behavioral changes.

4.1 Introduction

Septic encephalopathy and delirium are a major problem in hospitalized patients, affecting approximately 30% of general hospital and up to 80% of intensive care unit (ICU) patients [216, 127]. Elderly populations are particularly susceptible to encephalopathy [119, 78], especially those with dementia or pre-dementia [79], usually triggered by minor systemic infections (i.e., not involving the central nervous system, CNS) [268, 269]. Characteristically, the encephalopathy resolves after treatment of the instigating peripheral infection. Instances of mental status change can be very costly (estimated up to 4 billion USD), both by incurring additional costs during hospital stays and by increasing risk of accidental injury secondary to confusion [119]. In severe cases, there is evidence that permanent brain injury may result, and symptoms may outlast the time frame of peripheral infection [100, 64, 200]. Current neurological treatments are inadequate and aimed at sedation rather than the underlying cause for the encephalopathy. Studies have demonstrated acute activation of neuroinflammatory mediators after an infectious insult, leading to speculation that these cellular and molecular underpinnings somehow affect neural function [269, 116, 60]. However, little is known about the underlying mechanisms causing acute septic encephalopathy (ASE) because there has not been a direct link between the activation of these inflammatory mediators, behavioral modifications, and the breakdown of neural function on the immediate timescale of ASE. Indeed, studying ASE has been difficult because quantitatively assessing altered mental status in animal models has been challenging.

Clinically, electroencephalography (EEG) is acquired to diagnose encephalopathy and rule out seizures. However, the spatially sparse nature of EEG recording confines this diagnostic output to non-specific generalized increases in slow wave activity [94]. Other neuroimaging techniques offer a unique approach to this patient demographic as these techniques are spatially sensitive to underlying pathologies [25] and predictive of behavioral phenotypes

[23]. However, ASE also poses some unique difficulties to the neuroimaging community. Patients undergoing mental status changes are less likely to comply with instruction and sit still [78] in a neuroimaging device for lengthy scans, which are often necessary for functional analysis. Thus, functional neuroimaging studies in this patient population are rare [182, 52] and focused on other forms of delirium (e.g. postoperative), but nevertheless set a precedent for altered brain connectivity during peak illness that resolves at recovery. While there is frequent use of magnetic resonance imaging (MRI) in this patient population [273, 97, 229, 120], these instances are more for quick diagnostic purposes and not functional study. Indeed, positron emission tomography (PET) and MRI are commonly used to study functional networks in the context of neuroinflammation, but these studies are usually focused on understanding a longer lasting neurological disease (e.g. Alzheimer's disease [190], multiple sclerosis [2], stroke [211]) and not acute encephalopathy.

One recent study examined functional connectivity using resting state fMRI in a case of N-methyl-D-aspartate (NMDA)-receptor encephalitis in a patient during active disease and after recovery [36]. This unique study revealed an overall depression in global correlation strength as well as notable decreases in blood oxygen level dependent (BOLD) fluctuations that resolved after recovery. Several recent studies have applied functional neuroimaging to rodent models of septic encephalopathy. One study demonstrated diminished brain neurovascular response to whisker stimulation with laser speckle and optical intrinsic signal (OIS) imaging in the rat barrel cortex 4-6 hours after lipopolysaccharide (LPS) injection [33]. Another fMRI study demonstrated altered functional networks 24 hours after injection with LPS in anesthetized rats [272]. While these studies have begun to investigate altered brain dynamics during the acute time period following septic insult, both of these studies were limited to hemoglobin based dynamic contrasts, the former only investigated changes in barrel cortex, the latter had confounding effects of anesthesia, and neither studied the entire time course of ASE from baseline to maximal encephalopathy to recovery.

Wide-field optical imaging in mice expressing the genetically engineered fluorescent GCaMP6 reporter (under a Thy1 promoter) permits the direct visualization of neural calcium dynamics across the cerebral cortex [61, 265, 150]. In addition to being a more direct reporter of neural dynamics compared to traditionally hemodynamic contrasts, the increased temporal resolution of calcium imaging allows for increased signal-to-noise ratio (SNR), allowing us to map the coordinate activity of neural populations to quantify neural Pearson functional connectivity (FC) across the cortex in awake mice [34]. In addition to mapping connectivity, there are multiple calcium analytical tools that can give unique insights into a disease model such as ASE. For instance, we can adapt metrics such as the global variance of the temporal derivatives (GVTD) used to capture fluctuations in diffuse optical tomography (DOT) data [214], neural dynamic temporal standard deviation, and power spectral analysis to estimate the amount of neural activity present throughout the disease course [265, 34]. Using this broad set of wide-field calcium analytical tools, we can develop a putative biomarker in a mouse model of ASE in order to better understand the network level alterations during peak encephalopathy and how they may recover.

Intraperitoneal injection of LPS, a cell wall component of gram-negative bacteria, induces an acute septic response in mice [135, 148, 54]. LPS acutely induces systemic inflammation including upregulation of many of the neuroimmunological components hypothesized to be responsible for altering neural function in the context of ASE (e.g., IL-1β, TNFα, complement proteins) [200, 148, 45]. Further, behavioral changes have been documented after LPS administration [48, 59, 172, 193, 231], and while these experiments have taken place outside of the time frame of ASE, they nevertheless suggest encephalopathy. Here, we image mice over a time course consistent with ASE and recovery; at baseline and then 8Hrs, 24Hrs, and 72Hrs after injection with LPS or phosphate buffered saline (PBS). Based on previous literature [36], we hypothesize there to be a global depression in neural activity accompanied by a decrease in global FC strength. We monitored disease load by taking weights and as-

sessed neurological status by quantifying a neuroscore at each timepoint. We describe neural connectivity over the experimental time course using standard Pearson FC analysis. Finally, we investigate the global variation in calcium time traces at each timepoint.

4.2 Methods

4.2.1 Animals

A total of 16 female (PBS, N=8, LPS, N=8) ranging from 3-7 months old Thy1-GCaMP6f mice were used in the present study (Jackson Laboratories Strain: C57BL/6J-Tg(Thy1-GCaMP6f)GP5.5Dkim; stock: 024276). These mice express the protein GCaMP6f in excitatory neurons, primarily in cortical layers ii, iii, v, and vi [265]. All studies were approved by the Washington University School of Medicine Animals Studies Committee and follow the guidelines of the National Institutes of Health's Guide for the Care and Use of Laboratory Animals.

4.2.2 Surgical Preparations

Prior to imaging, typical surgical preparations were implemented [34, 218]. Briefly, an optically transparent plexiglass window was implanted with translucent dental cement (C&B-Metabond, Parkell Inc., Edgewood, New York) following a midline incision and clearing of skin and periosteal membranes. The window covered the majority of the dorsal cortical surface and provided an anchor for head fixation and allowed for chronic, repeatable imaging. Stainless steel EEG self-tapping screws (BASI Inc., West Lafayette, IN, USA) were fixed at approximately -1mm posterior to bregma, and +/- 5mm lateral to bregma (near barrel/auditory cortex), although EEG recording was omitted for the present experiments.

4.2.3 Lipopolysaccharide Injections

Lipopolysaccharide (LPS, Eschirichia coli O55:B5, Sigma Aldrich) suspended in phosphate buffered saline (PBS) was injected intraperitoneally in experimental mice at 5mg/kg with an injection volume of 5mL/kg (LPS, N=8). An equal volume of PBS only was injected into control mice (PBS, N=8).

4.2.4 Weight Change and Neuroscore

Mice were weighed and examined at each imaging timepoint by author LMB, who was blinded to experimental group. As previously published [164], a sepsis score was recorded based on a composite record of general ambulation and response to stimuli at each timepoint. Scores ranged from 0 (normal spontaneous movements and response to stimuli) to 5 (no spontaneous movements or response to stimuli, presence of tremors) with a score of 4 being the threshold for a humane endpoint. No mouse in this study reached a score of 4 during the experiment thus each mouse was evaluated and imaged at each timepoint. As the acute time frame of this study precludes behavioral testing to definitively prove altered mental status (e.g., Barnes maze navigation), this "neuroscore" was an attempt to record abnormal phenotypes associated with ASE.

4.2.5 Fluorescence and Optical Intrinsic Signal (OIS) Imaging

Mice were head-fixed in a stereotaxic frame and body secured in a black felt pouch for imaging. Sequentially firing LEDs (Mightex Systems, Pleasanton California) passed through a series of dichroic lenses (Semrock, Rochester New York) into a liquid light guide (Mightex Systems, Pleasanton California) that terminated in a 75mm f/1.8 lens (Navitar, Rochester New York) to focus the light onto the dorsal cortical surface. LEDs consisted of 470nm (GCaMP6f excitation), 530nm, 590nm, and 625nm light. An sCMOS camera (Zyla 5.5,

Andor Technologies, Belfast, Northern Ireland, United Kingdom) coupled to an 85mm f/1.4 camera lens (Rokinon, New York New York) was used to capture fluorescence/reflectance produced at 16.8 Hz per wavelength of LED. A 515nm longpass filter (Semrock, Rochester New York) was used to discard GCaMP6f excitation light. Cross polarization (Adorama, New York New York) between the illumination lens and collection lens discarded artifacts due to specular reflection. The field-of-view (FOV) recorded covered the majority of the convexity of the cerebral cortex (1.1cm^2), extending from the olfactory bulb to the superior colliculus. All imaging data were acquired as 5-min runs and binned in 156x156 pixel^2 images at approximately 100 μm^2 per pixel. Mice were imaged before receiving either LPS or PBS, 8Hrs, 24Hrs, and 72Hrs after injection.

4.2.6 Imaging Data Processing

Image processing followed methods previously described [265, 150] and briefly summarized here. Images were spatially downsampled to 78x78 pixel^2 and a frame of ambient baseline light levels was subtracted from the time series data. Data were temporally downsampled by a factor of 2 and then spatially and temporally detrended. Data were affine-transformed to common Paxinos atlas space and pixel-wise time traces were mean normalized. Frames corresponding to reflection data produced by the 530nm, 590nm, and 625nm light were used to solve the modified Beer Lambert law to yield fluctuations in oxygenated and deoxygenated hemoglobin. Frames corresponding to fluorescence data were corrected by approximating hemoglobin absorption of the excitation and emission light. All data were spatially smoothed with a 5x5 Gaussian filter. The global signal was regressed from the time series data, and data were filtered with a 0.4-4.0Hz Butterworth bandpass filter.

4.2.7 Functional Connectivity

Functional connectivity (FC) analysis refers to the calculation of a Pearson correlation coefficient between two time traces:

$$\rho_{x,y} = \frac{cov(x,y)}{\sigma_x \sigma_y} \tag{4.1}$$

where ρ is the Pearson correlation coefficient between time trace x and y, $cov(x,y)$ is the covariance between time trace x and y, and σ are the standard deviations within time traces x and y.

4.2.8 Node Analysis

A matrix was assembled where each row or column contained the Pearson correlation between a specific pixel time trace and the remaining pixel time traces in the FOV (this was done for every pixel in the FOV, generating a pixels x pixels matrix). As previously done [103], this matrix was thresholded at $z(0.3)$ and binarized to isolate positive connections. The summation of each row or column provides a vector with the node strength for each pixel in the FOV which can then be reshaped and mapped onto our two-dimensional FOV.

4.2.9 Global Variance of the Temporal Derivatives

Global variance of the temporal derivatives (GVTD) [214] was calculated on pixel-wise filtered time traces. The pixel-wise difference between successive time-frames was taken. Following, the rms value across the FOV was calculated for each frame.

4.2.10 Spectral Analysis

Power spectral analysis of the GCaMP6f data was performed on 10 second segments by applying a Hann window and an FFT (squared to obtain power).

4.2.11 Statistics

Pixel-wise t-tests were performed on connectivity and power maps to compare LPS and PBS populations. These t-test maps were then thresholded, leaving pixels with a t-value corresponding to $p < 0.05$. We then used a cluster-size based thresholding method to ensure the pixel-wise error and family-wise error (FWE) rate did not exceed 0.1% and any clusters of surviving pixels had a pixel count greater than k_α (see derivation of k_α in General Methods, Chapter 2).

4.3 Results

A baseline measurement of weight, neuroscore [164], and imaging was taken before either group of mice received injection of LPS or PBS (Pre-LPS, N=8, Pre-PBS, N=8). Mice were injected with either LPS (N=8) or PBS (N=8) and weight, neuroscore, and imaging data were recorded at 8Hrs, 24Hrs, and 72Hrs after injection. As expected, mice lost weight (Figure 4.2) across the experimental timeline and neuroscore transiently increased (Figure 4.1A) in the time frame of peak encephalopathy (Hrs8-24) and returned to baseline by 72Hrs.

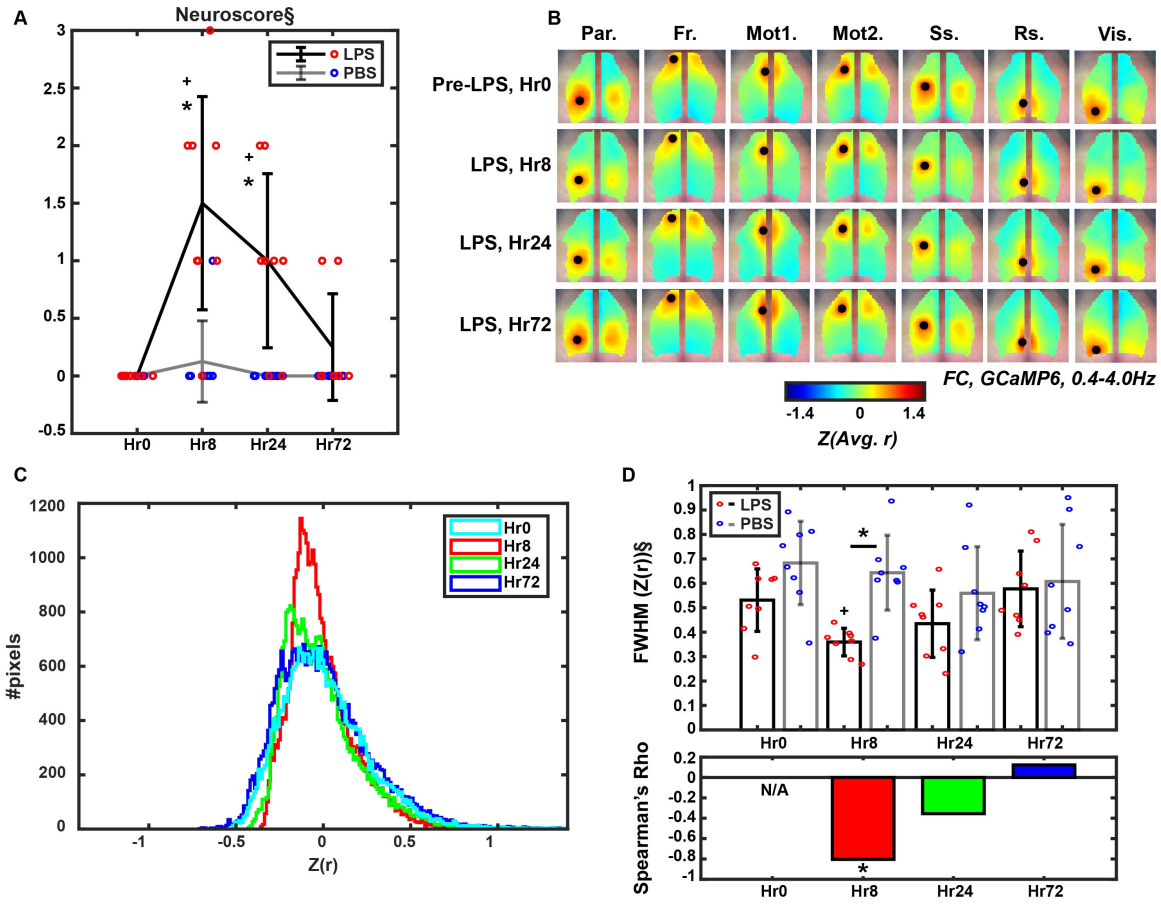

Figure 4.1: A) Neuroscore measured at baseline (Hr0), Hr8, Hr24, and Hr72 after intraperitoneal injection of LPS or PBS. Error bars are standard deviations. § denotes significance on 2-way rm-ANOVA (HF corrected p=0.0024) and 1-way rm-ANOVA (LPS only, p=0.0002). * denotes significance via two-sample t-test at the indicated timepoint between PBS and LPS populations (Hr8 p=0.0015, Hr24 p=0.0022). + denotes significance via paired t-test between the timepoint and Hr0 (LPS only, Hr8 p=0.0025, Hr24 p=0.0072). B) Average (N=8) LPS seed-based FC maps using Parietal (Par.), Frontal (Fr.), Cingulate (Cing.), Motor (Mot.), Somatosensory (Ss.), Retrosplenial (Rs.), and Visual (Vis.) seeds at each timepoint. C) Histograms displaying the overall distribution of FC correlation values from each row in B). D) (top) Average FWHM of the histograms displayed in C). Error bars are standard deviations of the mean. § denotes significance on 1-way rm-ANOVA (LPS only, p=0.0087). * denotes significance via two-sample t-test at the indicated timepoint between PBS and LPS populations (Hr8 p=2.3e-4). + denotes significance via paired t-test between the timepoint and Hr0 (LPS only, Hr8 p=0.016). (bottom) Spearman's rho signifies the correlation between FWHM values and neuroscore values for LPS and PBS mice. * signifies p=1.7e-4.

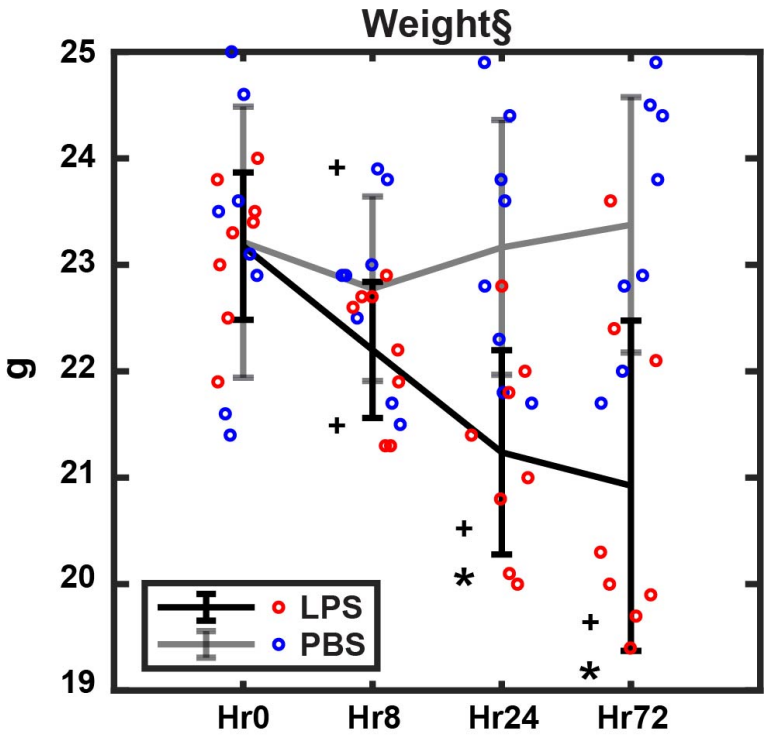

Figure 4.2: Weight (N=8) measured at baseline (Hr0), Hr8, Hr24, and Hr72 after intraperitoneal injection of LPS or PBS. Error bars are standard deviations. § denotes significance (HF corrected p=0.0001) on a 2-way rm-ANOVA and 1-way rm-ANOVA (LPS, p=0, PBS, p=0.0034). * denotes significance via two-sample t-test at the indicated timepoint between PBS and LPS populations (Hr24 p=0.0032, Hr72 p=0.0033). + denotes significance via paired t-test between the timepoint and Hr0 (LPS, Hr8 p=2.2e-4, Hr24 p=1.2e-4, Hr72 p=0.0041, PBS, Hr8 p=0.025).

Baseline imaging separated into "Pre-LPS" (N=8) refers to the mice that would immediately receive an LPS injection following the first imaging timepoint. Average connectivity maps were displayed for 7 seed-regions sampling the FOV presented here at baseline, Hr8, Hr24, and Hr72 post LPS injection (Figure 4.1B). The overall distribution of FC correlations from the maps in Figure 4.1B were plotted for each timepoint (Figure 4.1C), displaying a narrowing of a normal distribution at Hr8 that returns to baseline by Hr72. This was quantified by calculating the full width half maximum (FWHM) of the distributions shown in Figure 4.1C (Figure 4.1D), noting a significant decrease at Hr8. The same analysis was performed on the mice that received PBS injections and yielded no significant changes in FC or FWHM over the course of the experiment (Figure 4.3). Further, Spearman's rho was calculated to compare the rank ordered FWHM values across LPS and PBS populations to the respective neuroscores at each timepoint. A significant inverse relationship between neuroscore and FWHM was demonstrated at Hr8.

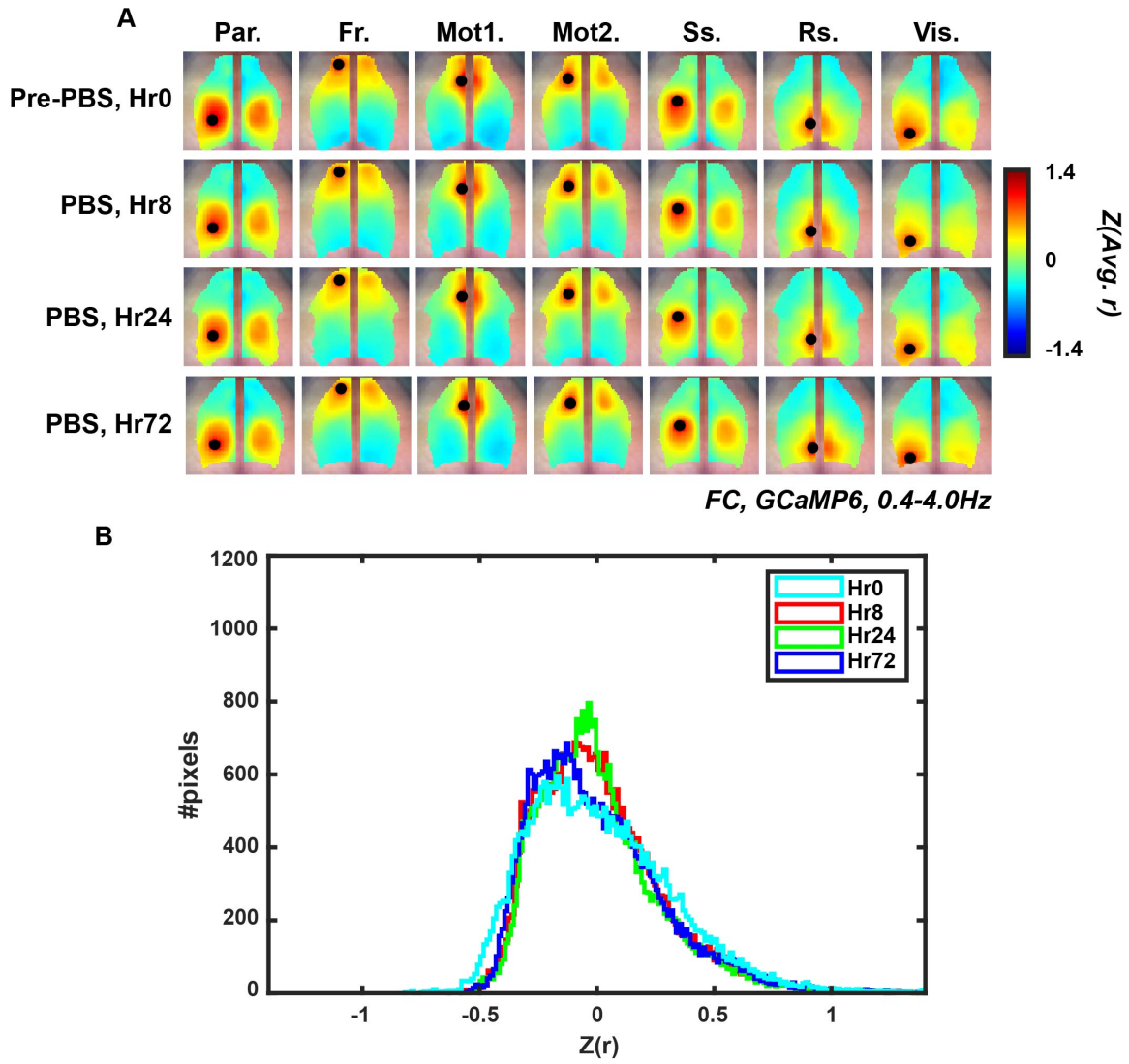

Figure 4.3: A) Average (N=8) PBS seed-based FC maps using Parietal (Par.), Frontal (Fr.), Cingulate (Cing.), Motor (Mot.), Somatosensory (Ss.), Retrosplenial (Rs.), and Visual (Vis.) seeds for each timepoint. B) Histograms displaying the overall distribution of FC correlation values from each row in A).

Pixel-wise correlation (i.e., node) strength was determined by summing the number of positive connections in a FC map using each pixel within the FOV as a seed region of interest (ROI, Figure 4.4A,B). At each timepoint after Hr0, a pixel-wise t-test was performed between the specified timepoint and Hr0. A cluster size-based statistical thresholding method [106, 85] was used to select clusters satisfying the pixel-wise false positive rate and overall family-wise error rate. The majority of the FOV contained nodes with high numbers of connections at baseline for both PBS and LPS mice. However, at Hr8 posterior brain pixels, isolated as those within somatosensory and parietal cortex (Figure 4.4C), lost a large number of positive correlations in LPS mice that were regained by Hr72. Spearman's rho was calculated to compare the rank ordered spatially averaged node values within the deficit presented in LPS mice between Hr0 and Hr8 across LPS and PBS populations to the respective neuroscores at each timepoint. A significant inverse relationship between neuroscore and node strength was demonstrated at Hr8 and Hr24.

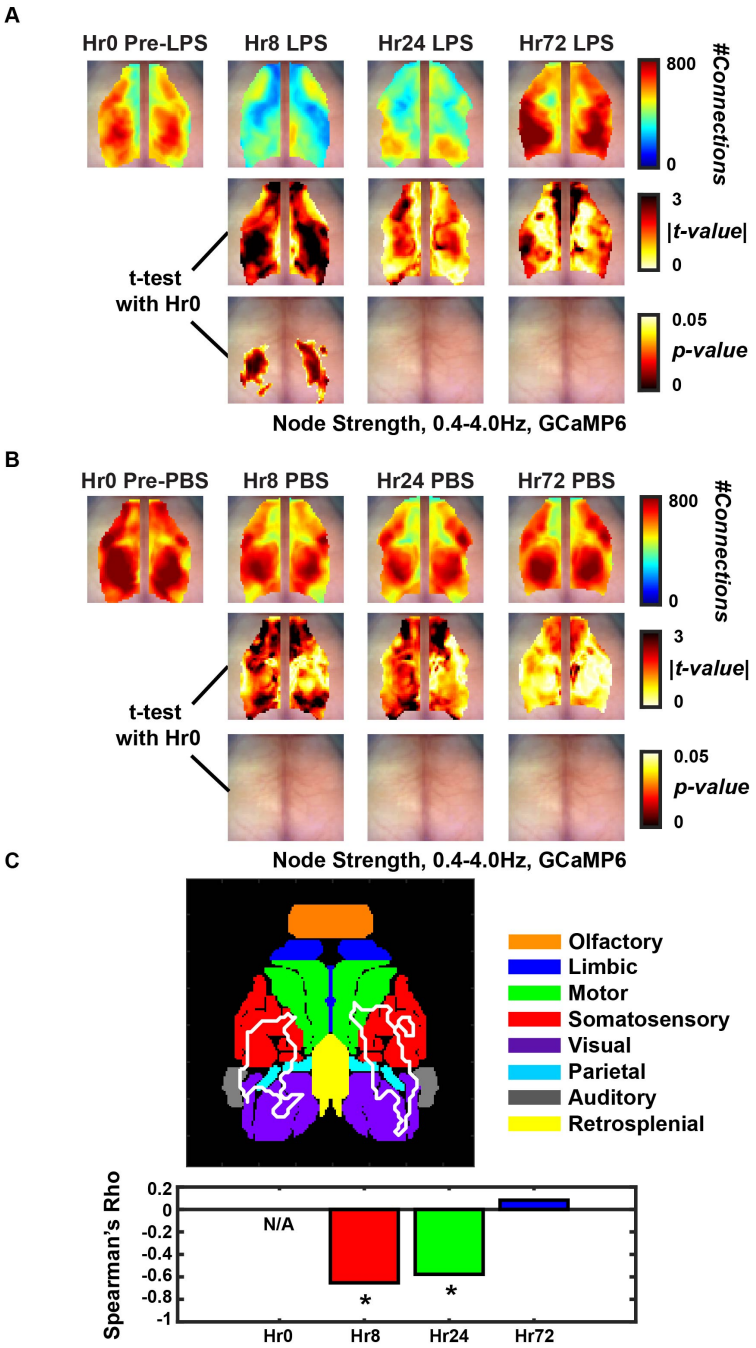

Figure 4.4: A) (top row) Average (N=8) node strength for LPS and B) PBS mice at each timepoint. (middle row) pixel-wise paired t-test between the timepoint and Hr0 for A) LPS and B) PBS mice. (bottom row) p-value maps resultant from the paired t-tests above (middle row). Maps are thresholded to display clusters with a family wise error rate of 0.001. C) (top) Overlay of the deficit between Hr0 and Hr8 in LPS mice from part A) on an adapted map of parcellated cortical regions (adapted from White et al. [259]). (bottom) Spearman's rho signifies the correlation between average node value within the deficit area in A) and neuroscore values for LPS and PBS mice. * signifies Hr8 p=0.0061, Hr24 p=0.019.

To directly sample the affected region discovered in Figure 4.4, PBS and LPS imaging results were directly compared using a somatosensory (Ss) seed to generate FC maps across all four timepoints (Figure 4.5, top 2 rows). A pixel-wise 2-sample t-test was performed for each time-wise LPS and PBS comparison (Figure 4.5, 3rd row). The cluster size-based thresholding method was used to isolate significantly different regions between the two groups (Figure 4.5, 4th row). There was a transient decrease in correlation strength in the proximal areas surrounding the seed region as well as on the contralateral side in the LPS mice that was not present in the PBS mice. This result peaked at Hr8, began to return to normal at Hr24, and matched baseline by Hr72. Homotopic connectivity strength was determined by averaging the FC correlation value within the seed-region on the contralateral side for the map displayed (Figure 4.5, bottom row) illustrating the same decrease in correlation strength during the experimental time course. Again, Spearman's rho was calculated to compare the rank ordered Ss homotopic FC strength across LPS and PBS populations to the respective neuroscores at each timepoint. A significant inverse relationship between neuroscore and homotopy was demonstrated at Hr8 and Hr24.

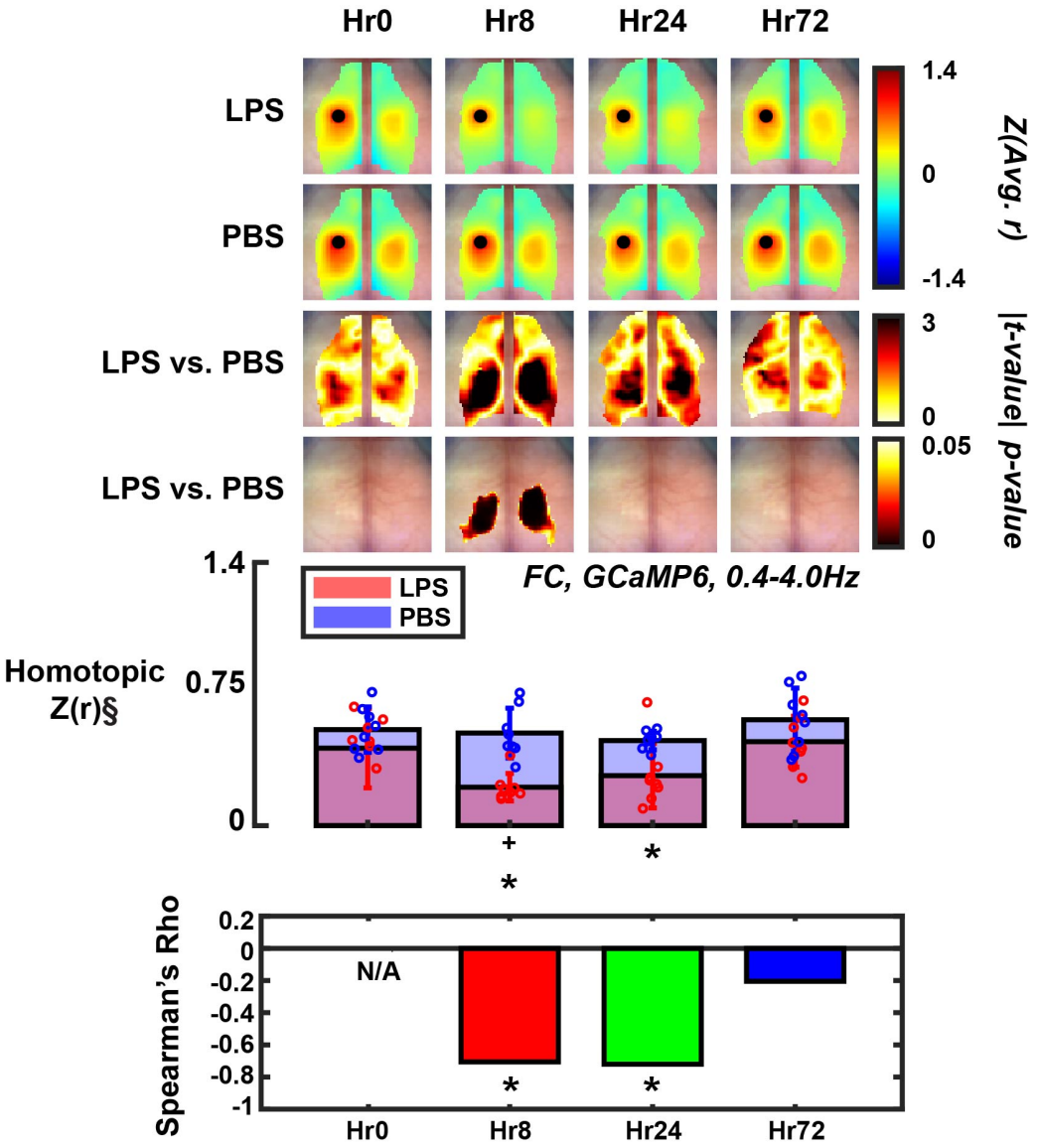

Figure 4.5: Average (LPS, N=8, PBS, N=8) seed-wise connectivity maps utilizing a Ss seed in mice that received LPS (top row) or PBS (second row). Pixel-wise two-sample t-test (third row) between LPS and PBS mice. Thresholded maps (fourth row) for significant differences between LPS and PBS mice using a cluster size-based thresholding technique with a FWE rate of 0.001. Average homotopic connectivity strength (fifth row) for each timepoint. The homotopic region here is defined by the circular seed region reflected across midline. Error bars are standard deviations. § denotes significance on 1-way rm-ANOVA (LPS only, p=0.0031). * denotes significance via two-sample t-test at the indicated timepoint between PBS and LPS populations (Hr8 p=0.0001, Hr24 p=0.01). + denotes significance via paired t-test between the timepoint and Hr0 (LPS only, Hr8 p=0.04). (bottom) Spearman's rho signifies the correlation between homotopic FC strength (fifth row) and neuroscore values for LPS and PBS mice. * signifies Hr8 p=0.0023, Hr24 p=0.0016.

Previous reports [36] have shown that during encephalopathy contrast fluctuations can be significantly dampened. We investigated this possibility in our data using multiple analytical techniques. The spatially mapped delta GCaMP6 power remained relatively unchanged across the experiment (Figure 4.6A) and the average GCaMP6 delta power over the FOV did not correlate well with neuroscore (Figure 4.6B). The power spectra for LPS and PBS mice both demonstrated a nice 1/f fall-off (Figure 4.7) with small separations at the extremes of the delta range (0.4-4.0Hz) in the LPS mice at Hr8 and Hr24. We therefore used two approaches to quantify delta GCaMP6 fluctuations that specifically sample the lower and upper extremes of the temporal bandwidth. The first invokes a method curated from the spatial root mean square of the data after temporal differentiation (DVARS) [197] literature and is used for scrubbing motion artifacts from diffuse optical tomography (DOT) data. The global variance of the temporal derivatives (GVTD) method hinges on the assumption that large, high frequency ($\sim$1-2Hz) spikes in the GVTD time trace of infraslow filtered data (0.009-0.08Hz) should represent large, transient motion artifacts, rather than actual BOLD signal (which hits a noise floor >0.2Hz). However, here, GVTD is being calculated on mouse calcium fluorescence and hemoglobin reflectance data filtered to delta band (0.4-4.0Hz) dynamics. Due to the increased temporal resolution of calcium dynamics, spikes in this band could correspond to real neural activity tone as well as extraneous motion noise. In contrast to calcium, hemoglobin is more likely to reflect high frequency artifacts such as heart rate, respiratory rate, or movement artifacts. Interestingly, following an example ten-minute GVTD trace in an LPS infected animal at each timepoint shows a drastic dampening of fluctuations at 8Hrs in the calcium trace (Figure 4.8A) that is much more subtle or non-existent in the hemoglobin trace (Figure 4.8B). The traces seem relatively unaffected in the PBS injected mouse (Figures 4.8C,D). To quantify this finding across all mice, we took the average standard deviation of the calcium GVTD traces for each timepoint in LPS and PBS mice (Figure 4.10A) and found that the decrease in GVTD corresponded with increased

neuroscores at Hr8. Additionally, we took the FFT of the calcium and hemoglobin GVTD traces and display the power spectra for each timepoint (Figures 4.9A,B).

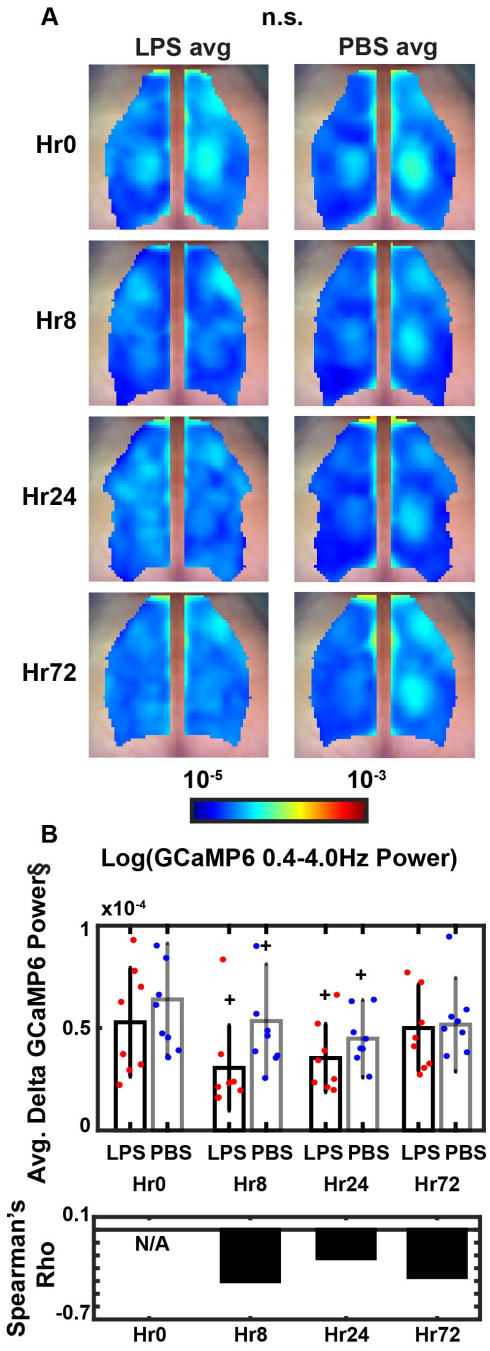

Figure 4.6: A) Average (N=8) delta GCaMP6 power maps for each timepoint. There were no significant regions surviving cluster size-based thresholding when comparing LPS and PBS mice at each timepoint. B) (top) Average (LPS, N=8, PBS, N=8) delta GCaMP6 power over the FOV at each timepoint. § denotes significance on 1-way rm-ANOVA (LPS only, p=0.0005). + denotes significance via paired t-test between the timepoint and Hr0 (LPS, Hr8 p=0.012, Hr24 p=0.019, PBS, Hr8 p=0.018, Hr24 p=0.022). (bottom) Spearman's rho signifies the correlation between average delta power values and neuroscore values for LPS and PBS mice.

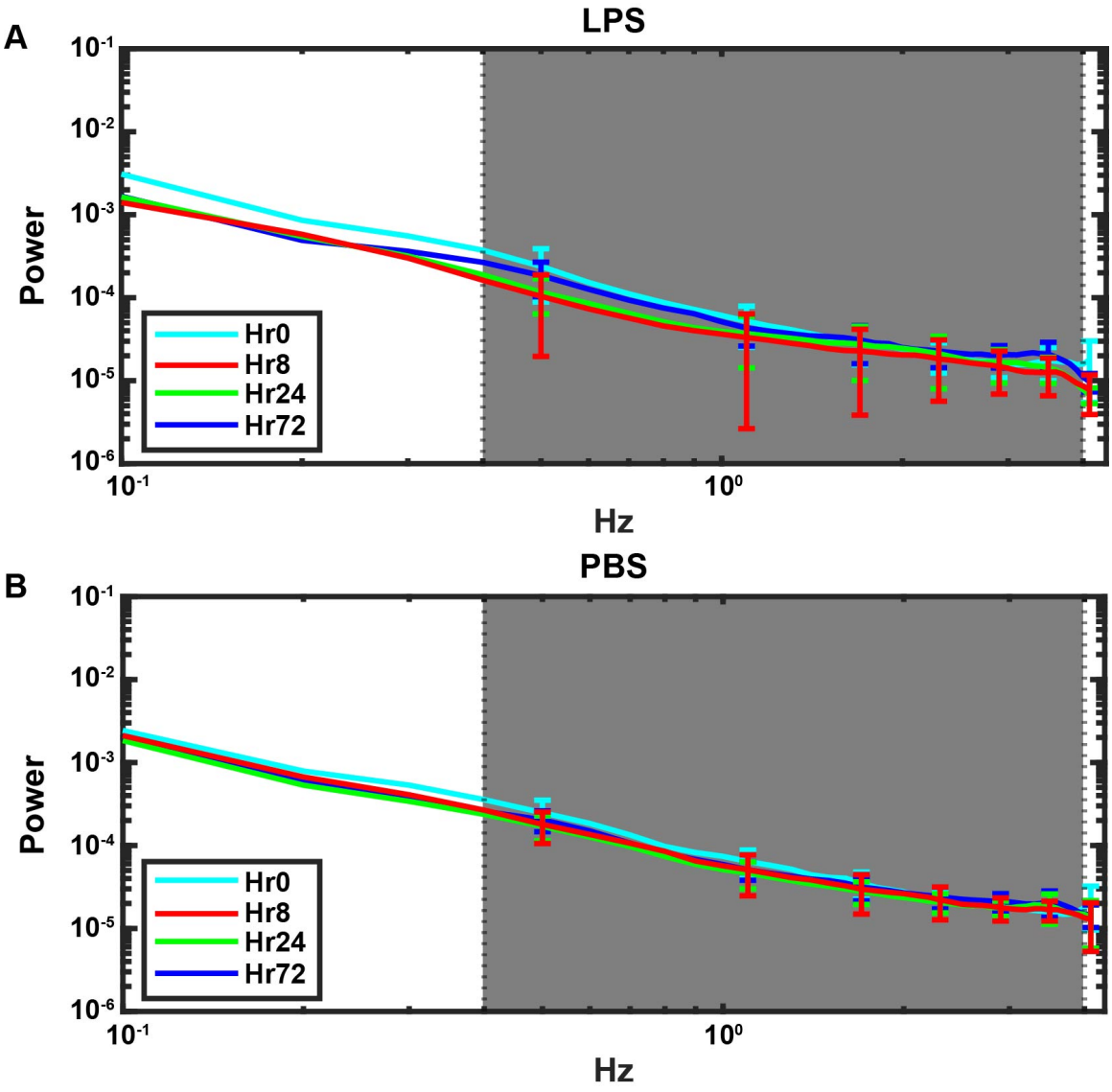

Figure 4.7: A) Average (N=8) power spectra up to 4.2Hz for LPS and B) PBS mice. The delta band (0.4-4.0Hz) is highlighted in grey.

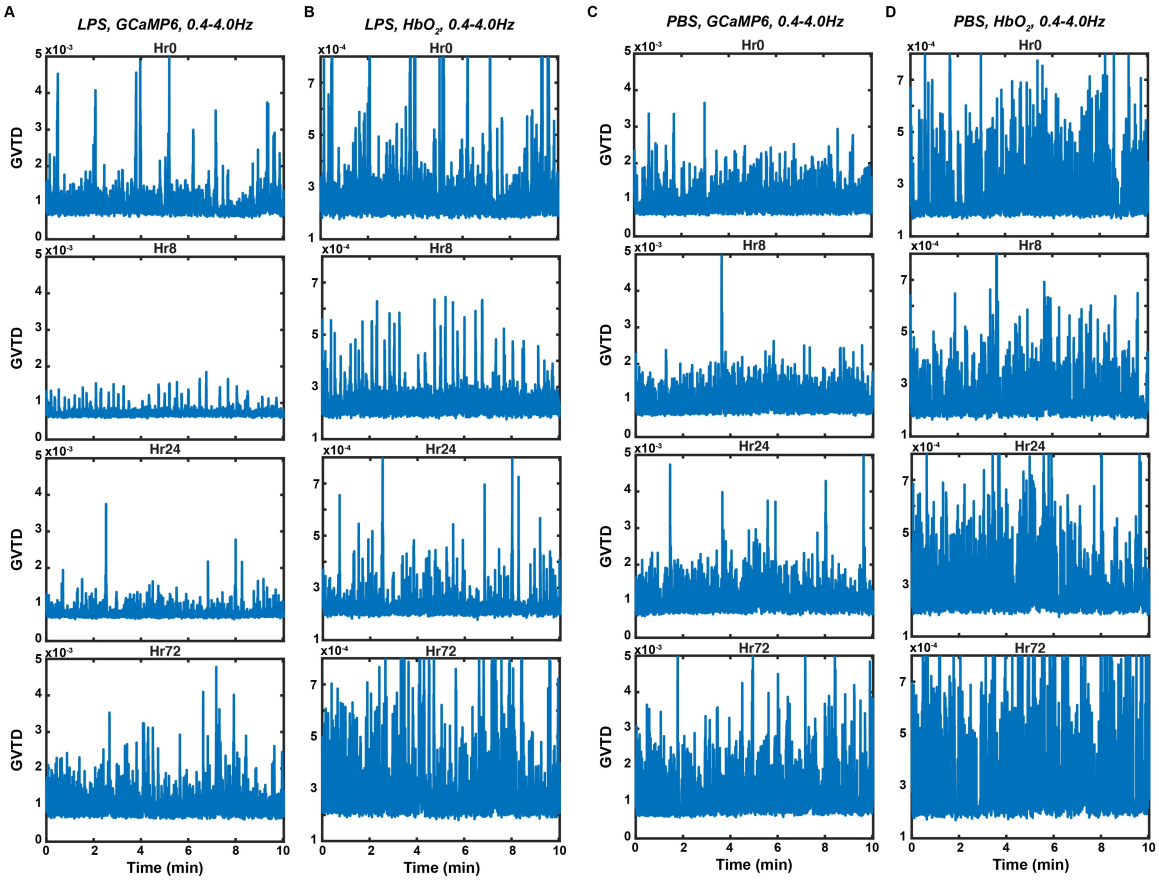

Figure 4.8: A) Example 10-minute delta GCaMP6 GVTD traces across the experimental timepoints in an LPS mouse. B) Example 10-minute delta HbO_2 GVTD traces across the experimental timepoints in an LPS mouse. C) Example 10-minute delta GCaMP6 GVTD traces across the experimental timepoints in a PBS mouse. D) Example 10-minute delta HbO_2 GVTD traces across the experimental timepoints in a PBS mouse.

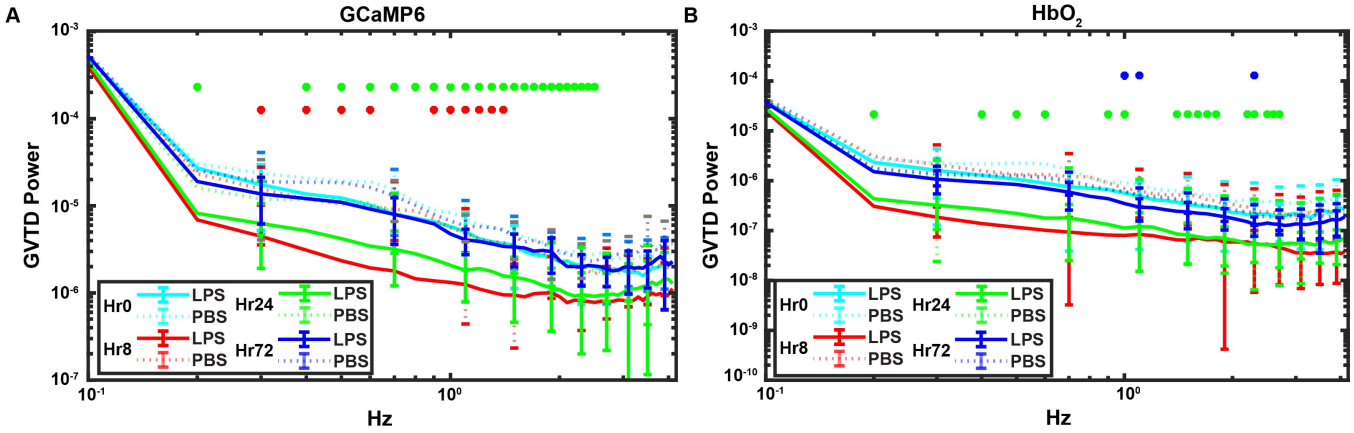

Figure 4.9: A) GVTD GCaMP6 power per Hz within the delta band. * denotes significance ($p<0.05$) via a two-sample t-test between LPS and PBS mice per Hz within a timepoint. B) GVTD HbO_2 power per Hz within the delta band. * denotes significance ($p<0.05$) via a two-sample t-test between LPS and PBS mice per Hz within a timepoint.

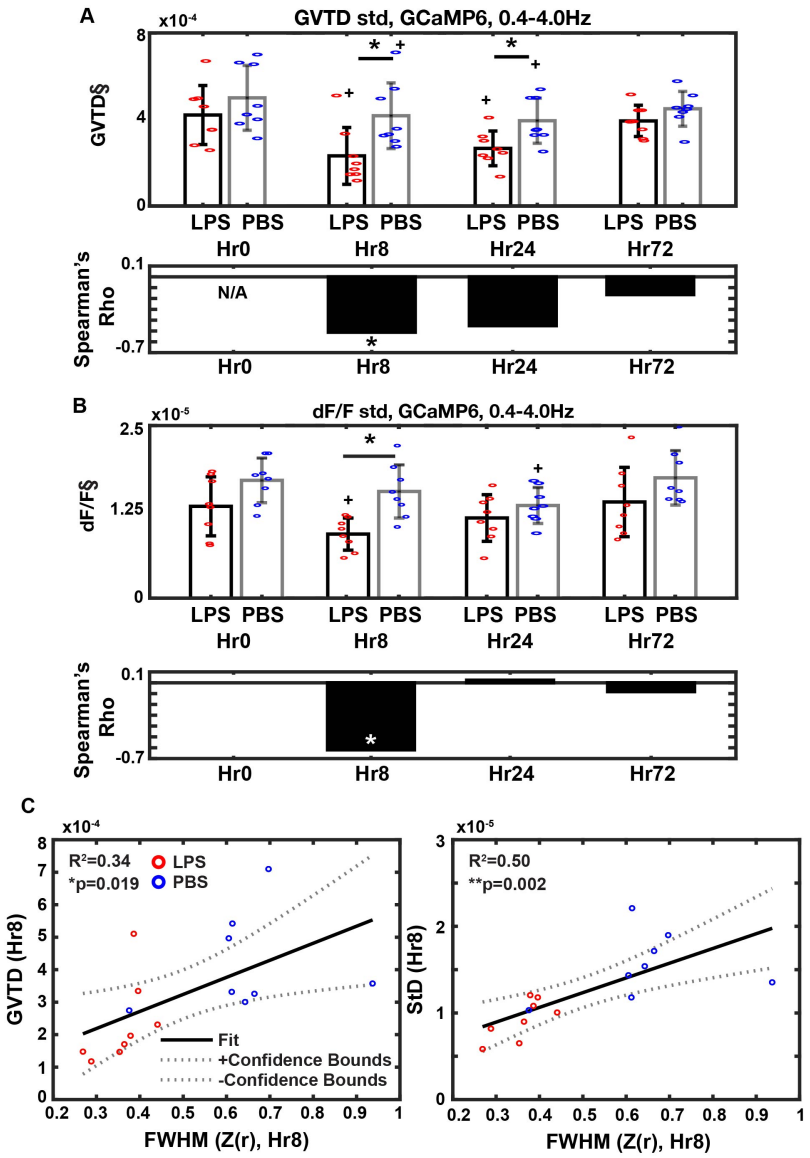

Figure 4.10: A) (top) Average (LPS, N=8, PBS, N=8) standard deviation of GVTD traces using delta GCaMP6 dynamics at each timepoint. § denotes significance on 1-way rm-ANOVA (LPS only, p=0.0005). * denotes significance via two-sample t-test at the indicated timepoint between PBS and LPS populations (Hr8 p=0.02, Hr24 p=0.016). + denotes significance via paired t-test between the timepoint and Hr0 (LPS, Hr8 p=0.03, Hr24 p=0.015, PBS, Hr8 p=0.019, Hr24 p=0.0043). (bottom) Spearman's rho signifies the correlation between GVTD values and neuroscore values for LPS and PBS mice. * signifies p=0.043. B) (top) Average (LPS, N=8, PBS, N=8) temporal standard deviation of dF/F traces using delta GCaMP6 dynamics at each timepoint. § denotes significance on 1-way rm-ANOVA (LPS only, p=0.0043). * denotes significance via two-sample t-test at the indicated timepoint between PBS and LPS populations (Hr8 p=0.0017). + denotes significance via paired t-test between the timepoint and Hr0 (LPS, Hr8 p=0.047, PBS, Hr24 p=0.0069). (bottom) Spearman's rho signifies the correlation between temporal standard deviation values and neuroscore values for LPS and PBS mice. * signifies p=0.01. C) (left) Linear regression between GVTD fluctuations at Hr8 and FWHM values at Hr8 determined in Figure 4.1D. (right) Linear regression between temporal standard deviation fluctuations at Hr8 and FWHM values at Hr8 determined in Figure 4.1D.

Our second approach to quantify overall calcium fluctuations across the experimental time course was to take the standard deviation of the spatially averaged dF/F calcium GCaMP6 trace (Figure 4.10B). Similar to the GVTD approach, we saw a transient decline in fluctuation at 8Hrs that returned by 72Hrs (initially returned to baseline by 24Hrs) which inversely and significantly correlated with neuroscore at Hr8. Finally, there was a linear relationship between GVTD fluctuations and the FWHM result (Figure 4.10C, left) and the temporal standard deviation and FWHM result (Figure 4.10C, right). Interestingly there was no linear relationship between GVTD fluctuation and weight change when using both the LPS and PBS data (Figure 4.11A), and there was a trending inverse linear relationship when using LPS data only (Figure 4.11B).

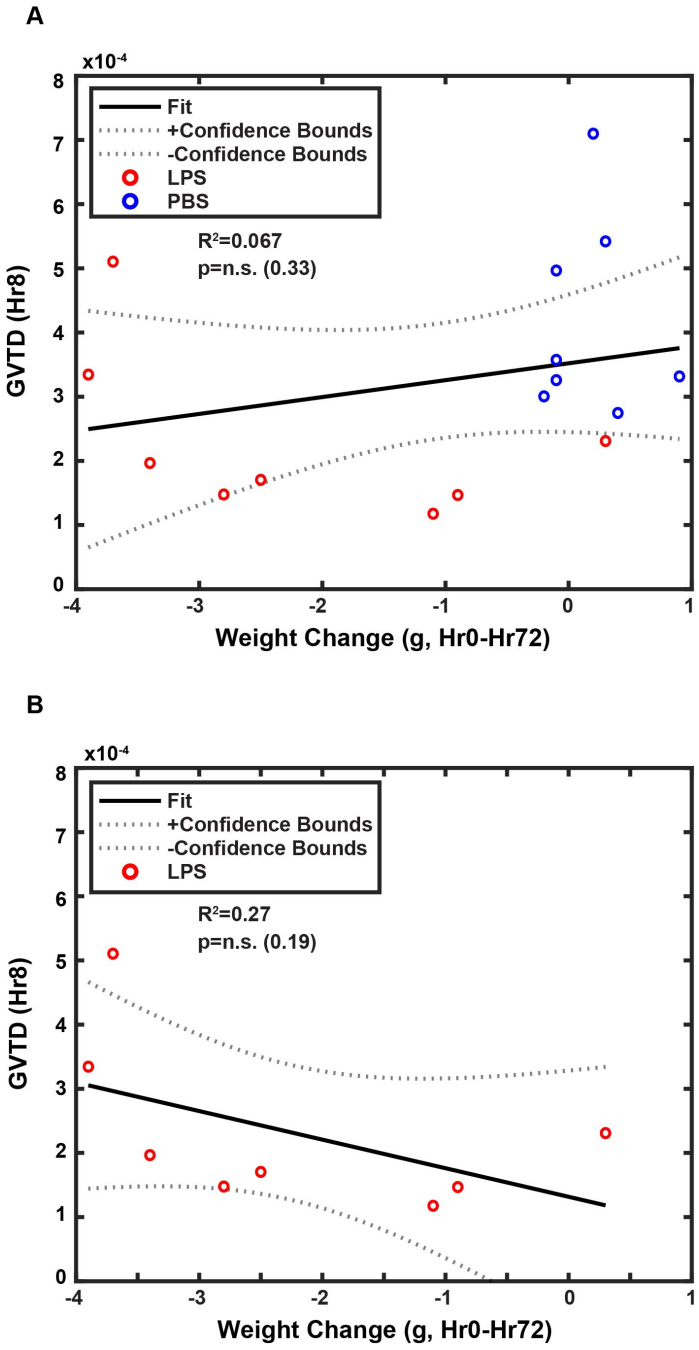

Figure 4.11: A) Linear regression between GVTD fluctuations at Hr8 and weight change over the course of the experiment using data from LPS and PBS mice. B) Linear regression between GVTD fluctuations at Hr8 and weight change over the course of the experiment using data from LPS mice only.

4.4 Discussion

We imaged mice injected with LPS or PBS across a time course consistent with ASE. Behavioral metrics (Figure 4.1A, Figure 4.2) acquired suggested septic encephalopathy and recovery on our time scale, with the neuroscore displaying peak alterations at 8Hrs, and recovery by 72Hrs. More advanced behavioral assays necessary to dissect other symptoms of encephalopathy (e.g., Barnes maze testing for learning and memory) take multiple days to complete and outlast this time frame for ASE. Therefore, we proposed creating an imaging biomarker over the course of the disease utilizing connectivity modeling and temporal fluctuation quantification analyses. Further, we were able to dissect a breakdown in neural connectivity consistent with peak encephalopathy and track the recovery of these deficits paralleling a transient decline and return of global neural activity tone.

We sought to establish any potential connectivity deficits introduced by acute LPS injection. Connectivity metrics have proven to be sensitive and spatially specific to various types of disease pathologies, however not typically studied on such an acute time scale. Here, mice were imaged at baseline, 8Hr, 24Hr, and 72Hrs after an injection with either LPS or PBS and connectivity was modeled at each timepoint. The main imaging finding from the qualitative FC maps (Figures 4.1B, 4.4A,B) was an overwhelming disappearance of high correlation values at Hr8 that returned by Hr72 in LPS mice (PBS-injected mice remained unchanged, Figure 4.3). This observation was quantified by plotting the distribution of FC correlations (Figure 4.1C) across maps of all seeds across timepoints (Figure 4.1B). The FWHM of these distributions became significantly narrowed (Figure 4.1D), representing a decrease in higher magnitude connectivity values and a convergence to a connectivity value of 0 (i.e., a global reduction in connectivity). This deficit peaked at 8Hrs and resolved by the Hr72 timepoint. A random field theory approach was used to spatially locate the deficit (Figures 4.4A,C) and further analysis using a somatosensory (Ss) seed illustrated the loss

of proximal ipsilateral and contralateral connectivity to the seed region (Figure 4.5). This statistical approach operates on the hypothesis that neighboring pixels are likely not independent samples (i.e., a Bonferroni correction for multiple comparisons would be too stringent) and therefore large-grouped differences via independent pixel-wise t-tests are more likely to represent a significant change somewhere within that cluster. This method is set up to have a FWE rate of 0.1%, meaning in the collection of thresholded pixel-wise t-tests, there is a 0.1% chance of having at least one false positive result. Using this approach, we were able to prove the loss of connectivity strength surrounding the seed region and on the homotopic contralateral side (Figure 4.5). Overlaying the FC deficit present in Figures 4.4 and 4.5 onto an adapted cortical parcellation [259] (Figure 4.4C) illustrates the focus of the deficit in Ss and parietal cortex. Interestingly, Ss cortex is particularly implicated in sensory processing and relaying this information to hippocampus [194, 21, 65, 38]. Additionally, parietal cortex is involved in spatial navigation and memory retrieval [134, 19]. It is interesting that these regions were most affected since they are part of the cortical-hippocampal circuit necessary for the performance of cognitive tasks that are usually disrupted in ASE [260, 142, 168].

While previous optical imaging studies of LPS injected mice have shown disruption in response to stimuli 4-6Hrs post [33], or connectivity deficits 24Hrs post [272], none have illustrated the entire course of the disease, from onset to recovery. The closest study with this experimental design tracks one patient with NMDA-receptor encephalitis using fMRI [36]. During peak encephalopathy, there was a decrease in BOLD fluctuations that returned to normal by recovery. Similarly, we took the standard deviation of the spatially average dF/F calcium signal at each timepoint and noticed a significant transient depression in fluctuation in LPS mice at 8Hrs (Figure 4.10B). Additionally, we implemented GVTD as a surrogate representation of neural activity tone over the course of the experiment (Figure 4.10A). This independent measure converged onto the same conclusion as the temporal standard deviation of dF/F result. We thought that the altered connectivity result could be explained by

this decrease in calcium fluctuations, especially since there was a linear relationship between the imaging FWHM result and GVTD fluctuations and FWHM and temporal standard deviation results (Figure 4.10C). However, this would only partly explain the result at best, since neither linear regression result exceeded $R^2 = 0.5$ and since the Pearson correlation calculation is also looking at the temporal synchrony between two ROIs. Further, mapping the pixel-wise delta power resulted in no significant differences between LPS and PBS mice at each timepoint utilizing the same cluster size-based threshold as before (Figure 4.6A). Additionally, the connectivity results have a spatial specificity for ipsilateral proximal regions to somatosensory seed regions and homotopic contralateral regions while calcium power seems rather unaffected globally. Altogether, these imaging findings provide evidence that there is both a depression in neural fluctuations and functional temporal desynchrony introduced by ASE that resolves by Hr72. There are only a few instances reporting a pathological decrease in imaging contrast fluctuations, one being the aforementioned NMDA-receptor encephalitis fMRI study. Elsewhere in fMRI, there are notable depressions in BOLD fluctuations in deep anesthesia with sevoflurane [187]. In both anesthetized and encephalopathic neurological states, the subject cannot normally process and is less responsive to surrounding stimuli. In this model of ASE with LPS, a pro-inflammatory stimulus, there is a large acute activation of glial cells, which can often lead to decreased synaptic integrity or increased cell death [63], here, quantified as decreased fluctuations and altered connectivity.

GVTD has originally been used to scrub motion artifacts in infraslow DOT data [214]. The technique relies on the assumption that any large transient globally shared variance due to motion artifacts would appear as a spike that is orders of magnitude higher than the baseline fluctuations. Therefore, in order to maximize the sensitivity of GVTD to noise due to motion, it is recommended to calculate it after filtering the data to suppress the baseline fluctuations due to respiratory and heart rates. However, in this paper, we take advantage of the baseline fluctuation values of GVTD in the delta filtered calcium data. While there

could still be large global fluctuations representative of quick motion artifacts in this data, it is much more likely that baseline noise in this spectral band is due to physiological noise such as heart rate or respiratory rate. Further, in the 0.4-4.0Hz spectral frequencies, hemoglobin dynamics hit a noise floor [34], so GVTD of this contrast should overwhelmingly represent sources of noise, such as heart rate and respiratory rate, rather than our signal of interest. When comparing delta calcium and hemoglobin GVTD side-by-side (Figure 4.8), there is a large decrease in GVTD fluctuations in the former and only subtle, perhaps non-existent, changes in the latter. Looking at the spectral content of calcium and hemoglobin GVTD (Figures 4.9A,B), there is at least an order of magnitude more power in the calcium GVTD content, suggesting that the changes in hemoglobin GVTD cannot completely account for all the change in calcium GVTD. Further, due to the larger variance-to-effect size ratio in hemoglobin GVTD, there isn't a significant change in spectral GVTD content from baseline until 24Hrs, while this result is present in the calcium data as early as 8Hrs. This temporal mismatch in effect further advocates for the idea that the hemoglobin GVTD change cannot completely account for the calcium effect. Lastly, weight change on this acute experimental timescale is a reasonable index of overall illness (which often results in altered heart rate, respiratory rate), and this did not correlate well with GCaMP GVTD (Figure 4.11A). In fact, if anything, there was a trending negative relationship between weight loss (indicative of very sick) and GVTD (Figure 4.11B), indicating GVTD is outputting more than just physiologically confounding variables.

4.5 Conclusions

Here, we use optical imaging of mice under an experimental time course consistent with acute septic encephalopathy. Functional connectivity was compared between mice injected with LPS or PBS at Hr0, Hr8, Hr24, and Hr72, showing a transient decrease in correlation

strength at Hr8 that recovered by Hr72. Specifically, functional connectivity was disrupted in somatosensory and parietal cortical regions. This transient decrease in functional connectivity correlated with changes in neuroscore. Further, there was a significant transient decrease in GCaMP fluctuations at Hr8 that returned to baseline by Hr72. Imaging offers a unique, acutely-available snapshot and biomarker for this experimental animal model. Future work will focus on the cellular and molecular mechanisms that drive connectivity changes in this LPS-induced septic encephalopathy animal model.

Chapter 5

SIRT1 Mediates Hypoxic Postconditioning- and Resveratrol-Induced Protection against Functional Connectivity Deficits in Subarachnoid Hemorrhage

Similar to the study of acute septic encephalopathy (ASE), we investigate the functional neuroimaging changes in an endovascular perforation model of subarachnoid hemorrhage (SAH). In contrast with the ASE study, this mouse model is more established, yet the neuroimaging results have yet to be reported. Various molecular mechanisms for treatment of SAH have been elucidated and the effects of certain treatments are explored through behavioral assessment and functional connectivty assays.

5.1 Introduction

Aneurysmal subarachnoid hemorrhage (SAH) is a devastating condition that affects roughly 30,000 people in the US per year [131, 96, 162]. While advances in the phenomenological understanding and management of the pathophysiology of SAH have occurred, morbidity and mortality remain high – 30% of patients die [37], and 50% of survivors have long term deficits that preclude returning-to-work [163, 102]. The largest treatable cause of poor SAH outcome is delayed cerebral ischemia (DCI), which leads to death or disability in roughly 30% of all SAH patients [32]. For years, DCI was solely attributed to large artery vasospasm (constriction of large arteries 4-12 days after SAH) [241, 77, 152, 202]. Recently, several additional pathologies affecting the cerebral microvasculature have been linked to DCI, such as autoregulatory dysfunction [196, 166], microvessel thrombosis [247, 248, 84], and blood-brain barrier breakdown [255, 87], challenging this canonical view of DCI pathophysiology. Past trial failures have resulted from targeting only single elements of DCI, which we now know to be a multifactorial process. As a result, future therapies likely need to target both large artery vasospasm and microcirculatory deficits to be effective. This is the primary reason why conditioning-based therapy, which capitalizes on powerful and pleiotropic endogenous protective cascades, is so attractive for SAH patients.

Conditioning harnesses the brain's inherent resistance to injury by exposure to a sublethal injurious stimulus. While hypoxia and ischemia are the most commonly studied conditioning stimuli, many drugs, including some that are already FDA-approved for other conditions, can be used to induce epigenetic-based protective mechanisms [140, 68, 165, 20, 144, 70, 186, 161, 93, 69, 233]. For years, neurons were felt to be the principal target of this protective response (neuronal conditioning) [228] but multiple lines of evidence now show that glia (glial conditioning) [237] and vessels (vascular conditioning) [253] are also involved. The latter is of special interest for SAH, given the central role vascular deficits (large

artery vasospasm, autoregulatory dysfunction, microvessel thrombosis, and blood-brain barrier breakdown) play in DCI and the subsequent poor patient outcome. In past studies, we have shown that hypoxic conditioning provides profound protection against large artery vasospasm, microvascular thrombi, and neurological deficits in an endovascular perforation mouse model of SAH. We have also linked this neurovascular protection to eNOS and most recently Sirtuin 1 (SIRT1). Sirtuin 1 (SIRT1) has been the most extensively studied of all sirtuins and is an established regulator of various molecular pathways that have been implicated in the phenomenology and pathophysiology of DCI [245]. For example, SIRT1 expression results in increased eNOS and decreased MMP-9 expression, which are essential for hypoxic conditioning-induced protection and prevention of large artery vasospasm and microvascular thrombi, respectively [51, 243, 160, 205, 244]. The protective role of SIRT1 against cerebrovascular injury has also been demonstrated pharmacologically, as treatment with the SIRT1 activator Resveratrol can induce protection against ischemic stroke, recurrent stroke, and neonatal hypoxia-ischemia [66, 207, 219, 88, 121, 173]. SAH-induced neurovascular dysfunction is multifactorial with complex pathophysiology. SIRT1 is a promising target for treatment that can positively affect various molecular pathways implicated in DCI and address these multi-faceted downstream effects of SAH.

This study examines SAH in mice using a functional neuroimaging readout. While many functional neuroimaging techniques, such as functional magnetic resonance imaging (fMRI), have significantly improved the field of human cognitive neuroscience [204], the small brain size makes it difficult to use these technologies to yield the same level of detail in a mouse model. Fortunately, there are optical methods for analyzing and mapping the mouse cerebral cortex that provide comparable resolution to fMRI [259, 128, 30, 71]. Functionally related brain networks exhibit patterns of spontaneous activity that are temporally coherent and can be quantified via functional connectivity (FC) analysis. This phenomenon has been observed in the mouse cerebral cortex with optical intrinsic signal (OIS) imaging, where changes in re-

flected light intensity off the surface of the brain are converted to changes in local hemoglobin concentrations [99, 238, 263, 72, 157]. Due to the close coupling of neurovascular activity, this hemoglobin-based imaging strategy gives a population-based surrogate readout of neural, as well as vascular reactivity [259, 22, 26]. Mouse OIS has proven to be a sensitive and effective assay for many neurological diseases, including Alzheimer's disease [25, 145], ischemic stroke [17], and glioma growth [185]. Here, we use the endovascular perforation model of SAH induction, which is widely considered to be the closest representation of human SAH, replicating the trauma experienced by the cerebrovascular system following aneurysm rupture [212, 138, 132]. Given that DCI is the largest modifiable risk factor for patient outcome, mapping the differences in FC post-SAH during DCI allows for further understanding of the neurovascular deficits caused by SAH and its sequela. By applying a translational therapeutic framework, we can investigate any potential alterations in functional architecture post-SAH as well as determine if previously proven efficacious treatment strategies attenuate these alterations in the mouse. This will allow for further exploration of the protective effects afforded by hypoxia and other SIRT1 based treatments against SAH.

5.2 Materials and Methods

5.2.1 Ethics Statement

All animal studies were approved by the Washington University School of Medicine Animal Studies Committee under guidelines and regulations consistent with the Guide for the Care and Use of Laboratory Animals, Public Health Service Policy on Humane Care and Use of Laboratory Animals, and the Animal Welfare Act and Animal Welfare Regulations. Animal reporting is according to ARRIVE guidelines.

5.2.2 Animals

Three to four-month-old male wild-type (WT) mice (C57BL/6J) mice from Jackson Laboratories (Bar Harbor, Maine, stock 000664) were used. Experimental animals were housed in an AAALAC-accredited facility in temperature- and humidity-controlled rooms with a 12h light-dark cycle. Mice were housed five to a cage and had ad libitum access to laboratory chow and tap water.

5.2.3 Cranial Window Technique

Cranial window placement occurred as described previously [218], and briefly summarized here (Figure 5.1A). Each mouse head was shaved, and a midline sagittal incision was made across the dorsal cortical surface. The scalp was retracted, and periosteal membranes were removed. A Plexiglass plate was adhered to an intact skull using dental cement (C&B MetaBond), which allowed for consecutive, repeatable imaging experiments. The mice were placed in an incubator post-surgery until they sufficiently recovered to return to a clean cage with laboratory chow and tap-water.

A

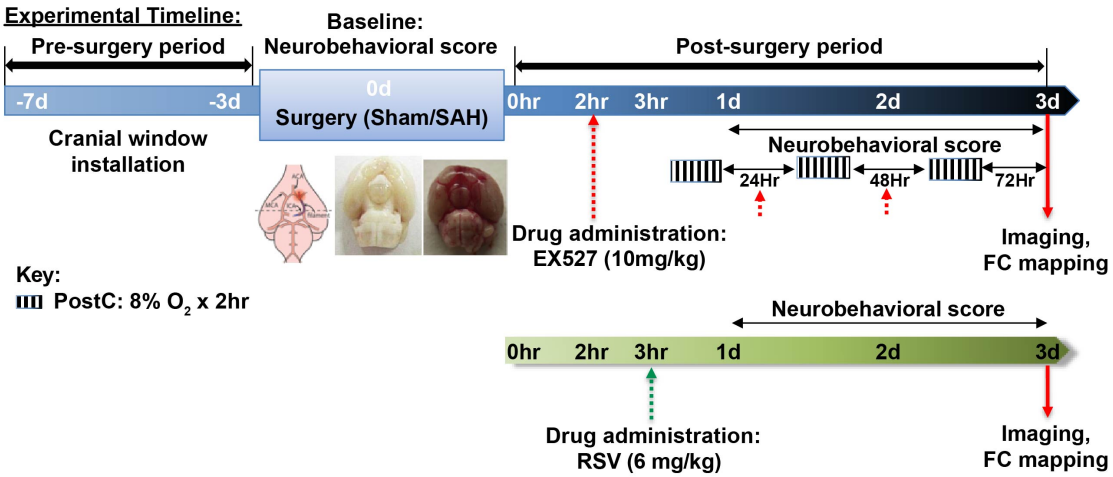

B

Surgery	Treatment	N
Sham	None	19
SAH	None	29
SAH	Hypoxic Postconditioning (PostC)	14
SAH	PostC + EX527	12
SAH	Resveratrol (RSV)	16

Figure 5.1: A) Timeline outlining the surgical, treatment, behavior recording, and imaging schedule for the present study. B) Final number of mice used in the analysis for each condition.

5.2.4 Experimental SAH

Endovascular perforation SAH was performed as described (Figures 5.1A,B) [189]. Briefly, mice were anesthetized with isoflurane (4% induction, 1.5% maintenance) in room air, with their core body temperature maintained at 37°C by a thermoregulated heating pad. A midline incision was made in the neck to expose the external carotid artery (ECA). Next, a 5-0 nylon suture was introduced into the ECA and advanced through the internal carotid artery (ICA) until the ICA bifurcation. The suture was then advanced to induce SAH, then removed and the ECA ligated. Mice in the sham surgery groups underwent the above procedures except for suture-perforation [189].

5.2.5 Hypoxic Postconditioning

Mice were placed in a hypoxia chamber for hypoxic postconditioning (PostC) and exposed to air containing 8% O2/92% N2 for 2 h with access to food and water ad libitum as indicated (Figures 5.1A,B). Mice were then returned to their vivarium containing room air.

5.2.6 Drug Administration

The Sirt1 inhibitor EX527 (10mg/kg i.p., QD, Tocris Bioscience, Bristol, UK, 2780) was first dissolved in dimethyl sulfoxide (DMSO) and then diluted to the final concentration with 1.2% β-cyclodextrin in PBS. WT mice underwent sham or SAH surgery and were then administed EX527 beginning 2h after surgery and 1h prior to hypoxic PostC and continued once daily thereafter (Figures 5.1A,B). Resveratrol (RSV, 6mg/kg i.p., BID Sigma, R5010) was prepared in DMSO, mice were administered RSV starting 3h after SAH or sham surgery (Figures 5.1A,B). In pilot studies, EX527 or resveratrol administration to Sham-operated mice did not induce any changes in body weight.

5.2.7 Neurobehavioral Testing

Neurobehavioral outcome was examined daily using Neuroscore tests, as described [189]. Briefly, neurological function was graded based on a motor score (0–12) that evaluated spontaneous activity, symmetry of limb movements, climbing, balance and coordination, and a sensory score (4–12) that evaluated body proprioception and vibrissae, visual, and tactile responses (Figure 5.1A).

5.2.8 Imaging

Mice were head-fixed in a stereotaxic frame under a high-powered, cooled, frame-transfer EMCCD camera (iXon 897, Andor Technologies, Belfast, Northern Ireland, United Kingdom). Sequential illumination was provided by a ring (7cm diameter) of LEDs: 478nm, 588nm, 610nm, and 625nm (Roithner Lasertechnik). External triggering of the camera and LEDs was provided by custom MATLAB software (MathWorks) at a frame rate of 30Hz per LED. The field-of-view ($\sim$1cm^2) covered the anterior-posterior axis from the olfactory bulbs to the superior colliculus, and the majority of the cerebral cortex convexity. Time series were binned in 128x128 pixel images with a resolution of about 80 μm per pixel. Mice were imaged on day 3 under each condition, corresponding with the timeframe of DCI in mice. Up to 45 minutes of resting state data was collected for each mouse in 5-minute data sets.

5.2.9 Image Processing

Imaging data was processed as described [259] and briefly summarized here. Reflected light intensities were filtered to 0.009-0.08Hz and translated to concentrations of oxy- and deoxy-hemoglobin by solving the modified Beer Lambert law. For each mouse, the outline of brain region was traced manually to create a binary mask (using the roipoly.m MATLAB function) indicating brain regions for processing within the field-of-view. The global signal within this

brain region was averaged and regressed from the time series data. Zero-lag functional connectivity (FC) analysis was performed using pre-specified seed regions corresponding to various cortical regions. Hemoglobin time traces within these seed regions were averaged and the resultant Pearson correlation with remaining brain pixels was calculated and plotted. Bilateral FC analysis was plotted by computing the Pearson correlation coefficient between each left hemisphere pixel and its corresponding symmetrical right hemisphere pixel.

5.2.10 Data Exclusion

Each imaging run was inspected manually. Runs with light level variance $> 1\%$ across the 5 minutes recorded were discarded. Additionally, the average bilateral FC Pearson correlation coefficient was calculated over the entire field-of-view for each mouse and calculated outliers within each experimental group were discarded (N discarded=5, 3 from SAH, 1 from Sham, and 1 from SAH:PostC+EX527).

5.2.11 Statistical Analysis

A 2-way repeated measures ANOVA (rm-ANOVA) containing one between-subjects variable (treatment) and one within-subjects variable (day) was used to evaluate differences in Neuroscore. A two-sample student's t-test was used to compare FC scores at the 3 day timepoint. A linear regression model was used to fit FC and Neuroscore under various conditions and a subsequent t-test was performed on the coefficient of determination.

5.3 Results

5.3.1 SAH Causes FC Deficit at 3 Days Post Injury

To determine whether aneurysmal SAH induces FC deficits, wild-type mice underwent the cranial window placement procedure at a minimum of 3 days before baseline neurological testing and either sham (n=19) or SAH (n=29) surgery. Neuroscore behavioral testing was performed at 24h increments until the day of imaging in order to confirm neurological deficits in SAH mice compared to Sham (Figure 5.2A, 2-way ANOVA for repeated measures (rm-ANOVA), $F(1,46)=68.715$, $p=1e\text{-}10$). Surgery was followed by OIS imaging at 3 days post-SAH, corresponding to peak occurrence of DCI. Bilateral homotopic connectivity maps displaying correlation between left and right pixels across whole-brain showed marked deficits in correlation patterns between Sham and SAH conditions (Figure 5.2B). To further elucidate the differences between groups, histograms were used to compare the number of pixels displaying a given bilateral Pearson's correlation coefficient, "r", in the homotopic maps of the SAH and Sham conditions (Figure 5.2C). The histogram comparing the entire cerebral cortical surface (Figure 5.2C, left) shows that Sham mice have a globally stronger bilateral correlation than SAH mice, as seen by the right shift on the histogram. A region of interest (ROI) was manually traced along the area of greatest deficit in the SAH bilateral map (black, Figure 5.2C, upper right corner). The histogram comparing this lower somatosensory and parietal cortical region (Figure 5.2C, right) illustrates a region specific effect induced by SAH. To further illustrate this region specific effect, FC maps with seeded regions of interest were compared between SAH and Sham (Figure 5.4A, top 2 rows). Seeds were specifically chosen within frontal (Fr), cingulate (Cing), motor (Mot), somatosensory (Ss), retrosplenial (Rs), visual (Vis), and auditory (Aud) cortices in order to sample the major cortical regions within our field-of-view. These seeded maps displayed high similarity between SAH and Sham groups for seeds placed in anterior brain regions (e.g. Fr, Cing, Mot). Loss of homo-

topic connections are visible in posterior seeds (e.g. Ss, Vis, Aud). Calculating the average bilateral Pearson correlation coefficient across the entire field-of-view resulted in significant differences between Sham and SAH global connectivity (Figure 5.2D). These large changes in global connectivity were correlated with behavioral deficits as quantified through Neuroscore (Figure 5.2E).

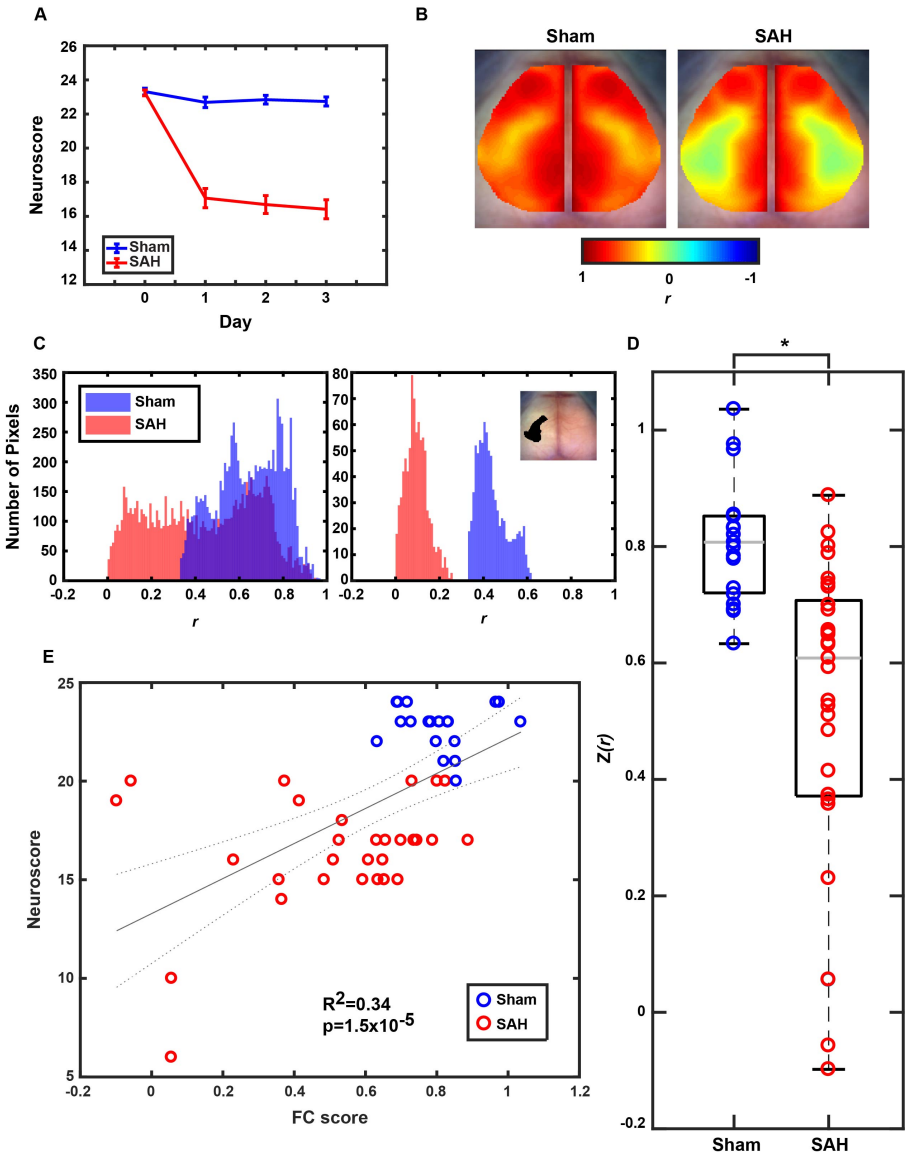

Figure 5.2: A) Average Neuroscore for Sham and SAH mice at baseline and Days 1-3. Error bars are SEM. B) Group average bilateral homotopic connectivity maps for Sham and SAH. C) Left, every Pearson correlation coefficient value per pixel plotted between Sham and SAH groups. Right, only Pearson correlation coefficients within the black outline plotted between Sham and SAH groups. D) Global average Pearson correlation coefficient from each mouse within each condition. Grey horizontal bar is the median, each box edge marks the 25th/75th percentile, whiskers extend to most extreme values not considered outliers (*$p<0.05$, two sample student's t-test). E) Linear fit of Neuroscore vs the global FC average plotted in D). Dotted grey line corresponds to confidence bounds.

5.3.2 Hypoxic Post-Conditioning Affords SIRT1-Mediated Protection against SAH-Induced FC Deficits

In addition to establishing a model for SAH injury and visualizing both global and regional-specific deficits in FC, the effects of hypoxic postconditioning (PostC) on FC were examined in wild-type mice with (n=12) and without (n=14) the SIRT1 inhibitor EX527. Cranial window and SAH surgery followed the same timeline as above (Figure 5.1A). Neuroscore was performed at 24h increments until the day of imaging in order to confirm that hypoxic PostC effectively protected against SAH-induced neurological deficits, and that EX527 removed this protection (Figure 5.3A, 2-way rm-ANOVA, Sham vs SAH:PostC, $F(1,31)=10.893$, $p=0.002$, Sham vs SAH:PostC+EX527 $F(1,29)=102.1$, p=5e-11, SAH:PostC vs SAH:PostC+EX527, $F(1,24)=49.589$, p=2e-7, SAH vs SAH:PostC, $F(1,41)=30.125$, p=2e-6, SAH vs SAH:PostC+EX527, $F(1,39)=0.029$, $p=0.86$). Bilateral homotopic connectivity maps show an improvement in global FC in the hypoxic PostC group, providing evidence that hypoxic PostC is protective against FC deficits in SAH mice (Figure 5.3B). The maps also show that EX527 removes the protective effect provided by hypoxic PostC, suggesting that the protection is SIRT1-mediated (Figure 5.3B). Visualized using the same histogram ROI-based analysis as described above, we can see that there is a specific protective effect in the highly effected somatosensory/parietal regions provided by hypoxic PostC, as exhibited by the right shifted mean correlation coefficient that is similar to the sham group (Figure 5.3C). The group that underwent hypoxic PostC with administration of EX527 displayed similar FC characteristics to the SAH group, with strong deficits in somatosensory/parietal specific regions (Figure 5.3C). FC maps with the same six seed regions (detailed above) exhibit clear differences between SAH mice treated with hypoxic PostC, and SAH mice treated with hypoxic PostC and co-treated with EX527, across the posterior seed regions (e.g. Ss, Vis, Aud). Seed maps also display similarities between SAH and SAH:PostC+EX527 groups, as well as

between Sham and SAH:PostC groups, across all regions (Figure 5.4A, rows 1-4). Comparing the global correlation coefficients, hypoxic PostC treatment greatly improved FC score but remained significantly different from the Sham and SAH groups. Adding the EX527 co-treatment, global FC became very similar to the SAH group and was significantly worse than the SAH:PostC and Sham groups. These changes in global connectivity were correlated with behavioral deficits as quantified through Neuroscore (Figure 5.3E). This data strongly indicates that hypoxic PostC is protective against FC deficits induced by aneurysmal SAH injury, and that this protection is primarily mediated via SIRT1.

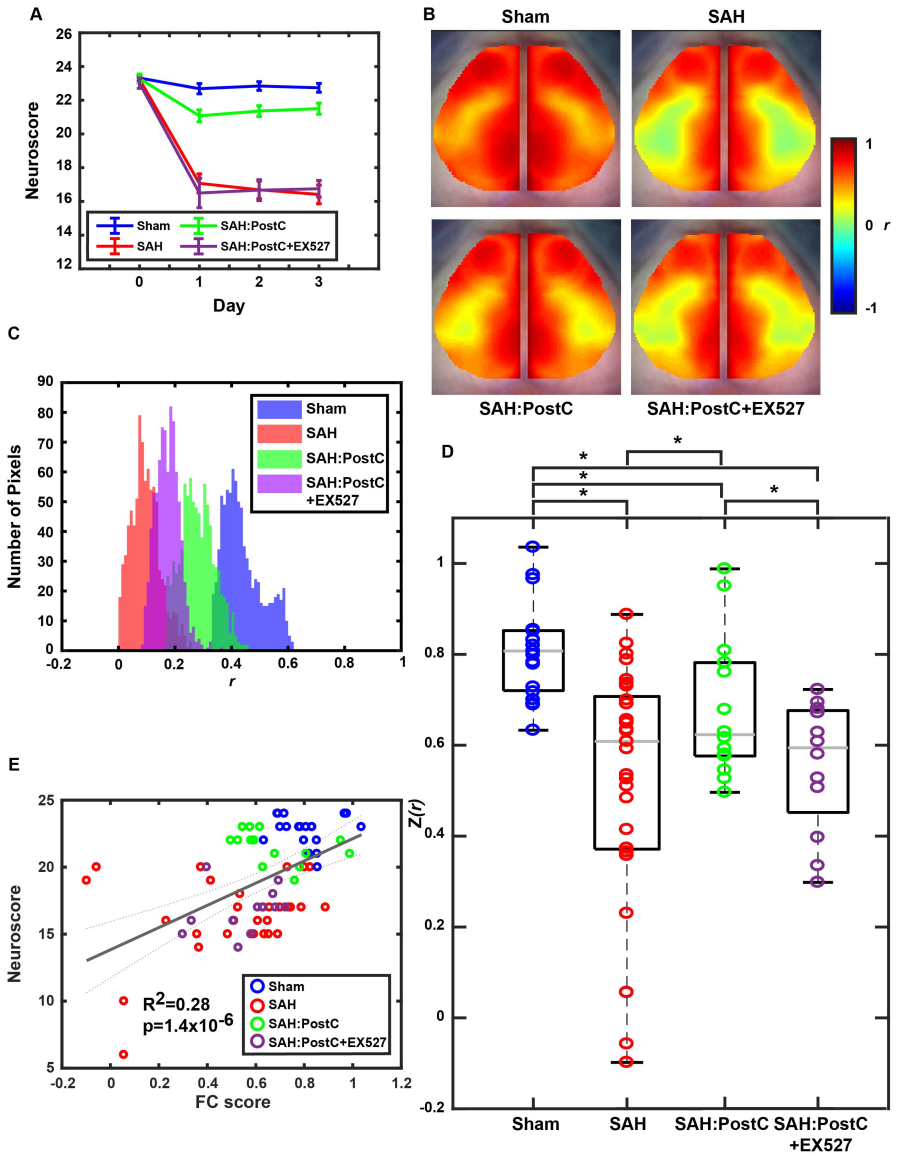

Figure 5.3: A) Average Neuroscore for Sham and SAH mice compared to SAH mice that have been treated with hypoxic PostC with or without the SIRT1 inhibitor EX527 at baseline and Days 1-3. Error bars are SEM. B) Group average bilateral homotopic connectivity maps for Sham, SAH, SAH:PostC, and SAH:PostC+EX527. C) Pearson correlation coefficient values per pixel plotted between Sham, SAH, SAH:PostC, and SAH:PostC+EX527 groups using the same ROI delineated in Figure 5.2C. D) Global average Pearson correlation coefficient from each mouse within each condition. Grey horizontal bar is the median, each box edge marks the 25th/75th percentile, whiskers extend to most extreme values not considered outliers (*$p<0.05$, two sample student's t-test). E) Linear fit of Neuroscore vs the global FC average plotted in D). Dotted grey line corresponds to confidence bounds.

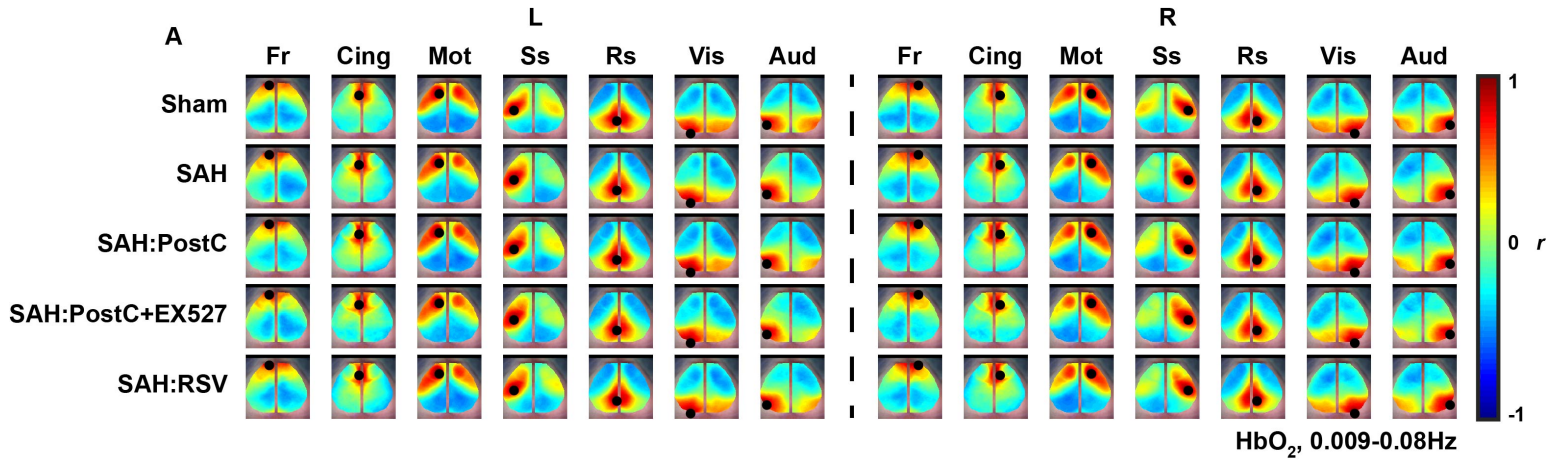

Figure 5.4: A) FC maps generated using seed-based analysis for left and right cortical seeds (black dots) for each condition.

5.3.3 SIRT1 Agonist Resveratrol Provides Protection against SAH-Induced FC Deficits

After providing strong evidence that SIRT1 provides a protective effect against FC deficits following SAH, the next step was to examine whether this protection could be mediated pharmacologically with the SIRT1 activator Resveratrol (RSV). Mice underwent cranial windowing, SAH surgery, and RSV treatment following the experimental timeline (Figure 5.1A,B, n=16). Neuroscore assessment was performed at 24h increments until the day of imaging to confirm the protective effect of RSV against SAH (Figure 5.5A, 2-way rm-ANOVA, Sham vs RSV, $F(1,33)=14.833$, $p=5e\text{-}4$, SAH vs RSV, $F(1,43)=12.098$, $p=0.0011$). Bilateral homotopic connectivity maps show an improvement in global FC in the RSV group when compared to the SAH group (Figure 5.5B). Somatosensory/parietal site-specific histogram comparisons display that RSV has a protective effect when compared to the SAH group in this highly effected area, as evident by the right shift (Figure 5.5C). While this effect is not as strong as hypoxic PostC, it is still indicative of the protection afforded by SIRT1 against FC deficits post-SAH. This protective phenomenon can be observed in the posterior seed maps comparing SAH, Sham, and RSV, as there are strong differences between sham and SAH groups, while the RSV group improves in comparison to SAH, but is still different when compared to Sham (by comparison, the seed maps for hypoxic PostC showed fewer differences from Sham, Figure 5.4A). Also noted is the trending increase in global connectivity in RSV compared to SAH (Figure 5.5D). These changes in connectivity were correlated with behavioral Neuroscore (Figure 5.5E). This data is evidence that RSV exhibits a protective effect against FC deficits after SAH. These results also suggest that SIRT1, while heavily involved, may not be the only mediator of the protection afforded by hypoxic PostC.

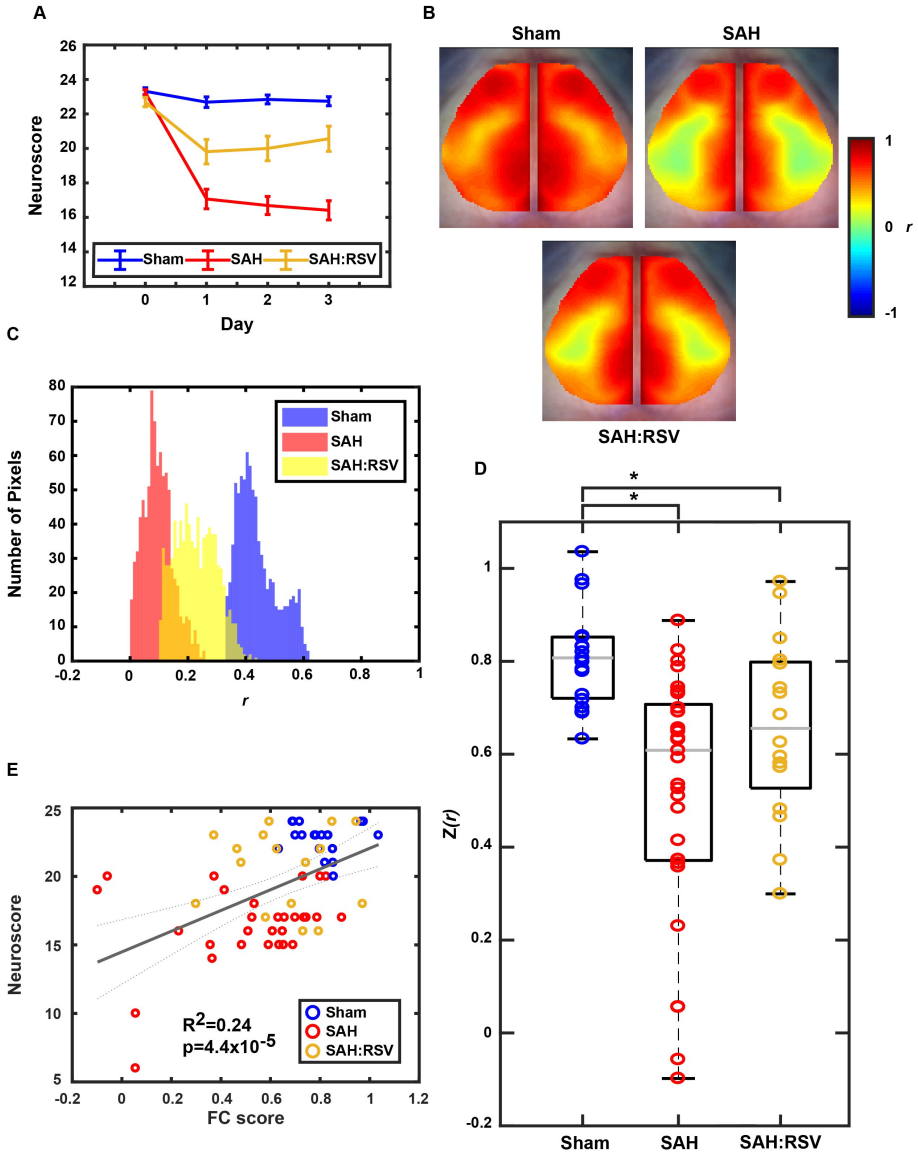

Figure 5.5: A) Average Neuroscore for Sham and SAH mice compared to SAH mice that have been treated with RSV at baseline and Days 1-3. Error bars are SEM. B) Group average bilateral homotopic connectivity map for RSV. C) Pearson correlation coefficient values per pixel plotted between Sham, SAH, and RSV groups using the same ROI delineated in Figure 5.2C. D) Global average Pearson correlation coefficient from each mouse within each condition. Grey horizontal bar is the median, each box edge marks the 25th/75th percentile, whiskers extend to most extreme values not considered outliers (*$p<0.05$, two sample student's t-test). E) Linear fit of Neuroscore vs the global FC average plotted in D). Dotted grey line corresponds to confidence bounds.

5.4 Discussion

The key novel findings from the present study are as follows: 1) The endovascular perforation model of SAH induction causes profound global deficits in FC; 2) Hypoxic PostC initiated at a clinically relevant time point after SAH induction provides robust protection against neurological deficits and FC deficits; 3) Hypoxic PostC-induced protection against FC deficits is critically dependent on SIRT1; 4) A therapeutic strategy designed to activate SIRT1 mimics the protective effects of hypoxic PostC against FC deficits. These data strongly suggest that conditioning, or molecular therapies based on conditioning, carry great promise as a novel strategy against SAH-induced brain injury and neurological deficits. They also suggest SAH-induced deficits in FC may represent a measurable imaging biomarker that could be leveraged when assessing efficacy of new therapeutics in SAH including conditioning-based agents.

DCI is the most common treatable cause of secondary neurovascular injury following aneurysmal SAH [249]. Our first objective was to determine whether or not experimental SAH causes deficits in functional connectivity (FC) that correspond to the timeline of DCI onset. Mice underwent SAH or sham surgery and were imaged 3 days later using OIS, corresponding to peak DCI in mice. Significant neurological deficits in mice that underwent SAH induction were noted. Functional neuroimaging displayed deficits that mirrored this behavioral readout, providing strong evidence that experimental SAH causes both global and region-specific deficits in mouse FC. Using a translational therapeutic approach, we then sought to use this FC readout to monitor whether hypoxic PostC would provide functional neuroprotection following experimental SAH. Hypoxic PostC has been proven to mitigate major deleterious effects of DCI and protect against both large artery vasospasm and microvascular thrombosis in a SIRT1-mediated fashion. Here, we demonstrated that moderate repetitive hypoxia, when initiated at the clinically relevant time point of 3 hours post-SAH,

provided robust protection against the FC deficits caused by SAH while also improving the neurological outcome. We also showed that co-treatment with the SIRT1 inhibitor, EX527, blocked the protective effect on both FC and neurological deficits, validating the hypothesis that the protection afforded by hypoxic PostC is mediated primarily by SIRT1.

Next, we sought to determine whether the SIRT1 activator, resveratrol, mimics the protection afforded by hypoxic PostC against FC deficits. Following the same experimental timeline, but replacing hypoxic PostC with resveratrol administration, we discovered that resveratrol also provided significant protection against both global and regional-specific FC deficits caused by SAH, but that the magnitude of this protective effect was less than that seen with hypoxic PostC. The potential reasons for this differential level of protection are varied. While resveratrol is a SIRT1 activator, it has relatively low bioavailability due to its short half-life, poor water solubility, and chemically instability [254, 10, 82]. This low bioavailability may have hampered drug accumulation in concentrations strong enough to match the effect of hypoxic PostC [24]. Alternatively, the protective effects of hypoxic PostC on SAH-induced FC deficits may be multifaceted, with SIRT1 serving as a key inducer, but other molecules also playing important secondary roles in the overall protective effect.

While FC hadn't been explored previously in the context of experimental SAH, other studies have examined FC deficits in ischemic stroke, a cerebrovascular injury that is one of the leading causes of death and disability in adults [171]. Bauer et al. first examined ischemic stroke using OIS in 2014, imaging before and 72h after transient middle cerebral artery occlusion (tMCAO) [17]. This study demonstrated that FC patterns within the regions supplied by the middle cerebral artery (MCA) were most negatively affected by ischemic stroke, and that tMCAO causes homotopic FC metrics to incrementally decline towards zero with increasing infarct severity [17]. The largest infarcts resulted in no significant homotopic correlations over the entire field-of-view, suggesting that temporal synchrony between homotopic brain regions is globally affected by ischemia; similar to the severe decline

in homotopic FC we present 72h post-SAH. Mice that experienced ischemic stroke with moderate and large infarctions also seemed to have more motor and visual cortex deficits 72h post-injury, while SAH mice seem to have more severe somatosensory deficits. Other studies examining stroke using OIS looked at prothrombotic (PT) stroke 14 days post-injury; while 14 days isn't as relevant in DCI, which has a more acute time course, brain hemispheres 14 days post-PT still showed a strong decrease in homotopic FC in two separate studies [103, 201]. Additionally, one study by Hakon et al. displayed that mice given access to an enriched environment that provided multisensory stimulation (through cages equipped with toys, tubes, chains, ladders, and platforms) after ischemic stroke had improved FC in the motor cortex after 14 days, but not in the somatosensory cortex [103]. We have shown that SIRT1-mediated therapies can improve FC in the somatosensory cortex post-SAH in 3 days, and it may be worth exploring this same SIRT1 therapy method in the context of ischemic stroke.

Functional connectivity is just one of the many endpoints that have been explored in the context of hypoxic PostC after SAH, along with vasospasm and microvascular thrombosis. One thing that separates FC from other endpoints is that it is a viable option to examine the effects of SIRT1-mediated therapies in humans through fMRI. It has already been demonstrated using fMRI that cognitive impairments due to aneurysmal SAH can be characterized by alterations in FC, with seed-based FC maps showing significant differences in impaired SAH patients in the frontoparietal network, left thalamus, left parahippocampal gyrus, and left inferior temporal gyrus [154, 227]. Memory impairment after aneurysmal SAH has also been examined using fMRI, with one study suggesting that SAH-induced memory deficits may be related to disruption of critical functional connections involving the medial temporal lobe [227, 74]. Recently, it was also demonstrated that FC examined using magnetoencephalography (MEG) also displays differences in FC patterns between controls and aneurysmal SAH patients [213]. We therefore propose that the FC analysis presented here

provides a promising future for the utilization of novel therapies, such as SIRT1 activation, for SAH in human populations.

5.5 Future Experimental Studies

This study has established that aneurysmal SAH causes FC deficits in wild-type C57/B6 mice, and that hypoxic PostC and resveratrol effectively protect against these deficits in a SIRT1-mediated fashion. As increasing evidence suggests that protection through SIRT1 is effective in SAH, an alternative method of confirming this protection would be through experiments using genetically modified mice. Tamoxifen-inducible whole-body *Sirt1-null* mice (*Cre-ert2*$^{+/-}$; *Sirt1*$^{\delta ex4/\delta ex4}$) could be used to further examine the SIRT1-mediated protective effects of hypoxic PostC against FC deficits after SAH. Constitutive whole-body Sirt1-overexpressing transgenic mice (*Sirt1-Tg*) on a pure C57BL/6J background could also be used to examine the effect of increased SIRT1 expression on FC deficits after SAH. Further, crossing these models with a mouse expressing a genetically encoded calcium indicator (GECI) driven by a *Thy1* promotor (GCaMP6, JAX stock 024276) would allow for mesoscopic, neural specific imaging across the same field-of-view as presented here [34, 265]. Using concurrent fluorescent (provided by GCaMP6) and OIS imaging, we could obtain a direct neural calcium-based and hemoglobin-based readout. This approach would allow for further applications such as examining neurovascular coupling or determining if functional deficits are vascular or neural based, throughout SAH.

5.6 Conclusions

This study demonstrates that experimental SAH causes significant deficits in functional connectivity, and that hypoxic PostC, as well as the pharmacological approach resveratrol,

exhibits a strong protective effect against these deficits along with robust improvement in neurological outcome after SAH. These protective effects are critically dependent on SIRT1. These results raise the possibility that SIRT1-directed therapies may provide protection against functional connectivity deficits in other cerebrovascular conditions, such as ischemic stroke. They also provide further evidence that the delay between SAH and DCI is a window of opportunity for a SIRT1-based postconditioning strategy. Future studies should not only continue to examine the effect that conditioning-based therapies have on FC in rodents, but also explore the possibility of testing these therapies in humans using FC monitoring.

Chapter 6

ZIKV Acutely Reduces Global Hemodynamic and Focal Somatosensory-Parietal Neural Calcium Functional Connectivity that Completely Resolves with Recovery from Infection

Previous chapters have focused on neurological disorders that have either resolved or undergone treatment after a few days. In this chapter we will use longitudinal imaging to investigate the functional connectivity fingerprints of Zika virus encephalitis over the course of multiple weeks. Based on previous work, we track functional connections from peak infection through recovery and find a robust correlation with basic behavioral measures as well as increased delta calcium power, suggesting the utility of functional connectivity as a

sensitive biomarker of disease processes. Further, neural connectivity deficits were specific to somatosensory and parietal cortical regions, similar to the finding in the ASE report, suggesting these regions as being most effected during periods of encephalopathy/encephalitis.

6.1 Introduction

Zika virus (ZIKV) is a mosquito-transmitted flavivirus of prominent global health concern that leads to a mild, flu-like illness in most adolescents and adults, but may be associated with a range of neuroimmunological disorders, including Guillain-Barré syndrome, meningoencephalitis, acute disseminated encephalomyelitis, and myelitis [43, 44]. Many patients with ZIKV neuroinvasive disease present with learning and memory deficits, even long after recovery from acute ZIKV infection [178]. The pathogenesis is likely complex and multifaceted as learning and memory processes reside within hippocampal regions, and require an intact trisynaptic circuit between the entorhinal cortex (EC), the dentate gyrus (DG), and the cornu ammonis (CA), and the generation of new neurons within the subgranular zone (SGZ) of the DG [129, 101, 177]. Murine models, developed to address mechanisms of neurocognitive disorders, have shown that ZIKV targets neural stem cell progenitors, leading to decreased proliferation within neurogenic niches of the adult brain [232]. Additional studies using a ZIKV infection model in mice indicate a specific tropism of the virus for the frontal cortex and hippocampal regions, targeting not only diffuse mature neuronal populations, but also immature populations in the DG. In this model, peak encephalitis occurs at approximately 7 days post infection (dpi) with associated infiltration of antiviral CD8+ T-cells, which activate microglia via interferon gamma receptor (IFNγR) signaling. Mice also exhibit microglial-mediated elimination of post-synaptic termini and neuronophagia within the CA regions in parallel with this acute inflammatory response, and display spatial learning deficits post-recovery [89]. While convincing hypotheses have been put forth linking these

cellular processes to symptoms experienced by those infected with ZIKV, a complete understanding of ZIKV neuropathology is lacking. Specifically, the cortical phenotype is unclear, especially with regard to the high level of communication between cortex and hippocampus during many neurological processes including cognition and memory consolidation during sleep [217, 260, 142, 168]. To date, we do not have a complete illustration of all other brain regions that may be affected by ZIKV or how the virus may affect interactions between brain regions that extend outside of this trisynaptic circuit.

One method to characterize ZIKV-induced cortical changes is by examining regional correlations of intrinsic activity that are necessary for cerebral homeostasis and cognition [153, 250, 36]. The functional magnetic resonance imaging (fMRI) community has made great strides in mapping the connections necessary for multiple brain processes using a relatively simple and straightforward seed-based analysis to calculate the temporal synchrony between any two brain regions at rest (i.e., "functional connectivity", FC) [81, 80]. fMRI of encephalitic patients offers unique challenges to the neuroimaging community because altered mental status, which is common in encephalitis patients, results in non-compliance with lengthy scans necessary for functional analysis [78]. Thus, while structural MRI is used as a diagnostic tool for patients infected with ZIKV [266], no functional neuroimaging studies have been done likely due to limitations previously noted. In contrast to fMRI, optical imaging can be performed with fewer restrictions, reduced cost and greater availability than fMRI. In animal models, an optical approach (optical intrinsic signal imaging, OIS) has elucidated cortical FC networks in the mouse [259, 265]. This method also has added advantages of imaging study subjects while awake and with head fixation, increasing data fidelity and eliminating effects of sedation on functional networks. Previous OIS studies have shown sensitivity to disease and have elucidated local perturbations associated with glioma growth [185], molecular dependent mechanisms for functional remapping post stroke [133], and FC deficits corresponding with cortical areas most effected by Aβ deposition in a mouse model of

Alzheimer's Disease (AD) [25]. While OIS only has the imaging depth to capture layers ∼i-iv of the cortex, alterations in connectivity in cortical regions that interface with hippocampus were found in the mouse model of AD (e.g., retrosplenial cortex) [25]. While FC in ZIKV infected mice has not been previously examined, we hypothesized that cortical networks, specifically those that communicate with the hippocampus, will display altered connectivity in parallel with encephalitis and subsequent cognitive decline. Previously, intracranial (i.c.) infection with ZIKV demonstrated tropism for hippocampal formations, particularly the CA [89]. Here, 8-week-old mice were infected i.c. with a mouse adapted Dakar strain (ZIKV-MA Dakar) which exhibits increased cortical infection in addition to hippocampal infection. Functional imaging between ZIKV- and mock-infected mice was compared at 7 and 42dpi. Severity of ZIKV infection (encephalitis as scored through a behavioral encephalitis score) was predicted by FC deficits and spectral densities, rendering functional neuroimaging as a potentially useful biomarker to track disease severity during the acute phase. All imaging effects resolved with recovery from infection at 42dpi.

6.2 Methods

6.2.1 Animals

A total of 45 two month old mice (mock, N=22, ZIKV, N=23) consisting of 24 female and 21 male mice total (N=12 female, N=10 male mock and N=12 female, N=11 male ZIKV mice) Thy1-GCaMP6f mice were used in the present study (Jackson Laboratories Strain: C57BL/6J-Tg(Thy1-GCaMP6f)GP5.5Dkim; stock: 024276). These mice express the protein GCaMP6f in excitatory neurons, primarily in cortical layers ii, iii, v, and vi [265]. All studies were approved by the Washington University School of Medicine Animals Studies Committee and follow the guidelines of the National Institutes of Health's Guide for the Care and Use of Laboratory Animals.

To evaluate for effects of intracranial needle insertion, mock mice are compared to mice injected peripherally with PBS 72 hours prior (N=8, all female, 3-7 months old). These mice underwent typical surgical preparations as described below, with additional bilateral EEG implantation (not used in the present study).

6.2.2 ZIKV Infection

The ZIKV mouse adapted (MA) Dakar strain utilized for intracranial infections was obtained from M. Diamond at Washington University in St Louis. The MA Dakar strain of ZIKV was obtained by passage of the original Dakar strain of ZIKV through Rag -/- mice [95], resulting in a strain of ZIKV that was found to replicate more efficiently in the mouse brain than the parent strain. Mice were deeply anesthetized and intracranially administered $1x10^4$ plaque-forming units (p.f.u.) of ZIKV MA Dakar. Viruses were diluted in 10 μl of 0.5% fetal bovine serum in Hank's balanced salt solution (HBSS) and injected into the midline of the brain with a guided 29-guage needle. Mock-infected mice were intracranially injected with 10 μl of 0.5% fetal bovine serum in HBSS into the midline of the brain with a guided 29-guage needle. BHK21 cells were used for viral plaque assays to determine stock titers of both viruses (as described in Garber et al. [89]).

6.2.3 Surgical Windowing

Prior to imaging, a plexiglass optically transparent window was implanted with translucent dental cement (C&B-Metabond, Parkell Inc., Edgewood, New York) following a midline incision and clearing of skin and periosteal membranes. The window covered the majority of the dorsal cortical surface and provided an anchor for head fixation and allowed for chronic, repeatable imaging [218].

6.2.4 Encephalitis Scores

Mice were observed daily and given a numerical score for behavioral signs of encephalitis (0, no detectable sign of disease; 1, ruffled fur; 2, slightly hunched back and ruffled fur; 3, very hunched back and lethargy; and 4, death) [42].

6.2.5 Fluorescence and Optical Intrinsic Signal (OIS) Imaging

Mice were head-fixed in a stereotaxic frame and body secured in a black felt pouch for imaging. Sequentially firing LEDs (Mightex Systems, Pleasanton California) passed through a series of dichroic lenses (Semrock, Rochester New York) into a liquid light guide (Mightex Systems, Pleasanton California) that terminated in a 75mm f/1.8 lens (Navitar, Rochester New York) to focus the light onto the dorsal cortical surface. LEDs consisted of 470nm (GCaMP6f excitation), 530nm, 590nm, and 625nm light. An sCMOS camera (Zyla 5.5, Andor Technologies, Belfast, Northern Ireland, United Kingdom) coupled to an 85mm f/1.4 camera lens (Rokinon, New York New York) was used to capture fluorescence/reflectance produced at 16.8 Hz per wavelength of LED. A 515nm longpass filter (Semrock, Rochester New York) was used to discard GCaMP6f excitation light. Cross polarization (Adorama, New York New York) between the illumination lens and collection lens discarded artifacts due to specular reflection. The field-of-view (FOV) recorded covered the majority of the convexity of the cerebral cortex (1.1cm^2), extending from the olfactory bulb to the superior colliculus. All imaging data were acquired as 5-min runs and binned in 156x156 pixel^2 images at approximately 100 μm per pixel. All 45 mice were imaged at 7dpi while a smaller cohort (mock, N=11, ZIKV, N=8) were imaged post recovery at 42dpi.

6.2.6 Imaging Data Processing

Image processing followed methods previously described [265, 149] and briefly summarized here. Images were spatially downsampled to 78x78 pixel^2 and a frame of ambient baseline light levels was subtracted from the time series data. Data were temporally downsampled by a factor of 2 and then spatially and temporally detrended. Data were affine-transformed to common Paxinos atlas space and pixel-wise time traces were mean normalized. Frames corresponding to reflection data produced by the 530nm, 590nm, and 625nm light were used to solve the modified Beer Lambert law to yield fluctuations in oxygenated and deoxygenated hemoglobin. Frames corresponding to fluorescence data were corrected by approximating hemoglobin absorption of the excitation and emission light. All data were spatially smoothed with a 5x5 Gaussian filter. The global signal was regressed from the time series data, and data were filtered with a 0.4-4.0Hz Butterworth bandpass filter.

6.2.7 Image Data Analysis

For functional connectivity (FC) analysis we calculated the Pearson correlation coefficient between the time traces from two different regions:

$$\rho_{x,y} = \frac{cov(x,y)}{\sigma_x \sigma_y} \tag{6.1}$$

where ρ is the Pearson correlation coefficient between time trace x and y, $cov(x,y)$ is the covariance between time trace x and y, and σ are the standard deviations within time traces x and y.

Bilateral FC maps represent Pearson correlation coefficients calculated between pixel-wise time traces on the left hemisphere and their corresponding symmetrical right hemisphere pixel-wise time trace. Seed-based FC refers to the traditional seed-based approach utilizing an average time trace within a cluster of pixels distributed in various cortical regions (e.g.,

parietal, frontal, motor, somatosensory, retrosplenial, and visual cortex) and the remaining pixels within the FOV. FC matrices display the Pearson correlation coefficient of the average time trace between two seed regions.

Power spectral analysis of the GCaMP6f data was performed on 10 second segments by applying a Hann window and an FFT (squared to obtain power).

6.2.8 Statistics

Pixel-wise t-tests were performed on connectivity and power maps to compare ZIKV and mock populations. These t-test maps were then thresholded, leaving pixels with a t-value corresponding to $p < 0.05$. We then used a cluster-size based thresholding method to ensure the pixel-wise error and family-wise error (FWE) rate did not exceed 0.1% and 1%, respectively, and any clusters of surviving pixels had a pixel count greater than k_α (see derivation of k_α in General Methods, Chapter 2).

A Bonferroni correction was used to threshold FC matrices. The correction consisted of dividing the overall false positive rate (0.05) by the number of unique comparisons.

6.3 Results

6.3.1 ZIKV-Infected Mice Displayed Decreased Functional Connectivity at Peak Encephalitis

We intracranially injected a mouse adapted strain of ZIKV into 8-week-old mice [95]. Infection with this strain produces heightened encephalitis. We hypothesized that use of this model will accentuate the molecular pathological findings described earlier, resulting in altered hippocampal functionality and cortical FC. To evaluate the effects of acute ZIKV on FC we analyzed the difference between ZIKV (N=23) and mock (N=22) infected mice that

were imaged at 7 days post infection (dpi) in accordance with peak encephalitis [89, 109]. Bilateral FC analysis (Figures 6.1A,B left) revealed high levels of homotopic connectivity in mock-infected mice using both delta (0.4-4.0Hz) calcium and infraslow (0.009-0.08Hz) hemoglobin contrasts. Calcium dynamics produced by GECI's provide improved temporal resolution and a more direct neural recording than downstream hemodynamics, while the latter provides an approximation for what the blood oxygen level dependent (BOLD) fMRI signal might produce in human subjects. Cluster size-based statistical thresholding revealed an FC deficit using delta calcium dynamics that was constrained to parietal and somatosensory regions (Figure 6.1C) while there was a more global decrease in FC strength using infraslow hemodynamics (Figure 6.1D). Overlay of the deficit in Figure 6.1C onto an adapted Paxinos atlas-based cortical parcellation [259] confirmed ZIKV-induced deficits in delta calcium bilateral FC clustered in parietal and somatosensory areas (Figure 6.2A). The average bilateral FC value over the entire FOV for both contrasts was significantly lowered in ZIKV-infected mice (Figures 6.1E,F) and rank-ordered bilateral FC values inversely correlated with corresponding encephalitis score (Figure 6.1G, Table 6.1). A histogram of all the delta calcium individual pixel-wise Pearson correlation coefficients both across the entire FOV (Figure 6.3A, top), and in the cluster-defined region of significant bilateral FC change shown in Figure 6.1C (Figure 6.3A, bottom) for both mock and ZIKV-infected groups illustrate a separation between the distributions of both groups. This same histogram analysis is done for infraslow hemoglobin dynamics (Figure 6.3B). We investigated the potential of sex as an independent variable and compared the average bilateral FC values for males and females using delta calcium and infraslow hemoglobin at 7dpi and found no significant difference between these populations in either contrast (Figure 6.3C,D).

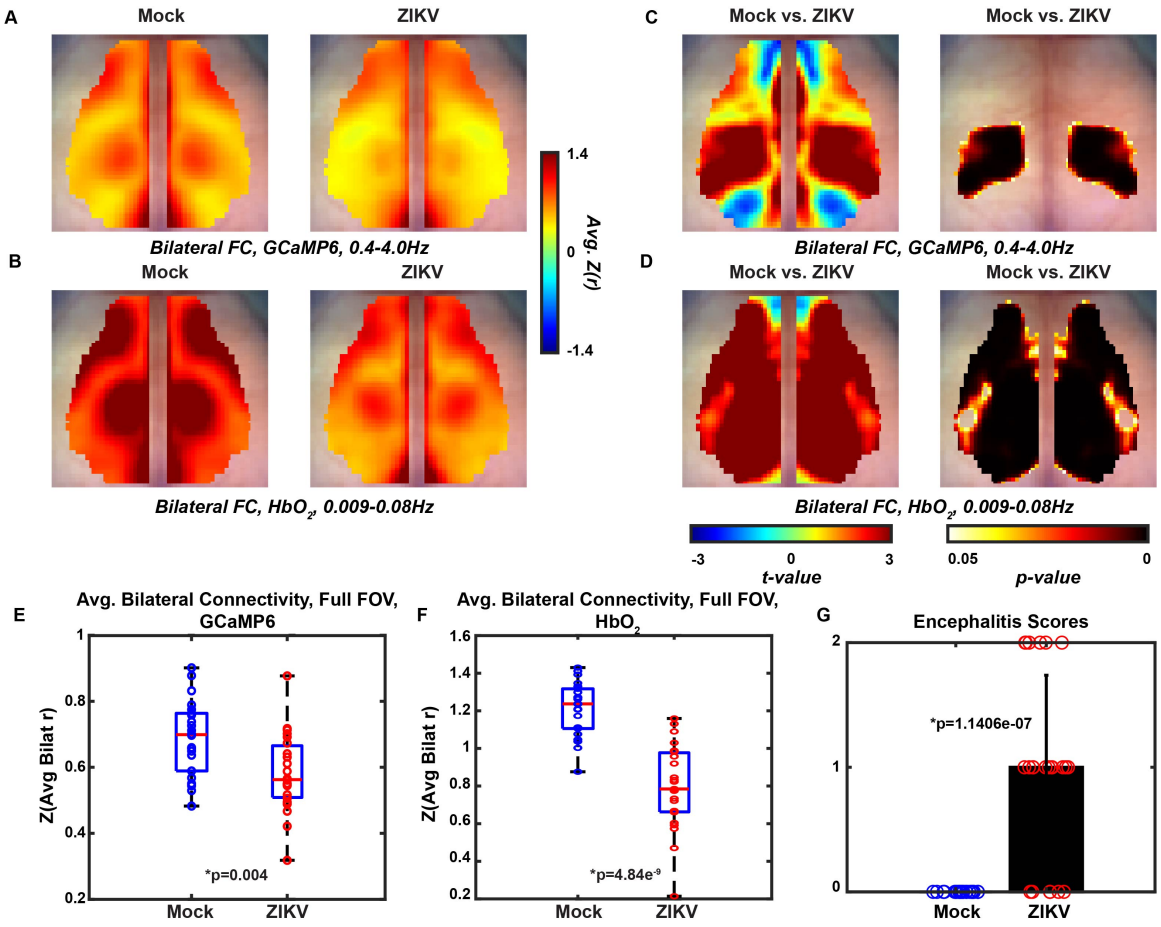

Figure 6.1: Average (mock, N=22, ZIKV, N=23) pixel-wise bilateral FC maps across mice for A) delta calcium and B) infraslow hemoglobin. Pixel-wise two-sample t-test (left) and thresholded image (right) for $p<0.01$ by a cluster-based thresholding method for C) delta calcium and D) infraslow hemoglobin. Spatially averaged Pearson correlation value over the whole FOV for E) delta calcium and F) infraslow hemoglobin. Red horizontal bars represent the median value, while the box edges represent the interquartile range. Extending lines represent the maximum and minimum values. Significance determined by a two-sample t-test. G) Average encephalitis score for mock (N=22) and ZIKV (N=23) mice. Error bars are standard deviations and significance is determined by a two-sample t-test.

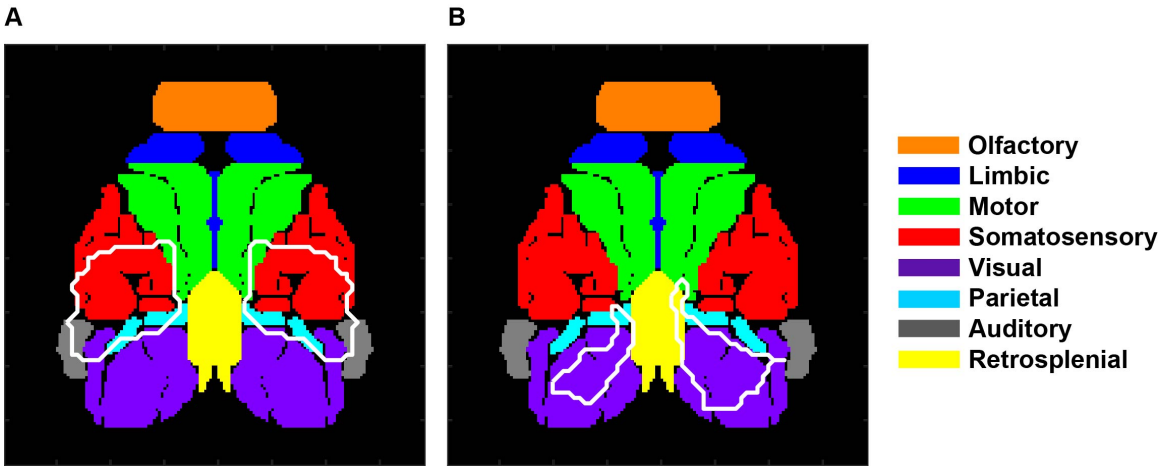

Figure 6.2: Cortical Paxinos atlas parcellation adapted by White et al. [259] with cortical regions defined and deficit from A) Figure 6.1C (bilateral FC) and B) Figure 6.8C (delta GCaMP6 power) outlined in white.

	Calcium FC	Hemoglobin FC	Calcium Delta Power
Rho	-0.34	-0.66	0.36
p-value	0.023	7.03×10^{-7}	0.016

Table 6.1: Spearman's Rho and associated p-value between encephalitis scores and average bilateral FC or calcium delta power.

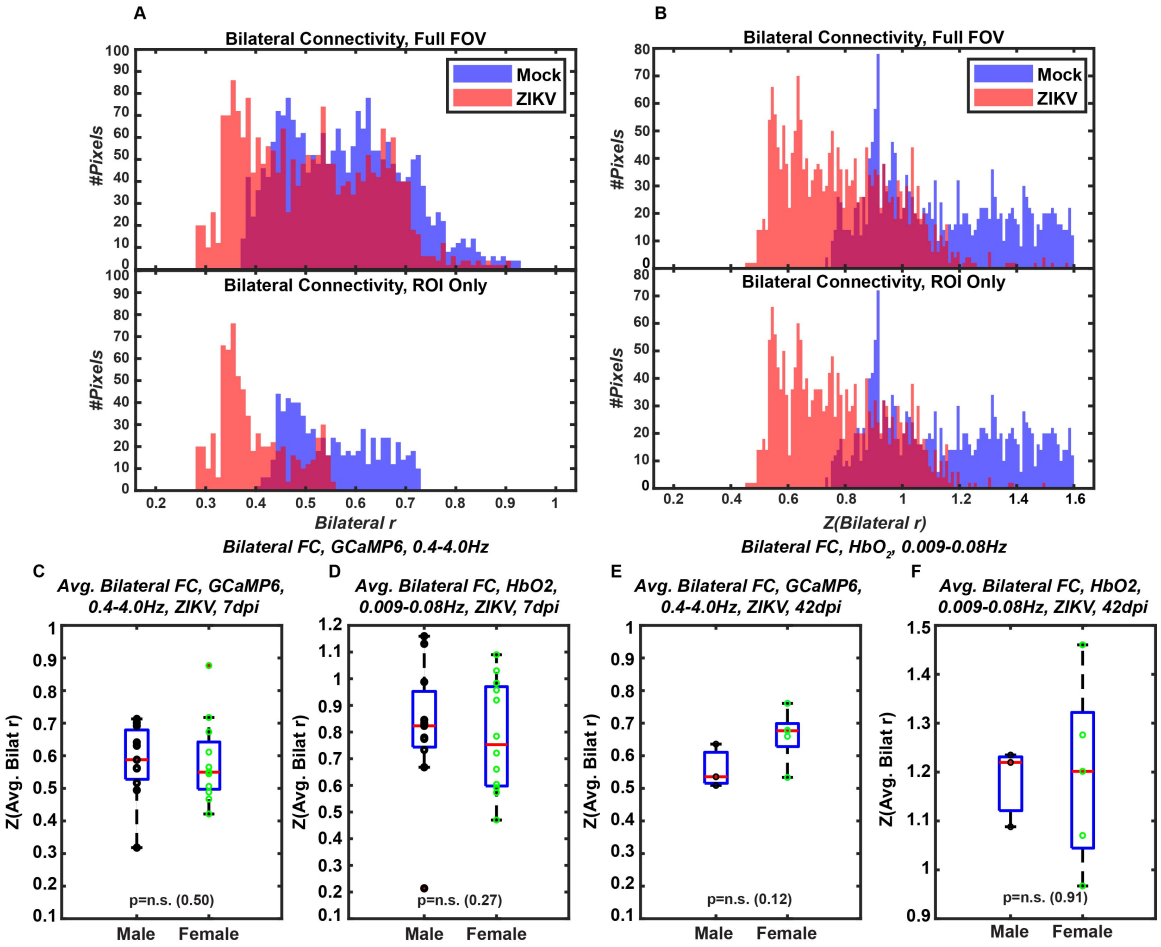

Figure 6.3: Histogram of Pearson correlation values in the average bilateral FC maps from Figure 6.1 showing the whole FOV (top) and only the regions in the cluster-defined ROI (bottom) for A) delta calcium and B) infraslow hemoglobin. Average (mock N=22, ZIKV N=23) bilateral FC over the FOV separated by sex at 7dpi for C) delta calcium and D) infraslow hemoglobin. Average (mock N=11, ZIKV N=8) bilateral FC over the FOV separated by sex at 42dpi for C) delta calcium and D) infraslow hemoglobin. Significance testing by a two-sample t-test.

There was concern that the cortical needle prick necessary for cranial infections would result in FC differences that would be of a truly technical nature and non-specific to ZIKV. There was no significant FC difference when comparing mock-infected delta calcium bilateral FC (N=22) to bilateral FC calculated on mice that had only received a peripheral phosphate buffered saline (PBS) injection 72 hours prior (N=8, Figure 6.4). Seed-based functional connectivity (FC) analysis was performed on the delta calcium mock and ZIKV-infected groups (Figure 6.5A) yielding normal homotopic FC patterns in mock infected mice, with significantly altered FC correlation strength in ZIKV-infected mice. Specifically, there was a decrease in homotopic connectivity strength when seeds were placed in parietal and somatosensory cortex. Additionally, seeds placed in the remaining cortical regions resulted in global connectivity alterations as determined by cluster size-based thresholding. Additional seeds were placed throughout somatosensory regions (Figure 6.5B) to highlight the connectivity changes present when sampling this region that was isolated in the bilateral connectivity analysis. These alterations were strongest in homotopic somatosensory regions and extended forward to pre-frontal and motor regions. FC matrices were calculated on the delta calcium data and organized into brain networks as delineated by previous parcellation methods [259], and emphasized the decrease in cortical connectivity between left and right hemispheres (Figure 6.6). Specifically, ZIKV-infection induced altered connectivity when somatosensory, visual, retrosplenial, and motor regions were involved in the FC calculation (two-sample t-test, Bonferroni correction for multiple comparisons). Similarly, multiple network connectivity deficits were discovered using this matrix approach on the infraslow hemoglobin data (Figure 6.7).

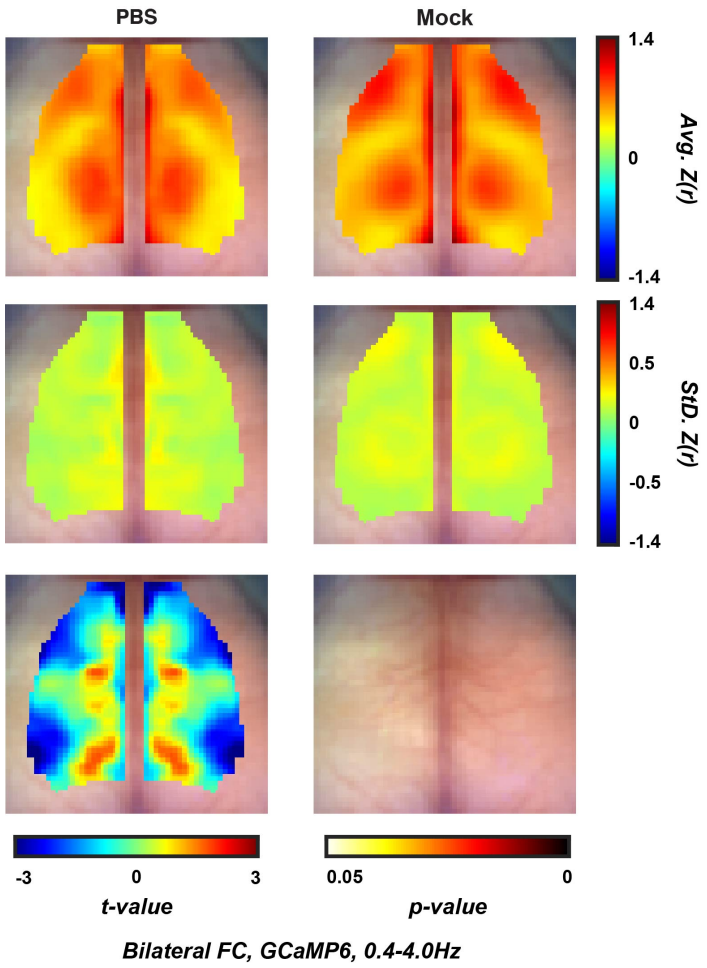

Figure 6.4: Average pixel-wise (PBS N=8, mock N=22) bilateral correlation maps (top row) and standard deviations (middle row) across mice. Pixel-wise two-sample t-test (bottom row, left) and thresholded image (bottom row, right) for p¡0.01 by a cluster-based thresholding method.

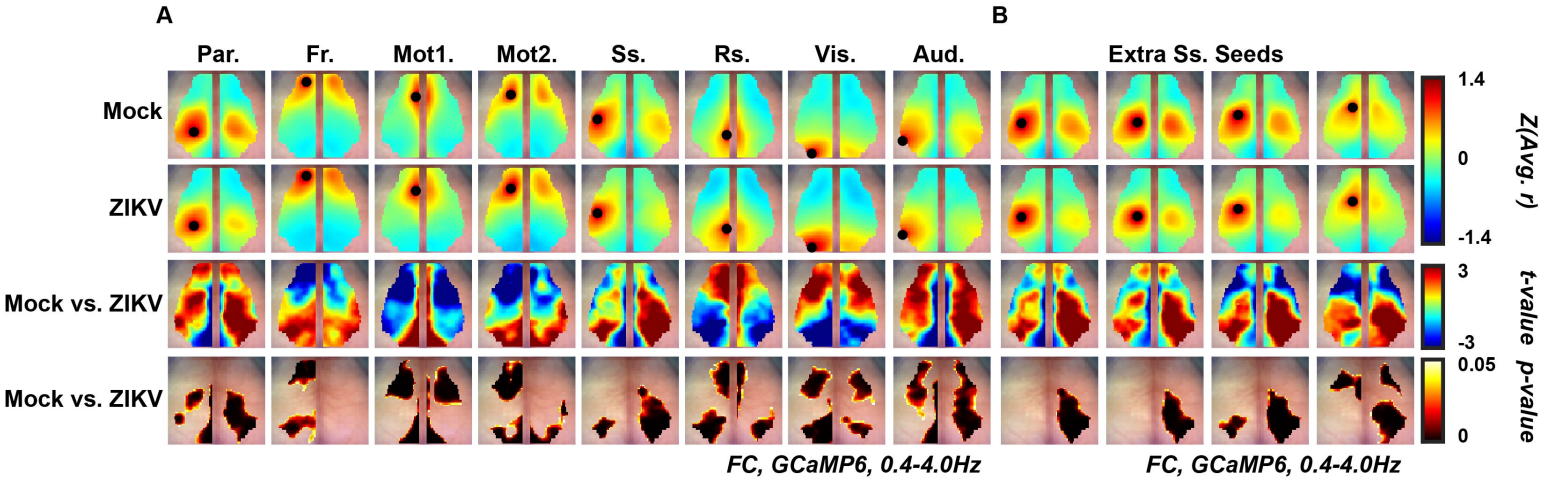

Figure 6.5: A) Traditional Pearson seed-based correlation analysis using canonical seed regions across the FOV. Top two rows: Average (mock N=22, ZIKV N=23) FC maps. Bottom two rows: Pixel-wise two-sample t-test and thresholded images for p¡0.01 using a cluster-based thresholding technique. B) The same analysis as outlined by the rows in A) but using seeds specifically assigned to sample somatosensory cortex (the main affected region in analysis displayed in Figure 6.1D (right)).

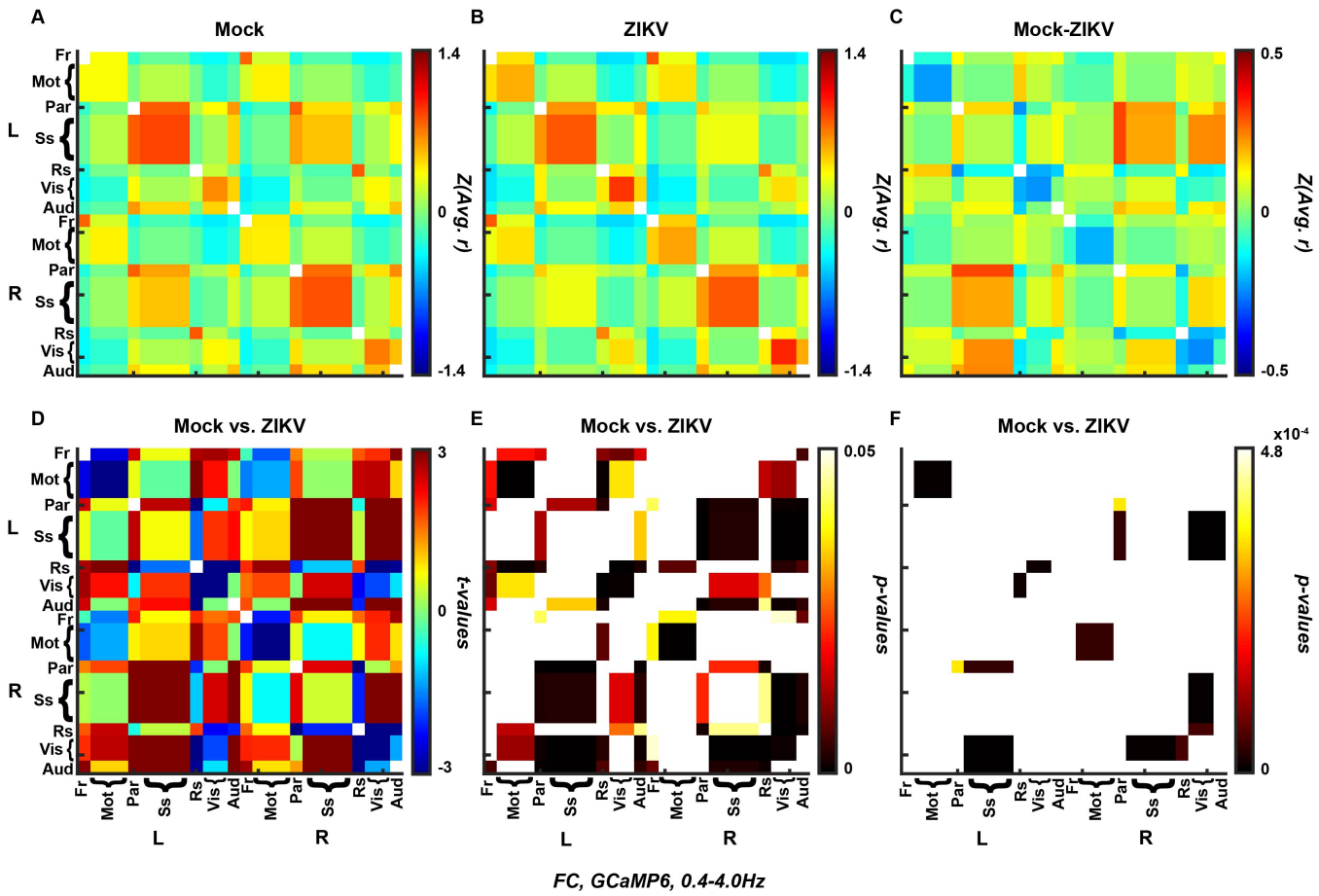

FC, GCaMP6, 0.4-4.0Hz

Figure 6.6: A,B) Average (mock N=22, ZIKV N=23) FC matrices displaying the Pearson correlation between network seeds shown on the x and y-axis, as well as the C) difference in Pearson correlation between the mock and ZIKV matrices. D) Network-wise two-sample t-test, and E) corresponding result highlighting regions with a p-value¡0.05 (uncorrected for multiple comparisons). F) Matrices are thresholded to display p-values below the Bonferroni threshold for significance (two-sample t-test).

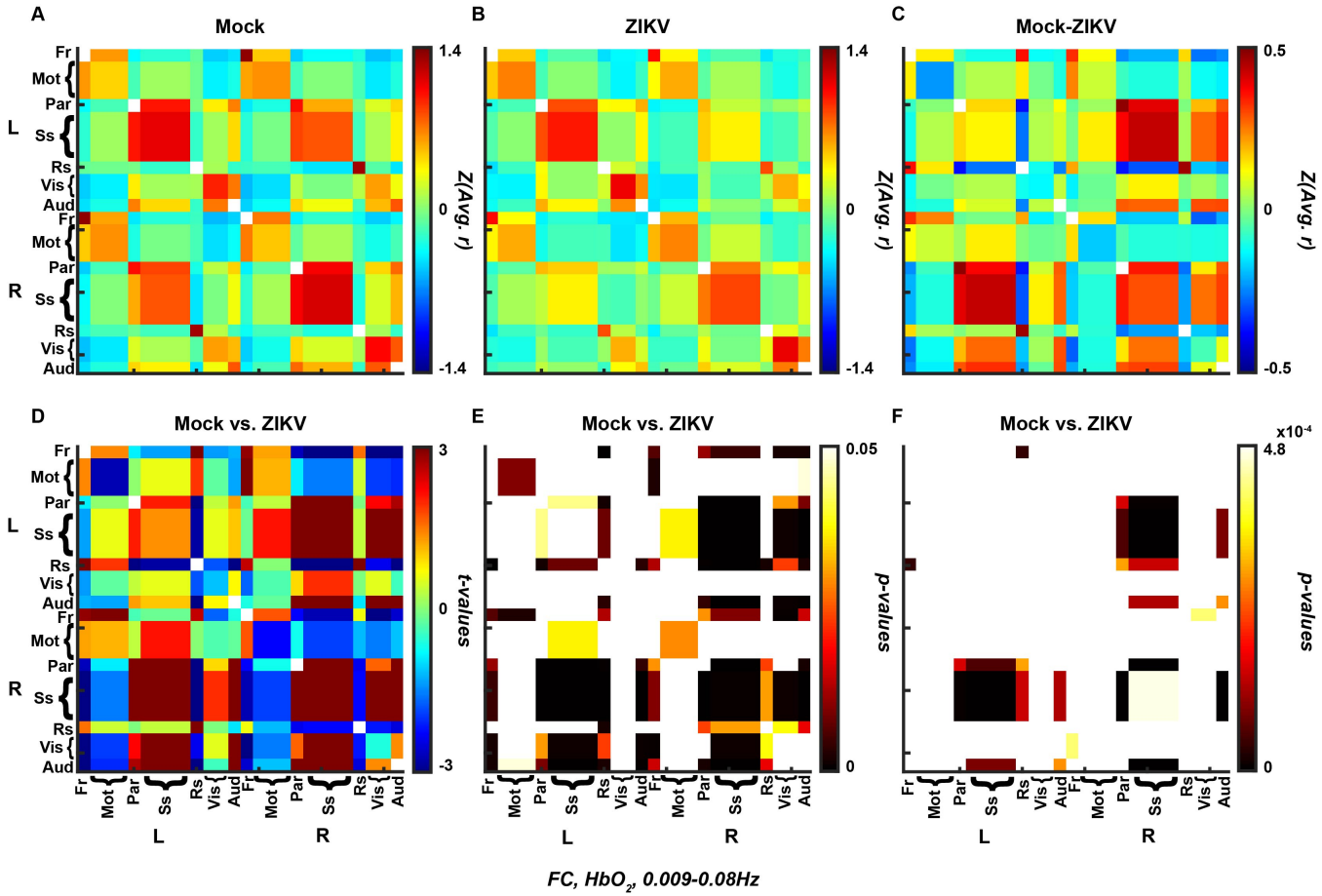

Figure 6.7: A,B) Average (mock N=22, ZIKV N=23) FC matrices displaying the Pearson correlation between network seeds shown on the x and y-axis, as well as the C) difference in Pearson correlation between the mock and ZIKV matrices. D) Network-wise two-sample t-test, and E) corresponding result highlighting regions with a p-value¡0.05 (uncorrected for multiple comparisons). F) Matrices are thresholded to display p-values below the Bonferroni threshold for significance (two-sample t-test).

6.3.2 Delta Power Increases in ZIKV- Versus Mock-Infected

Previous studies using i.c. infection demonstrated that, at 7dpi (the imaging timepoint used here), ZIKV-infected mice exhibit peak levels of viral replication and inflammatory infiltrates [89], which is often accompanied by an increase in delta power via electroencephalogram (EEG) [120]. Here, using the fast dynamics of calcium [34, 169] relative to traditional hemoglobin imaging (where dynamics are limited to <0.2Hz [107, 8]), we were able to examine GCaMP6 power up to 4.2Hz (Figure 6.8A). We took the average delta power (0.4-4.0Hz) of the GCaMP6 signal over the FOV (Figure 6.8B) and elucidated an increase in delta power in ZIKV-infected mice (top row). Both groups of mice had seemingly equal levels of variance when looking at pixel-wise standard deviations across mice (bottom row) and discrepancies in delta power congregated in visual cortical regions as indicated by the cluster-extent thresholding method (Figure 6.8C, top row, Figure 6.2B). Additionally, three symmetric cortical regions stood out as having significant changes in delta power and bilateral FC (Figure 6.8C, bottom left, anterior, medial, and posterior red regions) and plotting the pixel-wise t-values of both measures yielded a significant linear relationship (Figure 6.8C, bottom row). A histogram displaying pixel-wise delta power illustrates the shift in the distribution of delta power in ZIKV- relative to mock-infected mice (Figure 6.8D). Rank-ordered average delta power over the FOV correlated positively with rank-ordered encephalitis score (Table 6.1).

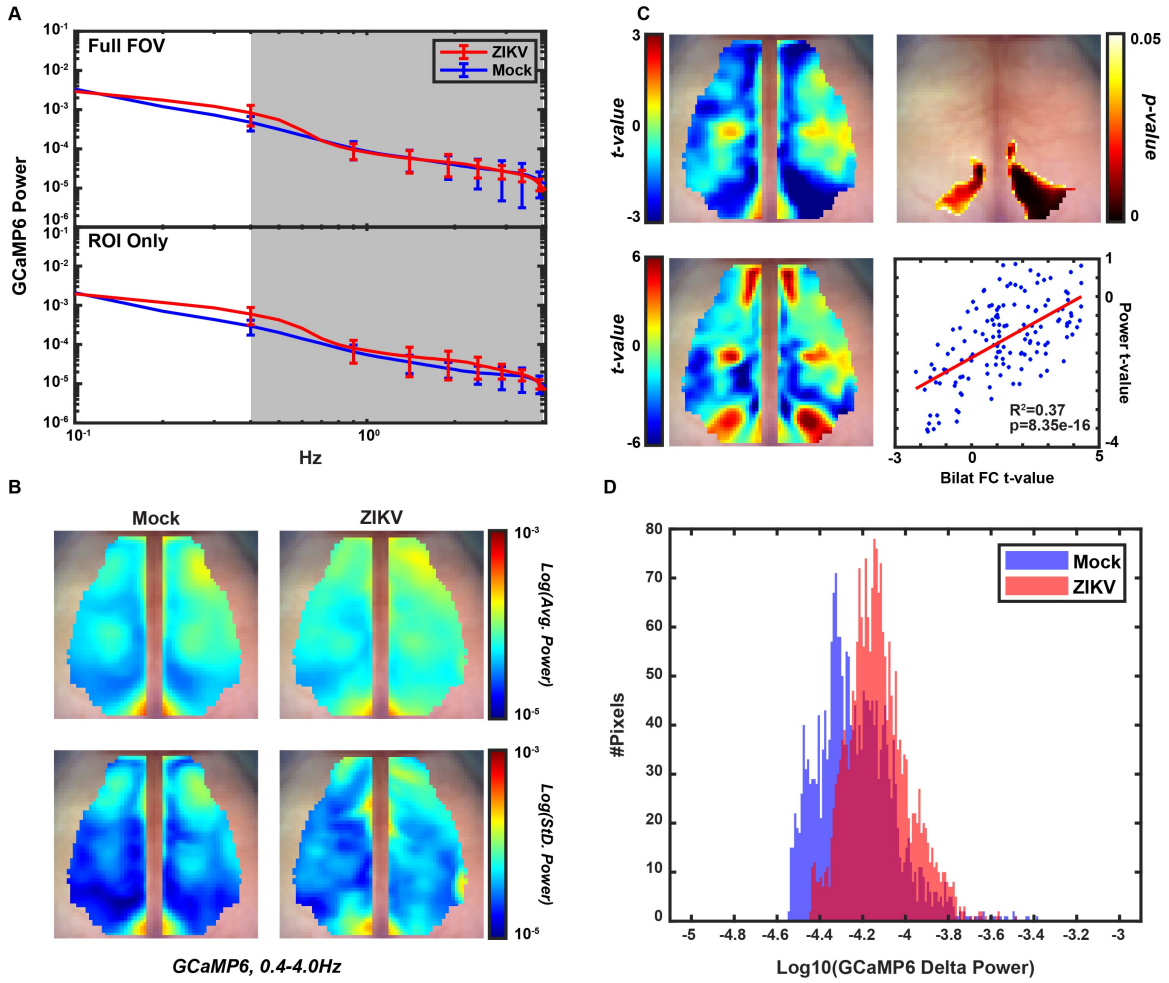

Figure 6.8: A) Power spectra for mock and ZIKV mice averaged over the whole FOV (top) or only within the region defined in part C). Error bars are standard deviations. The shaded region represents the delta band (0.4-4.0Hz). B) Average (mock N=22, ZIKV N=23) pixel-wise delta power (top row) and standard deviation (bottom row) across mice. C) Pixel-wise two-sample t-test (top left) and thresholded image (top right, ROI used in part A)) for $p<0.01$ by a cluster-based thresholding method. Delta power pixel-wise t-map multiplied by the bilateral FC pixel-wise t-map in Figure 6.1C (bottom left). Linear regression of pixel values (images down sampled by a factor of 4) comparing delta power and bilateral FC t-values (bottom right). D) Histogram displaying pixel-wise GCaMP6 delta power across the whole FOV.

6.3.3 FC Deficits Observed during Acute ZIKV Infection Resolved in Recovered Animals

Given prior studies demonstrating persistently activated microglia with synapse elimination and spatial learning defects during recovery from ZIKV i.c. infection [89], we wondered whether the imaging deficits reported during the acute time-point persisted in recovered animals. Average (mock, N=11, ZIKV, N=8) paired bilateral FC maps are presented at 7dpi (Figures 6.9,6.10) and 42dpi (Figures 6.11A,B) using delta calcium and infraslow hemoglobin dynamics. Note the same parietal/somatosensory deficit from the N=23 ZIKV dataset is present with the limited N=8 ZIKV dataset for delta calcium and a similar global FC deficit is present in the infraslow hemoglobin data at 7dpi via cluster extent-based thresholding (Figures 6.9,6.10) while no deficit in either contrast remained at 42dpi (Figures 6.11C,D). The bilateral maps for each mouse at 42dpi were spatially averaged across the whole FOV, as done at 7dpi, and displayed as boxplots for mock and ZIKV groups (Figures 6.11E,F) with no significant difference between groups for either contrast. Additionally, there were no sex-dependent significant differences in average bilateral FC at 42dpi (Figures 6.3E,F). Given that mice have recovered from acute ZIKV infection by 42dpi [89], we did not expect to see the same increase in delta power, as previously observed at 7dpi (Figure 6.8). The pixel-wise delta power did not vary significantly between the mock and ZIKV-infected mice imaged at 42dpi (Figure 6.11G, n.s. via cluster extent-based thresholding). All mice received an encephalitis score of 0 at 42dpi.

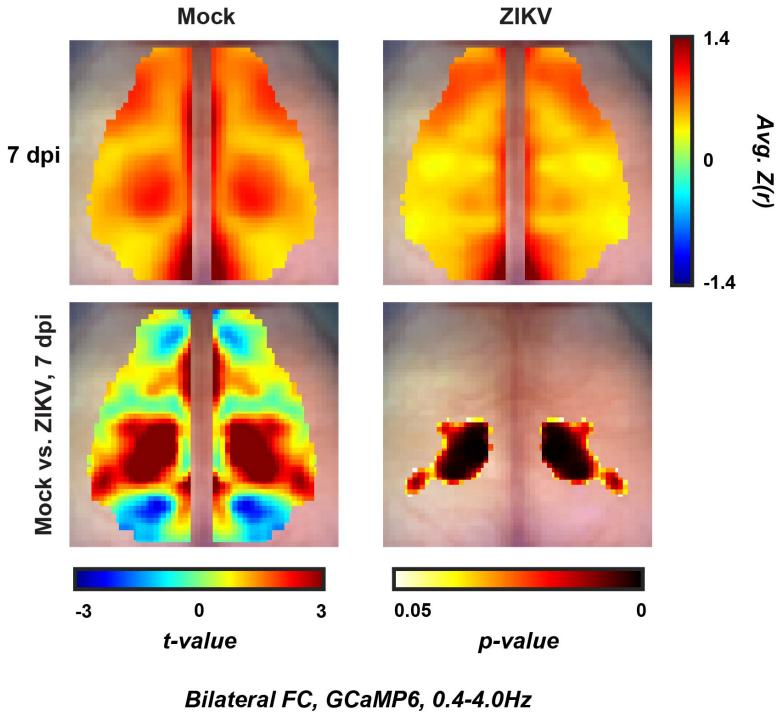

Figure 6.9: Top row) Average (mock, N=11, ZIKV, N=8) pixel-wise bilateral FC maps across mice. Bottom row) Pixel-wise two-sample t-test (left) and thresholded image (right) for $p<0.01$ by a cluster-based thresholding method.

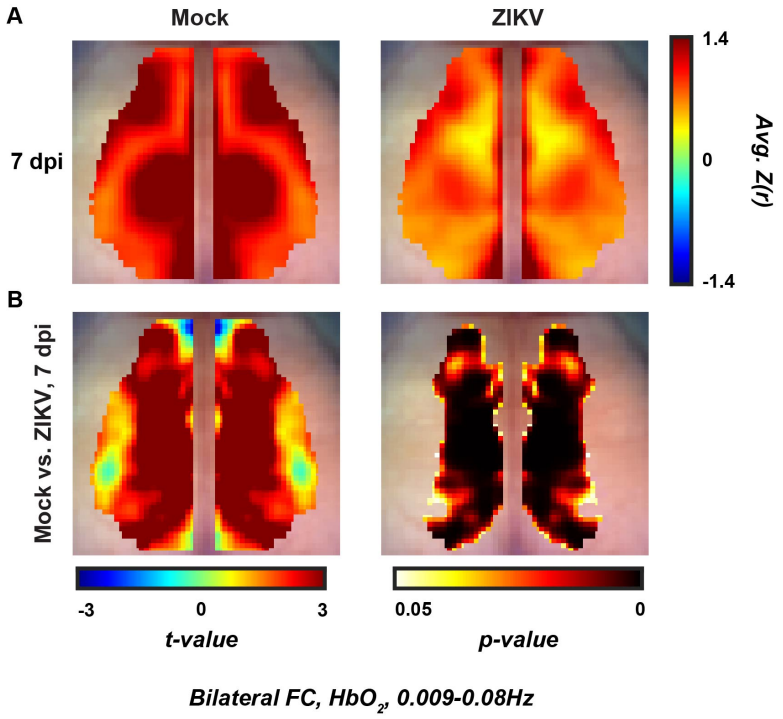

Figure 6.10: Top row) Average (mock, N=11, ZIKV, N=8) pixel-wise bilateral FC maps across mice. Bottom row) Pixel-wise two-sample t-test (left) and thresholded image (right) for $p<0.01$ by a cluster-based thresholding method.

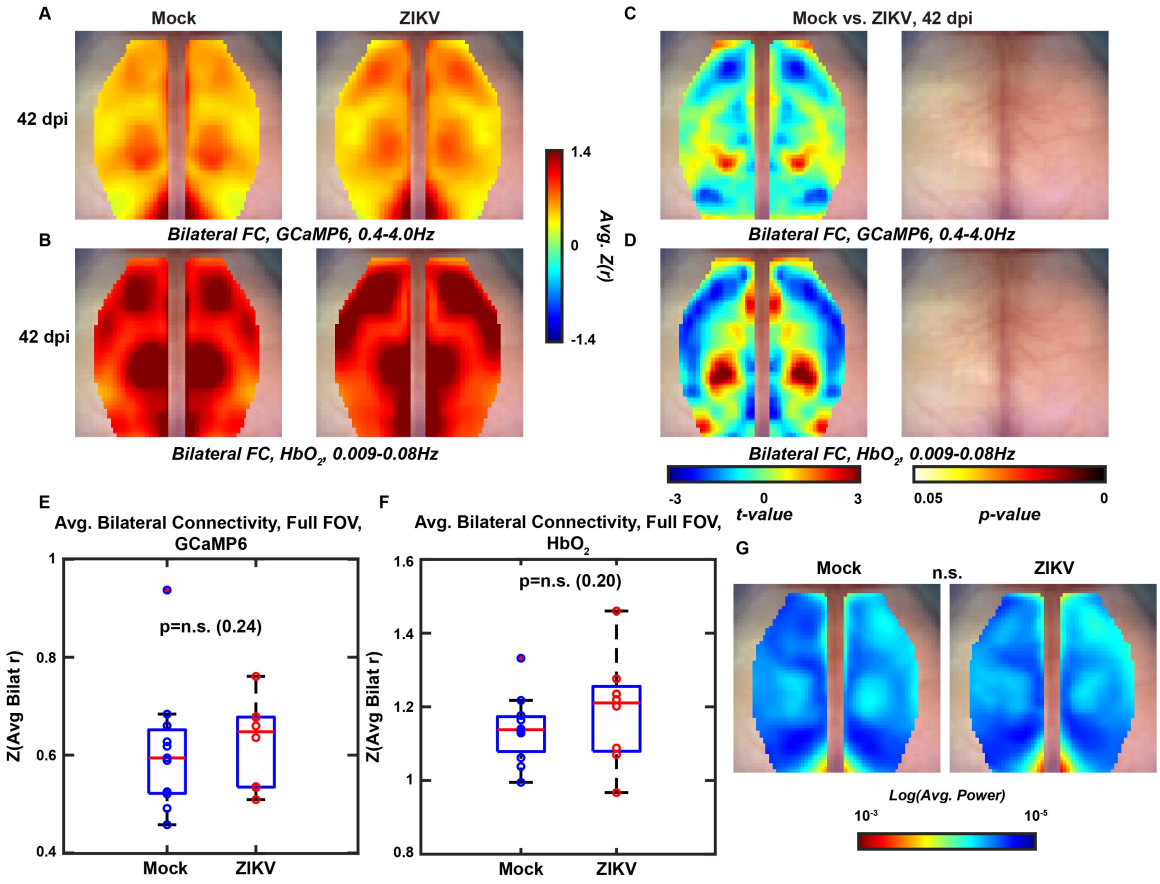

Figure 6.11: Average (mock, N=11, ZIKV, N=8) bilateral FC maps at 42dpi for A) delta calcium and B) infraslow hemoglobin. Pixel-wise two-sample t-test (left) between 42dpi mock and ZIKV infected bilateral FC maps and Cluster extent-based thresholding yielded no clusters surviving thresholding with $p<0.01$ (right) for both C) delta calcium and D) infraslow hemoglobin. Spatially averaged (over the whole FOV) bilateral FC for mock and ZIKV-infected mice at 42dpi for E) delta calcium and F) infraslow hemoglobin. The one data point extending beyond the maximum value is a statistical outlier in the mock group. No significance via a paired t-test (outlier removed). G) Average delta power maps at 42dpi for mock and ZIKV-infected mice. No significance via cluster extent-based thresholding.

6.4 Discussion

Behavioral and molecular work has demonstrated a decrease in learning and memory and an increase in pathological hippocampal alterations, respectively, resulting from ZIKV infection [178, 232, 89]. While hippocampal regions are largely the focus of experiments examining learning and memory, there is a significant cortico-hippocampal and cortico-cortico axis which has been documented in the setting of various neurological phenomenon (e.g. memory consolidation during sleep, general cognition) [217, 260, 142, 168]. In fact, retrosplenial cortical neurons exhibit "hippocampal place cell-like" activity during learning and memory tasks [156]. Additionally, various sensory regions display high levels of functional connectivity with hippocampus as proven by fMRI [21]. Therefore, we hypothesized that although previous studies of ZIKV demonstrate a certain tropism for hippocampal regions [89], using a mouse adapted strain of ZIKV could increase cortical infiltrates or hippocampal alteration could ripple to affect non-hippocampal regions, specifically the cerebral cortex. In this study, we imaged adult mock and ZIKV-infected mouse cortical dynamics using wide-field fluorescence imaging at 7dpi, in accordance with the onset of peak encephalitis [149, 107]. Calcium FC revealed a focused parietal/somatosensory-based deficit while hemoglobin FC deficits were more global. Both calcium and hemoglobin FC deficits resolved by 42dpi. Additionally, delta calcium power transiently rose at 7dpi and returned to equivalent mock levels by 42dpi.

In addition to the cortico-hippocampal axis, cortico-cortico (i.e., within cortex) functional connectivity has been highly implicated in successfully maintaining cognitively normal behavior [153, 250, 36] and could thus be a target of ZIKV independent of hippocampal alterations. By utilizing optical fluorescence imaging, we were able to investigate cortical connectivity patterns previously described as being involved within these cortico-cortico and cortico-hippocampal networks. One particularly large deficit was a decrease in homotopic FC within somatosensory and through parietal regions (Figure 6.1C, Figure 6.2A). Previous

studies using fMRI have placed seed regions within hippocampus and isolated somatosensory regions as having high functional correlations with the seed region [21]. Elsewhere, somatosensory regions have proven to be more metabolically demanding than other cortical regions. Interestingly, 7dpi hemoglobin-based FC maps displayed global disruption (Figure 6.1D) suggesting that deficits in the calcium-based imaging could represent a more global mismatch between metabolic demand and supply manifesting in desynchronized neural activity. Cluster-extent thresholding (a random field theory approach) allows us to isolate clusters in our cortical imaging data beyond a solvable threshold size that would appear with a family-wise error rate of 0.01 [85]. There were additional clusters in the cingulate/retrosplenial cortical regions near midline of the calcium bilateral pixel-wise t-map (Figure 6.1C, left) that were approaching this significance threshold cutoff. We wondered if any of these areas nearing or crossing significance could be strictly due to the cranial injection and surgical preparation procedure [191]. In order to address this, we compared mock infected (N=22) bilateral FC maps to bilateral FC maps of mice who had been peripherally injected with PBS 72 hours prior (N=8), i.e., did not have a cranial needle injection (Figure 6.4). Utilizing the same cluster-size threshold as in Figure 6.1, we did not isolate the same somatosensory and parietal-based deficit as when ZIKV and mock mice were compared. Therefore, the absence of the somatosensory and parietal-based deficit in this comparison (Figure 6.4) further supports that this is truly a difference induced by ZIKV. Interestingly, in the ZIKV-infected population, there was a large spread of bilateral FC values when averaging over the whole FOV (Figures 6.1E,F). This could, in part, be reflective of the variance associated with ZIKV infection in the human population (e.g. only 20% develop encephalitis [31]). While the dynamic range for encephalitis score is narrow (scores are either 0, 1, or 2), Spearman's Rho elicited a significant relationship between bilateral FC values and encephalitis scores (Table 6.1), indicating that FC is a useful biomarker for disease severity. This somatosensory and parietal-focused deficit proved to be transient and disappeared after recovery from acute

ZIKV infection (Figure 6.11C, the same was true for infraslow hemoglobin data; the entire global FC deficit resolved by 42dpi, Figure 6.11D).

To understand the extent to which neural dynamics were altered, we specifically sampled each cortical network within our FOV via seed-based Pearson FC analysis on the delta calcium data (Figure 6.5). While the loss of homotopic connectivity when using parietal and somatosensory seeds was expected based on the result from Figure 6.1, and was recapitulated using this seed-based approach, there were multiple instances of altered cortico-cortico connectivity, particularly there were alterations involving retrosplenial cortex when seeds were placed in parietal, motor, visual, and auditory cortices. Using another approach and plotting the Pearson correlation between time traces within two seed regions (Figure 6.6) yielded more evidence that connections involving somatosensory cortex are most substantially affected within our FOV (in this case using an even more stringent statistical method-a Bonferroni correction for multiple comparisons). Based on previous literature, while retrosplenial cortical neural populations are in many ways the most like hippocampal populations [156, 55], cortical regions such as pre-frontal and other sensory regions (e.g. visual, auditory), have been implicated to highly interface with each other along the cortico-hippocampal axis [21, 174]. Therefore, deficits in connectivity within these regions could help explain the phenotype of encephalitis and learning and memory deficits secondary to ZIKV-infection in adults. In a few instances, there were increases in ipsilateral (relative to the seed), proximal correlation values, such as the increased correlation values surrounding frontal, motor, and visual seeds. In only one instance did this also result in increased homotopic connectivity (Mot1 seed, Figure 6.5). Instances of increased connectivity (proximal, ipsilateral regions) in ZIKV-infected mice are surprising. Upon infectious insult, neuro-immunological pathways are activated, such as CD8+ T-cells responding by releasing IFNγ to activate a microglial response by our time point of interest (7dpi). Astrocytes are also activated at this time point [89], and it is possible that when these multi-functional glial cells get activated, there is an

abundance of metabolites delivered to neurons to allow for a surge in synchronized activation in a concerted effort to clear the infection [240]. This could potentially explain why neighboring neural populations, which share contact with these neighboring supporting cell types, become more temporally synchronized than distal homotopic regions. This overstimulation of neurons could also precede and lead to the high levels of neural cell death reported during this type of infection [192]. While functional neuroimaging studies of ZIKV do not currently exist, and functional neuroimaging of encephalitidis in general is in the early stages, one unique case report has illustrated the transient global breakdown of resting state networks throughout the course of NMDA-receptor encephalitis in one human patient [36], similar to the result we see here with ZIKV using hemoglobin-based mapping (Figures 6.1B,D).

We noticed a slight increase in GCaMP6 delta power (0.4-4.0Hz, as defined in the EEG literature [62]) in accordance with encephalitic presentation on EEG (Figure 6.8) [120], with little variance between ZIKV- and mock-infected groups. Along with the FC result, this increase in delta power correlated with encephalitis score (Table 6.1) and resolved by 42dpi (Figure 6.11G). Together, this suggests that this FC and power imaging biomarker is reflective of acute ZIKV encephalitis and underlying associated pathology, but not reflective of any long-term deficits. Similar to molecular work [89], where (some) neuroinflammatory mediators get elevated during peak encephalitis and then return to baseline during recovery, it is possible that alterations needed to longitudinally impact cognition or learning and memory capabilities occurred during peak infection and that effect is outlasting any pathological imaging finding. The cortico-cortico and cortical-hippocampal axis is only one asset of learning and memory consolidation, and it is certain we are not capturing all that is being altered over the time course of ZIKV infection and recovery.

6.5 Conclusions and Future Directions

Here, we imaged ZIKV- and mock-infected mice at 7dpi and demonstrated multiple cortical connectivity deficits with a large somatosensory/parietal focus that resolved by 42dpi. We observed many expected results such as increased encephalitis score and increased delta power in infected mice compared to controls. Lastly, there was a significant relationship between the transient imaging result (utilizing both calcium and hemoglobin contrasts) and encephalitis score across both groups of animals, suggesting a potential usefulness and translatability of this imaging biomarker in the context of ZIKV infection. Our experimental ZIKV-infected cohort displayed substantial variance in symptom presentation (as quantified through encephalitis score) and FC results, mirroring what has been reported in human populations (20% exhibit encephalitic symptoms [31]).

Chapter 7

A Multivariate Functional Connectivity Approach to Mapping Brain Networks and Imputing Neural Activity in Mice

Previous chapters have explored functonal neuroimaging in mice in the context of various neurological diseases. These studies have utilized a quick and efficient method to compute the temporal synchrony between brain regions (e.g., Pearson's correlation). Here, we investigate a multivariate approach to imputing neural time traces using support vector regression. We propose that the regression weights serve as a metric of connectivity with multiple advantages over the widely used Pearson-based technique.

7.1 Introduction

Over the last decade, functional connectivity (FC) analysis of neuroimaging data has provided unique insights into the functional architecture and organization of the human brain [81]. Traditionally, FC analysis is built upon calculation of correlation coefficients between two brain regions in isolation. Predominantly used in functional magnetic resonance imaging (fMRI) [81, 80], but also in functional near infrared spectroscopy (fNIRS) [270], this type of analysis has been used to determine the regional temporal synchrony of blood-based surrogates of neural activity [208]. Due to synchronous spontaneous brain activity at rest, FC analysis has uncovered hierarchical brain connectivity patterns (i.e., networks) that are detectable without the need for a stimulus [80] (e.g. the Default Mode Network [6]). Motion scrubbing algorithms such as the spatial standard deviation of successive differentiation images (DVARs) [197], or the optical equivalent, global variance of the temporal derivatives (GVTD) [214], have been implemented to increase the signal-to-noise ratio (SNR) of spontaneous neuroimaging data and resultant FC maps. FC patterns have proven to be sensitive and specific biomarkers of disease and are useful for clinical applications such as predicting Alzheimer's Disease onset [35] or stroke outcome [58]. As wide-field optical imaging (WOI) has become more popular in small rodents, this same FC analysis has been used to study the hierarchical organization of the mouse cerebral cortex at rest [259]. Now, with the addition of genetically encoded calcium indicators (GECI's) [49], specific cell populations can be labeled and calcium transients can be encoded into FC patterns affording higher temporal resolution and signal-to-noise than traditionally measured hemodynamics [265, 34]. However, this method has largely incorporated simple bivariate Pearson correlation analysis.

In contrast to isolated, bivariate FC analysis, there are a number of exciting multivariate alternatives being used for human fMRI analyses [57, 90, 12, 16]. In particular, multivariate regression methods can synthesize time trace information from multiple (e.g., 1,000) brain

regions within a given field-of-view (FOV) in order to impute or predict a time trace within a single brain region of interest (ROI) [53, 57]. This type of analysis is asking the question; "for a given brain region X, how predictive of region X are, either all of or a subset of, the remaining brain regions?". Whereas bivariate FC is simply asking the question "how correlated is the activity in region X and region Y?". The difference between the two questions involves two conceptual shifts. First, there is a shift from a passive descriptive measure of correlation to an active analysis of predictive accuracy. Second, there is a shift from bivariate analysis to self-consistent multivariate analysis. Recently, support vector regression (SVR) has emerged as a simple, yet powerful supervised machine learning technique for multivariate analysis that can successfully predict region-specific brain activity from fMRI data [67, 57, 126]. With human fMRI, SVR was used to compute a weight vector optimized such that a weighted sum of the time courses for each voxel produced an expected time course for an ROI that was matched to its experimental time course [57]. This SVR approach to generating a weight vector was tested for prediction accuracy and reproducibility. However, this fMRI study relied on hemoglobin-based assays of neuronal signal (i.e., the blood oxygen level dependent BOLD signal), whereas with WOI of GCaMP6f mice, we are able to directly assay neural dynamics with calcium neuroimaging. If this multivariate approach yields high prediction accuracy in mouse WOI data, the resultant prediction weights could be useful in generating an improved hierarchical connectivity model of the brain by incorporating all brain regions into each calculation, instead of analyzing each brain region in isolation. Further, this multivariate functional connectivity (MFC) analysis might provide improved reproducibility and improved spatial detail of connectivity relative to standard FC. If these performance gains were to be realized, this multivariate method could find broad applicability in WOI of mice, particularly in studies working to dissect the mechanisms of connectivity (e.g., the role of inter-neurons in forming connectivity patterns). While the focus here is preclinical imaging, advancements in connectivity methods using mouse models of disease could pave the way for

translation back to human clinical imaging. In particular, this MFC methodology could have major clinical applications by identifying brain regions most heavily weighted and necessary for correctly predicting brain activity in other regions. Identification of such regions, or "hubs" [223], could be informative when mapping and predicting the outcome after a stroke, or when drafting plans for re-mapping the tasks formerly mapped to ischemic areas [262].

A common problem arising when acquiring spontaneous calcium neuroimaging data in small rodents at rest, is the presence of small epochs of NREM sleep [252]. Due to the ∼1Hz quasiperiodic slow oscillation that propagates largely anterior to posterior throughout periods of NREM sleep [224, 158], large amplitude global variations are introduced into the neuroimaging data when the data is filtered into delta band frequencies (0.4-4.0Hz, as defined in the EEG literature [62]). Resultant FC patterns can become fairly bimodal (large regions of high correlations and anti-correlations) when this analysis is performed on mice in NREM or under certain types of anesthesia known to induce the slow oscillation (e.g., Ketamine/Xylazine, K/X) [265, 34]. These large scale waves disrupt traditional FC correlations and can obscure the underlying functional architecture throughout NREM sleep or K/X anesthesia [34]. We hypothesize that this more nuanced MFC approach might be less affected by these large global fluctuations in the neuroimaging data and therefore provide a more robust approach to characterizing the functional organization of the brain.

Here, we use calcium neuroimaging data collected via wide-field fluorescent imaging of Thy1-GCaMP6 mice while either awake, during NREM, under K/X anesthesia, or before and after photothrombosis. Linear SVR offers a multivariate approach that allows us to accurately and reproducibly impute brain activity on a parcel-by-parcel basis. By mapping regions highly contributing to the prediction accuracy of a chosen ROI (MFC maps), we are able to identify brain region subsets that are more influential and predictive than other brain regions. Throughout the figures we provide comparisons between MFC and standard FC. To provide anatomical context we evaluated MFC against axonal projection maps from

the Allen institute. Further, we evaluate the performance of MFC in the presence of largely variable global phenomenon (e.g., the slow oscillation introduced by altered consciousness). Finally, while developing a model of connectivity with the aim of being more impervious to noise has obvious signal-to-noise-ratio (SNR) benefits, it is important to also judge the ability to detect true connectivity deficits in the context of disease models. WOI studies of focal photothrombosis have well documented the loss of homotopic connectivity surrounding the infarct [17, 133]. We compare the proposed MFC mapping to traditional FC approaches in mice subjected to photothrombotic stroke to determine which approach is more sensitive to disruption of connectivity.

7.2 Methods

7.2.1 Animals and Shared Surgical Preparations

A total of nine transgenic mice (12-16 weeks of age) expressing GCaMP6f in excitatory neurons (driven by a Thy1 promotor) were acquired from Jackson Laboratories (JAX Strain: C57BL/6J-Tg(Thy1-GCaMP6f)GP5.5Dkim; stock: 024276) and used in the experiments in this study. All studies were approved by the Washington University School of Medicine Animals Studies Committee and follow the guidelines of the National Institutes of Health's Guide for the Care and Use of Laboratory Animals. Prior to data collection, the head of each mouse was shaven, and a midline incision was made to expose the skull. Following scalp retraction, a Plexiglass head cap was fixed with a translucent adhesive cement (C&B-Metabond, Parkell Inc., Edgewood, New York) to allow for chronic, repeated imaging [218]. The main objective of the present study to provide an in-depth analysis and comparison of MFC and FC mapping techniques should not depend on sex as a biological variable and therefore was not analyzed as such.

7.2.2 EEG Placement

In N=5 mice (all male), stainless steel EEG self-tapping screws (BASI Inc., West Lafayette, IN, USA) were fixed at approximately -1mm posterior to bregma, and +/- 5mm lateral to bregma (near barrel/auditory cortex). This dataset was previously monitored for awake, NREM sleep, and K/X anesthesia data as described [34] and repeated here.

7.2.3 Awake, NREM, and K/X Anesthesia Imaging

The mice used for Awake, NREM, and K/X imaging were the N=5 mice surgically implanted with EEG screws. For K/X imaging, the mice were anesthetized by an intraperitoneal injection of a ketamine/xylazine cocktail (86.9mg/kg ketamine, 13.4mg/kg xylazine). Anesthetic effect was confirmed when the animal was un-responsive to hind-paw pinch. For imaging of NREM sleep, a 6-hour sleep deprivation protocol was implemented [236] starting at lights-on (6am) in order to increase the probability of NREM activity occurring during recording. This sleep deprivation protocol was followed by an hour of continuous recording for NREM data. For awake imaging, the mice were imaged for one hour. Two to three days passed between each experiment (awake, NREM, or K/X anesthesia) to allow for recovery from anesthesia or sleep deprivation. The order of the experiments was randomized across mice. The dataset used in the following analyses consists of two five-minute imaging runs from each mouse per the three different brain states.

7.2.4 Electroencephalography (EEG) Sleep Scoring

The mice used for sleep scoring were the N=5 mice surgically implanted with EEG screws. Cortical EEG signals were recorded from the two bilateral screws and referenced to a cerebellar screw. On the day of imaging, the electrodes were connected to an amplifier and data were collected at 1 kHz (Power Lab EEG Amplifier, AD Instruments, Dunedin, New

Zealand). The data was down sampled to 256 Hz offline and scored within 10s epochs according to standard criteria [184] as either awake, NREM, anesthesia activity, or movement artifact.

7.2.5 Photothrombosis

In N=4 mice (2 male, 2 female, all are mice that did not receive EEG screws), mice were secured in a stereotaxic frame under isoflurane anesthesia. 200 μl of Rose Bengal (Sigma Aldrich) dissolved in saline (10 g/liter) was injected intraperitoneally. After 4 minutes, a 532-nm diode-pumped solid-state laser (Shanghai Laser & Optics Century) was focused to 2.2mm left and 0.5mm anterior to bregma with a 0.5mm spot size and at 23mW for 10 minutes [133]. Mice were imaged at baseline (i.e., prior to photothrombosis (Day 0), and 72 hours post (Day 3). MFC and FC analyses were anchored to a Somatosensory (Ss) and Motor (Mot) circular seed since the Ss seed was within the infarct, while the Mot seed was outside of the injured area. Circular seeds were used here (in contrast to the parcel-based approach used elsewhere) to better sample and reflect the shape of the necrosed area. The dataset used in the following analyses consists of two five-minute imaging runs from each mouse.

7.2.6 Imaging Calcium Transients

Mice were placed in a black felt pouch with their head secured. For the N=5 mice with concurrent EEG recording, sequential illumination was provided by four LEDs: 454 nm (GCaMP6 excitation), 523 nm, 595 nm, and 640 nm (Mightex Systems, Pleasanton, California). A cooled, frame-transfer EMCCD camera overhead (iXon 897, Andor Technologies, Belfast, Northern Ireland, United Kingdom) in combination with an 85mm f/1.4 camera lens (Rokinon, New York, NY, USA) at a framerate of 16.8Hz per channel was used for image

acquisition. The FOV was adjusted to cover the majority of the convexity of the cerebral cortex with anterior-posterior coverage from the olfactory bulb to the superior colliculus resulting in an area of approximately 1cm^2 with pixel resolution of 78 μm^2 each. All imaging data were acquired and stored in separate 5-min imaging runs.

For the N=4 mice that underwent photothrombosis, sequential illumination was provided by four LEDs: 470 nm (GCaMP6 excitation), 530 nm, 590 nm, and 625 nm (Mightex Systems, Pleasanton, California). A cooled, frame-transfer sCMOS camera overhead (Zyla 5.5, Andor Technologies, Belfast, Northern Ireland, United Kingdom) in combination with an 85mm f/1.4 camera lens (Rokinon, New York, NY, USA) at a framerate of 16.8Hz per channel was used for image acquisition. The FOV was adjusted to cover the majority of the convexity of the cerebral cortex with anterior-posterior coverage from the olfactory bulb to the superior colliculus resulting in an area of approximately 1.1cm^2 with pixel resolution of 100 μm^2 each. All imaging data were acquired and stored in separate 5-min imaging runs.

7.2.7 Data Pre-Processing

The pre-processing of GCaMP6 images was as described previously [150, 265], and briefly summarized here. A representative frame of baseline light levels in a dark environment was subtracted from the raw data. A binary mask denoting brain regions was applied and the time courses of all pixels were detrended spatially and temporally to remove globally shared variance. The GCaMP6 fluorescent signal was corrected by using a ratiometric correction between the green-fluorescent (blue-excitation) and green-reflection channels accounting for dynamic absorption of the light in the fluorescence channel by oxyhemoglobin and deoxyhemoglobin [265]. The global signal averaged across all brain pixels was regressed out and images were smoothed with a 5x5 Gaussian filter. Image sequences for each mouse were affine-transformed to a common Paxinos mouse atlas space. All GCaMP6 data were filtered to the delta frequency band (0.4-4.0Hz). A total of 36 brain parcels defined by the

Paxinos atlas were visible in our FOV and therefore used in our study [259] (Figure 7.1A). Some parcels (olfactory, prelimbic, colliculi, and cerebellum) were excluded because they were outside the FOV presented here.

7.2.8 Pearson Correlation FC Analysis

Traditional seed-based Pearson FC analysis [85] was computed using each parcel as a seed region (Figures 2,4,5):

$$\rho_{x,y} = \frac{cov(x,y)}{\sigma_x \sigma_y} \tag{7.1}$$

where ρ is the Pearson correlation coefficient between parcel x and pixel y, $cov(x,y)$ is the covariance between parcel x and pixel y, and σ are the standard deviations within parcel x and pixel y.

FC matrices (e.g., Figure 7.8) were computed by taking the Pearson correlation of average time traces between two parcels.

Similarly, more traditional circular seeds were used when calculating MFC and FC on the stroke data (Figure 7.12). In this case, ρ is the Pearson correlation coefficient between seed x and pixel y, $cov(x,y)$ is the covariance between seed x and pixel y, and σ are the standard deviations within seed x and pixel y.

7.2.9 Support Vector Regression

For the SVR analysis we generally followed the exemplary work done by Craddock et al. [57]. We start with the full data set $X \in R^{nxm}$, with a FOV of n-pixels in the brain and m-time points. The data is then divided up into r ROIs, denoted as parcels, wherein the time course of the r^{th} ROI is $y_r \in R^{1xm}$ calculated as an average of the time courses for all pixels within the ROI. For SVR we need to remove the r^{th} parcel data from X and use the

remaining subset of pixels, $X_{\neg,r}$, to predict a time trace for each parcel (y_r) (Figure 7.1B) [222]. Each time course, y_r, can be modeled as a weighted linear combination of time courses in $X_{\neg,r}$:

$$y_r = w_r^T X_{\neg,r} + b \tag{7.2}$$

where w_r is a vector containing the pixel weights within the FOV for the specific r^{th} region being analyzed and b is the bias solved for during optimization. For a given training dataset where y_r and $X_{\neg,r}$ are known, SVR is used to solve for w_r by:

$$\text{minimize } \tfrac{1}{2} \parallel w_r \parallel^2 + C\Sigma_1^n(\xi_n + \xi_n^*)$$

$$\text{subject to } \begin{cases} y_r - w_r^T X_{\neg,r} - b < \epsilon + \xi \\ w_r^T X_{\neg,r} + b - y_r < \epsilon + \xi^* \\ \xi, \xi^* \geq 0 \end{cases} \tag{7.3}$$

The free parameters in the SVR model are the regularization parameter, C, and the half width of the insensitive zone, ϵ. $C > 0$ determines the trade-off between the flatness of y_r and the degree to which deviations larger than ϵ, defined by slack variables ξ and ξ^*, are tolerated. In this study, we used a linear kernel, $C = 1$, and $\epsilon = 0.1$. We investigate the effect of modifying the half width of the insensitive zone by additionally displaying results for $\epsilon = 0, 0.001, 0.01$, and 1.

Notably, all timeseries data were z-score normalized prior to training. The regression weights, w_r, are unwrapped onto a 2D image and plotted topographically with the parcel ROI left out.

Similarly, in the case of performing SVR on the stroke data, we used more traditional circular seed ROIs. In this instance, the weight maps are plotted topographically with the seed ROI left out (e.g., Figure 7.12).

To compute SVR weight matrices (e.g., Figure 7.8), we took the weight vector for each ROI and plotted the singular average weight within each parcel remaining in the FOV.

7.2.10 Evaluation of Prediction Accuracy and Reproducibility

The dataset used in the following analyses consists of two five-minute imaging runs from each mouse per the three different brain states. Prediction accuracy and reproducibility were evaluated for each mouse following a previous fMRI study [225]: in the first phase, Run 1 is treated as training data and Run 2 is treated as test data. Then, using the SVR weight vector for an ROI (w_r) trained on Run 1, a time trace for that ROI in Run 2 is imputed/predicted using the Run 2 neuroimaging data outside the given ROI. The prediction accuracy is defined as the Pearson correlation coefficient between the predicted time course and the observed average time course in the same ROI from Run 2. In phase two, in order to evaluate reproducibility, Run 2 is used as training data. The reproducibility is defined as the Pearson correlation between the SVR weight vector from phase one and the weight vector from phase two. A second evaluation of the prediction accuracy is done, using the weight vector from Run 2, and using Run 1 as test data. The prediction accuracy evaluation process is the same as in phase 1. This process was repeated for all ROIs in the FOV (denoted by index r). The same prediction and reproducibility calculations were done using FC correlation vectors as "weight" vectors (w_r, from the SVR analysis).

7.2.11 Wavestrapping

To prove the SVR approach was resulting in higher prediction accuracy and reproducibility values than would be expected due to chance, null time traces were created for each parcel via a 1-D wavestrapping procedure [40]. An SVR model was then re-trained using these null time traces and then used to predict a time trace for each ROI. The prediction accuracy was

determined by comparing these predicted traces with the true observed calcium neuroimaging data. Reproducibility represents the correlation between weight vectors produced during the two phases of training the SVR model.

7.2.12 Dice Coefficient

In order to spatially compare MFC and FC maps, weight maps generated by MFC analysis were rescaled to [-1, 1]. The adapted Dice coefficient (s) was used to quantify spatial similarity between MFC and FC maps as follows:

$$s = \frac{2\Sigma_{i=1}^{d} A_i B_i}{\Sigma_{i=1}^{d} A_i^2 + \Sigma_{i=1}^{d} B_i^2} \tag{7.4}$$

Where i indexes through the number of pixels, d, in either the MFC maps (A) or FC maps (B).

7.2.13 Axonal Projection Connectivity Maps

As described elsewhere [18] and briefly summarized here, axonal projection connectivity (APC) maps were downloaded from the Allen Mouse Brain Connectivity (AMBC) atlas. These maps reflect enhanced green fluorescent protein-labeled monosynaptic connections with an injection site (C57BL/6J mice were injected with a pan-neural adeno-associated virus under the promoter Syn1) [139, 183], Allen Mouse Brain Connectivity (AMBC) atlas. APC maps were chosen based on the proximity of the injection site to parcels analyzed using MFC and FC techniques. APC maps were turned into projection images using the AMBC cortical map signal viewer and we applied a binary mask and affine-transformed APC images to be within the same atlas space as our WOI data. Each APC map was normalized to its maximum fluorescence prior to analysis. APC maps were thresholded at 50% intensity while MFC and FC maps were thresholded at a z(r) or a z(prediction weight) of 0.3. All maps

were then binarized and the Dice similarity coefficient was calculated between APC and MFC maps, and APC and FC maps.

7.2.14 Stroke Homotopic Connectivity Maps

Average MFC and FC maps were thresholded at z(prediction weight) or z(r) of 0.3, as described previously [18]. The overlap of surviving contralateral regions (relative to the seed) between Day 0 and Day 3 was visualized. Overlap maps are visualized using a seed in an affected region (somatosensory, Ss) and an unaffected region (motor, Mot). The average prediction weight (MFC) or correlation (FC) contralateral to the seed region was calculated for each mouse and compared between Day 0 and Day 3 in an affected region (Ss). Only the homotopic pixels were visualized/averaged for these calculations based on a previous study describing that necrotic tissue would not form these homotopic connections [17]. In order to estimate the statistical power for each method, we also displayed the t- and p-values resultant of a paired t-test between Day 0 and Day 3 homotopic Ss connectivity strength.

7.2.15 Data and Code Availability

In order to promote validation and comparative analyses by external groups, data and specific code will be made available through requests. WOI pre-processing code and FC, SVR/MFC analysis code is available online (Mouse WOI GitHub). Awake, NREM, and K/X data is available on Figshare (Sample Awake NREM data) and (Sample NREM and K/X data).

7.3 Results

7.3.1 Prediction Accuracy and Reproducibility of SVR Brain Activity Imputation

Our first goal was to evaluate whether the time course for a given brain region (parcel) could be predicted from time courses in the remaining other pixels, using SVR regression weights. Fluorescently labelled mice (N=5) expressing GCaMP6 under the Thy1 promoter were imaged while simultaneous EEG was recorded, as presented elsewhere [34]. A binary MATLAB parcellation file was used to delineate specific cortical regions within our FOV [259] (Figure 7.1A). A five-minute run from each mouse was used to train SVR (Figure 7.1B). Briefly, an average time trace was extracted from a parcel (ROI) and a weight vector was generated with linear SVR to estimate the connection between the remaining pixels and the ROI. This weight vector was then used on a subsequent five-minute run (solving equation 7.2) to predict the activity in the same parcel using the subset of pixels in the FOV that excluded the parcel being evaluated. This same procedure was repeated for all parcels within the FOV. The prediction accuracy, evaluated by calculating the Pearson correlation between the predicted time trace and the observed time trace, was between 0.8 and 1.0 (Figure 7.1C). Further, to prove that SVR was performing better than chance, we used a wavestrapping procedure to synthesize a null time trace for each ROI [40]. SVR was then trained using these null time traces and new time traces for each ROI were predicted. The resultant weight vectors trained on the null data produced prediction accuracy and reproducibility with a $\sim$ 5X reduction compared to when SVR was trained on the measured neuroimaging data (Figure 7.1D).

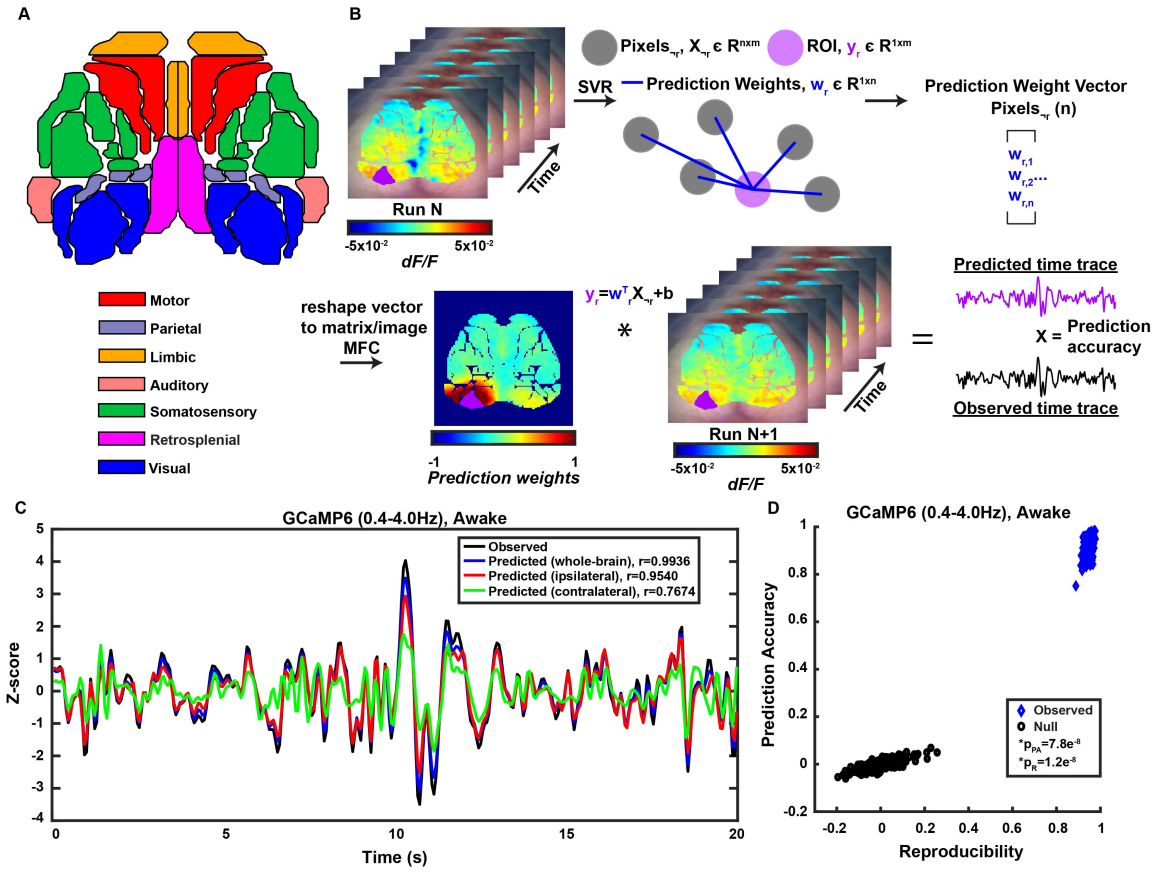

Figure 7.1: A) Graphic of cortical parcellation adapted from White et al. B) Schematic showing how the optical neuroimaging data is used to train SVR. SVR determines the amount of weight each pixel in the FOV excluding the ROI ($Pixels_{\neg,r}$, grey) has in predicting an average time trace within a whole ROI (purple). These weights are assembled into a prediction vector that can be used to impute the brain activity in an ROI in a subsequent run. Here, run N corresponds to either Run 1 or Run 2, the opposite of whichever run will be predicted. Once SVR is trained, the weight vector is used to create a weighted sum of time traces from all pixels in the FOV excluding the ROI ($X_{\neg,r}$) from the subsequent run to arrive at an imputed time trace for the ROI. Note the weight vector (w_r) can be unwrapped into a 2D image to represent multivariate functional connectivity (MFC). C) An example observed time trace (black) overlaid with imputed time traces using whole-brain (blue), ipsilateral (red), or contralateral (green) pixels to train SVR. D) Prediction accuracy and reproducibility of SVR trained on actual neuroimaging data compared to SVR trained on a null distribution. Each data point represents the result for a single ROI for each mouse (36 total parcels in the field-of-view x 5 mice = 180 data points). Reproducibility and prediction accuracy were significantly improved when SVR was trained on the actual neuroimaging data compared to the null time traces (p_R for reproducibility, p_{PA} for prediction accuracy, paired t-tests).

7.3.2 Multivariate Functional Connectivity Patterns of the SVR Regression Weights Overlay with Axonal Projection Images

The weight vectors generated via SVR can be plotted as multivariate functional connectivity (MFC) maps (Figure 7.2A, top row) and show a connectivity pattern analogous to traditionally calculated Pearson correlation FC (Figure 7.2A, bottom row). The parcel to be predicted (SVR) or used as a seed region (FC) is outlined in white. All pixels within that parcel were excluded from each type of analysis. The patterns generally show symmetry about midline and the prediction accuracy and reproducibility using SVR vectors was high (Figure 7.2B, top row, around $r = 1$) across the whole FOV. For comparisons to FC, we utilized the correlation vectors generated via standard FC analysis for prediction purposes and substituted w_r from equation 7.2 with the correlation vector generated via FC analysis. While the FC vectors have fairly high reproducibility, the prediction accuracy of FC vectors fell significantly compared to the SVR technique (Figure 7.2B, bottom row, $p<0.05$, paired t-test). Although similar, there are marked differences between the maps produced with either MFC or FC methods (see Figure 7.3 for Dice similarity coefficient between MFC and FC maps). When compared with fluorescent images representing axonal projection connections (APC) of a viral injection site (Figures 7.2C), MFC maps proved to overlay as well as those acquired with FC analysis (Figure 7.2D).

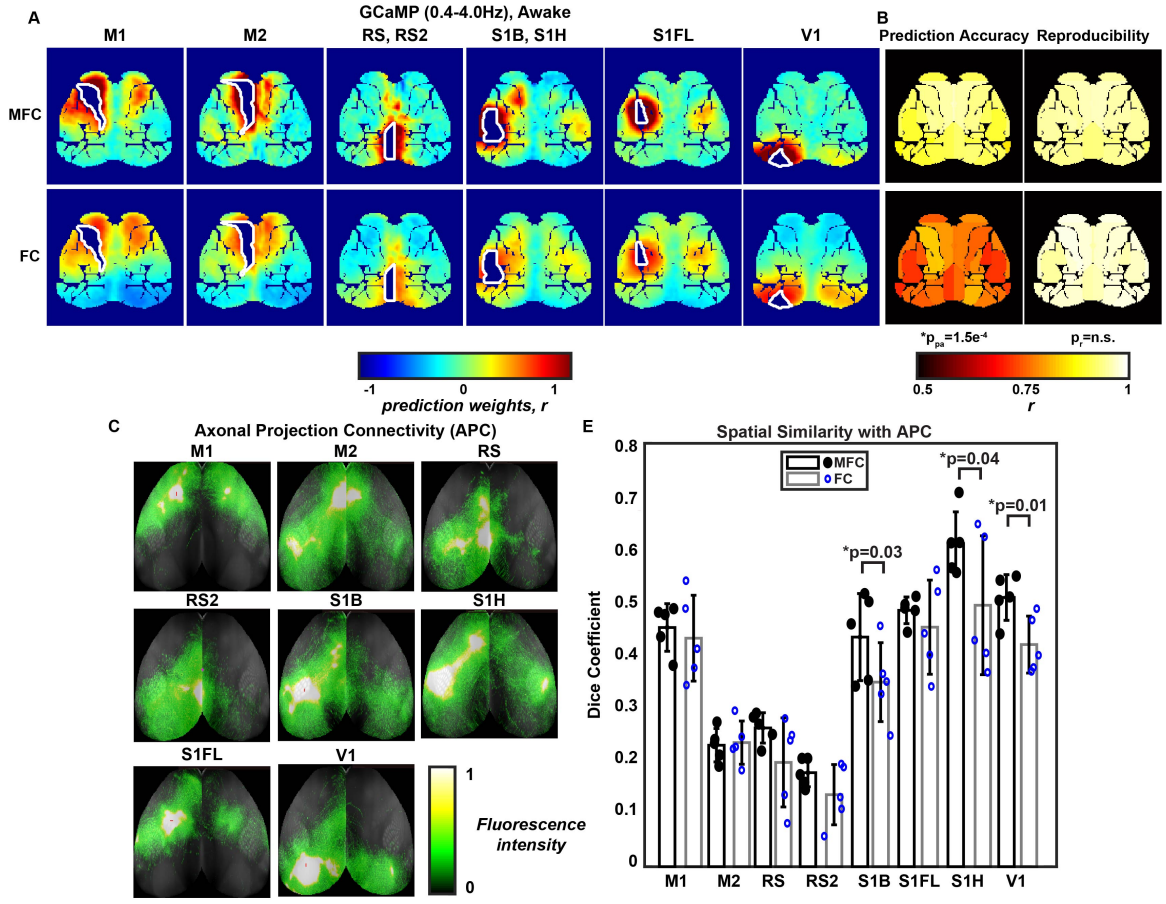

Figure 7.2: A) Average (N=5) MFC weight maps with corresponding FC maps using the outlined parcels as either the ROI (MFC) or the seed region in the standard Pearson based FC analysis. B) Average (N=5) prediction accuracy and reproducibility for each method across the field-of-view (significance is determined using the average value across the FOV for SVR or FC, followed by a paired t-test). C) APC maps with injection sites in proximity to the ROIs used in MFC and FC analysis. D) Dice similarity coefficient between APC and MFC maps, and APC and FC maps for each ROI in C). Significance is determined for the average Dice coefficient for each individual ROI with a paired t-test. Error bars are standard deviations.

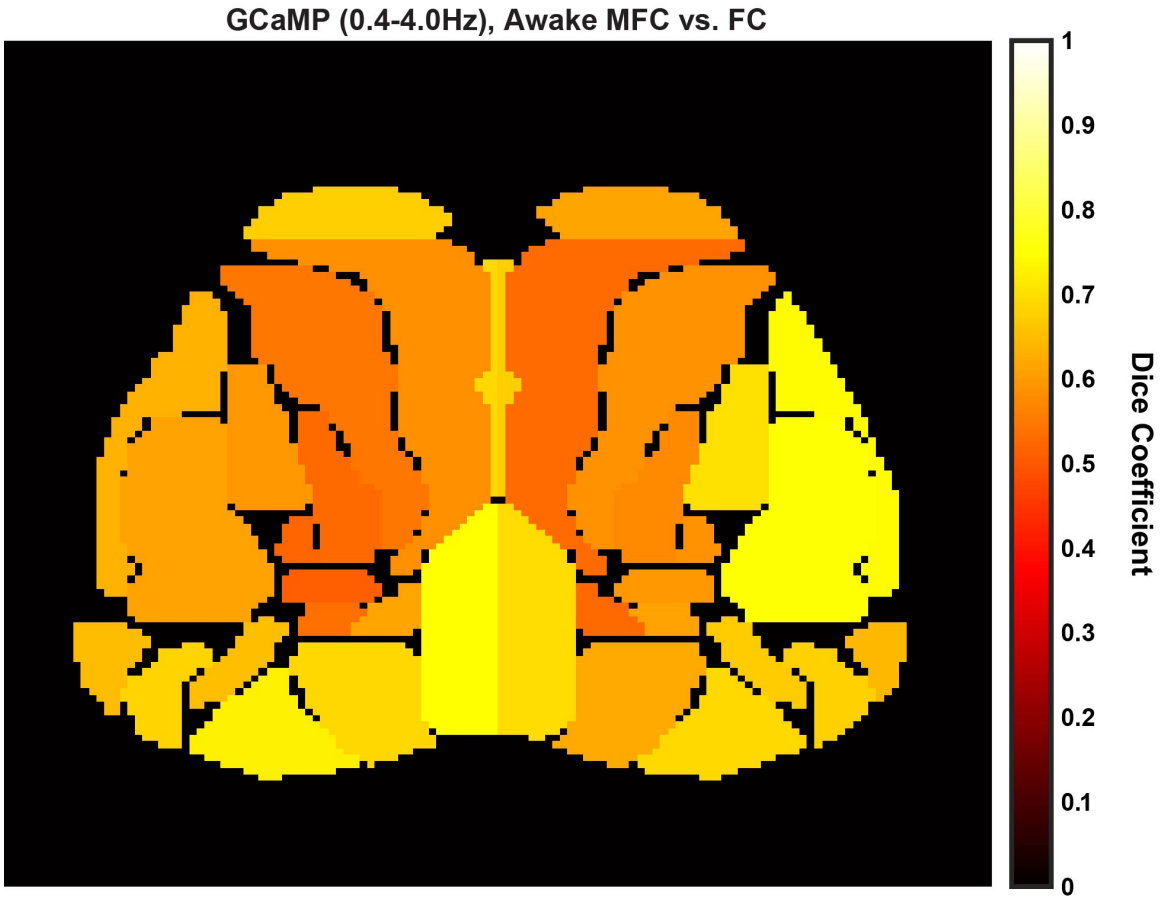

Figure 7.3: Average (N=5) Dice similarity coefficient between MFC and FC maps using the different 36 parcels within the field-of-view as either the ROI (MFC) or seed region (FC).

7.3.3 Ipsilateral Proximal Regions are Most Predictive for Accurate SVR Imputation

We were also interested in whether the SVR technique remained highly predictive if only a subset of pixels was used for training. For instance, can a parcel's dynamics be predicted using only pixels on the contralateral hemisphere? To evaluate this, we constrained the SVR algorithm to work with either just the ipsilateral or just the contralateral cortex (relative to the ROI). Even when restricted to a single hemisphere (either ipsilateral or contralateral) the SVR analysis was able to impute time traces with high prediction accuracy (example traces in Figure 7.1C). When using only ipsilateral or contralateral pixels for both training and imputation, SVR yielded topologically similar MFC prediction weight maps compared to when all brain pixels (excluding the ROI) were used to train SVR (Figure 7.4A). While reproducibility remained high across the ipsilateral and contralateral methods, prediction accuracy fell when only contralateral regions were used to train SVR (Figure 7.4B). We also evaluated the differences in prediction accuracy and reproducibility between the whole-brain, ipsilateral, and contralateral SVR training methods for each parcel (Figure 7.4C). A parcel-wise paired t-test was performed on the prediction accuracy and reproducibility calculated across all five mice using either the whole-brain, ipsilateral, or contralateral regions to train SVR (Figure 7.5). These statistical test results suggest full brain SVR has the highest accuracy and reproducibility, followed closely by ipsilateral SVR, and with the contralateral SVR method providing the least accurate prediction.

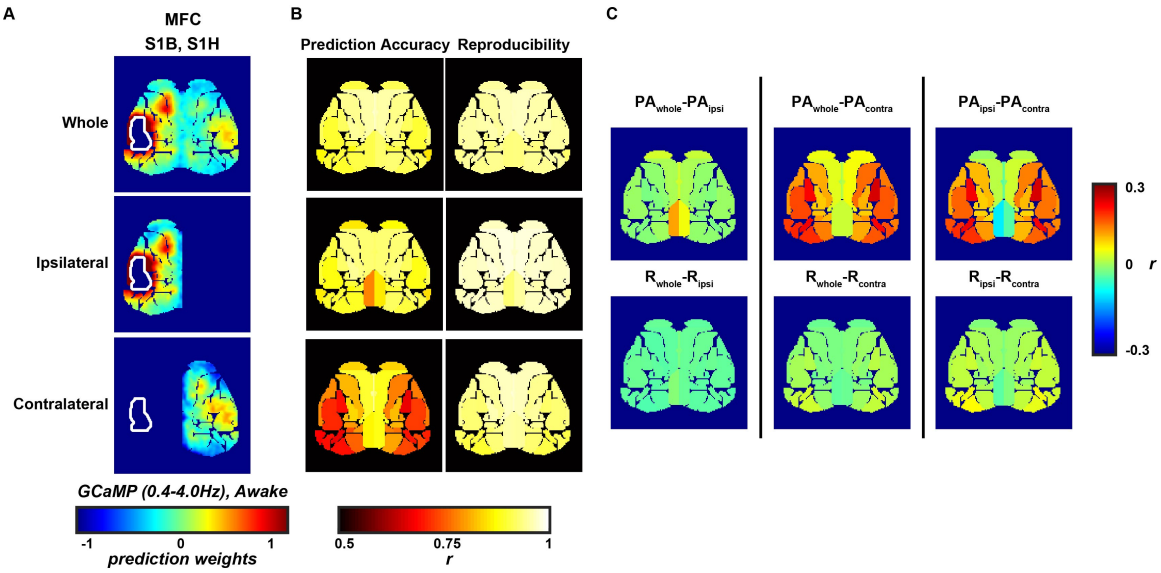

Figure 7.4: A) Average (N=5) MFC weight maps calculated using either whole-brain (top row), ipsilateral (middle row), or contralateral (bottom row) pixels only to train SVR. B) Average (N=5) prediction accuracy and reproducibility for all 36 ROIs using either whole-brain (top), ipsilateral (middle), or contralateral (bottom) pixels for training SVR. C) Difference maps comparing prediction accuracy (PA) and reproducibility (R) for the three different methods of training SVR: using either whole-brain, ipsilateral or contralateral cortical pixels.

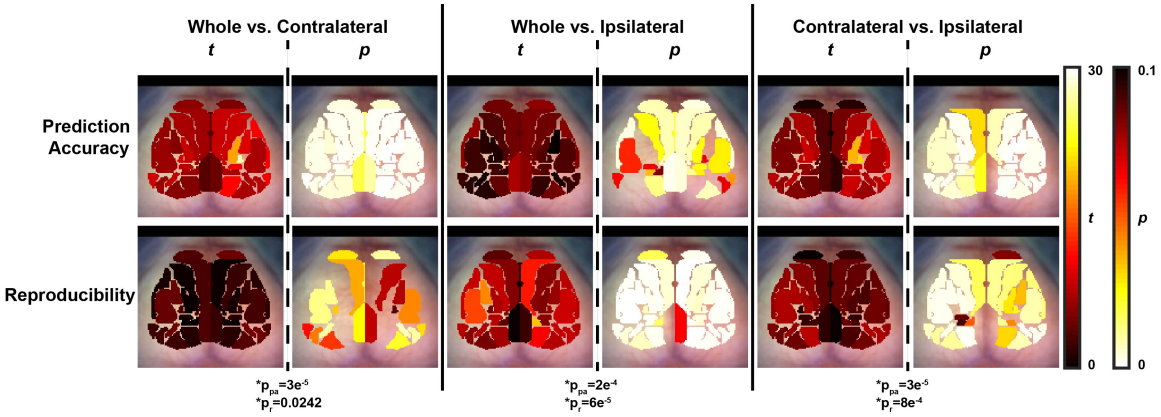

Figure 7.5: t- and p-maps showing the results of a paired t-test at each parcel for each comparison group. p-maps were thresholded to only show values of $p<0.1$. Results as shown were not corrected for multiple comparisons. Asterisks indicating significance were acquired by comparing the average reproducibility or prediction accuracy across the entire FOV (paired t-test) and are therefore corrected for multiple comparisons (comparisons=1).

7.3.4 MFC Maps are Impervious to Global Superficial Sources of Variance

MFC prediction weight maps were found to be relatively constant and remain more focal under various states of consciousness, compared to FC Pearson correlation maps. In addition to the awake state, calcium neuroimaging data was collected while mice were sleeping (in non-rapid eye movement, NREM sleep), and under ketamine/xylazine (K/X) anesthesia. Concurrently acquired EEG was scored offline to divide the calcium neuroimaging data into the respective states. MFC maps (Figure 7.6A, top row) and FC maps (bottom row) were calculated for each state. SVR provided high prediction accuracy and reproducibility for each state (Figure 7.7). To quantify the similarity between the maps for the three states, we calculated Dice similarity coefficients for each pairing of states (Awake vs K/X, Awake vs NREM, and NREM vs K/X). These were calculated for six example maps across each state and are plotted for MFC (white shading) and FC (grey shading) (Figure 7.6B). These six chosen parcels reasonably sampled the different cortical regions across the FOV. Here, MFC maps were relatively more similar across state compared to FC. Further, a measure termed "focality" was derived for MFC and FC maps, wherein a pixel-wise one-sample t-test was performed and the number of pixels above a t-value threshold was counted. The remaining pixels post-threshold were quantified and plotted for both MFC and FC for each brain state (Figure 7.6C), with MFC patterns emerging as more focal (fewer pixels left after thresholding) than FC.

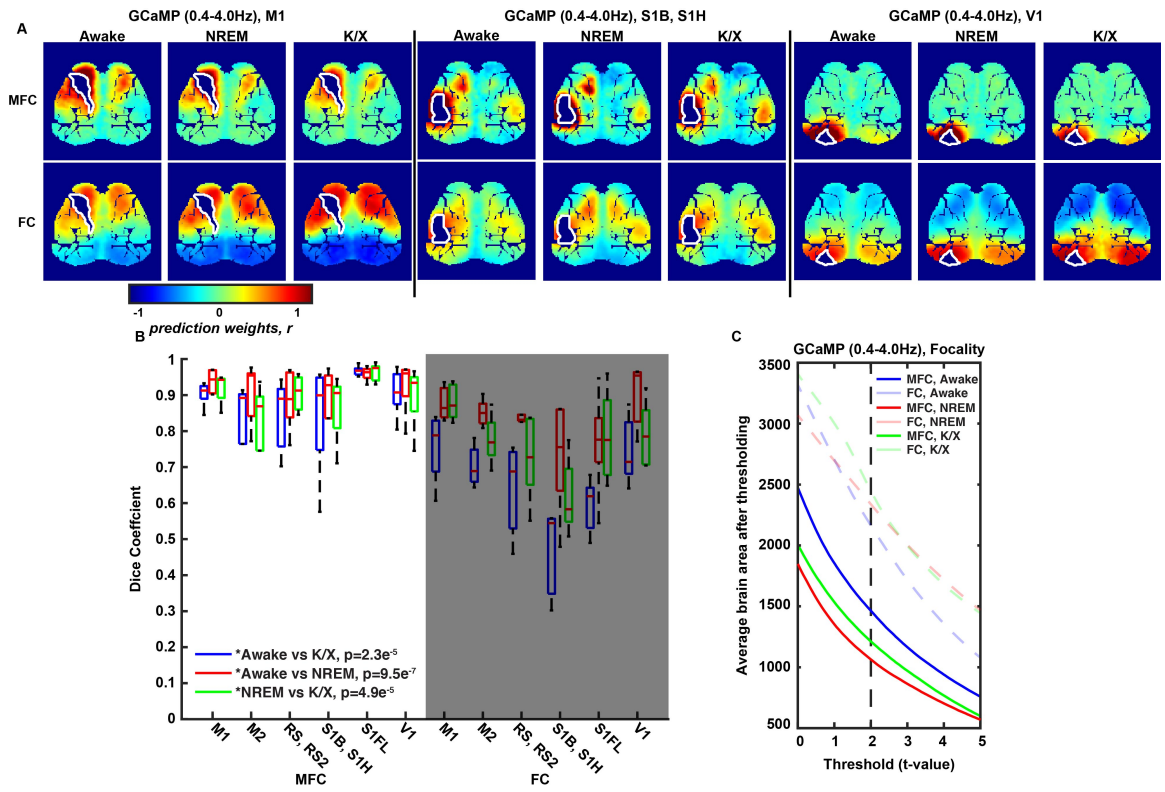

Figure 7.6: A) Average (N=5) example MFC and FC maps during wake, NREM sleep, and K/X anesthesia. B) Dice similarity coefficient comparing MFC (not shaded) and FC (shaded) maps across states of consciousness. Box plots represent N=5 mice. Red horizontal bars represent the median value, while the box edges represent the interquartile range. Extending lines represent the maximum and minimum values. Asterisks represent significance when comparing MFC and FC average Dice coefficients for all 6 brain regions across 5 mice (paired t-test). C) Pixel-wise one-sample t-tests were performed on brain maps as in A) and were thresholded by an increasing t-value cutoff. The number of pixels surviving the threshold are plotted using either MFC (solid) or FC (opaque, dashed) analysis (the ROI is excluded in calculation of focality for both MFC and FC). MFC maps created with SVR had a higher degree of focality (indicated by decreased number of pixels after thresholding) compared to FC maps. Vertical dashed line indicates a t-value of 2 and corresponds to $p<0.05$.

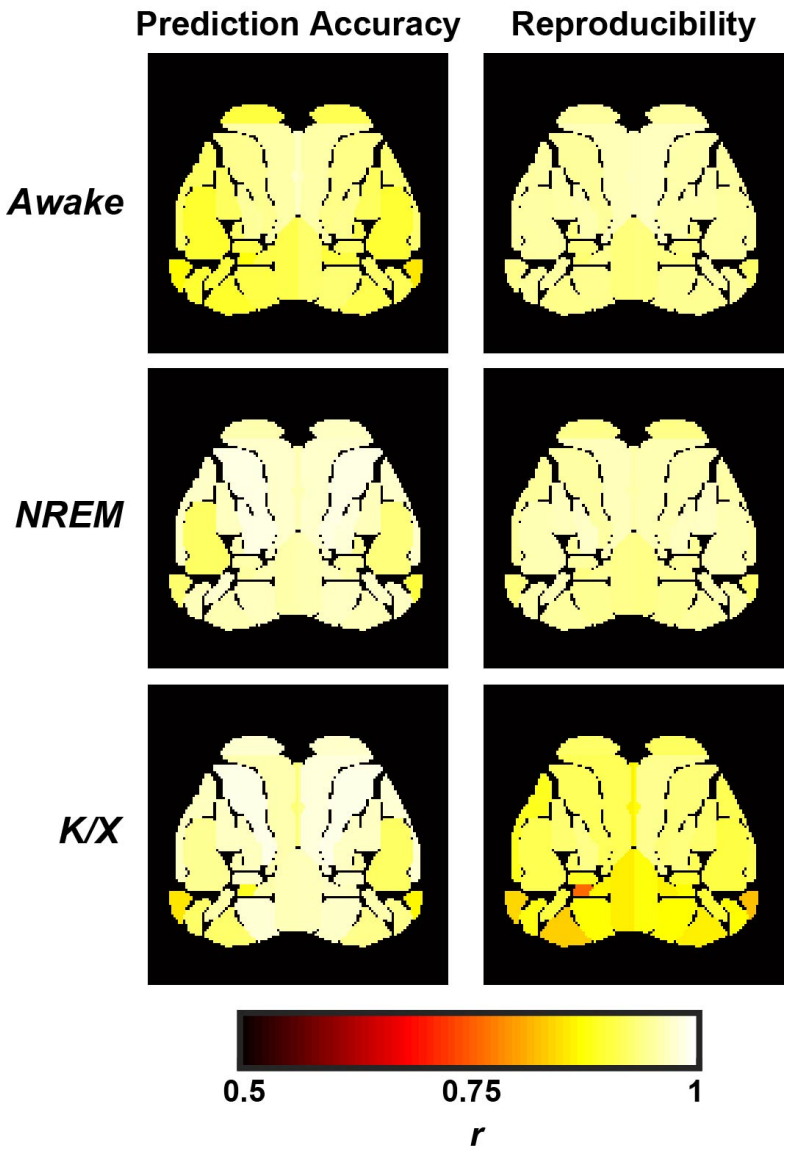

Figure 7.7: Average (N=5) prediction accuracy and reproducibility for SVR on awake, NREM sleep, and K/X anesthesia data.

Similarly, when matrices were calculated showing either the prediction weight (MFC) or the correlation coefficient (FC) between two parcels (Figures 7.8A,C, respectively) the MFC matrices lacked the broadly dispersed positive and negative connection values that are seen with FC (depicted in histograms displaying the matrix values in Figures 7.8A,C in Figures 7.8B,D, respectively). Instead, the largely positive values for MFC resided along the main diagonal and the homotopic contralateral off diagonal (Figure 7.8A). In agreement with MFC maps (Figure 7.6A), the MFC matrices remained relatively constant across brain state compared to the increasingly binary FC matrices under NREM and K/X anesthesia. Lastly, the focal nature of the positive prediction weights along the main diagonal within the MFC matrices, compared to the broad spread of positive/negative correlations in the FC matrices, was largely independent of the half width of the insensitive zone (ϵ) used in SVR optimization (Figure 7.9).

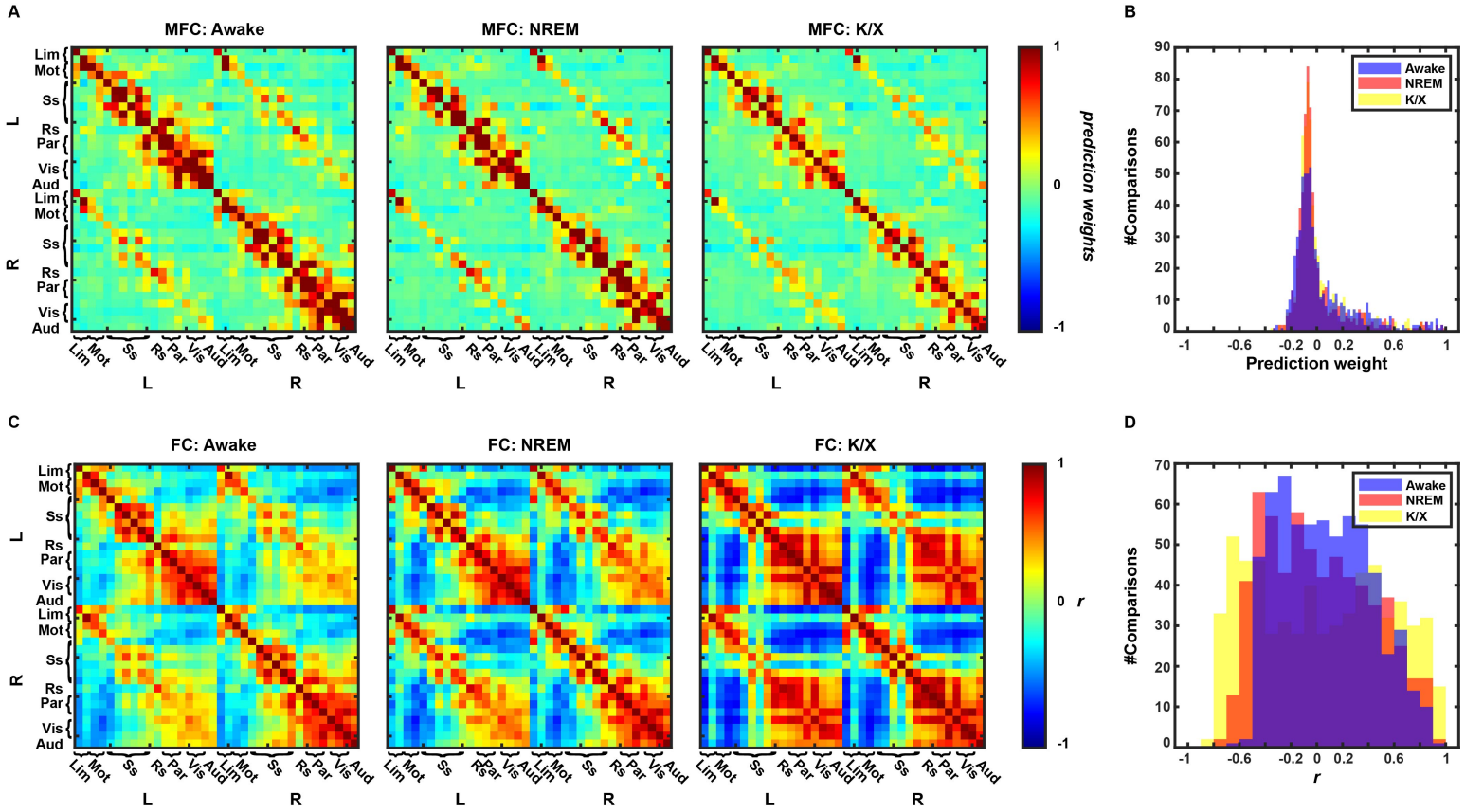

Figure 7.8: A) Average (N=5) MFC weight matrices for each consciousness state. B) Histogram plotting the number of comparisons from A) for each prediction weight value. C) Average (N=5) FC matrices for each consciousness state. D) Histogram plotting the number of comparisons from C) for each correlation value.

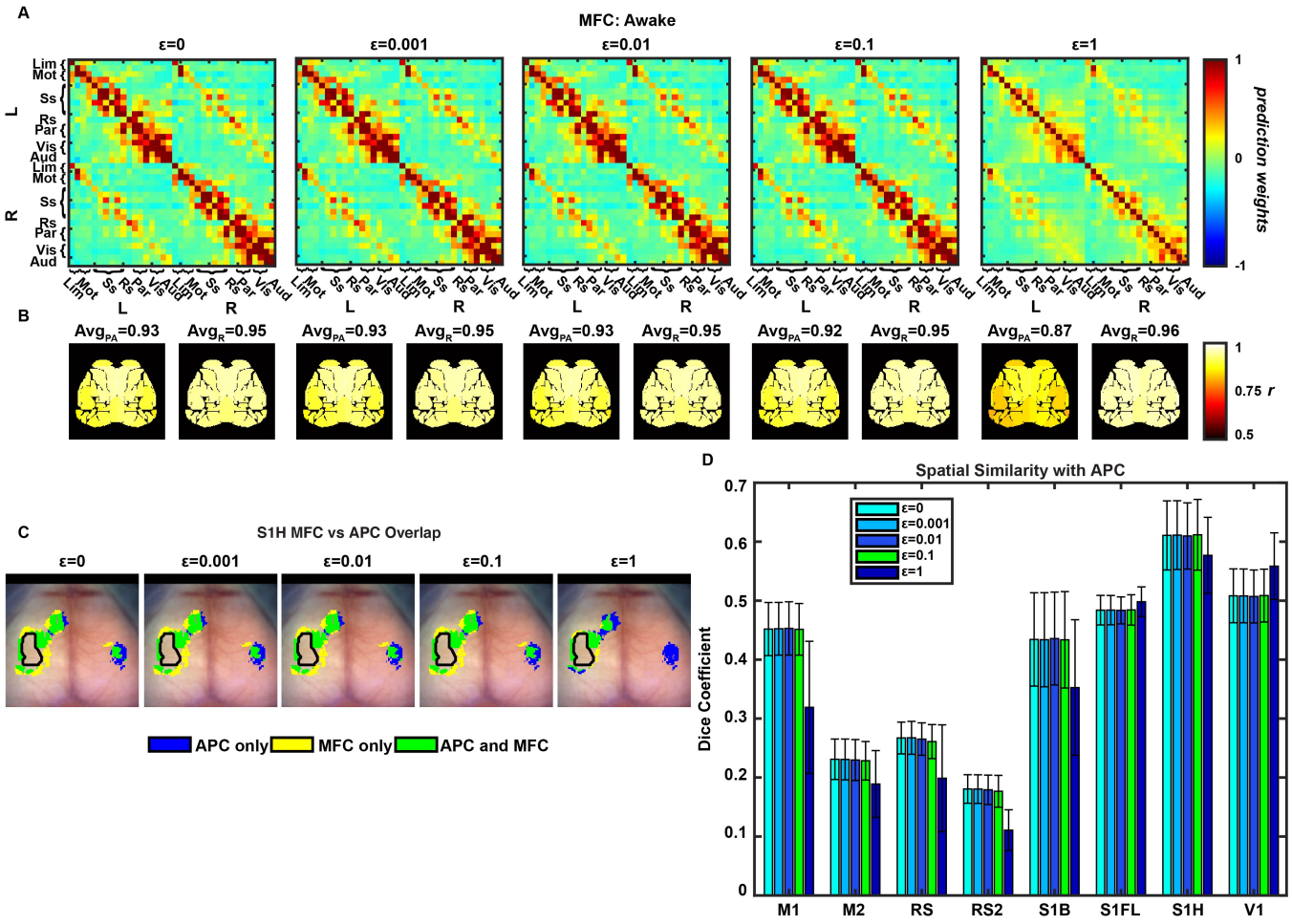

Figure 7.9: A) Average (N=5) MFC weight matrices for increasing value of ϵ. B) Prediction accuracy and reproducibility for increasing value of ϵ. The average prediction accuracy (PA) or reproducibility (R) over the FOV is printed above each image. C) Overlap maps as shown in Figure 7.10 between binarized APC and MFC maps for increasing epsilon values for parcel S1H. D) Dice coefficients between the MFC maps with various epsilon values and the 8 APC maps shown throughout the text (e.g., Figure 7.2C). Error bars are standard deviations.

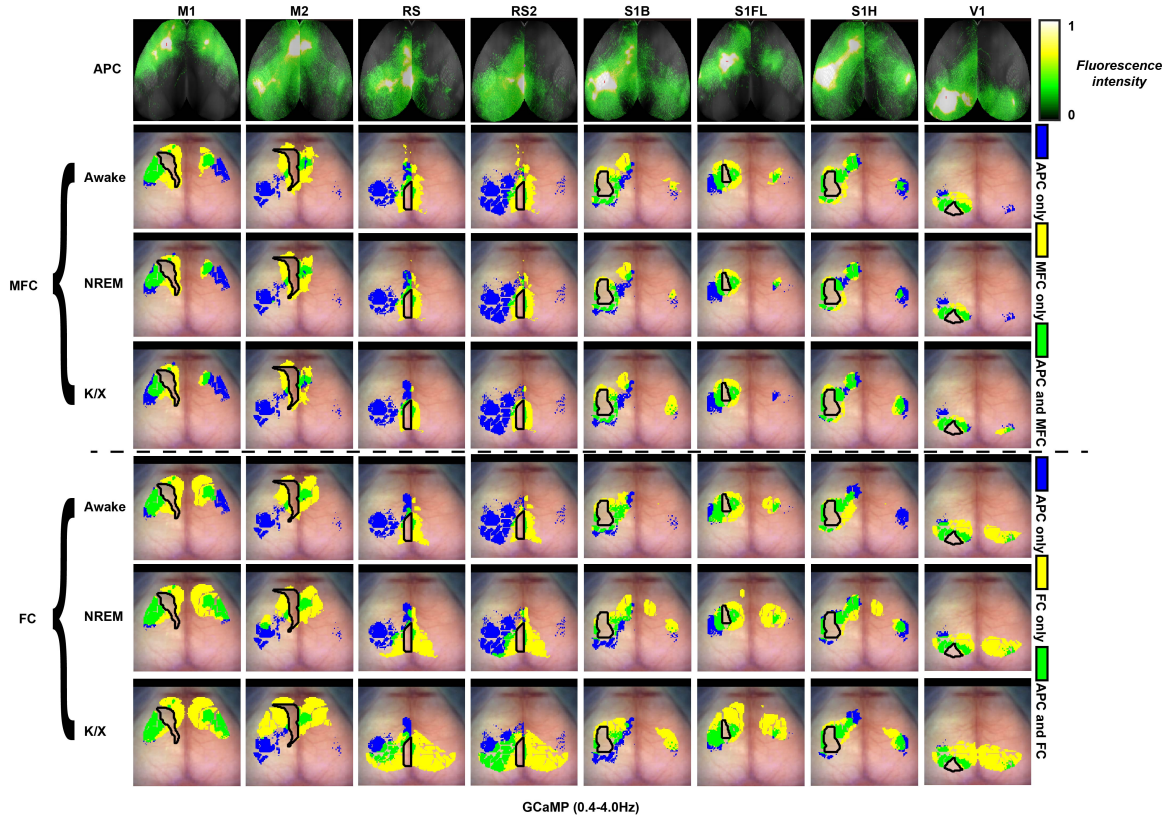

Figure 7.10: Individual APC maps (first row) and corresponding overlap maps between thresholded APC, MFC (rows 2-4), and FC (rows 5-7) maps. Overlap maps show the thresholded images (thresholded at 50% intensity for APC images, z(prediction weight) or z(r) of 0.3 for MFC/FC images, respectively). Blue represents pixels present in APC thresholded images only, yellow represents pixels present in MFC (rows 2-4) or FC (rows 5-7) thresholded images only, and green represents the overlap between APC and MFC/FC images. These overlap maps were used in the Dice similarity comparison calculations displayed in Figure 7.2E and Figure 7.11.

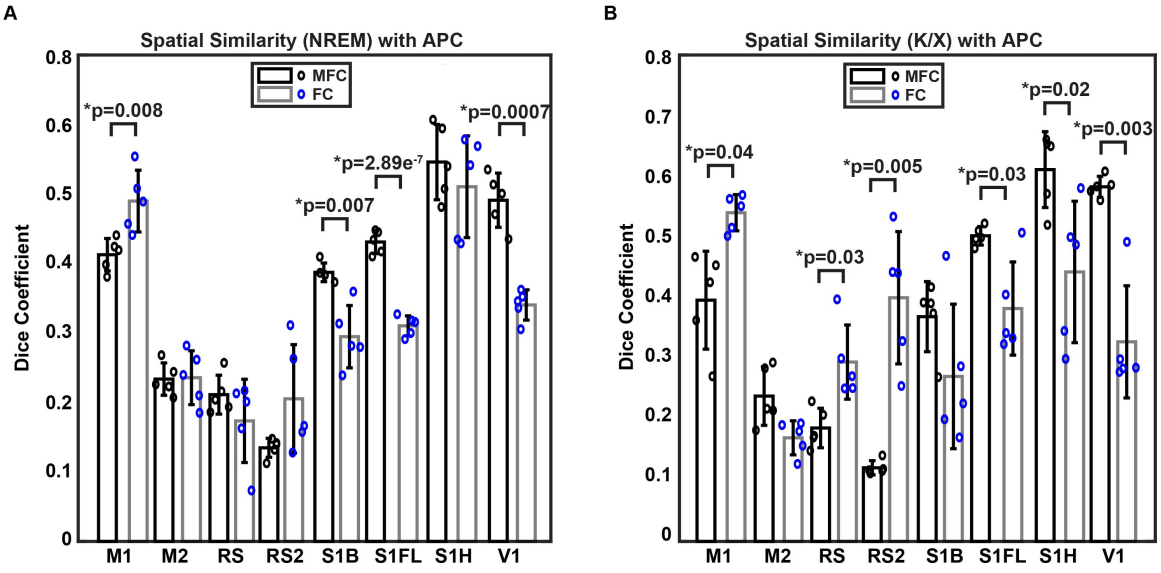

Figure 7.11: Dice similarity coefficient between APC and MFC maps, and APC and FC maps for each ROI shown in Figure 7.10. Significance is determined for the average Dice coefficient for each ROI with a paired t-test. Comparisons are shown for A) NREM and B) K/X data. Error bars are standard deviations.

7.3.5 MFC Mapping Locates Focal Connectivity Deficits in Stroke

Our final test was to investigate whether this new MFC methodology would detect connectivity deficits in an established disease model. We imaged N=4 mice before (Day 0) and after (Day 3) a photothrombotic event in left somatosensory forepaw cortex. MFC and FC maps are displayed using a more traditional, circular seed-based approach (Figure 7.12A) focusing on somatosensory (affected) and motor (unaffected) cortex. Additionally, average images across mice were thresholded and the binary overlap (or lack thereof) between Day 0 and Day 3 is displayed (Figure 7.12B) for the contralateral cortex relative to the seed displayed in the column in Figure 7.12A. The average homotopic prediction weight (MFC, Figure 7.12C) or correlation (FC, Figure 7.12D) for each mouse within the Ss seed was calculated and the averages and standard deviations across mice are plotted with significance testing between Day 0 and Day 3 results within the same hemisphere. Collectively, both methods show a loss of homotopic connectivity with the somatosensory seed, while normal homotopic connectivity patterns remain in the motor maps. However, the t- and p-values associated with the MFC statistical testing were more extreme compared to those with the FC method.

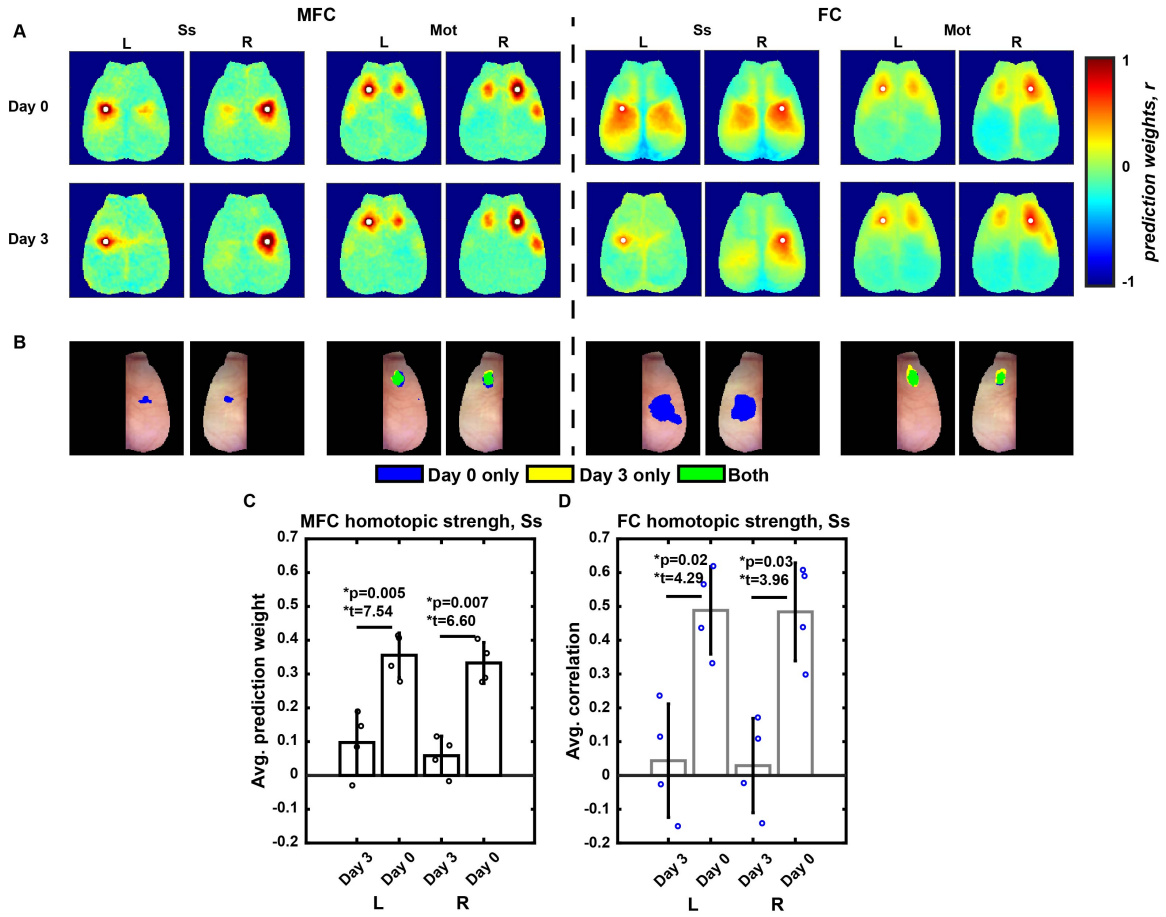

Figure 7.12: A) Average (N=4) MFC weight maps and FC correlation maps using a circular, seed-based approach (seeds in white). Somatosensory (Ss) and Motor (Mot) cortical seed maps are displayed at baseline (Day 0) and 72 hours post stroke (Day 3). B) Overlap maps display z(prediction weight) or z(r) greater than 0.3 in the contralateral hemisphere from A) between Day 0 only (blue), Day 3 only (yellow), or both (green). C) Average prediction weight (MFC) or D) correlation (FC) in the contralateral hemisphere across mice. Error bars are standard deviations. Significance was determined by a paired t-test between Ss seeds on Day 0 and Day 3 in the same hemisphere.

7.4 Discussion

We used mesoscopic calcium imaging data in mice to train SVR models to impute brain activity on a parcel-by-parcel basis (Figures 7.1A,B). This technique allowed us to impute brain activity with high prediction accuracy compared to chance (Figure 7.1D) and compared to imputations calculated with correlation vectors generated by standard FC analysis (Figure 7.2B). The multivariate functional connectivity (MFC) derived from this approach has several obvious similarities to traditional functional connectivity (FC) analysis. Each approach uses spontaneous brain activity as an input and outputs a vector linking different brain regions together. However, the MFC analysis of brain function has several potential advantages over FC analysis. First, the MFC approach, at a conceptual level, asks a fundamentally different and potentially more powerful question. Instead of asking how correlated two regions are, it asks how well different brain regions can predict another, and further asks for holistic optimization of the weights amongst the rest of the brain for a given region. Secondly, it has several potentially useful performance advantages including improved spatial specificity (Figure 7.6C, Figure 7.12A), less sensitivity of the mapping to states of consciousness (Figures 7.6A,B), a modest concordance with axonal tracer maps (Figure 7.2D), and improved connectivity deficit detection (Figure 7.12C,D) in the context of stroke.

While strategies beyond Pearson correlation analysis have been explored within human imaging, the translation of these techniques to the WOI mouse literature has not occurred. Here, we begin exploring the utility of multivariate connectivity techniques applied to mouse WOI by translating methods from an fMRI study in humans that used SVR to solve the multivariate analysis [57]. Compared to previous human SVR/fMRI study, SVR imputation of calcium dynamics in the mouse provided much higher values with less parcel-wise variance for prediction accuracy and reproducibility (with prediction accuracy $\sim$0.8-1.0 and reproducibility $\sim$0.8-1.0 for SVR of calcium dynamics vs prediction accuracy $\sim$0.5-1 and

reproducibility ∼0.1-0.5 for fMRI data as reported in Craddock et al. [57]). This could in part be due to the faster dynamics and therefore improved SNR provided by delta filtered calcium data [234] compared to the infraslow blood oxygen level dependent (BOLD) signal in fMRI. The calcium delta bandwidth is about 45x faster than the infraslow band (0.009-0.08Hz). Typically, at least twenty-five minutes of infraslow fMRI BOLD data are needed to generate FC maps with similar values of reproducibility (0.8 -1.0) to that which we are seeing with SVR using calcium dynamics in mice [137]. However, delta calcium dynamics provided highly accurate imputations (0.62-0.95) and reproducible (0.65-0.96) weight vectors with as little as thirty-sixty seconds of data (Figure 7.13). Also in contrast with the general themes in the fMRI literature, we found that SVR trained with ipsilateral regions outperformed SVR trained with contralateral regions only, in terms of prediction accuracy (Figures 7.4B,C).

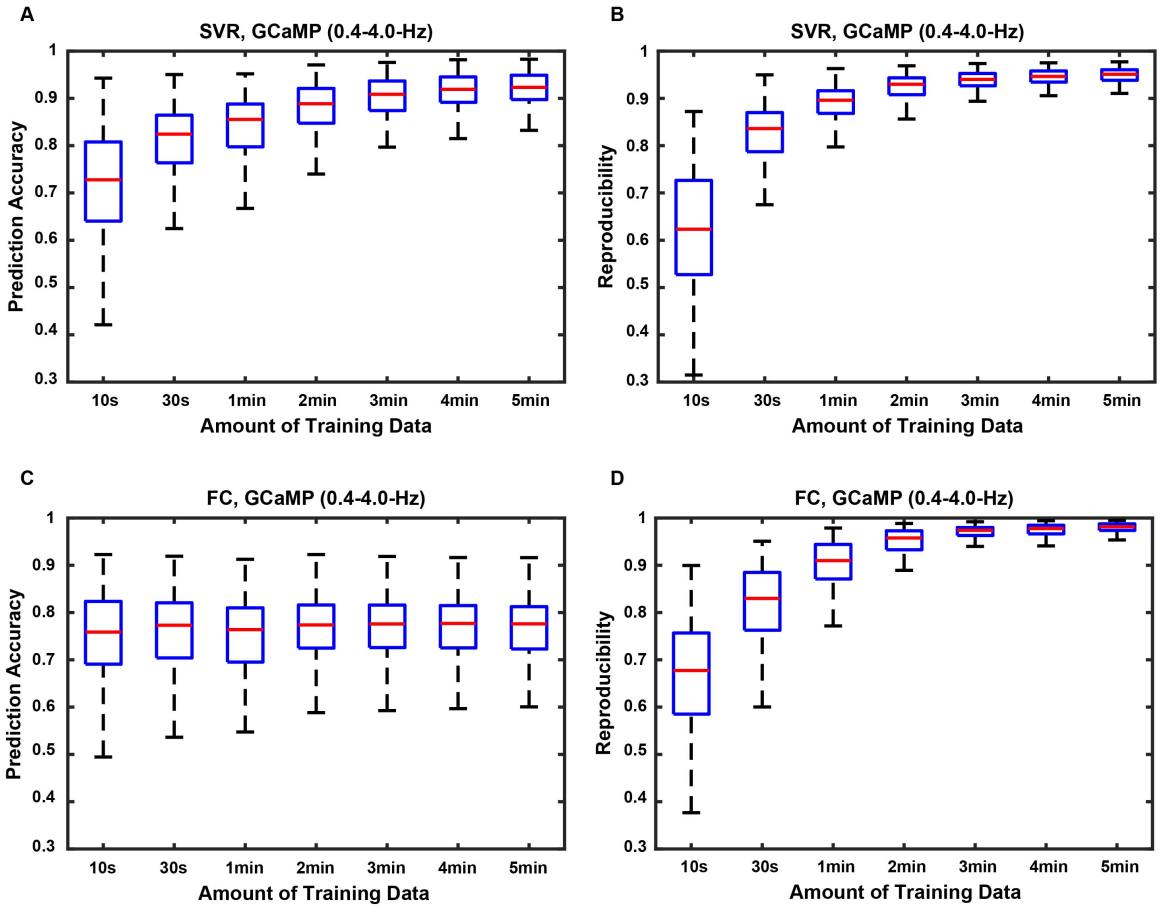

Figure 7.13: A) Prediction accuracy and B) Reproducibility as a function of increasing training data used for SVR. C) Prediction accuracy and D) Reproducibility as a function of increasing training data used for FC imputation. Red bars represent the median value, while the box edges represent the interquartile range. Extending lines represent the maximum and minimum values.

A hallmark of standard bivariate FC, with either fMRI or optical approaches, is the presence of networks displaying high levels of homotopic contralateral connectivity [242, 232, 256, 155]. While MFC does provide homotopic contralateral connectivity (with increased detail), our results suggest that ipsilateral regions are more heavily weighted when optimizing for predicting parcel time traces. To further test this theory, we looked at the prediction accuracy of SVR when trained with minimal spatial data (Table 7.1). Mainly, we focused on two ROIs, one from motor cortex and one from cingulate cortex. We used pixels within somatosensory (Ss) cortex to train SVR, given reports in the FC literature that Ss cortex is positively correlated with motor cortex and neutrally correlated with cingulate cortex [34]. In each case, prediction accuracies were much higher for network associated regions (Ss to motor) than non-associated regions (Ss to cingulate). Further SVR imputations trained with ipsilateral pixels had higher prediction accuracy than SVR trained with contralateral pixels. These results may be related to findings with fMRI that there exist brain hubs that are more highly connected to multiple networks. Interestingly, an injury in one of these hub regions proves more costly from a clinical perspective than when compared to injuries in non-hub regions [223]. This specific ipsilateral finding provides further support for clinical applications such as therapy to enhance brain re-mapping to connected ipsilateral regions after brain injury. During the critical period following stroke, when treatment is deemed most effective and opportunistic, tasks impaired by the ischemic area are often "re-mapped" to neighboring brain regions. This therapeutic approach targets re-mapping to the proximal, ipsilateral brain regions as nearby neurons can be more efficiently primed to re-create lost synapses than distal, contralateral populations [261, 262, 133]. The MFC model's enhanced ipsilateral/contralateral ratio, relative to FC, is consistent with these clinical treatment paradigms.

Training Data Used	Motor	Cingulate
All parcels in ipsilateral somatosensory cortex	0.7338	0.4979
All parcels in contralateral somatosensory cortex	0.5067	0.4579
All parcels in the brain except the one to be predicted	0.9426	0.9718
All parcels in ipsilateral cortex	0.9300	0.9365
All parcels in contralateral cortex	0.7984	0.9350

Table 7.1: Prediction accuracy for motor and cingulate parcels using limited spatial data from somatosensory cortex

Previous work has shown that FC analysis can be influenced by the presence of large, global variations in data which can be present due to multiple confounding factors. Physiology such as movement, heart rate, $EtCO_2$ or deep breaths can create artifacts that can be tricky to remove, particularly if their phase varies across the brain [198, 199]. Traditional FC might be susceptible because it is a bivariate analysis technique that analyzes two specific brain regions in isolation, instead of solving collectively for all of the observations within the FOV. In contrast, SVR is trained by time traces from every spatially independent region (e.g., point spread function, pixel or voxel) across the FOV to provide a multivariate approach that could be less likely to succumb to large scale global variations. In addition to the more mundane sources like motion or breathing, network dynamics can also be distorted by large scale neural oscillations that occur during sleep (e.g., NREM) and under anesthesia (e.g., K/X) wherein these slow oscillations propagate from anterior to posterior brain regions at ∼1Hz [224, 158]. We trained SVR and performed FC on data that was acquired on mice that were awake, in NREM, or under K/X anesthesia. For delta filtered calcium data (0.4-4.0Hz), the slow wave oscillation distorted the traditional FC structure seen during the awake state (Figure 7.6A). However, SVR provided highly similar MFC maps across all three states (Figure 7.6A) especially when compared to the high inter-state variance provided by FC analysis (Figure 7.6B). In fact, the MFC map patterns present during wake are fairly analogous to traditional FC map patterns present during wake (Figure 7.2A, Figure 7.3). However, only with MFC did these patterns remain robustly present throughout all three consciousness states, despite the presence of the slow oscillation. This result suggests that MFC can provide a readout of the functional architecture that separates out superficial global phenomena. Many neuroimaging studies collect data on mouse models of disease under anesthesia or not monitored for NREM by semi-invasive methods (e.g., EEG), therefore a more robust method for calculating connectivity in the presence of the confounding slow oscillation will allow for better dissection of alterations in disease.

While MFC methods have not been developed and tuned within the mouse WOI literature, there are several multivariate methods used in the human fMRI world where there is a well-established precedent to shift from simple bivariate correlation methods to multivariate methods [11]. The most widely reported use of multivariate techniques is not in the calculation of the functional connections but rather in the post-processing of FC maps, after standard FC has already been calculated. For instance, multivariate pattern analysis (MVPA) can be used to relate FC patterns and disease severity graded through a clinical score [271, 143]. More relevant to the current paper is literature focused on applying multivariate techniques to spatio-temporal data directly. For example, several studies have worked on decoding task-evoked data using time-series imaging. In this case, the task behaves as the object or output to be classified, and MVPA is used to build a classifier out of the spatio-temporal data [110, 181]. In this paper we have not used tasks, but rather spontaneous (or resting state) imaging data. Human fMRI studies have applied multivariate techniques to spontaneous data. For instance, techniques such as linear multivariate pattern dependence (MVPD) have been used to investigate the statistical dependency (connectivity) of the fusiform face area (FFA) and the posterior superior temporal sulcus (pSTS) with the remaining voxels in the FOV available with human fMRI [12]. This revealed novel interactions not previously characterized by simple correlation metrics, and further, the authors were able to break up the original ROI's used to define the FFA and pSTS, into smaller regions and determine a finer level of detail. Other multivariate techniques have also found success at improving the accuracy of network mapping relative to standard bivariate FC measures [90]. The SVR approach to MFC reported herein, maintains the inherent multivariate advantage of collectively optimizing the weights for all pixels within the FOV in order to provide estimates of connectivity that are more robust and detailed than bivariate FC. While in this paper we used SVR to solve the multivariate optimization for WOI, it will be of great interest to explore the wider variety of methods that are being explored in the

human fMRI literature [90, 16].

One crucial feature in this SVR model of connectivity is the half-width of the insensitive zone (ϵ). One risk associated with backwards modeling is the appearance of significant weights that are statistically independent from the ROI [108]. The tunable feature, ϵ, provides user-defined control of the spatial sparsity and amount of error to be included in the model. In order to investigate whether sparseness of the MFC matrices was simply due to setting the half width of the insensitive zone, $\epsilon = 0.1$, we generated MFC matrices using SVR with a range of ϵ values during optimization (Figure 7.9). Largely, MFC connectivity patterns, prediction accuracy, and reproducibility remained relatively unchanged across ϵ values (Figures 7.9A,B), although a modest decrease in prediction accuracy was observed for $\epsilon > 0.1$. Interestingly, this decrease in prediction accuracy was accompanied by a decrease in the magnitude of the prediction weights along the main diagonal for $\epsilon > 0.1$, indicating that increasing the width of the insensitive zone decreased the model's ability to correctly emphasize the prediction value of highly connected regions. Additionally, the spatial similarity between MFC maps and APC images decreased with $\epsilon > 0.1$ (Figures 7.9C,D), further proving that when $\epsilon < 0.1$, the ability to capture monosynaptic connections is improved (e.g., somato-motor and homotopic patterns usually represented in FC maps are represented with MFC using the S1H ROI with $\epsilon < 0.1$, Figure 7.9C). Although prediction accuracy and APC map overlap did not vary as much for $\epsilon < 0.1$, decreasing the value of ϵ increases training time and makes the model more prone to overfitting, which further supports a setting of $\epsilon = 0.1$. Mathematically speaking, while both FC and MFC techniques seek to describe the relationship between brain regions, there is stark contrast between the equations being solved when performing each. With MFC, the SVR prediction (equation 7.2) might more closely resemble commonly used techniques such as simple linear regression, although the optimization of SVR minimizes the L-2 norm of the prediction weight vector while linear regression minimizes the sum of squared errors. However, it is precisely the addition of the

tunable SVR features (e.g., ϵ, C in eqns. 7.2.9,7.3) that present a clear advantage, making the SVR model more malleable to modeling connectivity. It is also important to note that during wake, while the maps generated with MFC and FC do have marked differences, both MFC and FC techniques shared at least, on average, 50% similarity with monosynaptic connections (Figure 7.2D, see also Figure 7.10 for individual thresholded maps used to compare to the APC images). Comparable similarity to APC images was also present between MFC and FC methods performed on NREM and K/X data (Figures 7.10,7.11). This context of anatomical connectivity provides a basis along which functional connectivity patterns generally but do not completely overlay [115]. In fact, with the methodological and ideological shift to multivariate analysis occurring in the fMRI literature, a preference for calling these functional outputs patterns of "statistical dependence" instead of "functional connectivity" has emerged because the latter negates the importance of structural connectivity in the overall functional correlation structure [115, 11]. Comparable similarity between APC and either MFC or FC suggests that both approaches capture brain network connectivity as defined through anatomical connections, however, only with the MFC technique were more subtle structural and functional connections (e.g., somatomotor or contralateral homotopic somatosensory) present.

Lastly, we wanted to investigate whether MFC would perform as well as FC at detecting connectivity disruptions, here, in the context of stroke. Based on previous imaging work, necrotic tissue (post ischemic event) does not form homotopic connections as healthy tissue does [17]. Therefore, we calculated the significant homotopic connectivity overlap between Day 0 and Day 3 using a seed within affected (Ss) and unaffected (Mot) cortices (Figure 7.12). Interestingly, increased focality in the thresholded images with the MFC technique (Figure 7.12B) was observed again while both MFC and FC techniques showed absent homotopic connectivity within Ss cortex by Day 3 (when calculating overlap of thresholded average MFC/FC maps across mice, note motor cortex did have these homotopic connec-

tions). However, while the average homotopic connectivity strength in Ss cortex significantly decreased after the stroke with both methods (Figures 7.12C,D), the t-values for the difference between post-stroke and baseline were higher (and p-values lower) with MFC. Our results here suggest that MFC will potentially detect connectivity deficits with smaller effect sizes that would not be captured with FC.

7.5 Conclusions

Multivariate functional connectivity based on imputing brain dynamics with SVR can analyze and predict calcium brain activity in mice with high prediction accuracy and reproducibility. These results complement previous fMRI results in humans [57]. By uncovering brain regions that are heavily weighted in predicting a neighboring brain region, we present a new method for modeling calcium brain connectivity in mice that has attractive features both conceptually and performance wise. In particular, relative to traditional FC, the MFC approach provides improved predictive accuracy, improved spatial detail, less sensitivity to state of consciousness, and increased ability to detect connectivity deficits in the context of stroke.

While SVR is a rather straight forward machine learning technique (e.g., compared to convolutional neural networks or other deep learning methods), it was highly successful in this application of brain activity imputation. While this study demonstrates basic feasibility, there are a wide range of potential extensions and applications of this technique. Future directions include being able to train this model (or a more complex machine learning algorithm, if necessary) to detect and categorize the presence of confounding variables in imaging data (such as altered consciousness, movement, or physiological artifacts), and complex behavior (e.g., learning maze navigation, decisions).

Chapter 8

General Conclusions

This final chapter will attempt to synthesize overall conclusions from the previous chapters, not by restating the Discussion sections, but rather by highlighting the major takeaways.

8.1 Summary of Each Chapter

The following creates a list of major points from each stand-alone chapter:

8.1.1 WOI Data Processing Toolbox (Chapter 2)

- Herein, we describe a newly built wide-field optical imaging (WOI) data processing toolbox that is both user friendly and open source (Mouse WOI GitHub)
- Multiple statistical packages allow for simple, enriched functional connectivity (FC) matrix reduction allowing for a better handle on the multiple comparisons problem as well as improved data visualization techniques.
- A cluster size-based statistical thresholding method is translated from the functional magnetic resonance (fMRI) world (3-dimensional) into WOI (2-dimensional) to handle the multiple comparisons problem in pixel-wise statistical comparison maps.

- Multiple analyses toolboxes are currently available (e.g., FC, bilateral FC, spectral topography, neurovascular coupling, node degree), with more under development (e.g., data scrubbing).

8.1.2 WOI of Sleep (Chapter 3)

- WOI of genetically encoded calcium indicators (GECIs) enables whole cortex monitoring at the "mesoscale" with temporal resolution up to 8Hz. This improves on typical hemodynamic surrogates of neural activity by both providing a readout at a more direct metabolic step during the action potential (influx of calcium) and improves on the typically infraslow (<0.2Hz) dynamics analyzed with blood-based imaging contrasts.

- The increase in temporal resolution, afforded by GECIs, allows for mesoscale real-time imaging of the slow oscillation present during NREM and some forms of anesthesia.

- While this opens up multiple avenues of sleep research, the slow oscillation acts as a confounding variable that overwhelms typical measures of functional connectivity (FC), completely obscuring functional architecture in delta band frequencies (0.4-4.0Hz).

- Using principal component analysis (PCA), we proved the separability of the slow oscillation as a superficial event on top of ever-present "wake-like" FC.

8.1.3 WOI of Acute Septic Encephalopathy (Chapter 4)

- Little is known about the mechanisms by which peripheral infections can result in encephalopathies, largely because acutely available, good readouts of encephalopathy in mice do not exist.

- Mice injected peripherally with lipopolysaccharide (LPS) exhibit significant decreases in FC strength at 8Hrs post injection, and this effect recovers by 72Hrs, modeling the

transient nature of acute septic encephalopathy (ASE).

- Additionally, overall fluctuations in calcium dynamics become dampened at 8Hrs and reach normal amplitudes by 72Hrs.
- Both calcium fluctuation tone and FC strength correlated inversely with abnormal behavioral metrics, suggesting encephalopathy.
- Functional neuroimaging thus creates an acutely accessible and sensitive biomarker and can be used for further cross-sectional studies of ASE in this mouse model.
- Lastly, FC deficits clustered in somatosensory and parietal regions of the cortex, targeting these particular regions as particularly involved in the phenotypical presentation of ASE.

8.1.4 WOI of Subarachnoid Hemorrhage (Chapter 5)

- A novel endovascular mouse model of subarachnoid hemorrhage (SAH) effectively models the initial hemorrhage as well as delayed cerebral ischemic (DCI) events.
- This endovascular mouse model of SAH displayed significant reductions in FC at 3 days post SAH.
- Hypoxic conditioning is both an attractive therapeutic approach through the harnessing of the brain's intrinsic resistance to injury, but also was widely protective against FC deficits at 3 days post SAH.
- By injecting a specific Sirtuin1 channel blockade (EX527), we were able to prove that hypoxic conditioning works through a Sirtuin1 dependent mechanism to protect against the FC deficits at 3 days post SAH.

- Finally, a Sirtuin1 agonist Resveratrol, resulted in a protective effect as calculated by FC at 3 days post SAH, however, this treatment exhibited less of a protective effect than hypoxic conditioning. This indicates hypoxic conditioning additionally activates Sirtuin1 independent pathways.

8.1.5 WOI of Encephalitis Caused by Zika Infection (Chapter 6)

- Zika virus (ZIKV) rose to prominent global health concern due to severe neurological injury resulting in infants of infected pregnant adults. ZIKV also causes encephalitis in the non-pregnant adult and can often result in long lasting learning and memory deficits.

- Here, we imaged adult mice at 7 days post infection (dpi) with ZIKV and localized calcium-based FC deficits again (similar to the ASE study), to somatosensory and parietal cortex.

- Interestingly, hemoglobin-based dynamics resulted in FC deficits covering the entire field-of-view, suggesting an additional component of mismatched neurovascular coupling (e.g., mismatched metabolite supply and demand).

- All FC deficits resolved by 42 dpi (in parallel with recovery from ZIKV infection) using both hemoglobin and calcium-based contrasts.

- Similar to clinical presentation on EEG, encephalitic ZIKV-infected mice presented with an increase in delta calcium spectral density, reflecting the stereotypical finding of increased slow waves ($\sim$1Hz activity). This increase in delta power also resolved by 42 dpi.

8.1.6 Multivariate Statistical Dependencies in WOI Data (Chapter 7)

- Remarkably, the field of functional neuroimaging (across modality, e.g., fMRI, diffuse optical tomography, DOT, WOI, and across species, e.g., humans, rats, mice) uses simple bivariate Pearson correlation to calculate FC.
- While standard FC has led to multiple breakthroughs and established multiple networks, the accurate mapping of neurological processes is almost certainly multivariate.
- There is an emerging literature in human fMRI of a switch to more involved multivariate models of FC (i.e., MFC).
- Here, we transition one section of the human fMRI literature into the mouse WOI realm and expand on it in multiple ways.
- Support vector regression (SVR) can be used to solve the multivariate problem and explain the activity in one region of interest (ROI) by weighting the variance in the remaining pixels in the FOV, thus creating a holistically optimized map of MFC.
- We expand on the SVR MFC concept in several ways including; >40x faster contrast dynamics through mouse WOI, comparisons between MFC and histological axonal tracing maps, comparisons of MFC maps across awake/sleep/anesthesia, investigate MFC sensitivity to induced stroke and, finally, present comparisons between MFC and standard bivariate FC throughout all of these manipulations. Generally, MFC mapping produced better concordance with structural and functional connectivity, was more impervious to global superficial sources of variance, and produced a statistically stronger analysis of a well-established mouse model of stroke.

8.2 WOI for Neurological Disease and Sleep

Collectively, this work presents multiple advantages of using mouse WOI to study various aspects of health and disease. In addition to establishing WOI as a unique tool to study various sleep-related phenomenon and phenotypes, we were able to provide evidence that the hallmark of sleep (i.e., the slow oscillation) gets superimposed onto ever present wake-like functional architecture.

WOI in disease, offers multiple unique viewpoints. From creating a new, readily-available and sensitive readout of ASE, we open up many possibilities for cross-sectional studies to better investigate the underlying pathology resulting in mental status changes. In ZIKV encephalitis, we uncover additional areas of pathology outside the previously studied hippocampal tri-synaptic circuit. Finally, we prove the efficacy of various clinical therapeutics in the context of SAH.

8.3 Future Directions

While many new discoveries in biological phenomenon and algorithm development were made here, we only really applied a few of the advantages available when using WOI (as opposed to other modalities, e.g., fMRI or DOT). Wide-field high resolution optical imaging is becoming more and more widespread with the addition of wide-field one [130] and two-photon imaging instruments [41] as well as surgical procedures to produce chronic optically transparent craniotomy preparations to remove the light scattering effects of the skull in mice [130, 92]. Mesoscopic functional neuroimaging results in network-level investigation while the addition or substitution for wide-field high resolution optical imaging will allow for network-level investigation along with cell-specific tracking. This will open up multiple new avenues for investigation. For example, instead of using mesoscopic imaging to create a novel biomarker for future study of ASE, wide-field high resolution optical imaging would

allow for monitoring of this biomarker as well as insight into the cellular mechanisms driving mental status changes.

Chapter 9

References

[1] Richard A. Armstrong. *When to use the Bonferroni correction*, volume 34. 2014. doi: 10.1111/opo.12131.

[2] Laura Airas, Eero Rissanen, and Juha O Rinne. Imaging neuroinflammation in multiple sclerosis using TSPO-PET. *Clin. Transl. imaging*, 3(6):461–473, 2015. ISSN 2281-5872. doi: 10.1007/s40336-015-0147-6. URL `https://pubmed.ncbi.nlm.nih.gov/27331049https://www.ncbi.nlm.nih.gov/pmc/articles/PMC4887541/`.

[3] Oluwaseun Akeju, Seong-eun E Kim, Rafael Vazquez, James Rhee, Kara J Pavone, Lauren E Hobbs, Patrick L Purdon, and Emery N Brown. Spatiotemporal Dynamics of Dexmedetomidine-Induced Electroencephalogram Oscillations. *PLoS One*, 11(10): e0163431, 2016. doi: 10.1371/journal.pone.0163431. URL `https://www.ncbi.nlm.nih.gov/pubmed/27711165`.

[4] Oluwaseun Akeju, Andrew H Song, Allison E Hamilos, Kara J Pavone, Francisco J Flores, Emery N Brown, and Patrick L Purdon. Electroencephalogram signatures of

ketamine anesthesia-induced unconsciousness. *Clin. Neurophysiol.*, 127(6):2414–2422, 2016. doi: 10.1016/j.clinph.2016.03.005. URL https://www.ncbi.nlm.nih.gov/pubmed/27178861https://www.ncbi.nlm.nih.gov/pmc/articles/PMC4871620/.

[5] Michael T Alkire and Jason Miller. General anesthesia and the neural correlates of consciousness. In Steven Laureys, editor, *Prog. Brain Res.*, volume 150, pages 229–597. Elsevier, 2005. ISBN 0079-6123. doi: https://doi.org/10.1016/S0079-6123(05)50017-7. URL http://www.sciencedirect.com/science/article/pii/S0079612305500177.

[6] Pedro Nascimento Alves, Chris Foulon, Vyacheslav Karolis, Danilo Bzdok, Daniel S Margulies, Emmanuelle Volle, and Michel Thiebaut de Schotten. An improved neuroanatomical model of the default-mode network reconciles previous neuroimaging and neuropathological findings. *Commun. Biol.*, 2(1):370, 2019. ISSN 2399-3642. doi: 10.1038/s42003-019-0611-3. URL https://doi.org/10.1038/s42003-019-0611-3.

[7] F Amzica and M Steriade. Electrophysiological correlates of sleep delta waves. *Electroencephalogr. Clin. Neurophysiol.*, 107:69–83, 1998.

[8] J S Anderson. Origin of Synchronized Low-Frequency Blood Oxygen Level–Dependent Fluctuations in the Primary Visual Cortex. *Am. J. Neuroradiol.*, 29(9):1722 LP – 1729, oct 2008. doi: 10.3174/ajnr.A1220. URL http://www.ajnr.org/content/29/9/1722.abstract.

[9] J S Anderson, M A Ferguson, M Lopez-Larson, and D Yurgelun-Todd. Reproducibility of single-subject functional connectivity measurements. *AJNR. Am. J. Neuroradiol.*, 32 (3):548–555, 2011. doi: 10.3174/ajnr.A2330. URL https://www.ncbi.nlm.nih.gov/pubmed/21273356https://www.ncbi.nlm.nih.gov/pmc/articles/PMC3205089/.

[10] Stephanie Andrade, Maria João Ramalho, Maria do Carmo Pereira, and Joana A Loureiro. Resveratrol Brain Delivery for Neurological Disorders Prevention and

Treatment. *Front. Pharmacol.*, 9:1261, nov 2018. ISSN 1663-9812. doi: 10.3389/fphar.2018.01261. URL https://pubmed.ncbi.nlm.nih.gov/30524273https://www.ncbi.nlm.nih.gov/pmc/articles/PMC6262174/.

[11] Stefano Anzellotti and Marc N Coutanche. Beyond Functional Connectivity: Investigating Networks of Multivariate Representations. *Trends Cogn. Sci.*, 22(3):258–269, mar 2018. ISSN 1364-6613. doi: 10.1016/j.tics.2017.12.002. URL https://doi.org/10.1016/j.tics.2017.12.002.

[12] Stefano Anzellotti, Evelina Fedorenko, Alexander J E Kell, Alfonso Caramazza, and Rebecca Saxe. Measuring and Modeling Nonlinear Interactions Between Brain Regions with fMRI. *bioRxiv*, page 74856, jan 2017. doi: 10.1101/074856. URL http://biorxiv.org/content/early/2017/09/12/074856.abstract.

[13] Liana G Apostolova and Paul M Thompson. Brain mapping as a tool to study neurodegeneration. *Neurotherapeutics*, 4(3):387–400, 2007. doi: 10.1016/j.nurt.2007.05.009. URL https://www.ncbi.nlm.nih.gov/pubmed/17599704https://www.ncbi.nlm.nih.gov/pmc/articles/PMC2634605/.

[14] John Ashburner. SPM: a history. *Neuroimage*, 62(2):791–800, aug 2012. ISSN 1095-9572. doi: 10.1016/j.neuroimage.2011.10.025. URL https://pubmed.ncbi.nlm.nih.gov/22023741https://www.ncbi.nlm.nih.gov/pmc/articles/PMC3480642/.

[15] Danielle S Bassett and Olaf Sporns. Network neuroscience. *Nat. Neurosci.*, 20(3):353–364, 2017. ISSN 1546-1726. doi: 10.1038/nn.4502. URL https://doi.org/10.1038/nn.4502.

[16] Alessio Basti, Hamed Nili, Olaf Hauk, Laura Marzetti, and Richard N Henson. Multi-dimensional connectivity: a conceptual and mathematical review. *Neuroimage*, 221:117179, 2020. ISSN 1053-8119. doi: https://doi.org/10.

1016/j.neuroimage.2020.117179. URL https://www.sciencedirect.com/science/article/pii/S1053811920306650.

[17] Adam Q Bauer, Andrew W Kraft, Patrick W Wright, Abraham Z Snyder, Jin-Moo Lee, and Joseph P Culver. Optical imaging of disrupted functional connectivity following ischemic stroke in mice. *Neuroimage*, 99:388–401, oct 2014. ISSN 1095-9572. doi: 10.1016/j.neuroimage.2014.05.051. URL https://pubmed.ncbi.nlm.nih.gov/24862071https://www.ncbi.nlm.nih.gov/pmc/articles/PMC4332714/.

[18] Adam Q Bauer, Andrew W Kraft, Grant A Baxter, Patrick W Wright, Matthew D Reisman, Annie R Bice, Jasmine J Park, Michael R Bruchas, Abraham Z Snyder, Jin-Moo Lee, and Joseph P Culver. Effective Connectivity Measured Using Optogenetically Evoked Hemodynamic Signals Exhibits Topography Distinct from Resting State Functional Connectivity in the Mouse. *Cereb. Cortex*, 28(1):370–386, jan 2018. ISSN 1460-2199. doi: 10.1093/cercor/bhx298. URL https://pubmed.ncbi.nlm.nih.gov/29136125https://www.ncbi.nlm.nih.gov/pmc/articles/PMC6057523/.

[19] Aya Ben-Yakov, Yadin Dudai, and Mark R Mayford. Memory Retrieval in Mice and Men. *Cold Spring Harb. Perspect. Biol.*, 7(12):a021790, oct 2015. ISSN 1943-0264. doi: 10.1101/cshperspect.a021790. URL https://pubmed.ncbi.nlm.nih.gov/26438596https://www.ncbi.nlm.nih.gov/pmc/articles/PMC4665077/.

[20] M Bergeron, J M Gidday, A Y Yu, G L Semenza, D M Ferriero, and F R Sharp. Role of hypoxia-inducible factor-1 in hypoxia-induced ischemic tolerance in neonatal rat brain. *Ann. Neurol.*, 48(3):285–296, sep 2000. ISSN 0364-5134 (Print).

[21] Eyal Bergmann, Gil Zur, Guy Bershadsky, and Itamar Kahn. The Organization of Mouse and Human Cortico-Hippocampal Networks Estimated by Intrinsic Functional

Connectivity. *Cereb. Cortex*, 26(12):4497–4512, dec 2016. ISSN 1047-3211. doi: 10.1093/cercor/bhw327. URL https://doi.org/10.1093/cercor/bhw327.

[22] Karla M Bergonzi, Adam Q Bauer, Patrick W Wright, and Joseph P Culver. Mapping functional connectivity using cerebral blood flow in the mouse brain. *J. Cereb. blood flow Metab. Off. J. Int. Soc. Cereb. Blood Flow Metab.*, 35(3):367–370, mar 2015. ISSN 1559-7016 (Electronic). doi: 10.1038/jcbfm.2014.211.

[23] Elliot T Berkman and Emily B Falk. Beyond Brain Mapping: Using Neural Measures to Predict Real-World Outcomes. *Curr. Dir. Psychol. Sci.*, 22(1):45–50, feb 2013. ISSN 0963-7214. doi: 10.1177/0963721412469394. URL https://pubmed.ncbi.nlm.nih.gov/24478540https://www.ncbi.nlm.nih.gov/pmc/articles/PMC3903296/.

[24] Adi Berman, Rachel Motechin, Maia Wiesenfeld, and Marina Holz. The therapeutic potential of resveratrol: a review of clinical trials. *npj Precis. Oncol.*, 1, dec 2017. doi: 10.1038/s41698-017-0038-6.

[25] Adam W Bero, Adam Q Bauer, Floy R Stewart, Brian R White, John R Cirrito, Marcus E Raichle, Joseph P Culver, and David M Holtzman. Bidirectional relationship between functional connectivity and amyloid-β deposition in mouse brain. *J. Neurosci.*, 32(13):4334–4340, mar 2012. ISSN 1529-2401 (Electronic). doi: 10.1523/JNEUROSCI.5845-11.2012.

[26] B Biswal, F Z Yetkin, V M Haughton, and J S Hyde. Functional connectivity in the motor cortex of resting human brain using echo-planar MRI. *Magn. Reson. Med.*, 34 (4):537–541, oct 1995. ISSN 0740-3194 (Print). doi: 10.1002/mrm.1910340409.

[27] Bharat B Biswal, Maarten Mennes, Xi-Nian Zuo, Suril Gohel, Clare Kelly, Steve M Smith, Christian F Beckmann, Jonathan S Adelstein, Randy L Buckner, Stan Colcombe, Anne-Marie Dogonowski, Monique Ernst, Damien Fair, Michelle Hampson,

Matthew J Hoptman, James S Hyde, Vesa J Kiviniemi, Rolf Kötter, Shi-Jiang Li, Ching-Po Lin, Mark J Lowe, Clare Mackay, David J Madden, Kristoffer H Madsen, Daniel S Margulies, Helen S Mayberg, Katie McMahon, Christopher S Monk, Stewart H Mostofsky, Bonnie J Nagel, James J Pekar, Scott J Peltier, Steven E Petersen, Valentin Riedl, Serge A R B Rombouts, Bart Rypma, Bradley L Schlaggar, Sein Schmidt, Rachael D Seidler, Greg J Siegle, Christian Sorg, Gao-Jun Teng, Juha Veijola, Arno Villringer, Martin Walter, Lihong Wang, Xu-Chu Weng, Susan Whitfield-Gabrieli, Peter Williamson, Christian Windischberger, Yu-Feng Zang, Hong-Ying Zhang, F Xavier Castellanos, and Michael P Milham. Toward discovery science of human brain function. *Proc. Natl. Acad. Sci.*, 107(10):4734 LP – 4739, mar 2010. doi: 10.1073/pnas.0911855107. URL `http://www.pnas.org/content/107/10/4734.abstract`.

[28] M Boly, R Moran, M Murphy, P Boveroux, M A Bruno, Q Noirhomme, D Ledoux, V Bonhomme, J F Brichant, G Tononi, S Laureys, and K Friston. Connectivity changes underlying spectral EEG changes during propofol-induced loss of consciousness. *J Neurosci*, 32(20):7082–7090, 2012. doi: 10.1523/JNEUROSCI.3769-11.2012. URL `https://www.ncbi.nlm.nih.gov/pubmed/22593076`.

[29] Alexander A Borb and Peter Achermann. Sleep Homeostasis and Models of Sleep Regulation. *J. Biol. Rhythms*, 14(6):559–570, 1999. doi: 10.1177/074873099129000894. URL `https://doi.org/10.1177/074873099129000894`.

[30] Matthew B Bouchard, Brenda R Chen, Sean A Burgess, and Elizabeth M C Hillman. Ultra-fast multispectral optical imaging of cortical oxygenation, blood flow, and intracellular calcium dynamics. *Opt. Express*, 17(18):15670–15678, aug 2009. ISSN 1094-4087 (Electronic). doi: 10.1364/OE.17.015670.

[31] Patrícia Brasil, José P Pereira, M Elisabeth Moreira, Rita M Ribeiro Nogueira, Lu-

ana Damasceno, Mayumi Wakimoto, Renata S Rabello, Stephanie G Valderramos, Umme-Aiman Halai, Tania S Salles, Andrea A Zin, Dafne Horovitz, Pedro Daltro, Marcia Boechat, Claudia Raja Gabaglia, Patrícia Carvalho de Sequeira, José H Pilotto, Raquel Medialdea-Carrera, Denise Cotrim da Cunha, Liege M Abreu de Carvalho, Marcos Pone, André Machado Siqueira, Guilherme A Calvet, Ana E Rodrigues Baião, Elizabeth S Neves, Paulo R Nassar de Carvalho, Renata H Hasue, Peter B Marschik, Christa Einspieler, Carla Janzen, James D Cherry, Ana M Bispo de Filippis, and Karin Nielsen-Saines. Zika Virus Infection in Pregnant Women in Rio de Janeiro. *N. Engl. J. Med.*, 375(24):2321–2334, mar 2016. ISSN 0028-4793. doi: 10.1056/NEJMoa1602412. URL `https://doi.org/10.1056/NEJMoa1602412`.

[32] Shakira Brathwaite and R Loch Macdonald. Current management of delayed cerebral ischemia: update from results of recent clinical trials. *Transl. Stroke Res.*, 5(2):207–226, apr 2014. ISSN 1868-601X (Electronic). doi: 10.1007/s12975-013-0316-8.

[33] Gaia Brezzo, Julie Simpson, Kamar E Ameen-Ali, Jason Berwick, and Chris Martin. Acute effects of systemic inflammation upon the neuro-glial-vascular unit and cerebrovascular function. *Brain, Behav. Immun. - Heal.*, 5:100074, 2020. ISSN 2666-3546. doi: https://doi.org/10.1016/j.bbih.2020.100074. URL `http://www.sciencedirect.com/science/article/pii/S2666354620300399`.

[34] Lindsey M Brier, Eric C Landsness, Abraham Z Snyder, Patrick W Wright, Grant A Baxter, Adam Q Bauer, Jin-Moo Lee, and Joseph P Culver. Separability of calcium slow waves and functional connectivity during wake, sleep, and anesthesia. *Neurophotonics*, 6(3):35002, jul 2019. ISSN 2329-423X. doi: 10.1117/1.NPh.6.3.035002. URL `https://pubmed.ncbi.nlm.nih.gov/31930154https://www.ncbi.nlm.nih.gov/pmc/articles/PMC6952529/`.

[35] Matthew R Brier, Jewell B Thomas, Anne M Fagan, Jason Hassenstab, David M

Holtzman, Tammie L Benzinger, John C Morris, and Beau M Ances. Functional connectivity and graph theory in preclinical Alzheimer's disease. *Neurobiol. Aging*, 35(4):757–768, apr 2014. ISSN 1558-1497. doi: 10.1016/j.neurobiolaging.2013.10.081. URL https://pubmed.ncbi.nlm.nih.gov/24216223https://www.ncbi.nlm.nih.gov/pmc/articles/PMC3880636/.

[36] Matthew R Brier, Gregory S Day, Abraham Z Snyder, Aaron B Tanenbaum, and Beau M Ances. N-methyl-D-aspartate receptor encephalitis mediates loss of intrinsic activity measured by functional MRI. *J. Neurol.*, 263(6):1083–1091, jun 2016. ISSN 1432-1459 (Electronic). doi: 10.1007/s00415-016-8083-6.

[37] J P Broderick, T G Brott, J E Duldner, T Tomsick, and A Leach. Initial and recurrent bleeding are the major causes of death following subarachnoid hemorrhage. *Stroke*, 25 (7):1342–1347, jul 1994. doi: 10.1161/01.STR.25.7.1342. URL https://doi.org/10.1161/01.STR.25.7.1342.

[38] Emma J Bubb, Lisa Kinnavane, and John P Aggleton. Hippocampal - diencephalic - cingulate networks for memory and emotion: An anatomical guide. *Brain Neurosci. Adv.*, 1(1):2398212817723443, aug 2017. ISSN 2398-2128. doi: 10.1177/2398212817723443. URL https://pubmed.ncbi.nlm.nih.gov/28944298https://www.ncbi.nlm.nih.gov/pmc/articles/PMC5608081/.

[39] Sandra Buitrago, Thomas E Martin, Joanne Tetens-Woodring, Alan Belicha-Villanueva, and Gregory E Wilding. Safety and efficacy of various combinations of injectable anesthetics in BALB/c mice. *J. Am. Assoc. Lab. Anim. Sci.*, 47(1):11–17, 2008. URL https://www.ncbi.nlm.nih.gov/pubmed/18210992https://www.ncbi.nlm.nih.gov/pmc/articles/PMC2652618/.

[40] Ed Bullmore, Jalal Fadili, Voichita Maxim, Levent Şendur, Brandon Whitcher,

John Suckling, Brammer Michael, and Michael Breakspear. Wavelets and functional magnetic resonance imaging of the human brain. *Neuroimage*, 23:S234–S249, 2004. ISSN 1053-8119. doi: https://doi.org/10.1016/j.neuroimage.2004.07.012. URL http://www.sciencedirect.com/science/article/pii/S1053811904003775.

[41] Jonathan R Bumstead, Jasmine J Park, Isaac A Rosen, Andrew W Kraft, Patrick W Wright, Matthew D Reisman, Daniel C Côté, and Joseph P Culver. Designing a large field-of-view two-photon microscope using optical invariant analysis. *Neurophotonics*, 5(2):25001, apr 2018. ISSN 2329-423X (Print). doi: 10.1117/1.NPh.5.2.025001.

[42] Renaud Burrer, Michael J Buchmeier, Tom Wolfe, Joey P C Ting, Ralph Feuer, Antonio Iglesias, and Matthias G von Herrath. Exacerbated pathology of viral encephalitis in mice with central nervous system-specific autoantibodies. *Am. J. Pathol.*, 170(2):557–566, feb 2007. ISSN 0002-9440. doi: 10.2353/ajpath.2007.060893. URL https://pubmed.ncbi.nlm.nih.gov/17255324https://www.ncbi.nlm.nih.gov/pmc/articles/PMC1851853/.

[43] Van-Mai Cao-Lormeau, Alexandre Blake, Sandrine Mons, Stéphane Lastère, Claudine Roche, Jessica Vanhomwegen, Timothée Dub, Laure Baudouin, Anita Teissier, Philippe Larre, Anne-Laure Vial, Christophe Decam, Valérie Choumet, Susan K Halstead, Hugh J Willison, Lucile Musset, Jean-Claude Manuguerra, Philippe Despres, Emmanuel Fournier, Henri-Pierre Mallet, Didier Musso, Arnaud Fontanet, Jean Neil, and Frédéric Ghawché. Guillain-Barré Syndrome outbreak associated with Zika virus infection in French Polynesia: a case-control study. *Lancet*, 387(10027): 1531–1539, apr 2016. ISSN 0140-6736. doi: 10.1016/S0140-6736(16)00562-6. URL https://doi.org/10.1016/S0140-6736(16)00562-6.

[44] Guillaume Carteaux, Marianne Maquart, Alexandre Bedet, Damien Contou, Pierre Brugières, Slim Fourati, Laurent Cleret de Langavant, Thomas de Broucker, Christian

Brun-Buisson, Isabelle Leparc-Goffart, and Armand Mekontso Dessap. Zika Virus Associated with Meningoencephalitis. *N. Engl. J. Med.*, 374(16):1595–1596, mar 2016. ISSN 0028-4793. doi: 10.1056/NEJMc1602964. URL https://doi.org/10.1056/NEJMc1602964.

[45] Miryam Nava Catorce and Goar Gevorkian. LPS-induced Murine Neuroinflammation Model: Main Features and Suitability for Pre-clinical Assessment of Nutraceuticals. *Curr. Neuropharmacol.*, 14(2):155–164, 2016. ISSN 1875-6190. doi: 10.2174/1570159x14666151204122017. URL https://pubmed.ncbi.nlm.nih.gov/26639457https://www.ncbi.nlm.nih.gov/pmc/articles/PMC4825946/.

[46] Allen W Chan, Majid H Mohajerani, Jeffrey M LeDue, Yu Tian Wang, and Timothy H Murphy. Mesoscale infraslow spontaneous membrane potential fluctuations recapitulate high-frequency activity cortical motifs. *Nat. Commun.*, 6:7738, 2015. doi: 10.1038/ncomms8738https://www.nature.com/articles/ncomms8738#supplementary-information. URL http://dx.doi.org/10.1038/ncomms8738.

[47] Sylvain Chauvette, Sylvain Crochet, Maxim Volgushev, and Igor Timofeev. Properties of slow oscillation during slow-wave sleep and anesthesia in cats. *J. Neurosci.*, 31 (42):14998–15008, 2011. doi: 10.1523/JNEUROSCI.2339-11.2011. URL http://www.ncbi.nlm.nih.gov/pmc/articles/PMC3209581/.

[48] Jing Chen, Jessica B Buchanan, Nathan L Sparkman, Jonathan P Godbout, Gregory G Freund, and Rodney W Johnson. Neuroinflammation and disruption in working memory in aged mice after acute stimulation of the peripheral innate immune system. *Brain. Behav. Immun.*, 22(3):301–311, mar 2008. ISSN 1090-2139 (Electronic). doi: 10.1016/j.bbi.2007.08.014.

[49] Tsai-Wen Chen, Trevor J Wardill, Yi Sun, Stefan R Pulver, Sabine L Renninger, Amy

Baohan, Eric R Schreiter, Rex A Kerr, Michael B Orger, Vivek Jayaraman, Loren L Looger, Karel Svoboda, and Douglas S Kim. Ultrasensitive fluorescent proteins for imaging neuronal activity. *Nature*, 499(7458):295–300, jul 2013. ISSN 1476-4687. doi: 10.1038/nature12354. URL https://pubmed.ncbi.nlm.nih.gov/23868258https://www.ncbi.nlm.nih.gov/pmc/articles/PMC3777791/.

[50] Xifan Chen, Chuanjun Tong, Zhe Han, Kaiwei Zhang, Binshi Bo, Yanqiu Feng, and Zhifeng Liang. Sensory evoked fMRI paradigms in awake mice. *Neuroimage*, 204:116242, 2020. ISSN 1053-8119. doi: https://doi.org/10.1016/j.neuroimage.2019.116242. URL https://www.sciencedirect.com/science/article/pii/S105381191930833X.

[51] Zhen Chen, I-Chen Peng, Xiaopei Cui, Yi-Shuan Li, Shu Chien, and John Y-J. Shyy. Shear stress, SIRT1, and vascular homeostasis. *Proc. Natl. Acad. Sci.*, 107(22):10268 LP – 10273, jun 2010. doi: 10.1073/pnas.1003833107. URL http://www.pnas.org/content/107/22/10268.abstract.

[52] Soo-Hee Choi, Hyeongrae Lee, Tae-Sub Chung, Kyung-Min Park, Young-Chul Jung, Sun I Kim, and Jae-Jin Kim. Neural network functional connectivity during and after an episode of delirium. *Am. J. Psychiatry*, 169(5):498–507, may 2012. ISSN 1535-7228 (Electronic). doi: 10.1176/appi.ajp.2012.11060976.

[53] C Chu, D A Handwerker, P A Bandettini, and J Ashburner. Measuring the Consistency of Global Functional Connectivity Using Kernel Regression Methods. In *2011 Int. Work. Pattern Recognit. NeuroImaging*, pages 41–44, 2011. ISBN VO -. doi: 10.1109/PRNI.2011.11.

[54] Shannon Copeland, H Shaw Warren, Stephen F Lowry, Steve E Calvano, Daniel Remick, Inflammation Investigators, and the Host Response to Injury. Acute in-

flammatory response to endotoxin in mice and humans. *Clin. Diagn. Lab. Immunol.*, 12(1):60–67, jan 2005. ISSN 1071-412X. doi: 10.1128/CDLI.12.1.60-67. 2005. URL https://pubmed.ncbi.nlm.nih.gov/15642986https://www.ncbi.nlm.nih.gov/pmc/articles/PMC540200/.

[55] Kevin A Corcoran, Michael D Donnan, Natalie C Tronson, Yomayra F Guzmán, Can Gao, Vladimir Jovasevic, Anita L Guedea, and Jelena Radulovic. NMDA receptors in retrosplenial cortex are necessary for retrieval of recent and remote context fear memory. *J. Neurosci.*, 31(32):11655–11659, aug 2011. ISSN 1529-2401 (Electronic). doi: 10.1523/JNEUROSCI.2107-11.2011.

[56] C Correa-Sales, B C Rabin, and M Maze. A hypnotic response to dexmedetomidine, an alpha 2 agonist, is mediated in the locus coeruleus in rats. *Anesthesiology*, 76(6): 948–952, jun 1992. ISSN 0003-3022 (Print). doi: 10.1097/00000542-199206000-00013.

[57] R Cameron Craddock, Michael P Milham, and Stephen M LaConte. Predicting intrinsic brain activity. *Neuroimage*, 82:127–136, 2013. ISSN 1053-8119. doi: https://doi.org/10.1016/j.neuroimage.2013.05.072. URL http://www.sciencedirect.com/science/article/pii/S1053811913005727.

[58] Andrew Crofts, Michael E Kelly, and Claire L Gibson. Imaging Functional Recovery Following Ischemic Stroke: Clinical and Preclinical fMRI Studies. *J. Neuroimaging*, 30(1):5–14, jan 2020. ISSN 1552-6569. doi: 10.1111/jon.12668. URL https://pubmed.ncbi.nlm.nih.gov/31608550https://www.ncbi.nlm.nih.gov/pmc/articles/PMC7003729/.

[59] Deborah J Culley, Mary Snayd, Mark G Baxter, Zhongcong Xie, In Ho Lee, James Rudolph, Sharon K Inouye, Edward R Marcantonio, and Gregory Crosby. Systemic Inflammation Impairs Attention and Cognitive Flexibility but Not Associa-

tive Learning in Aged Rats: Possible Implications for Delirium , 2014. URL https://www.frontiersin.org/article/10.3389/fnagi.2014.00107.

[60] Colm Cunningham. Microglia and neurodegeneration: The role of systemic inflammation. *Glia*, 61(1):71–90, jan 2013. ISSN 0894-1491. doi: https://doi.org/10.1002/glia.22350. URL https://doi.org/10.1002/glia.22350.

[61] Hod Dana, Tsai-Wen Chen, Amy Hu, Brenda C Shields, Caiying Guo, Loren L Looger, Douglas S Kim, and Karel Svoboda. Thy1-GCaMP6 Transgenic Mice for Neuronal Population Imaging In Vivo. *PLoS One*, 9(9):e108697, sep 2014. URL https://doi.org/10.1371/journal.pone.0108697.

[62] Thien Thanh Dang-Vu, Martin Desseilles, Steven Laureys, Christian Degueldre, Fabien Perrin, Christophe Phillips, Pierre Maquet, and Philippe Peigneux. Cerebral correlates of delta waves during non-REM sleep revisited. *Neuroimage*, 28(1):14–21, 2005. ISSN 1053-8119. doi: https://doi.org/10.1016/j.neuroimage.2005.05.028. URL http://www.sciencedirect.com/science/article/pii/S1053811905003800.

[63] Barbara D'Angelo, Carlo Astarita, Silvia Boffo, Mina Massaro-Giordano, Carmelina Antonella Ianuzzi, Antonella Caporaso, Marcella Macaluso, and Antonio Giordano. LPS-induced inflammatory response triggers cell cycle reactivation in murine neuronal cells through retinoblastoma proteins induction. *Cell Cycle*, 16(24):2330–2336, 2017. ISSN 1551-4005. doi: 10.1080/15384101.2017.1363943. URL https://pubmed.ncbi.nlm.nih.gov/28820328https://www.ncbi.nlm.nih.gov/pmc/articles/PMC5788440/.

[64] Daniel H J Davis, Graciela Muniz Terrera, Hannah Keage, Terhi Rahkonen, Minna Oinas, Fiona E Matthews, Colm Cunningham, Tuomo Polvikoski, Raimo Sulkava, Alasdair M J MacLullich, and Carol Brayne. Delirium is a strong risk factor for

dementia in the oldest-old: a population-based cohort study. *Brain*, 135(Pt 9):2809–2816, sep 2012. ISSN 1460-2156 (Electronic). doi: 10.1093/brain/aws190.

[65] S A Deadwyler, T C Foster, and R E Hampson. Processing of sensory information in the hippocampus. *CRC Crit. Rev. Clin. Neurobiol.*, 2(4):335–355, 1987. ISSN 0742-941X (Print).

[66] D Della-Morte, K R Dave, R A DeFazio, Y C Bao, A P Raval, and M A Perez-Pinzon. Resveratrol pretreatment protects rat brain from cerebral ischemic damage via a sirtuin 1-uncoupling protein 2 pathway. *Neuroscience*, 159(3):993–1002, mar 2009. ISSN 1873-7544 (Electronic). doi: 10.1016/j.neuroscience.2009.01.017.

[67] Maria Grazia Di Bono and Marco Zorzi. Decoding Cognitive States from fMRI Data Using Support Vector Regression. *PsychNology J.*, 6:189–201, jan 2008.

[68] Murat Digicaylioglu and Stuart A Lipton. Erythropoietin-mediated neuroprotection involves cross-talk between Jak2 and NF-κB signalling cascades. *Nature*, 412(6847): 641–647, 2001. ISSN 1476-4687. doi: 10.1038/35088074. URL `https://doi.org/10.1038/35088074`.

[69] Ulrich Dirnagl, Kyra Becker, and Andreas Meisel. Preconditioning and tolerance against cerebral ischaemia: from experimental strategies to clinical use. *Lancet. Neurol.*, 8(4):398–412, apr 2009. ISSN 1474-4422 (Print). doi: 10.1016/S1474-4422(09)70054-7.

[70] F Domoki, J V Perciaccante, R Veltkamp, F Bari, and D W Busija. Mitochondrial potassium channel opener diazoxide preserves neuronal-vascular function after cerebral ischemia in newborn pigs. *Stroke*, 30(12):2713–2719, dec 1999. ISSN 0039-2499 (Print). doi: 10.1161/01.str.30.12.2713.

[71] Andrew K Dunn, Anna Devor, Hayrunnisa Bolay, Mark L Andermann, Michael A Moskowitz, Anders M Dale, and David A Boas. Simultaneous imaging of total cerebral hemoglobin concentration, oxygenation, and blood flow during functional activation. *Opt. Lett.*, 28(1):28–30, jan 2003. ISSN 0146-9592 (Print). doi: 10.1364/ol.28.000028.

[72] Andrew K Dunn, Anna Devor, Anders M Dale, and David A Boas. Spatial extent of oxygen metabolism and hemodynamic changes during functional activation of the rat somatosensory cortex. *Neuroimage*, 27(2):279–290, aug 2005. ISSN 1053-8119 (Print). doi: 10.1016/j.neuroimage.2005.04.024.

[73] Adam T Eggebrecht, Brian R White, Silvina L Ferradal, Chunxiao Chen, Yuxuan Zhan, Abraham Z Snyder, Hamid Dehghani, and Joseph P Culver. A quantitative spatial comparison of high-density diffuse optical tomography and fMRI cortical mapping. *Neuroimage*, 61(4):1120–1128, 2012. doi: https://doi.org/10.1016/j.neuroimage.2012.01.124. URL `http://www.sciencedirect.com/science/article/pii/S1053811912001516`.

[74] Timothy M Ellmore, Fiona Rohlffs, and Faraz Khursheed. FMRI of working memory impairment after recovery from subarachnoid hemorrhage. *Front. Neurol.*, 4:179, nov 2013. ISSN 1664-2295. doi: 10.3389/fneur.2013.00179. URL `https://pubmed.ncbi.nlm.nih.gov/24223572https://www.ncbi.nlm.nih.gov/pmc/articles/PMC3818578/`.

[75] Isabelle Ferezou, Sonia Bolea, and Carl C H Petersen. Visualizing the Cortical Representation of Whisker Touch: Voltage-Sensitive Dye Imaging in Freely Moving Mice. *Neuron*, 50(4):617–629, 2006. doi: https://doi.org/10.1016/j.neuron.2006.03.043. URL `http://www.sciencedirect.com/science/article/pii/S0896627306002704`.

[76] Bruce Fischl. FreeSurfer. *Neuroimage*, 62(2):774–781, aug 2012. ISSN 1095-9572.

doi: 10.1016/j.neuroimage.2012.01.021. URL https://pubmed.ncbi.nlm.nih.gov/22248573https://www.ncbi.nlm.nih.gov/pmc/articles/PMC3685476/.

[77] C M Fisher, G H Roberson, and R G Ojemann. Cerebral vasospasm with ruptured saccular aneurysm–the clinical manifestations. *Neurosurgery*, 1(3):245–248, 1977. ISSN 0148-396X (Print). doi: 10.1227/00006123-197711000-00004.

[78] Tamara G Fong, Samir R Tulebaev, and Sharon K Inouye. Delirium in elderly adults: diagnosis, prevention and treatment. *Nat. Rev. Neurol.*, 5(4):210–220, apr 2009. ISSN 1759-4766 (Electronic). doi: 10.1038/nrneurol.2009.24.

[79] Tamara G Fong, Daniel Davis, Matthew E Growdon, Asha Albuquerque, and Sharon K Inouye. The interface between delirium and dementia in elderly adults. *Lancet. Neurol.*, 14(8):823–832, aug 2015. ISSN 1474-4465. doi: 10.1016/S1474-4422(15)00101-5. URL https://pubmed.ncbi.nlm.nih.gov/26139023https://www.ncbi.nlm.nih.gov/pmc/articles/PMC4535349/.

[80] Michael D Fox and Marcus E Raichle. Spontaneous fluctuations in brain activity observed with functional magnetic resonance imaging. *Nat. Rev. Neurosci.*, 8(9):700–711, 2007. ISSN 1471-0048. doi: 10.1038/nrn2201. URL https://doi.org/10.1038/nrn2201.

[81] Michael D Fox, Abraham Z Snyder, Justin L Vincent, Maurizio Corbetta, David C Van Essen, and Marcus E Raichle. The human brain is intrinsically organized into dynamic, anticorrelated functional networks. *Proc. Natl. Acad. Sci. U. S. A.*, 102(27):9673 LP – 9678, jul 2005. doi: 10.1073/pnas.0504136102. URL http://www.pnas.org/content/102/27/9673.abstract.

[82] Antonio Francioso, Paola Mastromarino, Alessandra Masci, Maria D'Erme, and Lu-

ciana Mosca. Chemistry, stability and bioavailability of resveratrol. *Med. Chem.*, 10(3): 237–245, may 2014. ISSN 1875-6638 (Electronic). doi: 10.2174/15734064113096660053.

[83] W J Freeman, L J Rogers, M D Holmes, and D L Silbergeld. Spatial spectral analysis of human electrocorticograms including the alpha and gamma bands. *J Neurosci Methods*, 95(2):111–121, 2000. URL `http://www.ncbi.nlm.nih.gov/pubmed/10752481`.

[84] Benjamin Friedrich, Frank Müller, Sergej Feiler, Karsten Schöller, and Nikolaus Plesnila. Experimental subarachnoid hemorrhage causes early and long-lasting microarterial constriction and microthrombosis: an in-vivo microscopy study. *J. Cereb. blood flow Metab. Off. J. Int. Soc. Cereb. Blood Flow Metab.*, 32(3):447–455, mar 2012. ISSN 1559-7016 (Electronic). doi: 10.1038/jcbfm.2011.154.

[85] Karl J Friston. Functional and effective connectivity in neuroimaging: A synthesis. *Hum. Brain Mapp.*, 2(1-2):56–78, jan 1994. ISSN 1065-9471. doi: 10.1002/hbm.460020107. URL `https://doi.org/10.1002/hbm.460020107`.

[86] Karl J Friston, Andrew P Holmes, and Keith J Worsley. How Many Subjects Constitute a Study? *Neuroimage*, 10(1):1–5, 1999. doi: https://doi.org/10.1006/nimg.1999.0439. URL `http://www.sciencedirect.com/science/article/pii/S1053811999904391`.

[87] Mutsumi Fujii, Kamil Duris, Orhan Altay, Yoshiteru Soejima, Prativa Sherchan, and John H Zhang. Inhibition of Rho kinase by hydroxyfasudil attenuates brain edema after subarachnoid hemorrhage in rats. *Neurochem. Int.*, 60(3):327–333, feb 2012. ISSN 1872-9754 (Electronic). doi: 10.1016/j.neuint.2011.12.014.

[88] Fei Gao, Zhiqiang Liu, Wei Ren, and Wen Jiang. Acute lipopolysaccharide exposure facilitates epileptiform activity via enhanced excitatory synaptic transmission and neuronal excitability in vitro. *Neuropsychiatr. Dis. Treat.*, 10:1489–1495, 2014.

doi: 10.2147/NDT.S65695. URL http://www.ncbi.nlm.nih.gov/pmc/articles/PMC4144925/.

[89] Charise Garber, Allison Soung, Lauren L Vollmer, Marlene Kanmogne, Aisling Last, Jasmine Brown, and Robyn S Klein. T cells promote microglia-mediated synaptic elimination and cognitive dysfunction during recovery from neuropathogenic flaviviruses. *Nat. Neurosci.*, 22(8):1276–1288, aug 2019. ISSN 1546-1726 (Electronic). doi: 10.1038/s41593-019-0427-y.

[90] Linda Geerligs, Cam-Can, and Richard N Henson. Functional connectivity and structural covariance between regions of interest can be measured more accurately using multivariate distance correlation. *Neuroimage*, 135:16–31, jul 2016. ISSN 1095-9572 (Electronic). doi: 10.1016/j.neuroimage.2016.04.047.

[91] Ralph Gertler, H Cleighton Brown, Donald H Mitchell, and Erin N Silvius. Dexmedetomidine: a novel sedative-analgesic agent. *Proc. (Bayl. Univ. Med. Cent).*, 14(1):13–21, 2001. URL http://www.ncbi.nlm.nih.gov/pmc/articles/PMC1291306/.

[92] Leila Ghanbari, Russell E Carter, Mathew L Rynes, Judith Dominguez, Gang Chen, Anant Naik, Jia Hu, Md Abdul Kader Sagar, Lenora Haltom, Nahom Mossazghi, Madelyn M Gray, Sarah L West, Kevin W Eliceiri, Timothy J Ebner, and Suhasa B Kodandaramaiah. Cortex-wide neural interfacing via transparent polymer skulls. *Nat. Commun.*, 10(1):1500, 2019. doi: 10.1038/s41467-019-09488-0. URL https://doi.org/10.1038/s41467-019-09488-0.

[93] Jeffrey M Gidday. Cerebral preconditioning and ischaemic tolerance. *Nat. Rev. Neurosci.*, 7(6):437–448, jun 2006. ISSN 1471-003X (Print). doi: 10.1038/nrn1927.

[94] Teneille E Gofton and G Bryan Young. Sepsis-associated encephalopathy. *Nat. Rev.*

Neurol., 8(10):557–566, 2012. ISSN 1759-4766. doi: 10.1038/nrneurol.2012.183. URL https://doi.org/10.1038/nrneurol.2012.183.

[95] Matthew J Gorman, Elizabeth A Caine, Konstantin Zaitsev, Matthew C Begley, James Weger-Lucarelli, Melissa B Uccellini, Shashank Tripathi, Juliet Morrison, Boyd L Yount, Kenneth H Dinnon 3rd, Claudia Rückert, Michael C Young, Zhe Zhu, Shelly J Robertson, Kristin L McNally, Jing Ye, Bin Cao, Indira U Mysorekar, Gregory D Ebel, Ralph S Baric, Sonja M Best, Maxim N Artyomov, Adolfo Garcia-Sastre, and Michael S Diamond. An Immunocompetent Mouse Model of Zika Virus Infection. *Cell Host Microbe*, 23(5):672–685.e6, may 2018. ISSN 1934-6069. doi: 10.1016/j.chom.2018.04.003. URL https://pubmed.ncbi.nlm.nih.gov/29746837https://www.ncbi.nlm.nih.gov/pmc/articles/PMC5953559/.

[96] C J Graf and D W Nibbelink. Cooperative study of intracranial aneurysms and subarachnoid hemorrhage. Report on a randomized treatment study. 3. Intracranial surgery. *Stroke*, 5(4):557–601, 1974. ISSN 0039-2499 (Print). doi: 10.1161/01.str.5.4.557.

[97] J Granerod, N W S Davies, W Mukonoweshuro, A Mehta, K Das, M Lim, T Solomon, S Biswas, L Rosella, D W G Brown, N S Crowcroft, and U K Public Health England Aetiology of Encephalitis Study Group. Neuroimaging in encephalitis: analysis of imaging findings and interobserver agreement. *Clin. Radiol.*, 71(10):1050–1058, oct 2016. ISSN 1365-229X. doi: 10.1016/j.crad.2016.03.015. URL https://pubmed.ncbi.nlm.nih.gov/27185323https://www.ncbi.nlm.nih.gov/pmc/articles/PMC5021199/.

[98] Roberta Grech, Tracey Cassar, Joseph Muscat, Kenneth P Camilleri, Simon G Fabri, Michalis Zervakis, Petros Xanthopoulos, Vangelis Sakkalis, and Bart Vanrumste. Review on solving the inverse problem in EEG source analysis. *J. Neuro-*

eng. Rehabil., 5(1):25, 2008. ISSN 1743-0003. doi: 10.1186/1743-0003-5-25. URL https://doi.org/10.1186/1743-0003-5-25.

[99] A Grinvald, E Lieke, R D Frostig, C D Gilbert, and T N Wiesel. Functional architecture of cortex revealed by optical imaging of intrinsic signals. *Nature*, 324(6095):361–364, nov 1986. ISSN 0028-0836 (Print). doi: 10.1038/324361a0.

[100] Alden L Gross, Richard N Jones, Daniel A Habtemariam, Tamara G Fong, Douglas Tommet, Lien Quach, Eva Schmitt, Liang Yap, and Sharon K Inouye. Delirium and Long-term Cognitive Trajectory Among Persons With Dementia. *Arch. Intern. Med.*, 172(17):1324–1331, sep 2012. ISSN 1538-3679. doi: 10.1001/archinternmed.2012.3203. URL https://pubmed.ncbi.nlm.nih.gov/23403619https://www.ncbi.nlm.nih.gov/pmc/articles/PMC3740440/.

[101] John F Guzowski, James J Knierim, and Edvard I Moser. Ensemble Dynamics of Hippocampal Regions CA3 and CA1. *Neuron*, 44(4):581–584, nov 2004. ISSN 0896-6273. doi: 10.1016/j.neuron.2004.11.003. URL https://doi.org/10.1016/j.neuron.2004.11.003.

[102] M L Hackett and C S Anderson. Health outcomes 1 year after subarachnoid hemorrhage: An international population-based study. The Australian Cooperative Research on Subarachnoid Hemorrhage Study Group. *Neurology*, 55(5):658–662, sep 2000. ISSN 0028-3878 (Print). doi: 10.1212/wnl.55.5.658.

[103] Jakob Hakon, Miriana Jlenia Quattromani, Carin Sjölund, Gregor Tomasevic, Leeanne Carey, Jin-Moo Lee, Karsten Ruscher, Tadeusz Wieloch, and Adam Q Bauer. Multisensory stimulation improves functional recovery and resting-state functional connectivity in the mouse brain after stroke. *NeuroImage Clin.*, 17:717–730, 2017. ISSN 2213-1582. doi: https://doi.org/10.1016/j.nicl.2017.11.022. URL https://www.ncbi.nlm.nih.

gov/pubmed/29264113https://www.ncbi.nlm.nih.gov/pmc/PMC5726755/https://www.sciencedirect.com/science/article/pii/S2213158217303029.

[104] Hyemin Han and Andrea L Glenn. Evaluating methods of correcting for multiple comparisons implemented in SPM12 in social neuroscience fMRI studies: an example from moral psychology. *Soc. Neurosci.*, 13(3):257–267, jun 2018. ISSN 1747-0927 (Electronic). doi: 10.1080/17470919.2017.1324521.

[105] Y. Harrison and J. A. Horne. Occurrence of 'microsleeps' during daytime sleep onset in normal subjects. *Electroencephalogr. Clin. Neurophysiol.*, 98(5):411–416, 1996.

[106] Mahlega S Hassanpour, Brian R White, Adam T Eggebrecht, Silvina L Ferradal, Abraham Z Snyder, and Joseph P Culver. Statistical analysis of high density diffuse optical tomography. *Neuroimage*, 85:104–116, 2014. ISSN 1053-8119. doi: https://doi.org/10.1016/j.neuroimage.2013.05.105. URL http://www.sciencedirect.com/science/article/pii/S1053811913006083.

[107] G M Hathout, R K Gopi, P Bandettini, and S S Gambhir. The lag of cerebral hemodynamics with rapidly alternating periodic stimulation: modeling for functional MRI. *Magn. Reson. Imaging*, 17(1):9–20, jan 1999. ISSN 0730-725X (Print). doi: 10.1016/s0730-725x(98)00150-7.

[108] Stefan Haufe, Frank Meinecke, Kai Görgen, Sven Dähne, John-Dylan Haynes, Benjamin Blankertz, and Felix Bießmann. On the interpretation of weight vectors of linear models in multivariate neuroimaging. *Neuroimage*, 87:96–110, feb 2014. ISSN 1095-9572 (Electronic). doi: 10.1016/j.neuroimage.2013.10.067.

[109] Emina Hayashida, Zheng Lung Ling, Thomas M Ashhurst, Barney Viengkhou, So Ri Jung, Pattama Songkhunawej, Phillip K West, Nicholas J C King, and Markus J

Hofer. Zika virus encephalitis in immunocompetent mice is dominated by innate immune cells and does not require T or B cells. *J. Neuroinflammation*, 16(1):177, 2019. ISSN 1742-2094. doi: 10.1186/s12974-019-1566-5. URL https://doi.org/10.1186/s12974-019-1566-5.

[110] John-Dylan Haynes and Geraint Rees. Decoding mental states from brain activity in humans. *Nat. Rev. Neurosci.*, 7(7):523–534, 2006. ISSN 1471-0048. doi: 10.1038/nrn1931. URL https://doi.org/10.1038/nrn1931.

[111] B J He. Scale-free brain activity: past, present, and future. *Trends Cogn Sci*, 18 (9):480–487, 2014. doi: 10.1016/j.tics.2014.04.003. URL http://www.ncbi.nlm.nih.gov/pubmed/24788139.

[112] Ulrich Hemmeter, Roland Bischof, Martin Hatzinger, Erich Seifritz, and Edith Holsboer-Trachsler. Microsleep during Partial Sleep Deprivation in Depression. *Biol. Psychiatry*, 43(11):829–839, 1998. doi: https://doi.org/10.1016/S0006-3223(97)00297-7. URL http://www.sciencedirect.com/science/article/pii/S0006322397002977.

[113] Elizabeth M C Hillman. Coupling mechanism and significance of the BOLD signal: a status report. *Annu. Rev. Neurosci.*, 37:161–181, 2014. ISSN 1545-4126. doi: 10.1146/annurev-neuro-071013-014111. URL https://pubmed.ncbi.nlm.nih.gov/25032494https://www.ncbi.nlm.nih.gov/pmc/articles/PMC4147398/.

[114] Tuija Hiltunen, Jussi Kantola, Ahmed Abou Elseoud, Pasi Lepola, Kalervo Suominen, Tuomo Starck, Juha Nikkinen, Jukka Remes, Osmo Tervonen, Satu Palva, Vesa Kiviniemi, and J Matias Palva. Infra-Slow EEG Fluctuations Are Correlated with Resting-State Network Dynamics in fMRI. *J. Neurosci.*, 34(2):356, 2014. doi:

10.1523/JNEUROSCI.0276-13.2014. URL http://www.jneurosci.org/content/34/2/356.abstract.

[115] C J Honey, O Sporns, L Cammoun, X Gigandet, J P Thiran, R Meuli, and P Hagmann. Predicting human resting-state functional connectivity from structural connectivity. *Proc Natl Acad Sci U S A*, 106(6):2035–2040, 2009. doi: 10.1073/pnas.0811168106. URL http://www.ncbi.nlm.nih.gov/pubmed/19188601.

[116] Inge C M Hoogland, Carin Houbolt, David J van Westerloo, Willem A van Gool, and Diederik van de Beek. Systemic inflammation and microglial activation: systematic review of animal experiments. *J. Neuroinflammation*, 12:114, jun 2015. ISSN 1742-2094 (Electronic). doi: 10.1186/s12974-015-0332-6.

[117] S G Horovitz, A R Braun, W S Carr, D Picchioni, T J Balkin, M Fukunaga, and J H Duyn. Decoupling of the brain's default mode network during deep sleep. *Proc Natl Acad Sci U S A*, 106(27):11376–11381, 2009. doi: 10.1073/pnas.0901435106. URL http://www.ncbi.nlm.nih.gov/pubmed/19549821.

[118] Stuart W Hughes, Magor L Lorincz, H Rheinallt Parri, and Vincenzo Crunelli. Infraslow (<0.1 Hz) oscillations in thalamic relay nuclei basic mechanisms and significance to health and disease states. *Prog. Brain Res.*, 193:145–162, 2011. ISSN 1875-7855. doi: 10.1016/B978-0-444-53839-0.00010-7. URL https://pubmed.ncbi.nlm.nih.gov/21854961https://www.ncbi.nlm.nih.gov/pmc/articles/PMC3173874/.

[119] S K Inouye. Predisposing and precipitating factors for delirium in hospitalized older patients. *Dement. Geriatr. Cogn. Disord.*, 10(5):393–400, 1999. ISSN 1420-8008 (Print). doi: 10.1159/000017177.

[120] Jisu Elsa Jacob, Gopakumar Kuttappan Nair, Thomas Iype, and Ajith Cherian. Diagnosis of Encephalopathy Based on Energies of EEG Subbands Using Discrete

Wavelet Transform and Support Vector Machine. *Neurol. Res. Int.*, 2018:1613456, 2018. ISSN 2090-1852. doi: 10.1155/2018/1613456. URL https://doi.org/10.1155/2018/1613456.

[121] Sae Im Jeong, Jin A Shin, Sunghee Cho, Hye Won Kim, Ji Yoon Lee, Jihee Lee Kang, and Eun-Mi Park. Resveratrol attenuates peripheral and brain inflammation and reduces ischemic brain injury in aged female mice. *Neurobiol. Aging*, 44:74–84, aug 2016. ISSN 1558-1497 (Electronic). doi: 10.1016/j.neurobiolaging.2016.04.007.

[122] H Johansen-Berg. Human connectomics - what will the future demand? *Neuroimage*, 80:541–544, 2013. doi: 10.1016/j.neuroimage.2013.05.082. URL http://www.ncbi.nlm.nih.gov/pubmed/23727322.

[123] Y E Ju, B P Lucey, and D M Holtzman. Sleep and Alzheimer disease pathology–a bidirectional relationship. *Nat Rev Neurol*, 10(2):115–119, 2014. doi: 10.1038/nrneurol.2013.269. URL https://www.ncbi.nlm.nih.gov/pubmed/24366271.

[124] Yo-El S. Ju, Brendan P. Lucey, and David M. Holtzman. Sleep and Alzheimer disease pathology—a bidirectional relationship. *Nat. Rev. Neurol.*, 10(2):115, 2013. doi: 10.1038/nrneurol.2013.269. URL https://doi.org/10.1038/nrneurol.2013.269.

[125] Kalabalik Julie, Brunetti Luigi, El-Srougy Radwa, Julie Kalabalik, Luigi Brunetti, and Radwa El-Srougy. Intensive Care Unit Delirium: A Review of the Literature. *J. Pharm. Pract.*, 27(2):195–207, apr 2013. ISSN 1531-1937 (Electronic). doi: 10.1177/0897190013513804. URL https://doi.org/10.1177/0897190013513804.

[126] Thorsten Kahnt, Soyoung Q Park, John-Dylan Haynes, and Philippe N Tobler. Disentangling neural representations of value and salience in the human brain. *Proc. Natl. Acad. Sci.*, 111(13):5000 LP – 5005, apr 2014. doi: 10.1073/pnas.1320189111. URL http://www.pnas.org/content/111/13/5000.abstract.

[127] Julie Kalabalik, Luigi Brunetti, and Radwa El-Srougy. Intensive care unit delirium: a review of the literature. *J. Pharm. Pract.*, 27(2):195–207, apr 2014. ISSN 1531-1937 (Electronic). doi: 10.1177/0897190013513804.

[128] Valery A Kalatsky and Michael P Stryker. New paradigm for optical imaging: temporally encoded maps of intrinsic signal. *Neuron*, 38(4):529–545, may 2003. ISSN 0896-6273 (Print). doi: 10.1016/s0896-6273(03)00286-1.

[129] Raymond P Kesner, Paul E Gilbert, and Gene V Wallenstein. Testing neural network models of memory with behavioral experiments. *Curr. Opin. Neurobiol.*, 10(2):260–265, 2000. ISSN 0959-4388. doi: https://doi.org/10.1016/S0959-4388(00)00067-2. URL http://www.sciencedirect.com/science/article/pii/S0959438800000672.

[130] Tony Hyun Kim, Yanping Zhang, Jérôme Lecoq, Juergen C Jung, Jane Li, Hongkui Zeng, Cristopher M Niell, and Mark J Schnitzer. Long-Term Optical Access to an Estimated One Million Neurons in the Live Mouse Cortex. *Cell Rep.*, 17(12):3385–3394, 2016. ISSN 2211-1247. doi: https://doi.org/10.1016/j.celrep.2016.12.004. URL https://www.sciencedirect.com/science/article/pii/S221112471631676X.

[131] J T Jr King. Epidemiology of aneurysmal subarachnoid hemorrhage. *Neuroimaging Clin. N. Am.*, 7(4):659–668, nov 1997. ISSN 1052-5149 (Print).

[132] Elke Kooijman, Cora H Nijboer, Cindy T J van Velthoven, Annemieke Kavelaars, Jozef Kesecioglu, and Cobi J Heijnen. The rodent endovascular puncture model of subarachnoid hemorrhage: mechanisms of brain damage and therapeutic strategies. *J. Neuroinflammation*, 11(1):2, 2014. ISSN 1742-2094. doi: 10.1186/1742-2094-11-2. URL https://doi.org/10.1186/1742-2094-11-2.

[133] Andrew W Kraft, Adam Q Bauer, Joseph P Culver, and Jin-Moo Lee. Sensory deprivation after focal ischemia in mice accelerates brain remapping and im-

proves functional recovery through Arc-dependent synaptic plasticity. *Sci. Transl. Med.*, 10(426):eaag1328, jan 2018. doi: 10.1126/scitranslmed.aag1328. URL http://stm.sciencemag.org/content/10/426/eaag1328.abstract.

[134] Michael Krumin, Julie J Lee, Kenneth D Harris, and Matteo Carandini. Decision and navigation in mouse parietal cortex. *Elife*, 7:e42583, 2018. ISSN 2050-084X. doi: 10.7554/eLife.42583. URL https://doi.org/10.7554/eLife.42583.

[135] Elke Kuypers, Reint K Jellema, Daan R M G Ophelders, Jeroen Dudink, Maria Nikiforou, Tim G A M Wolfs, Ilias Nitsos, J Jane Pillow, Graeme R Polglase, Matthew W Kemp, Masatoshi Saito, John P Newnham, Alan H Jobe, Suhas G Kallapur, and Boris W Kramer. Effects of intra-amniotic lipopolysaccharide and maternal betamethasone on brain inflammation in fetal sheep. *PLoS One*, 8(12):e81644–e81644, dec 2013. ISSN 1932-6203. doi: 10.1371/journal.pone.0081644. URL https://pubmed.ncbi.nlm.nih.gov/24358119https://www.ncbi.nlm.nih.gov/pmc/articles/PMC3866104/.

[136] Linda J. Larson-Prior, John M. Zempel, Tracy S. Nolan, Fred W. Prior, Abraham Z. Snyder, and Marcus E. Raichle. Cortical network functional connectivity in the descent to sleep. *Proc. Natl. Acad. Sci.*, 106(11):4489, 2009. ISSN 0027-8424. doi: 10.1073/pnas.0900924106. URL http://www.pnas.org/cgi/doi/10.1073/pnas.0900924106http://www.pnas.org/content/106/11/4489.abstract.

[137] Timothy O Laumann, Evan M Gordon, Babatunde Adeyemo, Abraham Z Snyder, Sung Jun Joo, Mei-Yen Chen, Adrian W Gilmore, Kathleen B McDermott, Steven M Nelson, Nico U F Dosenbach, Bradley L Schlaggar, Jeanette A Mumford, Russell A Poldrack, and Steven E Petersen. Functional System and Areal Organization of a Highly Sampled Individual Human Brain. *Neuron*, 87(3):657–670, aug 2015. ISSN

1097-4199. doi: 10.1016/j.neuron.2015.06.037. URL https://pubmed.ncbi.nlm.nih.gov/26212711https://www.ncbi.nlm.nih.gov/pmc/articles/PMC4642864/.

[138] Jin-Yul Lee, Oren Sagher, Richard Keep, Ya Hua, and Guohua Xi. Comparison of experimental rat models of early brain injury after subarachnoid hemorrhage. *Neurosurgery*, 65(2):331–43; discussion 343, aug 2009. ISSN 1524-4040 (Electronic). doi: 10.1227/01.NEU.0000345649.78556.26.

[139] Ed S Lein, Michael J Hawrylycz, Nancy Ao, Mikael Ayres, Amy Bensinger, Amy Bernard, Andrew F Boe, Mark S Boguski, Kevin S Brockway, Emi J Byrnes, Lin Chen, Li Chen, Tsuey-Ming Chen, Mei Chi Chin, Jimmy Chong, Brian E Crook, Aneta Czaplinska, Chinh N Dang, Suvro Datta, Nick R Dee, Aimee L Desaki, Tsega Desta, Ellen Diep, Tim A Dolbeare, Matthew J Donelan, Hong-Wei Dong, Jennifer G Dougherty, Ben J Duncan, Amanda J Ebbert, Gregor Eichele, Lili K Estin, Casey Faber, Benjamin A Facer, Rick Fields, Shanna R Fischer, Tim P Fliss, Cliff Frensley, Sabrina N Gates, Katie J Glattfelder, Kevin R Halverson, Matthew R Hart, John G Hohmann, Maureen P Howell, Darren P Jeung, Rebecca A Johnson, Patrick T Karr, Reena Kawal, Jolene M Kidney, Rachel H Knapik, Chihchau L Kuan, James H Lake, Annabel R Laramee, Kirk D Larsen, Christopher Lau, Tracy A Lemon, Agnes J Liang, Ying Liu, Lon T Luong, Jesse Michaels, Judith J Morgan, Rebecca J Morgan, Marty T Mortrud, Nerick F Mosqueda, Lydia L Ng, Randy Ng, Geralyn J Orta, Caroline C Overly, Tu H Pak, Sheana E Parry, Sayan D Pathak, Owen C Pearson, Ralph B Puchalski, Zackery L Riley, Hannah R Rockett, Stephen A Rowland, Joshua J Royall, Marcos J Ruiz, Nadia R Sarno, Katherine Schaffnit, Nadiya V Shapovalova, Taz Sivisay, Clifford R Slaughterbeck, Simon C Smith, Kimberly A Smith, Bryan I Smith, Andy J Sodt, Nick N Stewart, Kenda-Ruth Stumpf, Susan M Sunkin, Madhavi Sutram, Angelene Tam, Carey D Teemer, Christina Thaller, Carol L Thompson, Lee R Varnam,

Axel Visel, Ray M Whitlock, Paul E Wohnoutka, Crissa K Wolkey, Victoria Y Wong, Matthew Wood, Murat B Yaylaoglu, Rob C Young, Brian L Youngstrom, Xu Feng Yuan, Bin Zhang, Theresa A Zwingman, and Allan R Jones. Genome-wide atlas of gene expression in the adult mouse brain. *Nature*, 445(7124):168–176, 2007. ISSN 1476-4687. doi: 10.1038/nature05453. URL https://doi.org/10.1038/nature05453.

[140] Gábor Lenzsér, Béla Kis, Ferenc Bari, and David W Busija. Diazoxide preconditioning attenuates global cerebral ischemia-induced blood-brain barrier permeability. *Brain Res.*, 1051(1-2):72–80, jul 2005. ISSN 0006-8993 (Print). doi: 10.1016/j.brainres.2005.05.064.

[141] Jacqueline M Leung, Laura P Sands, Stacey Newman, Gabriela Meckler, Yimeng Xie, Caryl Gay, and Kathryn Lee. Preoperative Sleep Disruption and Postoperative Delirium. *J. Clin. Sleep Med.*, 11(8):907–913, 2015. doi: 10.5664/jcsm.4944. URL http://www.ncbi.nlm.nih.gov/pmc/articles/PMC4513268/.

[142] Daniel Levenstein, György Buzsáki, and John Rinzel. NREM sleep in the rodent neocortex and hippocampus reflects excitable dynamics. *Nat. Commun.*, 10(1):2478, 2019. ISSN 2041-1723. doi: 10.1038/s41467-019-10327-5. URL https://doi.org/10.1038/s41467-019-10327-5.

[143] Chao Li, Yuanqi Mai, Mengshi Dong, Yi Yin, Kelei Hua, Shishun Fu, Yunfan Wu, and Guihua Jiang. Multivariate Pattern Classification of Primary Insomnia Using Three Types of Functional Connectivity Features , 2019. URL https://www.frontiersin.org/article/10.3389/fneur.2019.01037.

[144] Yun-Xia Li, Su-Ju Ding, Lin Xiao, Wei Guo, and Qing Zhan. Desferoxamine preconditioning protects against cerebral ischemia in rats by inducing expressions of hypoxia

inducible factor 1 alpha and erythropoietin. *Neurosci. Bull.*, 24(2):89–95, apr 2008. ISSN 1673-7067 (Print). doi: 10.1007/s12264-008-0089-3.

[145] Fan Liao, Yukiko Hori, Eloise Hudry, Adam Q Bauer, Hong Jiang, Thomas E Mahan, Katheryn B Lefton, Tony J Zhang, Joshua T Dearborn, Jungsu Kim, Joseph P Culver, Rebecca Betensky, David F Wozniak, Bradley T Hyman, and David M Holtzman. Anti-ApoE antibody given after plaque onset decreases Aβ accumulation and improves brain function in a mouse model of Aβ amyloidosis. *J. Neurosci.*, 34 (21):7281–7292, may 2014. ISSN 1529-2401. doi: 10.1523/JNEUROSCI.0646-14.2014. URL https://pubmed.ncbi.nlm.nih.gov/24849360https://www.ncbi.nlm.nih.gov/pmc/articles/PMC4028501/.

[146] Miranda M Lim, Jason R Gerstner, and David M Holtzman. The sleep–wake cycle and Alzheimer's disease: what do we know? *Neurodegener. Dis. Manag.*, 4(5):351–362, 2014. doi: 10.2217/nmt.14.33. URL http://www.ncbi.nlm.nih.gov/pmc/articles/PMC4257134/.

[147] Martin A Lindquist and Amanda Mejia. Zen and the art of multiple comparisons. *Psychosom. Med.*, 77(2):114–125, 2015. ISSN 1534-7796. doi: 10.1097/PSY.0000000000000148. URL https://pubmed.ncbi.nlm.nih.gov/25647751https://www.ncbi.nlm.nih.gov/pmc/articles/PMC4333023/.

[148] Olena Lykhmus, Nibha Mishra, Lyudmyla Koval, Olena Kalashnyk, Galyna Gergalova, Kateryna Uspenska, Serghiy Komisarenko, Hermona Soreq, and Maryna Skok. Molecular Mechanisms Regulating LPS-Induced Inflammation in the Brain , 2016. URL https://www.frontiersin.org/article/10.3389/fnmol.2016.00019.

[149] Y Ma, M A Shaik, M G Kozberg, S H Kim, J P Portes, D Timerman, and E M Hillman. Resting-state hemodynamics are spatiotemporally coupled to synchronized

and symmetric neural activity in excitatory neurons. *Proc Natl Acad Sci U S A*, 113 (52):E8463–E8471, 2016. doi: 10.1073/pnas.1525369113. URL https://www.ncbi.nlm.nih.gov/pubmed/27974609.

[150] Ying Ma, Mariel G Kozberg, Sharon H Kim, Mohammed A Shaik, Dmitriy Timmerman, Elizabeth M C Hillman, Mariel G Kozberg, Sharon H Kim, Jacob P Portes, Dmitriy Timerman, Elizabeth M C Hillman, Mohammed A Shaik, Dmitriy Timmerman, and Elizabeth M C Hillman. Resting - state hemodynamics are spatiotemporally coupled to synchronized and symmetric neural activity in excitatory neurons. *Proc. Natl. Acad. Sci.*, 113(52):E8463–E8471, 2016. ISSN 0027-8424. doi: 10.1073/pnas.1525369113. URL http://www.pnas.org/content/113/52/E8463.abstract.

[151] Ying Ma, Mohammed A Shaik, Sharon H Kim, Mariel G Kozberg, David N Thibodeaux, Hanzhi T Zhao, Hang Yu, and Elizabeth M C Hillman. Wide-field optical mapping of neural activity and brain haemodynamics: considerations and novel approaches. *Philos. Trans. R. Soc. Lond. B. Biol. Sci.*, 371(1705):20150360, oct 2016. ISSN 1471-2970. doi: 10.1098/rstb.2015.0360. URL https://pubmed.ncbi.nlm.nih.gov/27574312https://www.ncbi.nlm.nih.gov/pmc/articles/PMC5003860/.

[152] R Loch Macdonald, Ryszard M Pluta, and John H Zhang. Cerebral vasospasm after subarachnoid hemorrhage: the emerging revolution. *Nat. Clin. Pract. Neurol.*, 3(5): 256–263, may 2007. ISSN 1745-8358 (Electronic). doi: 10.1038/ncpneuro0490.

[153] Arianna Maffei and Alfredo Fontanini. Network homeostasis: a matter of coordination. *Curr. Opin. Neurobiol.*, 19(2):168–173, apr 2009. ISSN 1873-6882 (Electronic). doi: 10.1016/j.conb.2009.05.012.

[154] Monica Maher, Nathan W Churchill, Airton Leonardo de Oliveira Manoel, Simon J Graham, R Loch Macdonald, and Tom A Schweizer. Altered Resting-State Connec-

tivity within Executive Networks after Aneurysmal Subarachnoid Hemorrhage. *PLoS One*, 10(7):e0130483, 2015. ISSN 1932-6203 (Electronic). doi: 10.1371/journal.pone.0130483.

[155] Lorenzo Mancuso, Tommaso Costa, Andrea Nani, Jordi Manuello, Donato Liloia, Gabriele Gelmini, Melissa Panero, Sergio Duca, and Franco Cauda. The homotopic connectivity of the functional brain: a meta-analytic approach. *Sci. Rep.*, 9 (1):3346, 2019. ISSN 2045-2322. doi: 10.1038/s41598-019-40188-3. URL `https://doi.org/10.1038/s41598-019-40188-3`.

[156] Dun Mao, Adam R Neumann, Jianjun Sun, Vincent Bonin, Majid H Mohajerani, and Bruce L McNaughton. Hippocampus-dependent emergence of spatial sequence coding in retrosplenial cortex. *Proc. Natl. Acad. Sci.*, 115(31):8015 LP – 8018, jul 2018. doi: 10.1073/pnas.1803224115. URL `http://www.pnas.org/content/115/31/8015.abstract`.

[157] Chris Martin, John Martindale, Jason Berwick, and John Mayhew. Investigating neural-hemodynamic coupling and the hemodynamic response function in the awake rat. *Neuroimage*, 32(1):33–48, aug 2006. ISSN 1053-8119 (Print). doi: 10.1016/j.neuroimage.2006.02.021.

[158] M. Massimini, R. Huber, F. Ferrarelli, S. Hill, and G. Tononi. The SSO as a Traveling Wave. *J. Neurosci.*, 24(31):6862–6870, 2004. ISSN 0270-6474. doi: 10.1523/JNEUROSCI.1318-04.2004.

[159] Marcello Massimini, Reto Huber, Fabio Ferrarelli, Sean Hill, and Giulio Tononi. The Sleep Slow Oscillation as a Traveling Wave. *J. Neurosci.*, 24(31):6862, 2004. URL `http://www.jneurosci.org/content/24/31/6862.abstract`.

[160] Ilwola Mattagajasingh, Cuk-Seong Kim, Asma Naqvi, Tohru Yamamori, Timothy A Hoffman, Saet-Byel Jung, Jeremy DeRicco, Kenji Kasuno, and Kaikobad Irani. SIRT1 promotes endothelium-dependent vascular relaxation by activating endothelial nitric oxide synthase. *Proc. Natl. Acad. Sci. U. S. A.*, 104(37):14855–14860, sep 2007. ISSN 0027-8424 (Print). doi: 10.1073/pnas.0704329104.

[161] Keita Mayanagi, Tamás Gáspár, Prasad V Katakam, and David W Busija. Systemic administration of diazoxide induces delayed preconditioning against transient focal cerebral ischemia in rats. *Brain Res.*, 1168:106–111, 2007. ISSN 0006-8993. doi: https://doi.org/10.1016/j.brainres.2007.06.071. URL `https://www.sciencedirect.com/science/article/pii/S0006899307016411`.

[162] M R Mayberg, H H Batjer, R Dacey, M Diringer, E C Haley, R C Heros, L L Sternau, J Torner, H P Jr Adams, and W Feinberg. Guidelines for the management of aneurysmal subarachnoid hemorrhage. A statement for healthcare professionals from a special writing group of the Stroke Council, American Heart Association. *Stroke*, 25 (11):2315–2328, nov 1994. ISSN 0039-2499 (Print). doi: 10.1161/01.str.25.11.2315.

[163] S A Mayer, K T Kreiter, D Copeland, G L Bernardini, J E Bates, S Peery, J Claassen, Y E Du, and E S Jr Connolly. Global and domain-specific cognitive impairment and outcome after subarachnoid hemorrhage. *Neurology*, 59(11):1750–1758, dec 2002. ISSN 0028-3878 (Print). doi: 10.1212/01.wnl.0000035748.91128.c2.

[164] Jie Mei, Nico Riedel, Ulrike Grittner, Matthias Endres, Stefanie Banneke, and Julius Valentin Emmrich. Body temperature measurement in mice during acute illness: implantable temperature transponder versus surface infrared thermometry. *Sci. Rep.*, 8(1):3526, feb 2018. ISSN 2045-2322 (Electronic). doi: 10.1038/s41598-018-22020-6.

[165] Bruno P Meloni, Peta A Tilbrook, Sherif Boulos, Peter G Arthur, and Neville W

Knuckey. Erythropoietin preconditioning in neuronal cultures: signaling, protection from in vitro ischemia, and proteomic analysis. *J. Neurosci. Res.*, 83(4):584–593, mar 2006. ISSN 0360-4012 (Print). doi: 10.1002/jnr.20755.

[166] K Messeter, L Brandt, B Ljunggren, N A Svendgaard, L Algotsson, B Romner, and E Ryding. Prediction and prevention of delayed ischemic dysfunction after aneurysmal subarachnoid hemorrhage and early operation. *Neurosurgery*, 20(4):548–553, apr 1987. ISSN 0148-396X (Print). doi: 10.1227/00006123-198704000-00007.

[167] Róisín Ní Mhuircheartaigh, Debbie Rosenorn-Lanng, Richard Wise, Saad Jbabdi, Richard Rogers, and Irene Tracey. Cortical and subcortical connectivity changes during decreasing levels of consciousness in humans: a functional magnetic resonance imaging study using propofol. *J. Neurosci.*, 30(27):9095–9102, jul 2010. ISSN 1529-2401 (Electronic). doi: 10.1523/JNEUROSCI.5516-09.2010.

[168] Anish Mitra, Abraham Z Snyder, Carl D Hacker, Mrinal Pahwa, Enzo Tagliazucchi, Helmut Laufs, Eric C Leuthardt, and Marcus E Raichle. Human cortical–hippocampal dialogue in wake and slow-wave sleep. *Proc. Natl. Acad. Sci.*, 113(44):E6868 LP – E6876, nov 2016. doi: 10.1073/pnas.1607289113. URL `http://www.pnas.org/content/113/44/E6868.abstract`.

[169] Anish Mitra, Andrew Kraft, Patrick Wright, Benjamin Acland, Abraham Z Snyder, Zachary Rosenthal, Leah Czerniewski, Adam Bauer, Lawrence Snyder, Joseph Culver, Jin-Moo Lee, and Marcus E Raichle. Spontaneous Infra-slow Brain Activity Has Unique Spatiotemporal Dynamics and Laminar Structure. *Neuron*, 98(2):297–305.e6, apr 2018. ISSN 1097-4199 (Electronic). doi: 10.1016/j.neuron.2018.03.015.

[170] Majid H Mohajerani, David A Mcvea, Matthew Fingas, and Timothy H Murphy. Mirrored Bilateral Slow-Wave Cortical Activity within Local Circuits Revealed by

Fast Bihemispheric Voltage-Sensitive Dye Imaging in Anesthetized and Awake Mice. 30(10):3745–3751, 2010. ISSN 0270-6474. doi: 10.1523/JNEUROSCI.6437-09.2010.

[171] Dariush Mozaffarian, Emelia J Benjamin, Alan S Go, Donna K Arnett, Michael J Blaha, Mary Cushman, Sandeep R Das, Sarah de Ferranti, Jean-Pierre Després, Heather J Fullerton, Virginia J Howard, Mark D Huffman, Carmen R Isasi, Monik C Jiménez, Suzanne E Judd, Brett M Kissela, Judith H Lichtman, Lynda D Lisabeth, Simin Liu, Rachel H Mackey, David J Magid, Darren K McGuire, Emile R 3rd Mohler, Claudia S Moy, Paul Muntner, Michael E Mussolino, Khurram Nasir, Robert W Neumar, Graham Nichol, Latha Palaniappan, Dilip K Pandey, Mathew J Reeves, Carlos J Rodriguez, Wayne Rosamond, Paul D Sorlie, Joel Stein, Amytis Towfighi, Tanya N Turan, Salim S Virani, Daniel Woo, Robert W Yeh, and Melanie B Turner. Heart Disease and Stroke Statistics-2016 Update: A Report From the American Heart Association. *Circulation*, 133(4):e38–360, jan 2016. ISSN 1524-4539 (Electronic). doi: 10.1161/CIR.0000000000000350.

[172] Carol Murray, David J Sanderson, Chris Barkus, Robert M J Deacon, J Nicholas P Rawlins, David M Bannerman, and Colm Cunningham. Systemic inflammation induces acute working memory deficits in the primed brain: relevance for delirium. *Neurobiol. Aging*, 33(3):603–616.e3, mar 2012. ISSN 1558-1497 (Electronic). doi: 10.1016/j.neurobiolaging.2010.04.002.

[173] Srinivasan V Narayanan, Kunjan R Dave, Isa Saul, and Miguel A Perez-Pinzon. Resveratrol Preconditioning Protects Against Cerebral Ischemic Injury via Nuclear Erythroid 2-Related Factor 2. *Stroke*, 46(6):1626–1632, jun 2015. ISSN 1524-4628 (Electronic). doi: 10.1161/STROKEAHA.115.008921.

[174] Ignacio Negrón-Oyarzo, Nelson Espinosa, Marcelo Aguilar-Rivera, Marco Fuenzalida, Francisco Aboitiz, and Pablo Fuentealba. Coordinated prefrontal–hippocampal ac-

tivity and navigation strategy-related prefrontal firing during spatial memory formation. *Proc. Natl. Acad. Sci.*, 115(27):7123 LP – 7128, jul 2018. doi: 10.1073/pnas.1720117115. URL http://www.pnas.org/content/115/27/7123.abstract.

[175] Laura E Nelson, Jun Lu, Tianzhi Guo, Clifford B Saper, Nicholas P Franks, and Mervyn Maze. The α2-Adrenoceptor Agonist Dexmedetomidine Converges on an Endogenous Sleep-promoting Pathway to Exert Its Sedative Effects. *Anesthesiology*, 98(2):428–436, 2003. doi: 0000542-200302000-00024. URL http://dx.doi.org/0000542-200302000-00024.

[176] Garrett T Neske. The Slow Oscillation in Cortical and Thalamic Networks: Mechanisms and Functions. *Front. Neural Circuits*, 9(88):88, 2015. doi: 10.3389/fncir.2015.00088. URL https://www.ncbi.nlm.nih.gov/pubmed/26834569https://www.frontiersin.org/article/10.3389/fncir.2015.00088.

[177] Joshua P Neunuebel and James J Knierim. CA3 retrieves coherent representations from degraded input: direct evidence for CA3 pattern completion and dentate gyrus pattern separation. *Neuron*, 81(2):416–427, jan 2014. ISSN 1097-4199. doi: 10.1016/j.neuron.2013.11.017. URL https://pubmed.ncbi.nlm.nih.gov/24462102https://www.ncbi.nlm.nih.gov/pmc/articles/PMC3904133/.

[178] Emanuele Nicastri, Concetta Castilletti, Pietro Balestra, Simonetta Galgani, and Giuseppe Ippolito. Zika Virus Infection in the Central Nervous System and Female Genital Tract. *Emerg. Infect. Dis.*, 22(12):2228–2230, dec 2016. ISSN 1080-6059. doi: 10.3201/eid2212.161280. URL https://pubmed.ncbi.nlm.nih.gov/27617352https://www.ncbi.nlm.nih.gov/pmc/articles/PMC5189169/.

[179] Niels Niethard, Hong-Viet V Ngo, Ingrid Ehrlich, and Jan Born. Cortical circuit

activity underlying sleep slow oscillations and spindles. *Proc. Natl. Acad. Sci.*, 2018. URL http://www.pnas.org/content/early/2018/09/11/1805517115.abstract.

[180] Arun Niranjan, Isabel N Christie, Samuel G Solomon, Jack A Wells, and Mark F Lythgoe. fMRI mapping of the visual system in the mouse brain with interleaved snapshot GE-EPI. *Neuroimage*, 139:337–345, oct 2016. ISSN 1095-9572. doi: 10.1016/j.neuroimage.2016.06.015. URL https://pubmed.ncbi.nlm.nih.gov/27296012https://www.ncbi.nlm.nih.gov/pmc/articles/PMC4988789/.

[181] Kenneth A Norman, Sean M Polyn, Greg J Detre, and James V Haxby. Beyond mind-reading: multi-voxel pattern analysis of fMRI data. *Trends Cogn. Sci.*, 10(9):424–430, sep 2006. ISSN 1364-6613 (Print). doi: 10.1016/j.tics.2006.07.005.

[182] Jooyoung Oh, Jung Eun Shin, Kyu Hyun Yang, Sunghyon Kyeong, Woo Suk Lee, Tae-Sub Chung, and Jae-Jin Kim. Cortical and subcortical changes in resting-state functional connectivity before and during an episode of postoperative delirium. *Aust. N. Z. J. Psychiatry*, 53(8):794–806, aug 2019. ISSN 1440-1614 (Electronic). doi: 10.1177/0004867419848826.

[183] Seung Wook Oh, Julie A Harris, Lydia Ng, Brent Winslow, Nicholas Cain, Stefan Mihalas, Quanxin Wang, Chris Lau, Leonard Kuan, Alex M Henry, Marty T Mortrud, Benjamin Ouellette, Thuc Nghi Nguyen, Staci A Sorensen, Clifford R Slaughterbeck, Wayne Wakeman, Yang Li, David Feng, Anh Ho, Eric Nicholas, Karla E Hirokawa, Phillip Bohn, Kevin M Joines, Hanchuan Peng, Michael J Hawrylycz, John W Phillips, John G Hohmann, Paul Wohnoutka, Charles R Gerfen, Christof Koch, Amy Bernard, Chinh Dang, Allan R Jones, and Hongkui Zeng. A mesoscale connectome of the mouse brain. *Nature*, 508(7495):207–214, apr 2014. ISSN 1476-4687. doi: 10.1038/nature13186. URL https://pubmed.ncbi.nlm.nih.gov/24695228https://www.ncbi.nlm.nih.gov/pmc/articles/PMC5102064/.

[184] Yo Oishi, Yohko Takata, Yujiro Taguchi, Sayaka Kohtoh, Yoshihiro Urade, and Michael Lazarus. Polygraphic Recording Procedure for Measuring Sleep in Mice. *J. Vis. Exp.*, e53678(107):e53678–e53678, jan 2016. ISSN 1940-087X. doi: 10.3791/53678. URL https://pubmed.ncbi.nlm.nih.gov/26863349https://www.ncbi.nlm.nih.gov/pmc/articles/PMC4781694/.

[185] Inema E Orukari, Joshua S Siegel, Nicole M Warrington, Grant A Baxter, Adam Q Bauer, Joshua S Shimony, Joshua B Rubin, and Joseph P Culver. Altered hemodynamics contribute to local but not remote functional connectivity disruption due to glioma growth. *J. Cereb. blood flow Metab. Off. J. Int. Soc. Cereb. Blood Flow Metab.*, 40(1): 100–115, jan 2020. ISSN 1559-7016 (Electronic). doi: 10.1177/0271678X18803948.

[186] Joseph C O'Sullivan, Xiang-Lan Yao, Hasan Alam, and Joseph T McCabe. Diazoxide, as a postconditioning and delayed preconditioning trigger, increases HSP25 and HSP70 in the central nervous system following combined cerebral stroke and hemorrhagic shock. *J. Neurotrauma*, 24(3):532–546, mar 2007. ISSN 0897-7151 (Print). doi: 10.1089/neu.2006.0128.

[187] Ben Julian A Palanca, Anish Mitra, Linda Larson-Prior, Abraham Z Snyder, Michael S Avidan, and Marcus E Raichle. Resting-state Functional Magnetic Resonance Imaging Correlates of Sevoflurane-induced Unconsciousness. *Anesthesiology*, 123(2):346–356, aug 2015. ISSN 1528-1175. doi: 10.1097/ALN.0000000000000731. URL https://pubmed.ncbi.nlm.nih.gov/26057259https://www.ncbi.nlm.nih.gov/pmc/articles/PMC4509973/.

[188] Maria Panagiotou, Vladyslav V Vyazovskiy, Johanna H Meijer, and Tom Deboer. Differences in electroencephalographic non-rapid-eye movement sleep slow-wave characteristics between young and old mice. *Sci. Rep.*, 7(1):43656, 2017. ISSN 2045-2322. doi: 10.1038/srep43656. URL https://doi.org/10.1038/srep43656.

[189] Augusto Parra, Matthew J McGirt, Huaxin Sheng, Daniel T Laskowitz, Robert D Pearlstein, and David S Warner. Mouse model of subarachnoid hemorrhage associated cerebral vasospasm: methodological analysis. *Neurol. Res.*, 24(5):510–516, jul 2002. ISSN 0161-6412 (Print). doi: 10.1179/016164102101200276.

[190] L Passamonti, K A Tsvetanov, P S Jones, W R Bevan-Jones, R Arnold, R J Borchert, E Mak, L Su, J T O'Brien, and J B Rowe. Neuroinflammation and Functional Connectivity in Alzheimer's Disease: Interactive Influences on Cognitive Performance. *J. Neurosci.*, 39(36):7218 LP – 7226, sep 2019. doi: 10.1523/JNEUROSCI.2574-18.2019. URL http://www.jneurosci.org/content/39/36/7218.abstract.

[191] Mikhail Paveliev, Mikhail Kislin, Dmitry Molotkov, Mikhail Yuryev, Heikki Rauvala, and Leonard Khiroug. Acute brain trauma in mice followed by longitudinal two-photon imaging. *J. Vis. Exp.*, (86):51559, apr 2014. ISSN 1940-087X. doi: 10.3791/51559. URL https://pubmed.ncbi.nlm.nih.gov/24748024https://www.ncbi.nlm.nih.gov/pmc/articles/PMC4162478/.

[192] Marcela Pekna and Milos Pekny. The neurobiology of brain injury. *Cerebrum*, 2012:9, jul 2012. ISSN 1524-6205. URL https://pubmed.ncbi.nlm.nih.gov/23447795https://www.ncbi.nlm.nih.gov/pmc/articles/PMC3574788/.

[193] Mian Peng, Ce Zhang, Yuanlin Dong, Yiying Zhang, Harumasa Nakazawa, Masao Kaneki, Hui Zheng, Yuan Shen, Edward R Marcantonio, and Zhongcong Xie. Battery of behavioral tests in mice to study postoperative delirium. *Sci. Rep.*, 6:29874, jul 2016. ISSN 2045-2322. doi: 10.1038/srep29874. URL https://pubmed.ncbi.nlm.nih.gov/27435513https://www.ncbi.nlm.nih.gov/pmc/articles/PMC4951688/.

[194] Antonio Pereira, Sidarta Ribeiro, Michael Wiest, Leonardo C Moore, Janaina Pantoja, Shih-Chieh Lin, and Miguel A L Nicolelis. Processing of tactile information by the hip-

pocampus. *Proc. Natl. Acad. Sci.*, 104(46):18286 LP – 18291, nov 2007. doi: 10.1073/pnas.0708611104. URL http://www.pnas.org/content/104/46/18286.abstract.

[195] Dante Picchioni, Jeff H Duyn, and Silvina G Horovitz. Sleep and the functional connectome. *Neuroimage*, 80:387–396, oct 2013. ISSN 1095-9572 (Electronic). doi: 10.1016/j.neuroimage.2013.05.067.

[196] J D Pickard, M Matheson, J Patterson, and D Wyper. Prediction of late ischemic complications after cerebral aneurysm surgery by the intraoperative measurement of cerebral blood flow. *J. Neurosurg.*, 53(3):305–308, sep 1980. ISSN 0022-3085 (Print). doi: 10.3171/jns.1980.53.3.0305.

[197] Jonathan D Power, Kelly A Barnes, Abraham Z Snyder, Bradley L Schlaggar, and Steven E Petersen. Spurious but systematic correlations in functional connectivity MRI networks arise from subject motion. *Neuroimage*, 59(3):2142–2154, feb 2012. ISSN 1095-9572. doi: 10.1016/j.neuroimage.2011.10.018. URL https://pubmed.ncbi.nlm.nih.gov/22019881https://www.ncbi.nlm.nih.gov/pmc/articles/PMC3254728/.

[198] Jonathan D Power, Mark Plitt, Stephen J Gotts, Prantik Kundu, Valerie Voon, Peter A Bandettini, and Alex Martin. Ridding fMRI data of motion-related influences: Removal of signals with distinct spatial and physical bases in multiecho data. *Proc. Natl. Acad. Sci.*, 115(9):E2105 LP – E2114, feb 2018. doi: 10.1073/pnas.1720985115. URL http://www.pnas.org/content/115/9/E2105.abstract.

[199] Jonathan D Power, Charles J Lynch, Benjamin M Silver, Marc J Dubin, Alex Martin, and Rebecca M Jones. Distinctions among real and apparent respiratory motions in human fMRI data. *Neuroimage*, 201:116041, 2019. ISSN 1053-8119. doi: https://doi.org/10.1016/j.neuroimage.2019.116041. URL http://www.sciencedirect.com/science/article/pii/S1053811919306226.

[200] Liya Qin, Xuefei Wu, Michelle L Block, Yuxin Liu, George R Breese, Jau-Shyong Hong, Darin J Knapp, and Fulton T Crews. Systemic LPS causes chronic neuroinflammation and progressive neurodegeneration. *Glia*, 55(5):453–462, apr 2007. ISSN 0894-1491 (Print). doi: 10.1002/glia.20467.

[201] Miriana Jlenia Quattromani, Jakob Hakon, Uwe Rauch, Adam Q Bauer, and Tadeusz Wieloch. Changes in resting-state functional connectivity after stroke in a mouse brain lacking extracellular matrix components. *Neurobiol. Dis.*, 112:91–105, apr 2018. ISSN 1095-953X (Electronic). doi: 10.1016/j.nbd.2018.01.011.

[202] Alejandro A Rabinstein, Jonathan A Friedman, Stephen D Weigand, Robyn L McClelland, Jimmy R Fulgham, Edward M Manno, John L D Atkinson, and Eelco F M Wijdicks. Predictors of cerebral infarction in aneurysmal subarachnoid hemorrhage. *Stroke*, 35(8):1862–1866, aug 2004. ISSN 1524-4628 (Electronic). doi: 10.1161/01.STR.0000133132.76983.8e.

[203] Marcus E Raichle. The restless brain: how intrinsic activity organizes brain function. *Philos. Trans. R. Soc. London. Ser. B, Biol. Sci.*, 370(1668), may 2015. ISSN 1471-2970 (Electronic). doi: 10.1098/rstb.2014.0172.

[204] Marcus E Raichle and Mark A Mintun. Brain work and brain imaging. *Annu. Rev. Neurosci.*, 29:449–476, 2006. ISSN 0147-006X (Print). doi: 10.1146/annurev.neuro.29.051605.112819.

[205] Senthilkumar B Rajamohan, Vinodkumar B Pillai, Madhu Gupta, Nagalingam R Sundaresan, Konstantin G Birukov, Sadhana Samant, Michael O Hottiger, and Mahesh P Gupta. SIRT1 promotes cell survival under stress by deacetylation-dependent deactivation of poly(ADP-ribose) polymerase 1. *Mol. Cell. Biol.*, 29(15):4116–4129, aug 2009. ISSN 1098-5549 (Electronic). doi: 10.1128/MCB.00121-09.

[206] Sonja A Rasmussen, Denise J Jamieson, Margaret A Honein, and Lyle R Petersen. Zika Virus and Birth Defects — Reviewing the Evidence for Causality. *N. Engl. J. Med.*, 374(20):1981–1987, apr 2016. ISSN 0028-4793. doi: 10.1056/NEJMsr1604338. URL https://doi.org/10.1056/NEJMsr1604338.

[207] Ami P Raval, Kunjan R Dave, and Miguel A Pérez-Pinzón. Resveratrol mimics ischemic preconditioning in the brain. *J. Cereb. blood flow Metab. Off. J. Int. Soc. Cereb. Blood Flow Metab.*, 26(9):1141–1147, sep 2006. ISSN 0271-678X (Print). doi: 10.1038/sj.jcbfm.9600262.

[208] Baxter P Rogers, Victoria L Morgan, Allen T Newton, and John C Gore. Assessing functional connectivity in the human brain by fMRI. *Magn. Reson. Imaging*, 25(10):1347–1357, dec 2007. ISSN 0730-725X. doi: 10.1016/j.mri.2007.03.007. URL https://pubmed.ncbi.nlm.nih.gov/17499467https://www.ncbi.nlm.nih.gov/pmc/articles/PMC2169499/.

[209] P G Samann, R Wehrle, D Hoehn, V I Spoormaker, H Peters, C Tully, F Holsboer, and M Czisch. Development of the brain's default mode network from wakefulness to slow wave sleep. *Cereb Cortex*, 21(9):2082–2093, 2011. doi: 10.1093/cercor/bhq295. URL http://www.ncbi.nlm.nih.gov/pubmed/21330468.

[210] Harry Scheinin, Riku Aantaa, Markku Anttila, Pasi Hakola, Antti Helminen, and Sakari Karhuvaara. Reversal of the Sedative and Sympathetic Effects of Dexmedetomidine with a Specific alpha2-Adrenoceptor Antagonist Atipamezole. *Anesthesiology*, 89(3):574–584, 1998. ISSN 00015172.

[211] Jander Sebastian, Schroeter Michael, and Saleh Andreas. Imaging Inflammation in Acute Brain Ischemia. *Stroke*, 38(2):642–645, feb 2007. doi: 10.1161/01.STR.

0000250048.42916.ad. URL https://doi.org/10.1161/01.STR.0000250048.42916.ad.

[212] Fatima A Sehba. Rat endovascular perforation model. *Transl. Stroke Res.*, 5(6):660–668, dec 2014. ISSN 1868-601X (Electronic). doi: 10.1007/s12975-014-0368-4.

[213] Priyanka P Shah-Basak, Benjamin T Dunkley, Annette X Ye, Simeon Wong, Leodante da Costa, and Elizabeth W Pang. Altered beta-band functional connectivity may be related to 'performance slowing' in good outcome aneurysmal subarachnoid patients. *Neurosci. Lett.*, 699:64–70, apr 2019. ISSN 1872-7972 (Electronic). doi: 10.1016/j.neulet.2019.01.053.

[214] Arefeh Sherafati, Abraham Z Snyder, Adam T Eggebrecht, Karla M Bergonzi, Tracy M Burns-Yocum, Heather M Lugar, Silvina L Ferradal, Amy Robichaux-Viehoever, Christopher D Smyser, Ben J Palanca, Tamara Hershey, and Joseph P Culver. Global motion detection and censoring in high-density diffuse optical tomography. *Hum. Brain Mapp.*, 41(14):4093–4112, oct 2020. ISSN 1097-0193 (Electronic). doi: 10.1002/hbm.25111.

[215] Daisuke Shimaoka, Chenchen Song, and Thomas Knöpfel. State-Dependent Modulation of Slow Wave Motifs towards Awakening. *Front. Cell. Neurosci.*, 11:108, 2017. doi: 10.3389/fncel.2017.00108. URL https://www.ncbi.nlm.nih.gov/pubmed/28484371https://www.ncbi.nlm.nih.gov/pmc/PMC5401891/.

[216] Najma Siddiqi, Allan O House, and John D Holmes. Occurrence and outcome of delirium in medical in-patients: a systematic literature review. *Age Ageing*, 35(4):350–364, jul 2006. ISSN 0002-0729 (Print). doi: 10.1093/ageing/afl005.

[217] Torfi Sigurdsson and Sevil Duvarci. Hippocampal-Prefrontal Interactions in Cogni-

tion, Behavior and Psychiatric Disease , 2016. URL https://www.frontiersin.org/article/10.3389/fnsys.2015.00190.

[218] Gergely Silasi, Dongsheng Xiao, Matthieu P Vanni, Andrew C N Chen, and Timothy H Murphy. Intact skull chronic windows for mesoscopic wide-field imaging in awake mice. *J Neurosci Methods*, 267:141–149, 2016. doi: 10.1016/j.jneumeth.2016.04.012. URL https://www.ncbi.nlm.nih.gov/pubmed/27102043.

[219] Nilendra Singh, Megha Agrawal, and Sylvain Doré. Neuroprotective properties and mechanisms of resveratrol in in vitro and in vivo experimental cerebral stroke models. *ACS Chem. Neurosci.*, 4(8):1151–1162, aug 2013. ISSN 1948-7193. doi: 10.1021/cn400094w. URL https://pubmed.ncbi.nlm.nih.gov/23758534https://www.ncbi.nlm.nih.gov/pmc/articles/PMC3750679/.

[220] Jamie Sleigh, Martyn Harvey, Logan Voss, and Bill Denny. Ketamine – More mechanisms of action than just NMDA blockade. *Trends Anaesth. Crit. Care*, 4(2): 76–81, 2014. doi: https://doi.org/10.1016/j.tacc.2014.03.002. URL http://www.sciencedirect.com/science/article/pii/S2210844014200062.

[221] Stephen M Smith, Diego Vidaurre, Christian F Beckmann, Matthew F Glasser, Mark Jenkinson, Karla L Miller, Thomas E Nichols, Emma C Robinson, Gholamreza Salimi-Khorshidi, Mark W Woolrich, Deanna M Barch, Kamil Uğurbil, and David C Van Essen. Functional connectomics from resting-state fMRI. *Trends Cogn. Sci.*, 17(12): 666–682, dec 2013. ISSN 1879-307X (Electronic). doi: 10.1016/j.tics.2013.09.016.

[222] Alex J Smola and Bernhard Schölkopf. A tutorial on support vector regression. *Stat. Comput.*, 14(3):199–222, 2004. ISSN 1573-1375. doi: 10.1023/B:STCO.0000035301.49549.88. URL https://doi.org/10.1023/B:STCO.0000035301.49549.88.

[223] Olaf Sporns, Christopher J Honey, and Rolf Kötter. Identification and Classification of Hubs in Brain Networks. *PLoS One*, 2(10):e1049, oct 2007. URL https://doi.org/10.1371/journal.pone.0001049.

[224] M Steriade, A Nuñez, and F Amzica. A novel slow (< 1 Hz) oscillation of neocortical neurons in vivo: depolarizing and hyperpolarizing components. *J. Neurosci.*, 13 (8):3252–3265, aug 1993. ISSN 0270-6474. doi: 10.1523/JNEUROSCI.13-08-03252.1993. URL https://pubmed.ncbi.nlm.nih.gov/8340806https://www.ncbi.nlm.nih.gov/pmc/articles/PMC6576541/.

[225] Stephen C Strother, Jon Anderson, Lars Kai Hansen, Ulrik Kjems, Rafal Kustra, John Sidtis, Sally Frutiger, Suraj Muley, Stephen LaConte, and David Rottenberg. The Quantitative Evaluation of Functional Neuroimaging Experiments: The NPAIRS Data Analysis Framework. *Neuroimage*, 15(4):747–771, 2002. ISSN 1053-8119. doi: https://doi.org/10.1006/nimg.2001.1034. URL http://www.sciencedirect.com/science/article/pii/S1053811901910341.

[226] Maggie B Struck, Karl A Andrutis, Harvey E Ramirez, and August H Battles. Effect of a short-term fast on ketamine-xylazine anesthesia in rats. *J. Am. Assoc. Lab. Anim. Sci.*, 50(3):344–348, 2011. URL https://www.ncbi.nlm.nih.gov/pubmed/21640029https://www.ncbi.nlm.nih.gov/pmc/articles/PMC3103284/.

[227] Jiabin Su, Tongzhou E, Qihao Guo, Yu Lei, and Yuxiang Gu. Memory Deficits After Aneurysmal Subarachnoid Hemorrhage: A Functional Magnetic Resonance Imaging Study. *World Neurosurg.*, 111:e500–e506, mar 2018. ISSN 1878-8769 (Electronic). doi: 10.1016/j.wneu.2017.12.102.

[228] C L Sudlow and C P Warlow. Comparable studies of the incidence of stroke and its pathological types: results from an international collaboration. International Stroke

Incidence Collaboration. *Stroke*, 28(3):491–499, mar 1997. ISSN 0039-2499 (Print). doi: 10.1161/01.str.28.3.491.

[229] Raoul Sutter and Peter W Kaplan. Neuroimaging Correlates of Acute Encephalopathy. *J. Clin. Neurophysiol.*, 30(5), 2013. ISSN 0736-0258. URL https://journals.lww.com/clinicalneurophys/Fulltext/2013/10000/Neuroimaging{_}Correlates{_}of{_}Acute{_}Encephalopathy.11.aspx.

[230] E Tagliazucchi and H Laufs. Decoding wakefulness levels from typical fMRI resting-state data reveals reliable drifts between wakefulness and sleep. *Neuron*, 82(3):695–708, 2014. doi: 10.1016/j.neuron.2014.03.020. URL http://www.ncbi.nlm.nih.gov/pubmed/24811386.

[231] Sachiko Tanaka, Masatoshi Ide, Toshiomi Shibutani, Hirokazu Ohtaki, Satoshi Numazawa, Seiji Shioda, and Takemi Yoshida. Lipopolysaccharide-induced microglial activation induces learning and memory deficits without neuronal cell deathin rats. *J. Neurosci. Res.*, 83(4):557–566, mar 2006. ISSN 0360-4012 (Print). doi: 10.1002/jnr.20752. URL https://doi.org/10.1002/jnr.20752.

[232] Chaozheng Tang, Zhiyong Zhao, Chuang Chen, Xiaohui Zheng, Fenfen Sun, Xiaoli Zhang, Jing Tian, Mingxia Fan, Yi Wu, and Jie Jia. Decreased Functional Connectivity of Homotopic Brain Regions in Chronic Stroke Patients: A Resting State fMRI Study. *PLoS One*, 11(4):e0152875, apr 2016. URL https://doi.org/10.1371/journal.pone.0152875.

[233] John W Thompson, Kunjan R Dave, Juan I Young, and Miguel A Perez-Pinzon. Ischemic preconditioning alters the epigenetic profile of the brain from ischemic intolerance to ischemic tolerance. *Neurother. J. Am. Soc. Exp. Neurother.*, 10(4):789–797, oct 2013. ISSN 1878-7479 (Electronic). doi: 10.1007/s13311-013-0202-9.

[234] Lin Tian, S Andrew Hires, Tianyi Mao, Daniel Huber, M Eugenia Chiappe, H Chalasani, Leopoldo Petreanu, Jasper Akerboom, Sean A McKinney, R Eric, Cornelia I Bargmann, Vivek Jayaraman, Karel Svoboda, L Loren, Sreekanth H Chalasani, Leopoldo Petreanu, Jasper Akerboom, Sean A McKinney, Eric R Schreiter, Cornelia I Bargmann, Vivek Jayaraman, Karel Svoboda, and Loren L Looger. Imaging neural activity in worms, flies and mice with improved GCaMP calcium indicators. *Nat. Methods*, 6(12):875–881, 2009. ISSN 1548-7105. doi: 10.1038/nmeth.1398. URL `https://doi.org/10.1038/nmeth.1398`.

[235] I Timofeev and M Steriade. Low-frequency rhythms in the thalamus of intact-cortex and decorticated cats. *J. Neurophysiol.*, 76(6):4152–4168, 1996.

[236] Irene Tobler, Alexander A Borbrly, and Alexander A Borbély. The effect of 3-h and 6-h sleep deprivation on sleep and EEG spectra of the rat. *Behav. Brain Res.*, 36 (1):73–78, 1990. ISSN 0166-4328. doi: https://doi.org/10.1016/0166-4328(90)90161-7. URL `http://www.sciencedirect.com/science/article/pii/0166432890901617`.

[237] George Trendelenburg and Ulrich Dirnagl. Neuroprotective role of astrocytes in cerebral ischemia: focus on ischemic preconditioning. *Glia*, 50(4):307–320, jun 2005. ISSN 0894-1491 (Print). doi: 10.1002/glia.20204.

[238] D Y Ts'o, R D Frostig, E E Lieke, and A Grinvald. Functional organization of primate visual cortex revealed by high resolution optical imaging. *Science*, 249(4967):417–420, jul 1990. ISSN 0036-8075 (Print). doi: 10.1126/science.2165630.

[239] Tomokazu Tsurugizawa, Kota Tamada, Nobukazu Ono, Sachise Karakawa, Yuko Kodama, Clement Debacker, Junichi Hata, Hideyuki Okano, Akihiko Kitamura, Andrew Zalesky, and Toru Takumi. Awake functional MRI detects neural circuit dysfunction in a mouse model of autism. *Sci. Adv.*, 6(6):eaav4520, feb 2020.

doi: 10.1126/sciadv.aav4520. URL http://advances.sciencemag.org/content/6/6/eaav4520.abstract.

[240] Ilia D Vainchtein and Anna V Molofsky. Astrocytes and Microglia: In Sickness and in Health. *Trends Neurosci.*, 43(3):144–154, mar 2020. ISSN 0166-2236. doi: 10.1016/j.tins.2020.01.003. URL https://doi.org/10.1016/j.tins.2020.01.003.

[241] Jan van Gijn, Richard S Kerr, and Gabriel J E Rinkel. Subarachnoid haemorrhage. *Lancet (London, England)*, 369(9558):306–318, jan 2007. ISSN 1474-547X (Electronic). doi: 10.1016/S0140-6736(07)60153-6.

[242] Matthieu P. Vanni and Timothy H. Murphy. Mesoscale Transcranial Spontaneous Activity Mapping in GCaMP3 Transgenic Mice Reveals Extensive Reciprocal Connections between Areas of Somatomotor Cortex. *J. Neurosci.*, 34(48):15931–15946, nov 2014. ISSN 0270-6474. doi: 10.1523/JNEUROSCI.1818-14.2014. URL http://www.jneurosci.org/content/34/48/15931.abstracthttp://www.jneurosci.org/cgi/doi/10.1523/JNEUROSCI.1818-14.2014.

[243] Ananth K Vellimana, Eric Milner, Tej D Azad, Michael D Harries, Meng-Liang Zhou, Jeffrey M Gidday, Byung Hee Han, and Gregory J Zipfel. Endothelial nitric oxide synthase mediates endogenous protection against subarachnoid hemorrhage-induced cerebral vasospasm. *Stroke*, 42(3):776–782, mar 2011. ISSN 1524-4628 (Electronic). doi: 10.1161/STROKEAHA.110.607200.

[244] Ananth K Vellimana, Meng-Liang Zhou, Itender Singh, Diane J Aum, James W Nelson, Glenn R Harris, Umeshkumar Athiraman, Byung H Han, and Gregory J Zipfel. Minocycline protects against delayed cerebral ischemia after subarachnoid hemorrhage via matrix metalloproteinase-9 inhibition. *Ann. Clin. Transl. Neurol.*, 4(12):865–876, dec 2017. ISSN 2328-9503 (Print). doi: 10.1002/acn3.492.

[245] Ananth K Vellimana, Deepti Diwan, Julian Clarke, Jeffrey M Gidday, and Gregory J Zipfel. SIRT1 Activation: A Potential Strategy for Harnessing Endogenous Protection Against Delayed Cerebral Ischemia After Subarachnoid Hemorrhage. *Neurosurgery*, 65(CN_suppl_1):1–5, sep 2018. ISSN 1524-4040 (Electronic). doi: 10.1093/neuros/nyy201.

[246] Manasij Venkatesh, Joseph Jaja, and Luiz Pessoa. Comparing functional connectivity matrices: A geometry-aware approach applied to participant identification. *Neuroimage*, 207:116398, 2020. ISSN 1053-8119. doi: https://doi.org/10.1016/j.neuroimage.2019.116398. URL `https://www.sciencedirect.com/science/article/pii/S1053811919309899`.

[247] Mervyn D I Vergouwen, Marinus Vermeulen, Bert A Coert, Erik S G Stroes, and Yvo B W E M Roos. Microthrombosis after aneurysmal subarachnoid hemorrhage: an additional explanation for delayed cerebral ischemia. *J. Cereb. blood flow Metab. Off. J. Int. Soc. Cereb. Blood Flow Metab.*, 28(11):1761–1770, nov 2008. ISSN 1559-7016 (Electronic). doi: 10.1038/jcbfm.2008.74.

[248] Mervyn D I Vergouwen, Marinus Vermeulen, and Yvo B W E M Roos. Delayed cerebral ischemia after aneurysmal subarachnoid hemorrhage: is angiographic vasospasm an epiphenomenon?, feb 2009. ISSN 1524-4628 (Electronic).

[249] Mervyn D I Vergouwen, Marinus Vermeulen, Jan van Gijn, Gabriel J E Rinkel, Eelco F Wijdicks, J Paul Muizelaar, A David Mendelow, Seppo Juvela, Howard Yonas, Karel G Terbrugge, R Loch Macdonald, Michael N Diringer, Joseph P Broderick, Jens P Dreier, and Yvo B W E M Roos. Definition of delayed cerebral ischemia after aneurysmal subarachnoid hemorrhage as an outcome event in clinical trials and observational studies: proposal of a multidisciplinary research group. *Stroke*, 41(10):2391–2395, oct 2010. ISSN 1524-4628 (Electronic). doi: 10.1161/STROKEAHA.110.589275.

[250] Nathalia Vitureira, Mathieu Letellier, and Yukiko Goda. Homeostatic synaptic plasticity: from single synapses to neural circuits. *Curr. Opin. Neurobiol.*, 22(3):516–521, jun 2012. ISSN 1873-6882 (Electronic). doi: 10.1016/j.conb.2011.09.006.

[251] Vladyslav V Vyazovskiy, Umberto Olcese, Yaniv M Lazimy, Ugo Faraguna, Steve K Esser, Justin C Williams, Chiara Cirelli, and Giulio Tononi. Cortical Firing and Sleep Homeostasis. *Neuron*, 63(6):865–878, 2009. doi: https://doi.org/10.1016/j.neuron.2009.08.024. URL http://www.sciencedirect.com/science/article/pii/S0896627309006370.

[252] Vladyslav V. Vyazovskiy, Umberto Olcese, Erin C. Hanlon, Yuval Nir, Chiara Cirelli, and Giulio Tononi. Local sleep in awake rats. *Nature*, 472(7344):443–447, apr 2011. ISSN 1476-4687. doi: 10.1038/nature10009. URL https://pubmed.ncbi.nlm.nih.gov/21525926https://www.ncbi.nlm.nih.gov/pmc/articles/PMC3085007/.

[253] Bradley K Wacker, Jennifer L Perfater, and Jeffrey M Gidday. Hypoxic preconditioning induces stroke tolerance in mice via a cascading HIF, sphingosine kinase, and CCL2 signaling pathway. *J. Neurochem.*, 123(6):954–962, dec 2012. ISSN 1471-4159 (Electronic). doi: 10.1111/jnc.12047.

[254] Shuaishuai Wang, Zheng Wang, Shuo Yang, Tiemei Yin, Yaoli Zhang, Yuanjun Qin, Robert N Weinreb, and Xufang Sun. Tissue Distribution of trans-Resveratrol and Its Metabolites after Oral Administration in Human Eyes. *J. Ophthalmol.*, 2017:4052094, 2017. ISSN 2090-004X. doi: 10.1155/2017/4052094. URL https://pubmed.ncbi.nlm.nih.gov/28409021https://www.ncbi.nlm.nih.gov/pmc/articles/PMC5377058/.

[255] Zhong Wang, Cheng-Jie Meng, Xu-Ming Shen, Zhang Shu, Chao Ma, Guo-Qing Zhu, Hui-Xiang Liu, Wei-Chun He, Xue-Bo Sun, Lei Huo, Jian Zhang, and Gang Chen. Potential contribution of hypoxia-inducible factor-1α, aquaporin-4, and matrix

metalloproteinase-9 to blood-brain barrier disruption and brain edema after experimental subarachnoid hemorrhage. *J. Mol. Neurosci.*, 48(1):273–280, sep 2012. ISSN 1559-1166 (Electronic). doi: 10.1007/s12031-012-9769-6.

[256] Pengxu Wei, Zuting Zhang, Zeping Lv, and Bin Jing. Strong Functional Connectivity among Homotopic Brain Areas Is Vital for Motor Control in Unilateral Limb Movement. *Front. Hum. Neurosci.*, 11:366, jul 2017. ISSN 1662-5161. doi: 10.3389/fnhum.2017.00366. URL `https://pubmed.ncbi.nlm.nih.gov/28747880https://www.ncbi.nlm.nih.gov/pmc/articles/PMC5506200/`.

[257] David Wellington, Igor Mikaelian, and Laura Singer. Comparison of ketamine-xylazine and ketamine-dexmedetomidine anesthesia and intraperitoneal tolerance in rats. *J. Am. Assoc. Lab. Anim. Sci.*, 52(4):481–487, 2013. URL `https://www.ncbi.nlm.nih.gov/pubmed/23849447https://www.ncbi.nlm.nih.gov/pmc/articles/PMC3725934/`.

[258] David Wellington, Igor Mikaelian, Laura Singer, Vladyslav V. Vyazovskiy, Umberto Olcese, Erin C. Hanlon, Yuval Nir, Chiara Cirelli, Giulio Tononi, Enzo Tagliazucchi, Helmut Laufs, Maggie B Struck, Karl A Andrutis, Harvey E Ramirez, August H Battles, Jamie Sleigh, Martyn Harvey, Logan Voss, Bill Denny, Gergely Silasi, Dongsheng Xiao, Matthieu P Vanni, Andrew C N Chen, Timothy H Murphy, Daisuke Shimaoka, Chenchen Song, Thomas Knöpfel, Niels Niethard, Hong-Viet V Ngo, Ingrid Ehrlich, Jan Born, Anish Mitra, Abraham Z Snyder, Carl D Hacker, Mrinal Pahwa, Enzo Tagliazucchi, Helmut Laufs, Eric C Leuthardt, Marcus E Raichle, Marcello Massimini, Reto Huber, Fabio Ferrarelli, Sean Hill, Giulio Tononi, Miranda M Lim, Jason R Gerstner, David M Holtzman, Jacqueline M Leung, Laura P Sands, Stacey Newman, Gabriela Meckler, Yimeng Xie, Caryl Gay, Kathryn Lee, Y E Ju, B P Lucey, David M Holtzman, H Johansen-Berg, Silvina G Horovitz, A R Braun, W S Carr,

Dante Picchioni, T J Balkin, M Fukunaga, Jeff H Duyn, C J Honey, Olaf Sporns, L Cammoun, X Gigandet, J P Thiran, R Meuli, P Hagmann, Tuija Hiltunen, Jussi Kantola, Ahmed Abou Elseoud, Pasi Lepola, Kalervo Suominen, Tuomo Starck, Juha Nikkinen, Jukka Remes, Osmo Tervonen, Satu Palva, Vesa J Kiviniemi, J Matias Palva, Ulrich Hemmeter, Roland Bischof, Martin Hatzinger, Erich Seifritz, Edith Holsboer-Trachsler, B J He, G M Hathout, R K Gopi, P Bandettini, S S Gambhir, Ralph Gertler, H Cleighton Brown, Donald H Mitchell, Erin N Silvius, Karl J Friston, Andrew P Holmes, Keith J Worsley, W J Freeman, L J Rogers, M D Holmes, D L Silbergeld, Isabelle Ferezou, Sonia Bolea, Carl C H Petersen, Adam T Eggebrecht, Brian R White, Silvina L Ferradal, Chunxiao Chen, Yuxuan Zhan, Abraham Z Snyder, Hamid Dehghani, Joseph P Culver, Thien Thanh Dang-Vu, Martin Desseilles, Steven Laureys, Christian Degueldre, Fabien Perrin, Christophe Phillips, Pierre Maquet, Philippe Peigneux, Sylvain Chauvette, Sylvain Crochet, Maxim Volgushev, Igor Timofeev, Allen W Chan, Majid H Mohajerani, Jeffrey M LeDue, Yu Tian Wang, Timothy H Murphy, Sandra Buitrago, Thomas E Martin, Joanne Tetens-Woodring, Alan Belicha-Villanueva, Gregory E Wilding, M Boly, R Moran, M Murphy, P Boveroux, M A Bruno, Q Noirhomme, D Ledoux, V Bonhomme, J F Brichant, Giulio Tononi, Steven Laureys, Karl J Friston, Liana G Apostolova, Paul M Thompson, J S Anderson, M A Ferguson, M Lopez-Larson, D Yurgelun-Todd, F Amzica, M Steriade, Michael T Alkire, Jason Miller, Oluwaseun Akeju, Andrew H Song, Allison E Hamilos, Kara J Pavone, Francisco J Flores, Emery N Brown, Patrick L Purdon, M Steriade, Igor Timofeev, F Grenier, A A Borbély, P Achermann, Y Harrison, J A Horne, H Scheinin, R Aantaa, M Anttila, P Hakola, A Helminen, S Karhuvaara, Oluwaseun Akeju, S E Kim, R Vazquez, J Rhee, Kara J Pavone, L E Hobbs, Patrick L Purdon, Emery N Brown, Dongsheng Xiao, Matthieu P Vanni, C C Mitelut, Allen W Chan, Jeffrey M LeDue, Yimeng Xie, Andrew C N Chen, N V Swindale, Timothy H Murphy,

Yo Oishi, Yohko Takata, Yujiro Taguchi, Sayaka Kohtoh, Yoshihiro Urade, Michael Lazarus, Irene Tobler, Alexander A Borbrly, Laura E Nelson, Jun Lu, Tianzhi Guo, Clifford B Saper, Nicholas P Franks, Mervyn Maze, C Correa-Sales, B C Rabin, Mervyn Maze, Róisín Ní Mhuircheartaigh, Debbie Rosenorn-Lanng, Richard Wise, Saad Jbabdi, Richard Rogers, Irene Tracey, Majid H Mohajerani, David A Mcvea, Matthew Fingas, Timothy H Murphy, Philipp G Sämann, Renate Wehrle, David Hoehn, Victor I Spoormaker, Henning Peters, Carolin Tully, Florian Holsboer, Michael Czisch, Dante Picchioni, Jeff H Duyn, Silvina G Horovitz, Bharat B Biswal, F Z Yetkin, V M Haughton, James S Hyde, Stuart W Hughes, Magor L Lorincz, H Rheinallt Parri, Vincenzo Crunelli, Danielle S Bassett, Olaf Sporns, Stephen M Steve M Smith, Diego Vidaurre, Christian F Beckmann, Matthew F Glasser, Mark Jenkinson, Karla L Miller, Thomas E Nichols, Emma C Robinson, Gholamreza Salimi-Khorshidi, Mark W Woolrich, Deanna M Barch, Kamil Uğurbil, David C Van Essen, Marcus E Raichle, Bharat B Biswal, Maarten Mennes, Xi-Nian Zuo, Suril Gohel, Clare Kelly, Stephen M Steve M Smith, Christian F Beckmann, Jonathan S Adelstein, Randy L Buckner, Stan Colcombe, Anne-Marie Dogonowski, Monique Ernst, Damien Fair, Michelle Hampson, Matthew J Hoptman, James S Hyde, Vesa J Kiviniemi, Rolf Kötter, Shi-Jiang Li, Ching-Po Lin, Mark J Lowe, Clare Mackay, David J Madden, Kristoffer H Madsen, Daniel S Margulies, Helen S Mayberg, Katie McMahon, Christopher S Monk, Stewart H Mostofsky, Bonnie J Nagel, James J Pekar, Scott J Peltier, Steven E Petersen, Valentin Riedl, Serge A R B Rombouts, Bart Rypma, Bradley L Schlaggar, Sein Schmidt, Rachael D Seidler, Greg J Siegle, Christian Sorg, Gao-Jun Teng, Juha Veijola, Arno Villringer, Martin Walter, Lihong Wang, Xu-Chu Weng, Susan Whitfield-Gabrieli, Peter Williamson, Christian Windischberger, Yu-Feng Zang, Hong-Ying Zhang, F Xavier Castellanos, and Michael P Milham. Natural waking and sleep states: a view from inside neocortical neurons. *Neuroimage*, 4(3):1969–1985,

oct 2014. ISSN 0003-3022 (Print). doi: 10.1523/JNEUROSCI.6437-09.2010. URL http://www.pnas.org/content/107/10/4734.abstracthttps://doi.org/10.1038/nn.4502https://pubmed.ncbi.nlm.nih.gov/21854961https://www.ncbi.nlm.nih.gov/pmc/articles/PMC3173874/https://www.ncbi.nlm.nih.gov/pubmed/28160463https://www.ncbi.nlm.nih.gov/pubme.

[259] Brian R. White, Adam Q. Bauer, Abraham Z. Snyder, Bradley L. Schlaggar, Jin-Moo Moo Lee, and Joseph P. Culver. Imaging of functional connectivity in the mouse brain. *PLoS One*, 6(1):1–10, jan 2011. ISSN 1932-6203. doi: 10.1371/journal.pone.0016322. URL https://pubmed.ncbi.nlm.nih.gov/21283729https://www.ncbi.nlm.nih.gov/pmc/articles/PMC3024435/.

[260] Erik A Wing, Benjamin R Geib, Wei-Chun Wang, Zachary Monge, Simon W Davis, and Roberto Cabeza. Cortical Overlap and Cortical-Hippocampal Interactions Predict Subsequent True and False Memory. *J. Neurosci.*, 40(9):1920 LP – 1930, feb 2020. doi: 10.1523/JNEUROSCI.1766-19.2020. URL http://www.jneurosci.org/content/40/9/1920.abstract.

[261] Ian R Winship and Timothy H Murphy. Remapping the somatosensory cortex after stroke: insight from imaging the synapse to network. *Neurosci. a Rev. J. bringing Neurobiol. Neurol. psychiatry*, 15(5):507–524, oct 2009. ISSN 1089-4098 (Electronic). doi: 10.1177/1073858409333076.

[262] George F Wittenberg. Experience, cortical remapping, and recovery in brain disease. *Neurobiol. Dis.*, 37(2):252–258, feb 2010. ISSN 1095-953X. doi: 10.1016/j.nbd.2009.09.007. URL https://pubmed.ncbi.nlm.nih.gov/19770044https://www.ncbi.nlm.nih.gov/pmc/articles/PMC2818208/.

[263] T A Woolsey, C M Rovainen, S B Cox, M H Henegar, G E Liang, D Liu, Y E

Moskalenko, J Sui, and L Wei. Neuronal units linked to microvascular modules in cerebral cortex: response elements for imaging the brain. *Cereb. Cortex*, 6(5):647–660, 1996. ISSN 1047-3211 (Print). doi: 10.1093/cercor/6.5.647.

[264] Susan L Worley. The Extraordinary Importance of Sleep: The Detrimental Effects of Inadequate Sleep on Health and Public Safety Drive an Explosion of Sleep Research. *P T*, 43(12):758–763, dec 2018. ISSN 1052-1372. URL https://pubmed.ncbi.nlm.nih.gov/30559589https://www.ncbi.nlm.nih.gov/pmc/articles/PMC6281147/.

[265] Patrick. W Wright, Lindsey. M Brier, Adam. Q Bauer, Grant. A Baxter, Andrew. W Kraft, Matthew. D Reisman, Annie. R Bice, Abraham. Z Snyder, Jin-Moo Moo. Lee, and Joseph. P Culver. Functional Connectivity Structure of Cortical Calcium Dynamics in Anesthetized and Awake Mice. *PLoS One*, 12 (10):e0185759–e0185759, oct 2017. ISSN 1932-6203. doi: 10.1371/journal.pone.0185759. URL https://pubmed.ncbi.nlm.nih.gov/29049297https://www.ncbi.nlm.nih.gov/pmc/articles/PMC5648115/.

[266] Shanshan Wu, Yu Zeng, Alexander Lerner, Bo Gao, and Meng Law. Nervous System Injury and Neuroimaging of Zika Virus Infection. *Front. Neurol.*, 9:227, apr 2018. ISSN 1664-2295. doi: 10.3389/fneur.2018.00227. URL https://pubmed.ncbi.nlm.nih.gov/29740383https://www.ncbi.nlm.nih.gov/pmc/articles/PMC5926540/.

[267] Dongsheng Xiao, Matthieu P Vanni, Catalin C Mitelut, Allen W Chan, Jeffrey M LeDue, Yicheng Xie, Andrew C N Chen, Nicholas V Swindale, and Timothy H Murphy. Mapping cortical mesoscopic networks of single spiking cortical or sub-cortical neurons. *Elife*, 6:1–28, 2017. doi: 10.7554/eLife.19976. URL https://www.ncbi.nlm.nih.gov/pubmed/28160463.

[268] G B Young, C F Bolton, T W Austin, Y M Archibald, J Gonder, and G A Wells. The

encephalopathy associated with septic illness. *Clin. Invest. Med.*, 13(6):297–304, dec 1990. ISSN 0147-958X (Print).

[269] G Bryan Young. Encephalopathy of infection and systemic inflammation. *J. Clin. Neurophysiol. Off. Publ. Am. Electroencephalogr. Soc.*, 30(5):454–461, oct 2013. ISSN 1537-1603 (Electronic). doi: 10.1097/WNP.0b013e3182a73d83.

[270] Yujin Zhang and Chaozhe Zhu. Assessing Brain Networks by Resting-State Dynamic Functional Connectivity: An fNIRS-EEG Study , 2020. URL `https://www.frontiersin.org/article/10.3389/fnins.2019.01430`.

[271] Xue Zhong, Huqing Shi, Qingsen Ming, Daifeng Dong, Xiaocui Zhang, Ling-Li Zeng, and Shuqiao Yao. Whole-brain resting-state functional connectivity identified major depressive disorder: A multivariate pattern analysis in two independent samples. *J. Affect. Disord.*, 218:346–352, aug 2017. ISSN 1573-2517 (Electronic). doi: 10.1016/j.jad.2017.04.040.

[272] Xia Zhu, Mu-Huo Ji, Shu-Ming Li, Bin Li, Li Mei, and Jian-Jun Yang. Systemic Inflammation Impairs Mood Function by Disrupting the Resting-State Functional Network in a Rat Animal Model Induced by Lipopolysaccharide Challenge. *Mediators Inflamm.*, 2019:6212934, may 2019. ISSN 1466-1861. doi: 10.1155/2019/6212934. URL `https://pubmed.ncbi.nlm.nih.gov/31210750https://www.ncbi.nlm.nih.gov/pmc/articles/PMC6532295/`.

[273] Giulio Zuccoli and Nicolò Pipitone. Neuroimaging Findings in Acute Wernicke's Encephalopathy: Review of the Literature. *Am. J. Roentgenol.*, 192(2):501–508, feb 2009. ISSN 0361-803X. doi: 10.2214/AJR.07.3959. URL `https://doi.org/10.2214/AJR.07.3959`.